The Henryk Niewodniczański
Institute of Nuclear Physics
Polish Academy of Sciences

Exploring the electronic structure of Zinc Selenide Quantum Dots

MSc Rafał Fanselow

Doctoral thesis

Prepared under supervision of dr. hab. Jakub Szlachetko (prof. UJ)
and dr. hab. Joanna Czapla-Masztafiak (assistant supervisor)
in the Department of Applied Spectroscopy
Division of Interdisciplinary Research

Kraków 2024

Acknowledgments

I would like to express my deepest gratitude to:

My supervisor, ***dr. hab. Jakub Szlachetko*** *(prof. UJ)*
for providing me with the opportunity to realize such a fascinating research project, sharing his knowledge, support, inspiration, indulgence, and expanding my scientific horizons,

My assistant supervisor, ***dr. hab. inż. Joanna Czapla-Masztafiak***
for sharing her experience and supporting me during the preparation of this thesis,

All the present and former members of the Department of Applied Spectroscopy of IFJ PAN I had the pleasure to work with:
prof. dr. hab. Wojciech Kwiatek*,* ***dr. hab. Janusz Lekki, dr. Anna Wach, dr. Wojciech Błachucki, dr. Gabriela Imbir, dr. Artem Yakovliev, dr. Wiktoria Stańczyk, dr. Krzysztof Tyrała, dr. Klaudia Wojtaszek, Zbigniew Szaklarz, Tomasz Pieprzyca, Kamila Krzystanek and Monika Ławik*** *for their advice, fruitful discussions and pleasant working environment,*

Prof. Jacinto Sá, dr. Anna Zymaková, dr. Mateusz Rebarz, dr. Alexey Maximenko and all other scientists *I had an opportunity to meet, cooperate and learn from during my PhD Studies,*

My colleagues *from the Kraków School of Interdisciplinary PhD Studies, for a fun atmosphere and providing a space to share our thoughts and troubles,*

My friends and family*, especially my* ***Mum****,* ***Dad*** *and* ***Sister****, for their constant support and belief in me,*

My Fiancée*,* ***Aleksandra****, for always being there for me, understanding me like no other, and being an awesome life companion.*

Abstract

This work explores the quantum and structural effects in the electronic structure of ZnSe quantum dots (QDs). These are nanometer-scale semiconductor particles that, due to the quantum confinement effect, exhibit unique size-dependent optical and electronic properties that can be precisely controlled and potentially employed in a plethora of applications, including advanced display devices and energy-harvesting solar cells. The performance of the QDs-based technology is strongly affected by quantum confinement and surface and defect states that alter the energy landscape of the material. This thesis aims to characterize the effects influencing the electronic energy structure in ZnSe QDs.

The goals of the work were addressed by applying two groups of spectroscopic methods, each providing different information regarding the electronic states in investigated materials. The first, optical spectroscopies, probe outer-shell transitions in QDs systems, allowing assessing the size-dependent quantum confinement effects, manifested as a shift of energy spacings between valence and conduction electron levels, especially the bandgap energy. The second, X-ray spectroscopy, utilizes more energetic photons that interact with strongly bounded inner-shell electrons, allowing element-specific and structure-sensitive studies of the unoccupied and occupied electronic states of the system through X-ray absorption spectroscopy (XAS) or X-ray emission spectroscopy (XES), respectively.

ZnSe QDs samples with varying particle sizes were synthesized via a heat-up wet chemical route. Four QDs samples were obtained with mean particle diameters of 4.1 (±0.5), 5.2 (±0.6), 7.0 (±0.9), and 9.5 (±1.0) nm determined by the Scanning Transmission Electron Microscopy measurements. The steady-state UV-Vis absorption and photoluminescence spectroscopy, supplemented with electron microscopy images, allowed confirmation of the preparation of high-quality nanometer particles and established the size-dependent relation of QDs optical absorption. The initial XAS and XES experiments, conducted utilizing a laboratory-based von Hámos X-ray spectrometer, allowed preliminary evaluation of chemical and structural effects in investigated QDs. Notably, the studies were performed in the ZnSe QDs native environment, thanks to the dedicated development of the sample cell allowing for analysis of the liquid form of nanomaterial suspensions.

The two key experiments revealing the dominant contributions in ZnSe QDs electronic structure were realized at two of the most advanced large-scale facilities in east-central Europe for material science research, namely the SOLARIS National Synchrotron Radiation Centre and ELI Beamlines laser center. The first experiment allowed attributing the subtle effects in X-ray absorption spectra to the presence of Zn vacancies in the QDs lattice. The second experiment characterized the role of surface and defect channels in the charge carrier recombination dynamics through pump-probe time-resolved transient optical spectroscopy studies.

In the final part, the thesis theorizes about expanding the time-dependent studies of carrier dynamics in ZnSe QDs to experiments at X-ray free electron lasers (XFELs) with (sub-)fs temporal resolution. Such measurements, currently unavailable with any X-ray

facility, may potentially be realized by precise time profile characterization of femtosecond X-ray pulses, the basis of X-ray Chronoscopy. Performed simulations of X-ray-matter interactions showed that the proposed methodology can quantitatively follow the femtosecond electron processes in pump-probe experiments at XFELs.

Streszczenie

Celem niniejszej rozprawy doktorskiej jest zbadanie wpływu kwantowych i strukturalnych efektów na strukturę elektronową kropek kwantowych selenku cynku (ZnSe), czyli nanometrycznych półprzewodnikowych cząstek, które z powodu tzw. efektu ograniczenia kwantowego charakteryzują się unikalnymi właściwościami optycznymi determinowanymi przez rozmiar obiektu. Zrozumienie czynników wpływających na elektronowe poziomy energetyczne, takich jak rola atomów powierzchniowych czy defektów, pozwoli zoptymalizować wydajność i produkcję przyszłych technologii opartych na kropkach kwantowych, takich jak wyświetlacze nowej generacji czy hybrydowe ogniwa słoneczne.

W trakcie przeprowadzonych eksperymentów wykorzystano dwa typy technik spektroskopowych, dostarczających różnych, wzajemnie się uzupełniających, informacji na temat struktury elektronowej badanych materiałów. Po pierwsze, metody spektroskopii optycznej, próbkujące przejścia elektronowe między zewnętrznymi zapełnionymi poziomami walencyjnymi a nieobsadzonymi poziomami przewodnictwa, pozwoliły ocenić wpływ efektu ograniczenia kwantowego w nanostrukturach m.in.. poprzez pomiar, zależnej od rozmiaru kropek kwantowych, energetycznej przerwy wzbronionej. Drugim ze stosowanych narzędzi badawczych były techniki spektroskopii rentgenowskiej, wykorzystujące wysokoenergetyczne promieniowanie X, zdolne do oddziaływania z elektronami silnie związanymi na wewnętrznych powłokach atomowych. Rentgenowska spektroskopia absorpcyjna (XAS) oraz emisyjna (XES) umożliwiły zbadanie nieobsadzonych oraz zapełnionych stanów elektronowych z pierwiastkową i strukturalną selektywnością.

Próbki kropek kwantowych ZnSe o średnich rozmiarach cząstek wynoszących odpowiednio 4.1 (±0.5), 5.2 (±0.6), 7.0 (±0.9) i 9.5 (±1.0) nm zostały otrzymane na drodze wysokotemperaturowej chemicznej syntezy w środowisku ciekłym. Pomiary z wykorzystaniem spektroskopii UV-Vis i fotoluminescencji wsparte obrazami uzyskanymi za pomocą mikroskopii elektronowej potwierdziły otrzymanie wysokiej jakości próbek, a także umożliwiły powiązanie właściwości optycznych kropek kwantowych z ich rozmiarami. Analizy XAS i XES przeprowadzone z wykorzystaniem laboratoryjnego spektrometru rentgenowskiego pozwoliły na wstępną ocenę chemicznych i strukturalnych efektów w przygotowanych materiałach. Co ważne, eksperymenty rentgenowskie wykonano dla kropek kwantowych zawieszonych w rozpuszczalniku, dzięki zaprojektowanej celce pomiarowej dedykowanej do analizy ciekłych suspensji.

Kluczowe eksperymenty w kontekście realizacji celów pracy przeprowadzono w dwóch wielkoskalowych ośrodkach badawczych zajmujących się zaawansowanymi badaniami materiałowymi, czyli w Narodowym Centrum Promieniowania Synchrotronowego SOLARIS i centrum laserowym ELI Beamlines. Eksperyment z wykorzystaniem promieniowania synchrotronowego pozwolił na zidentyfikowanie strukturalnych efektów w zmierzonych widmach XAS i przypisanie ich do wakancji cynkowych obecnych w sieci badanych kropek kwantowych. Prace badawcze w ośrodku ELI Beamlines, podczas których zastosowano czasowo-rozdzielczą technikę optycznej

absorpcji przejściowej dostarczyły informacji dotyczących dominującej roli efektów powierzchniowych i innych defektów w procesach relaksacji wzbudzonych nośników ładunku.

Końcowa część pracy skupia się na teoretycznych rozważaniach związanych z rozszerzeniem czasowo-rozdzielczych pomiarów dynamiki elektronowej w kropkach kwantowych ZnSe o eksperymenty wykorzystujące lasery rentgenowskie na swobodnych elektronach (XFELs) w oparciu koncept Chronoskopii rentgenowskiej. Główną ideą proponowanej techniki jest precyzyjny pomiar profilów czasowych ultrakrótkich impulsów rentgenowskich transmitowanych przez badaną próbkę, co potencjalnie pozwoli ominąć obecne ograniczenia wynikające ze zbyt dużego rozmycia czasowego impulsów XFEL. Przeprowadzone w pracy numeryczne symulacje interakcji impulsów rentgenowskich z materią wykazały, że zastosowanie Chronoskopii rentgenowskiej umożliwia ilościowe śledzenie (sub-)femtosekundowych procesów elektronowych w tzw. eksperymentach pump-probe wykorzystujących źródła XFEL.

Table of contents

List of abbreviations

QDs – quantum dots

XAS – X-ray absorption spectroscopy

XES – X-ray emission spectroscopy

XFELs – X-ray free electron lasers

VB – valence band

CB – conduction band

NCs – nanocrystals

NPs – nanoparticles

DOS – density of states

IR – infrared

UV – ultraviolet

Vis – visible

IUPAC – the International Union of Pure and Applied Chemistry

RoHS - European Restriction of Hazardous Substances Directive

LED – light-emitting diode

QLED – quantum dot light-emitting diode

CCD – charge-coupled device

PL – photoluminescence

TA – transient absorption

ESA – excited state absorption

GSB – ground state bleach

SE – stimulated emission

IRF – instrument response function

XANES – X-ray absorption near edge structure

E_0 – absorption edge energy

EXAFS – extended X-ray absorption fine structure

FY– fluorescence yield

EY– electron yield

NXES – non-resonant X-ray emission spectroscopy

RXES – resonant X-ray emission spectroscopy

RXIS – resonant inelastic X-ray scattering

RF – radio frequency

SASE – Self Amplified Spontaneous Emission

EDS – energy-dispersive spectrometry

WDS – wavelength-dispersive spectrometry

SSD – silicon drift detector

OA – oleic acid

ODE – 1-Octadecene

$Zn(St)_2$ – zinc stearate

$Zn(OAc)_2 \cdot H_2O$ - zinc acetate dihydrate

SEM – scanning electron microscopy

TEM – transmission electron microscopy

STEM – scanning transmission microscopy

CMOS – complementary metal-oxide semiconductor

PLA – polylactide

PVC – polyvinyl chloride

DCM – double crystal monochromator

FWHM – full width at half maximum

1. Introduction

Nowadays, the world is in an uncertain state, with many challenges on the horizon, including the ever-growing energy demand, health prolongation, and environment preservation as one of the major concerns. A potential answer to these issues may be nanotechnology, which deals with objects with characteristic sizes of single nanometers (a billionth of a meter). Since the birth of the field, thousands of researchers around the globe participate in the studies and development of various nanostructures to create a better tomorrow for our society.

A milestone in nanotechnology history occurred in the early 1980s when, on both sides of the Iron Curtain, Aleksey Yekimov and Luis Brus independently observed intriguing size-dependent optical responses of tiny semiconductor nanocrystals. Both pursued research on these fascinating objects, unveiling the role of the quantum confinement effect as the reason behind the unique features of the nanometer semiconductor particles. After early successes, other researchers quickly joined the designated direction by Yekimov and Burs. In particular, Moungi Bawendi significantly improved chemical routes of producing monodisperse particles with precise size control, allowing a more detailed investigation of their size-dependent properties. In 2023, all three scientists shared the Nobel Prize in chemistry for the discovery and synthesis of the now-called quantum dots (QDs). Specifically, the award was given, highlighting numerous scopes of real-life applications, starting from energy harvesting and displays through communication technologies to medical diagnostics.

While the Nobel Prize undoubtedly summited the role of QDs among other key nanomaterials, it does not conclude the QDs research field. On the contrary, the subject is more vivid than ever, expanding the fundamental knowledge, producing more sophisticated multi-compound structures, and examining more material types to broaden the usage range. In particular, the latter aims at substituting well-explored Cd- and Pb-based QDs, which constitute significant health and environmental hazards, with alternative compounds simultaneously preserving the high performance of the materials. One of such specie is Zinc selenide (ZnSe), a wide-bandgap compound with promising electronic properties covering the high-energy part of the visible spectrum. Although ZnSe QDs have been on the horizon almost since the discovery of the quantum confined effect, only recently have emerged as the leading research target. However, obtaining ZnSe QDs technologies requires clarifying all factors influencing the electronic structure of these compounds. For example, Zn atoms are known to be very reactive and prone to undergo surface reactions, introducing trap states within the energy bandgap. Additionally, the difference between Zn and Se ion's radius may result in the appearance of lattice defects. These effects would highly modify the optical and electronic properties of ZnSe QDs, such as inducing alternative carrier relaxation channels. All of this is on top of the size-dependent quantum confinement effect, shifting the energy of the atomic levels. The research described in this work attempts to shine more light on the matter, paving the way for the future development of advanced ZnSe QDs structures.

This thesis aims to characterize size-dependent contributions influencing the electronic structure of ZnSe QDs.

The structure of the thesis is as follows. The work is divided into 11 chapters, including the present introductory section. The next three chapters constitute the theoretical part, which intends to familiarize the reader with essential information regarding the investigated materials and experimental techniques applied to achieve the thesis aims.

Chapter 2 is dedicated entirely to the science behind QDs. It starts by briefly recapping the basics of bulk semiconductor physics and changes associated with the transition into the quantum confinement regime. The unique size-dependent properties of QDs are discussed, separating the features resulting from quantum phenomena and geometrical scaling effects typical to all nanostructures. Particular interest is given to the relaxation of charge carriers as the electron and hole dynamics landscape in QDs is much more complicated than their bulk counterparts. Afterwards, the chapter describes the fundamental principles of nucleation and particle growth, followed by their implementation schemes to produce high-quality colloidal QDs. Different material classes are reviewed, highlighting their potential future applications. Finally, the section ends by discussing state-of-the-art research and the current knowledge gap, especially in the context of ZnSe QDs.

Chapter 3 is devoted to the principles and operation of optical spectroscopy that utilizes visible and ultraviolet radiation to probe outer shell electronic transitions in matter. These techniques play a central role in exploring the confinement effects in the electronic structure of QDs by providing a direct view into the materials' bandgap energy and recombination pathways of excited charge carriers. Fundamentals and instrumentation of UV-Vis absorption spectroscopy, photoluminescence spectroscopy, and time-resolved transient absorption spectroscopy are provided, focusing on their application in QDs research.

Chapter 4 presents the second group of methods widely utilized in this work, X-ray spectroscopy. Following a short introduction regarding X-ray-matter interactions, the section focuses on two main techniques, namely X-ray absorption spectroscopy (XAS) and X-ray emission spectroscopy (XES), indicating the specific information about examined objects each approach delivers. Particular attention is given to different levels of X-ray production, starting from low-cost X-ray tubes to large-scale facilities involving synchrotrons and X-ray free electron lasers (XFELs), discussing their role in X-ray spectroscopy research. Subsequently, an overview of X-ray detectors and spectrometer types is provided, emphasizing the advantages and limitations of each approach. The chapter ends with a few examples of case studies where X-ray spectroscopy was applied to solve research problems related to QDs.

Following the theoretical part, chapter 5 revisits the aims of the thesis, describing them in more detail and discussing intermediate steps covered in different sections of the subsequent experimental part, consisting of five additional chapters.

Chapter 6 describes the preparation of ZnSe QDs samples and the characterization of their essential parameters that confirm the quality of obtained products. The section starts with an overview of applied equipment for the oxygen-free wet chemical synthesis of colloidal QDs. The utilized procedure of QD fabrication is explained step-by-step,

discussing the purpose of each stage and added precursor. The material characterization involved scanning transmission electron microscopy to determine the particle size distribution of obtained samples. Additionally, steady-state UV-Vis and photoluminescence spectroscopy measurements allowed assessing the quantum confinement effects in prepared materials, primarily size-dependence of the bandgap energy. The acquired results are compared to literature reports to evaluate the representativity of the samples relative to other ZnSe QDs.

Chapter 7 presents the XAS and XES experiments performed on the custom-made laboratory-based X-ray spectrometer at the Institute of Nuclear Physics PAN to explore electronic structure in ZnSe QDs samples. First, attention is given to optimizing setup performance and developing calibration procedures, focusing on the energy range corresponding to investigated materials. Subsequently, the chapter describes the specialized sample cell designed for measuring liquid nanomaterial suspensions. Finally, the XAS and XES measurements on the synthesized ZnSe QDs supplemented with the reference compounds are presented and discussed. Results indicated the structural and chemical changes in the studied samples in relation to bulk ZnSe semiconductor material. Based on the available reports, these changes were attributed to the possible existence of defects in the QDs crystal lattice.

Chapter 8 transitions from laboratory-based X-ray spectroscopy to experiments conducted at a large-scale facility, namely, SOLARIS National Synchrotron Radiation Centre in Kraków (Poland). The superior X-ray beam qualities of the synchrotron source allowed a more detailed XAS examination of the synthesized samples, revealing subtle effects and trends in investigated ZnSe QDs samples. Acquired spectra are first compared with laboratory-based X-ray spectroscopy results to evaluate the capabilities of in-house instrumentation. Then, based on the theoretical calculations utilizing FEFF 9.6 code, the obtained synchrotron XAS spectra were analyzed, searching for surface and defect imprints in the electronic structure of studied samples. While the performed spectra simulations did not attribute the origin of all measured effects, the obtained results strongly point to the existence of Zn vacancies in each studied QDs sample, confirming and expanding the conclusions of laboratory experiments.

The work described in Chapter 9 attempts to evaluate the effects of surface and Zn defects on carrier relaxation dynamics in ZnSe QDs through pump-probe femtosecond optical transient absorption spectroscopy measurements carried out at ELI Beamlines facility in Dolní Břežany (Czech Republic). Analysis of the transient spectra and their kinetic traces revealed two dominant phenomena, dominating the decay of the excited electrons and holes. The first process was attributed to surface trapping. The second effect was assigned to in-lattice defects, which, based on synchrotron XAS studies, is the contribution of Zn vacancies. All results are discussed in the context of other QD types.

Chapter 10 expands the experimental part of the thesis with theoretical consideration regarding potential sub-fs time-dependent experiments on ZnSe QDs at X-ray free electron lasers using the novel approach of X-ray Chronoscopy. The chapter starts by presenting the current state of XFEL research, followed by an explanation of the X-ray Chronoscopy concept and its prospects of bypassing current limiting factors of time-resolved X-ray spectroscopy. Numerical simulations are conducted to evaluate the capabilities of the

proposed methodology to study electron dynamics in matter, specifically ZnSe QDs, induced by ultrashort optical pulses. Performed calculations allowed determining the expected experimental precision of X-ray Chronoscopy measurements at XFELs.

Conclusions made throughout the thesis are summarized in the final Chapter 11, accompanied by a brief discussion of its implications and future perspectives.

It is worth emphasizing that the results presented in Chapter 7 were also the subject of two publications: **Performance of a laboratory von Hámos type X-ray spectrometer in X-ray absorption spectroscopy study on 3d group metals** published in X-ray Spectrometry[1] and **Microliter-stirred sample setup for X-ray spectroscopy analysis of nanomaterials in suspension** published in Spectrochimica Acta Part B: Atomic Spectroscopy.[2] Additionally, the work discussed through chapters 7-9 was conducted as a part of the National Science Centre of Poland (NCN) OPUS 19 project number 2020/37/B/ST3/00555 entitled **Application of time-resolved X-ray spectroscopy to determine electron and hole energy distributions upon plasmonic excitation of metallic nanoparticles**. Similarly, the work presented in chapter 10 was supported by NCN under OPUS 14 grant number 2017/27/B/ST2/01890: **X-ray Chronoscopy – a new route for tracing sub-femtosecond dynamics in matter**.

2. Quantum Dots

2.1 From bulk semiconductors to 0-dimensional Quantum Dots

A good starting point for understanding the quantum dots' extraordinary features is the prior consideration of bulk semiconductors. Such materials comprise numerous atoms (~10^{22}-10^{23} per cm^3) typically arranged in an ordered structure. While a single isolated atom is characterized by discrete energy levels of its electrons, their large assembly, due to the Pauli exclusion principle, results in a blending of separate outer-shell states into a continuous energy band structure of a macroscopic object. From the point of view of material optical and electronic properties, the most essential are the valence band (VB) corresponding to bound electrons lying in the outermost (valence) atomic shell and the lowest conduction band (CB). In semiconductors, the VB is separated from the CB by the forbidden energy range called bandgap. Suppose sufficient energy (higher than the bandgap energy) is delivered to the bounded electron, for example, by absorption of a photon. In that case, the electron can be promoted to the CB, leaving an unoccupied state in the VB. This vacancy effectively acts as a positively charged quasiparticle (hole) that can interact with the newly created CB electron through attractive Coulombic forces, forming a bounded state called exciton.[3] Such electron-hole pair can be mathematically described using a simple Bohr model to evaluate the exciton binding energy and the distance at which electron and hole orbit each other (exciton Bohr radius).[4] For most inorganic compounds, the energy at which exciton dissociates is in the range of a few to tens of meV, often smaller than the thermal energy at room temperature (25.7 meV). As a result, in bulk semiconductors, both particles act as free charge carriers that propagate within the material's lattice.[5] However, the situation drastically changes when the semiconductor size is reduced to lengths corresponding to its exciton Bohr radius, typically several nanometers. The CB electron and VB hole are squashed into smaller volumes, increasing the exciton energy, a phenomenon known as the quantum confinement effect.[5] If only one dimension of the material shrinks to the quantum confinement regime, charge carriers can still move freely in two directions, and such structures are referred to as quantum wells.[6] Similarly, systems where 2-dimensional confinement of excitons occurs are called (1-dimensional) quantum wires. Finally, objects in which the quantum confinement effect manifests in all three directions are named quantum dots (QDs). These 0-dimensional crystals constitute a new class of materials with unique properties arising due to effects characteristic to the nanoworld.

Before proceeding to the following parts of the thesis, it is vital to take a side note, briefly discussing the terminology of nanoscale objects, as the scientific literature is full of specific terms often used differently with respect to the intended meaning.[7] Generally, all structures with at least one of its dimensions in the 1-100 nm range are called nanomaterials.[8] Some institutions extend this limit to several hundreds of nm.[9,10] If the objects are also crystalline, they can be called nanocrystals (NCs).[11] Nanomaterials, in which the nanometer length restriction is preserved in all three dimensions, are named nanoparticles (NPs).[12] The abovementioned definitions focus solely on the object's size. They are repeatedly interchangeably used with the term QDs introduced earlier in this

work. It should be emphasized, that the term QDs invokes a specific subgroup of semiconductor crystalline structures characterized by the confinement of excitonic states arising when the size of the particle approaches its' material-dependent excitonic Bohr radius. With a couple of exceptions, this typically translates to QDs' size range of 1-10 nm. In such cases, the definitions of NCs and NPs cover both bulk and quantum-confined regimes. On the other hand, in extreme examples, the exciton Bohr radius can substantially exceed nanomaterials' 100 nm upper limit.[13] Thus, the interchangeable use of "nano-" terms with QDs is ill-advised and will be avoided in this thesis.

2.2 Quantum dots' properties

The quantum confinement effect significantly alters the properties of semiconductor QDs as compared to their respective bulk counterparts (Fig. 2.1). Its influence on the bandgap energy in QDs ($E_{g,r}$) can be accounted for by applying a quantum "particle-in-a-sphere"[12-14] potential model approximation, in which charge carrier motion is restricted by impassible boundaries defined by QD's dimensions:

$$E_{g,r} = E_{g,bulk} + \frac{h^2}{2r^2}\left(\frac{1}{m_e} + \frac{1}{m_h}\right) - \frac{1.8e^2}{\varepsilon r} \quad (1)$$

$E_{g,bulk}$ is a bulk bandgap energy of a given material, r is QD's radius, h is a Planck constant, m_e and m_h are the effective masses of electron and hole, e is an elementary charge, and ε is an electric permittivity of the material. The second term describes the independent confinement energies of electrons and holes, both increasing with smaller particle radius, positively contributing to the total bandgap energy. The third part expresses the electron-hole Coulombic attractive interaction that lowers the bandgap energy. For small semiconductor radii, the second term ($\sim r^{-2}$) dominates over the third ($\sim r^{-1}$), and the bandgap energy grows with the reduction of QD's size.[16] For materials with low effective charge carrier masses, the bandgap energy can be continuously tuned over the range extending 1 eV.[17]

Another critical consequence of quantum confinement is an alteration of semiconductor density of states (DOS) from continuous band structure towards discrete (quantized) levels. As the number of atoms in a particle shrinks, so do the number of electrons and available states. The spacing between states becomes more pronounced. Thus, they no longer blend and lose the band-like appearance. For that reason, QDs are often referred to as artificial atoms, though the distance between energy states in natural atoms is much higher. The description of separated electron and hole states in QDs also resembles the terminology of atomic levels. In the simplified picture, they are denoted using two quantum numbers nL. L describes the orbital momentum of the carrier's envelope wave function and is indicated by a capital letter, S for $L = 0$, P when $L = 1$, etc. n orders the states in the series of states with identical L and is represented with natural numbers starting from 1. For example, the lowest unoccupied electron state is labeled 1S, the next 1P, and so on.[18] The spacing between energy states reaches 0.15-0.3 eV for most materials, meaning that the thermal transitions do not smear them out. Just as the bandgap energy, which is the

separation energy between 1S electron and 1S hole state, the separation between other quantized levels grows with the decrease of QD's size.

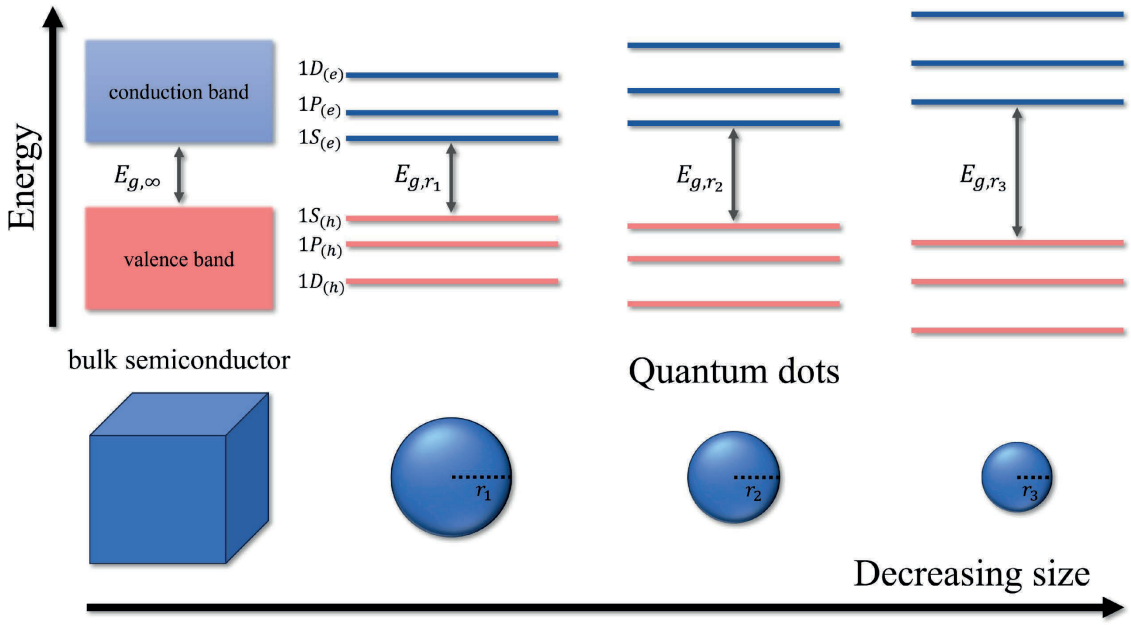

Figure 2.1 *Comparison between continuous band-like structure of bulk semiconductor to discrete energy levels of QDs. When the size of a particle approaches its exciton Bohr radius, the bandgap energy increases with the decrease of QD's size.*

The tunability of the bandgap and the quantization of allowed carrier states are responsible for extraordinary optical properties that made QDs a prominent target in the scientific and industrial community. The semiconductor's bandgap acts as a threshold separating photon energies that can be absorbed by the material ($> E_{g,r}$) from those that cannot ($< E_{g,r}$). In semiconductors with direct bandgap, exciton created upon absorption of a photon can undergo band-edge recombination, producing a photon with energy equal to $E_{g,r}$. The ability to continuously modify QDs' bandgap provides precise control over the absorption cutoff and emission wavelength. The atomic-like energy structure shifts the continuous absorption into a series of peaks.[17] This behavior fades at photon energies well above $E_{g,r}$, where the QDs absorb similarly to bulk semiconductors.[19] The discrete excitonic states also result in an intense fluorescence, characterized by the narrow width, that is red-shifted with respect to the first absorption peak.[20] The energy difference between maxima of the first absorption and band-edge emission peaks is known as Stokes shift. Its origin is typically attributed to the thermal relaxation of exciton occurring before the charge carrier's radiative recombination.[21,22] The energy released to the lattice in the form of phonons accounts for the observable difference between QDs absorption and emission.

In a sense, QDs bridge the optical qualities of bulk semiconductors and small chromophore molecules, combining the best features of both worlds. Similarly to some popular organic dyes, QDs manifest high fluorescence efficiency. However, their inorganic ordered structure, like in their macroscopic equivalents, makes them more resistant to degradation by either chemical or physical triggers.[23] Moreover, organic molecules typically absorb only a small part of the spectrum, which overlaps with their emission. QDs

absorb all photon energies that exceed the bandgap. Therefore, they can be excited with wavelengths far from their fluorescence peak. This feature also allows controlling the emission of multiple different-sized QDs with a single wavelength.[24]

All of the aforementioned size-dependent properties are strictly related to quantum mechanics. However, there is another type of size effect in QDs, typical to all nanoscale entities, that arises as a consequence of simple area-to-volume scaling law. In general, the surface area of an object changes with the square of its characteristic length l, whereas the volume scales with l^3. Thus, the contribution of surface atoms in QDs is much higher than in bulk solids. This effect is demonstrated in Fig. 2.2a, showing how the fraction of surface atoms changes with the diameter of a spherical particle. Since most of the chemical and physical interactions between the material and its surroundings are mediated by their interfaces, the high surface area significantly influences many QD properties, like catalytic activity, heat transfer, and melting temperature.[25] Any phenomenon related to surface effects is expected to scale as l^{-1} (area/volume) with particle size.[26] Note that atoms at the surface possess fewer neighbors compared to their bulk counterparts. These uncoordinated sites, called dangling bonds, alter QDs' electronic structure by introducing surface states to the energy landscape, as depicted in Fig. 2.2b. Such states, referred to as surface traps, often lie within the bandgap and provide new radiative and non-radiative decay pathways for electron and hole simultaneously competing with the band-edge radiative recombination process. Notably, trapping can also occur on other crystal defects, which are typically more abundant in nanometer structures than macroscale materials. The existence of trap states may be undesired or beneficial depending on the intended QDs' application. For example, QDs-based luminescent devices require high-yield band-edge fluorescence. Therefore, in such structures, the presence of additional recombination defect channels should be mitigated by adequate surface passivation schemes.[27] On the other hand, trapping states may promote efficient carrier extraction from QDs, which can serve in catalysis or solar energy conversion.[28] Either way, the presence of defect states complicates exciton dynamics, which will be the focus of the next section.

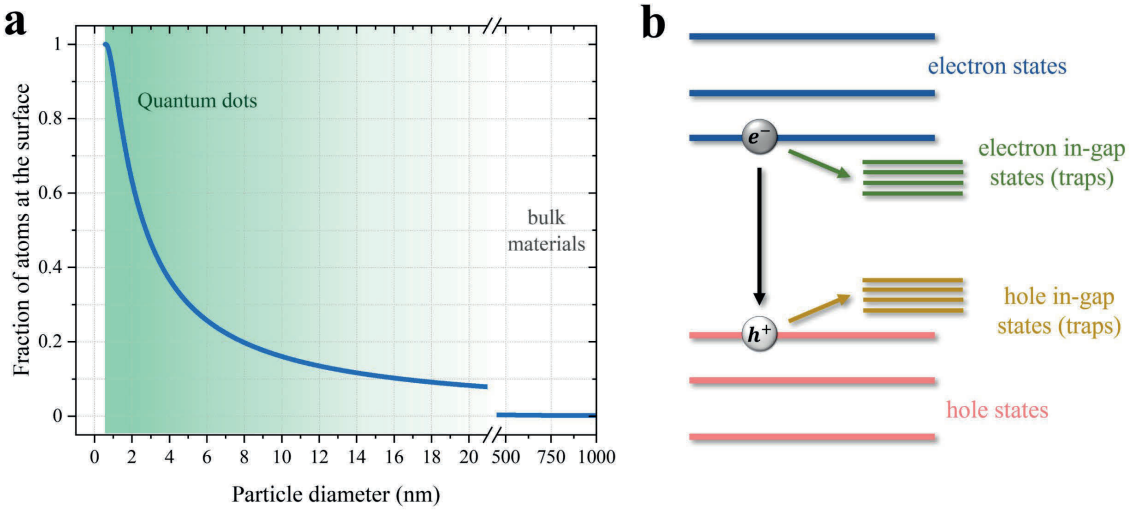

Figure 2.2 *a) Fraction of surface atoms plotted as a function of particle diameter calculated according to the model presented by Nanda and Nanda[29] for cubic zinc selenide particle with the lattice constant equal to 0.567 nm. b) Energy structure of quantum dot with surface atoms and/or*

in lattice defects. The presence of uncoordinated bonds results in the formation of mid-gap states that act as additional electron (green arrow) and hole (yellow arrow) recombination channels that compete with band-edge exciton recombination (black arrow).

2.3 Charge carrier dynamics

To efficiently utilize the unique attributes of QDs, one first needs to understand the underlying mechanisms of excitons' relaxation processes. Charge carrier transitions in QDs cover a broad range of timescales, spanning from femtoseconds[30,31] up to milliseconds[32,33]. Some of these phenomena occur sequentially, and some overlap with each other.

After an exciton is created in QDs upon absorption of a photon with the above bandgap energy, the first driving process is electronic dephasing.[34] It is a process in which the energy remains conserved while the momentum is changed and phase coherence of the quantum state is lost.[35] Electron dephasing occurs within a few to tens of fs as a result of electron-electron interactions.[34] If the excited charge carriers possess extra kinetic energy, then they undergo a series of intraband transitions until they reach the lowest states in their respective bands.[36] During each step, these so-called hot electrons and holes give away part of the excess energy in the form of heat (phonons) to the QDs' lattice. Intraband relaxation is referred to as thermal dissipation or electron/hole cooling and takes tens to hundreds of fs to complete. Following that, electrons and holes may further decay non-radiatively or through radiative recombination, with the production of a photon. For all direct bandgap semiconductor QDs, the second process dominates with mean decay times in the range of single to tens of ns.[35]

The considerations made in the previous paragraph apply to the QDs with ideal crystalline structure, where surface effects and other defects are not included in the exciton decay mechanisms. In a more realistic case, trap-mediated decay pathways have to be accounted for. The trapping time of charge carriers on defect sites may vary from hundreds of fs to tens of ps and is influenced by the density and energetic position of surface states, meaning that surface-assisted channels are much faster than band-edge radiative recombination. As a consequence of the competing mechanism, decreased QDs fluorescence yields are observed.[34] Additionally, in some scenarios, surface states may also affect the electron and hole intraband relaxation either by altering carrier cooling decay time with the presence of surface phonons or providing new relaxation routes through traps directly from higher energy states (1P-to-surface, etc.). The charge carriers' journey does not end after initial trapping. They can undergo transitions to subsequent states that lie deeper within the bandgap. Alternatively, non-radiative or radiative recombination may occur between trapped electron and VB hole, trapped hole and CB electron, or both trapped carriers. Particles in deep surface states may be long-lived, reaching lifetimes up to a millisecond regime. Notably, trap-assisted radiative recombination is characterized by the broad spectrum red-sifted relatively to the band-edge emission.

So far, we have discussed the case where, in a single QD, only one electron-hole pair is produced. If one illuminates QDs with a light beam of sufficient intensity, multiple excitons per particle can be generated. These carriers occupy the same confined volume. Therefore, they interact with each other, affecting their relaxation dynamics. In the multicarrier regime, non-radiative Auger processes become dominant, the most important

of which are Auger recombination, Auger ionization, carrier multiplication, and Auger cooling.[37]

The first refers to the effect in which conduction band electron and valance band hole recombine, but instead of emitting a photon, the excess energy is transferred to another free carrier, promoting it to a higher state. The second is analogous but results in the ionization of the third carrier. Auger recombination can occur via charged three-particle states consisting of two CB electrons and a VB hole or two VB holes and a CB electron called negative and positive trions.[38] Similarly, electrically natural multicarrier states, like the most widely studied biexciton (a bound state of two excitons), also undergo Auger recombination. In such case, one electron-hole pair recombines, simultaneously exciting either electron or hole. Compared to bulk-semiconductors, Auger recombination rates are much higher in QDs because of the relaxation of translational-momentum conversation for quantum-confined structures.[39,40] In macroscale semiconductors, the requirement of simultaneous energy and translational momentum conservation between three carriers hinders Auger recombination rates. However, in QDs, charge carriers occupy atomic-like states classified according to angular momentum rather than translational momentum, lifting the constraint caused by translational momentum conservation and increasing the probability of the Auger processes.[39,41] Typically, its timescales vary from tens to hundreds of ps depending on the specificity of the multicarrier state and QD size.[42]

Contrary to Auger recombination, which decreases exciton population in QD, carrier multiplication (sometimes called impact ionization), as the name suggests, produces additional excitons during the relaxation of hot electrons and holes.[43] This process is possible upon absorption of a single photon with energy exceeding twice the $E_{g,r}$. According to a few studies, carrier multiplication occurs within hundreds of fs after QD excitation.[44,45]

Auger cooling is a phenomenon of hot electron relaxation with simultaneous re-excitation of the VB hole. In some types of QDs, the energy spacing of conduction levels can reach hundreds of meV, which significantly slows phonon-assisted intraband relaxation of CB electrons.[46] In this instance, Auger cooling overtakes the decay of hot electrons, with a characteristic time from a few hundred fs to a single ps. Notably, because hole valence states are usually more densely packed than conduction levels, Auger cooling of the VB hole is less likely to occur.[37]

The characteristic timescales of the abovementioned processes are summarized in Fig. 2.3. As discussed, many different relaxation pathways significantly complicate the carrier dynamics in QDs. The fate of created exciton strongly depends on the excitation regime (intensity and energy of photons) and QDs' qualities like their composition, surface properties, or size. The latter is controlled by the application of appropriate QDs production routes.

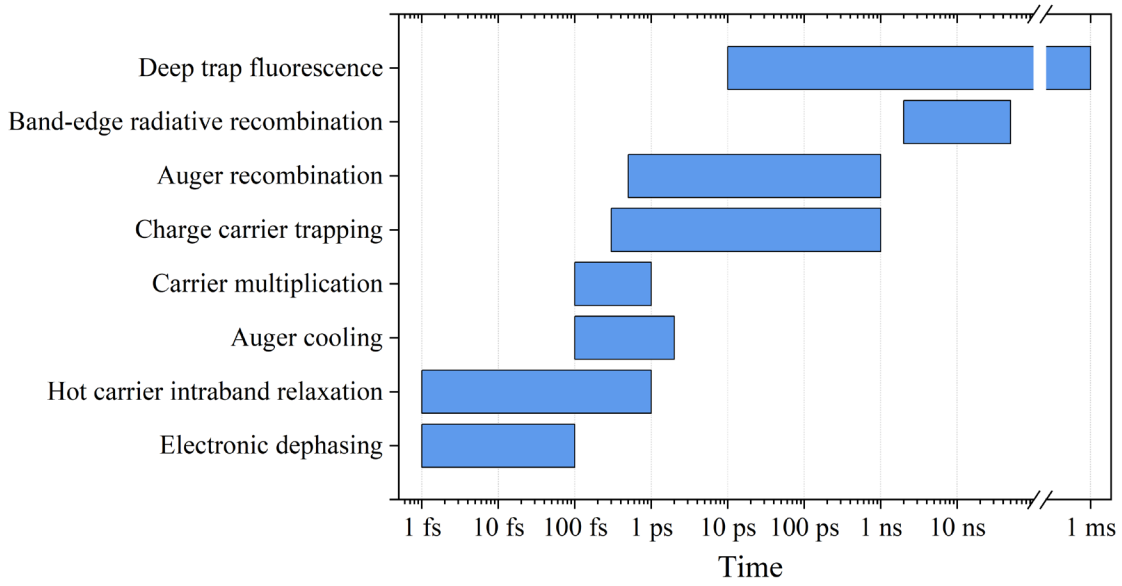

Figure 2.3 *Expected lifetimes of processes occurring in QDs during exciton relaxation.*

2.4 Quantum dots fabrication mechanisms

The growing popularity of the QDs over the last decades resulted in the development of their many different fabrication schemes. Broadly, these methods are divided into two categories: top-down and bottom-up.[47] The first group starts from macroscale precursors, which, under the influence of external stimuli, become fragmented into smaller and smaller pieces until the nanosized particles are obtained. In the second approach, atomic precursors self-assemble to form larger structures. While the top-down routes offer simplicity and easy scalability, the bottom-up approaches based on a wet chemical synthesis provide the best control over particle sizes and uniformity.[48] Thus, they are preferred when producing high-quality QDs, and they will be the focus of this section.

The fundamental mechanism of solution-based QDs (as well as other NCs) chemical synthesis is nucleation, a thermodynamical process in which a new phase (the nucleus) arises in a metastable parent phase.[49] When nuclei are born uniformly within a continuous primary phase, we speak of homogenous nucleation. In contrast, heterogeneous nucleation requires an additional solid-state constituent to induce particle formation at so-called nucleation sites.[50] In the colloidal QDs synthesis, both types of nucleation take place. The nuclei created in a homogenous solution act as seeds for the subsequent particle growth.

For the nucleation to occur, the primary solution phase has to contain a sufficient concentration of free monomer (smallest building block of a particle) to trigger particle precipitation.[51] In other words, the solution needs to be supersaturated. The homogenous nucleation can be described in terms of the nucleus' total free energy, which, in the simplest case of a spherical particle with radius R, is expressed as:

$$\Delta G = \frac{4}{3}\pi R^3 \Delta G_V + 4\pi R^2 \gamma \qquad (2)$$

where ΔG_V and γ are bulk and surface free energy. ΔG_V provides a negative contribution to ΔG, whereas γ is always negative. Therefore, the total free energy of the nucleus has a

maximum (ΔG_N) corresponding to particle critical radius (R_c), as demonstrated in Fig. 2.4. As in all physical systems, nuclei tend to minimize their total energy. In this context, ΔG_N represents an energy barrier that needs to be overcome to produce stable particles, and R_c marks a boundary between stable and unstable nuclei. The initially precipitated seeds with a radius smaller than R_c will redissolve to lower its ΔG. Analogously, for particles with sizes exceeding the critical radius, further growth through the accumulation of more monomers is energetically favorable. The nucleation rate depends mainly on the level of supersaturation, temperature, and surface free energy of the particles.[51]

The further growth (interpreted as heterogeneous nucleation) of as-created nuclei is governed by the diffusion of the free monomer to the nuclei surface and the subsequent reaction of these monomers at the nuclei surface to incorporate them into the particle.[52] Simultaneously, monomers can desorb from the particle surface back to the free state. Depending on the specific synthesis, one of these processes can occur much slower and will be the limiting factor of particle maturing. The diffusion-limited growth depends primarily on the monomer concentration in bulk solution and the temperature of the system. The surface-controlled accretion is highly influenced by the monomer concentration, specifically at the particle-solution interface and the surface free energy of the nucleus, with the fastest monomer accumulation rates achieved for lower γ. This second mechanism is considered the dominant growth factor in QDs synthesis. As predicted theoretically[53] and later verified experimentally[54], if the monomer concentration in the reaction solution is kept at a sufficiently high level, smaller particles will grow faster than larger ones. This phenomenon is known as size focusing and results in a narrowing of particle size distribution over time. On the other hand, if the monomer concentration drops too low, the equilibrium balance will shift toward a higher critical radius, leading to the Ostwald ripening, which is the dissolution of smaller crystals and the growth of larger ones, broadening the overall distribution.[55] Heterogenous nucleation can also occur on any impurities or bubbles present in the reaction solution. Therefore, it is vital to ensure uniform conditions in the whole volume of the mixture.

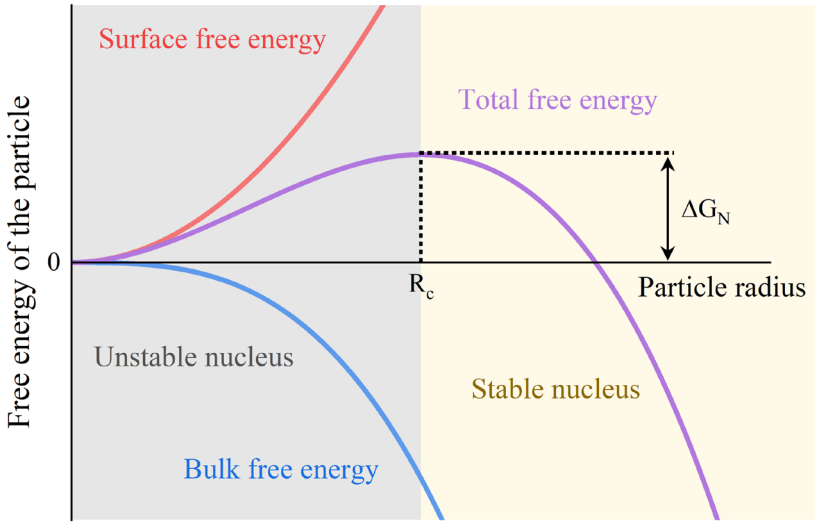

Figure. 2.4 *Surface (red), bulk (blue), and total (purple) free energy of the nucleus. The critical radius (R_c), corresponding to the maximum particle free energy (ΔG_N), represents a boundary between unstable (grey area) and stable (yellow area) nuclei.*

Notably, both homogeneous nucleation and particle growth require the presence of free monomer in the initial solution. In the considered case, these are free atoms (or molecules with active sites) that assemble into QDs. The monomers supplied to the reaction mixture are initially inactive, typically bounded in organic compounds or bulk granulates. Conversion from precursor to active monomer is necessary to initiate particle formation.[56] This transition usually occurs via either decomposition or reduction of precursors under the influence of temperature, sometimes supported by additional species introduced into the reaction solution. As most of the QDs have at least a diatomic composition, multiple types of precursor, each with a specific dissociation path, are typically utilized during one synthesis.

The critical factor in the QDs synthesis is the presence of special organic capping agents (ligands) that bind to the surface of growing seeds, regulating their properties.[57] Their primary role is to stabilize the nuclei, preventing their interparticle clustering (agglomeration), which would significantly broaden the size distribution of the final product. By providing an organic coating to the nuclei, each particle matures in a separate nano-reactor, with the monomer accumulation being the only growth mechanism. Moreover, adsorption of surface ligands modifies the surface energy of the particles.[58] Thus, employing capping agents with different coordination groups allows for control of the particle growth rate. Organic stabilators can be added to the reaction mixture as a separate ingredient. However, they are commonly introduced as monomer-ligand complexes (precursors). In such a case, dissociation of precursor activates both free monomers and capping agents. Additionally, surface ligands affect particle solubility and affinity to other species (like peptides and electron acceptors/donors), providing flexibility in post-synthetic QDs modifications.[59] After the synthesis, capping agents continue to stabilize QDs, slowing their degradation processes and prolonging their shelf-life.

Fig. 2.5 summarizes the processes occurring during conversion from substrates to fully-developed colloidal QDs. Initially, precursors under the influence of heat dissociate, transforming to free monomers. As the monomer concentration reaches the critical level, nucleation occurs, resulting in the creation of seeds. The newly born nuclei grow by accumulating more monomers, which diffuse to the particle-solvent interface and react to be integrated into the crystal lattice. To obtain the narrow distribution of the final product, temporal separation of each stage is highly desired. In particular, the overlap of nucleation and growth phases should be prevented.[60] Ideally, all nucleation events need to occur at once in the whole volume of the reaction mixture. No new seeds are produced when particles grow, so uniform QDs are obtained due to size focusing effect. In practice, most commonly, this is realized by two synthetic approaches: hot-injection and heat-up (non-injection) methods.[61]

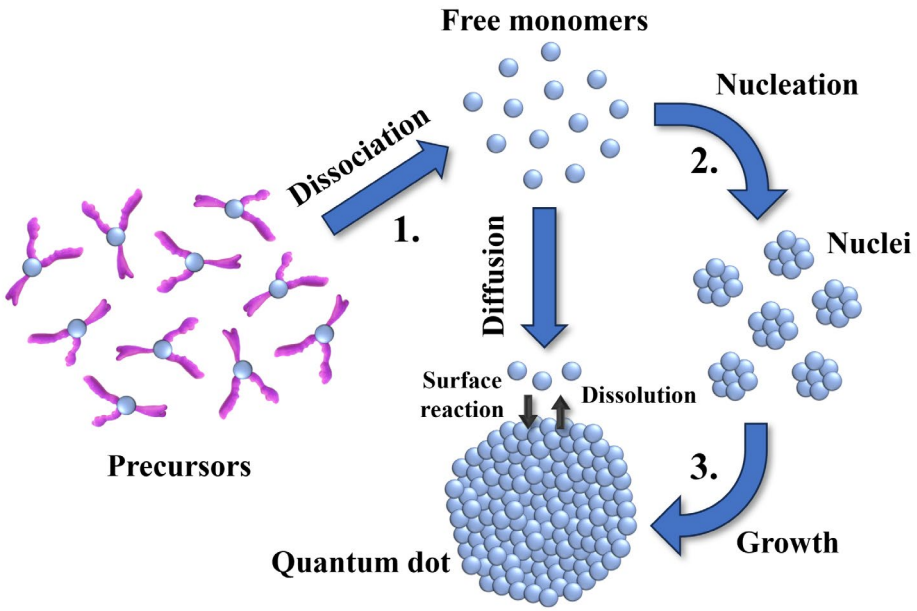

Figure 2.5 *Schematic illustration of processes of particle formation in solution. Dissociation of precursors (1) activates free monomers that trigger particle nucleation (2). Further growth of the nuclei (3) occurs through the accretion of more monomers that diffuse to the particle-solution interface, where they are incorporated into the bulk particle. Simultaneously, the monomer bound at the particle surface can undergo dissolution back to the reaction solution. Nucleation and growth of quantum dots in wet synthesis are regulated with the surface ligands (not shown in the scheme).*

In hot-injection synthesis, the critical reagents are initially prepared in separate vessels and then mixed upon rapid addition of one solution into the other.[62] The precursor solutions are either already activated before their injection or undergo rapid dissociation in the reaction mixture under high temperatures, routinely reaching 300°C. This results in a drastic increase in monomer concentration, momentarily reaching extreme supersaturation levels and resulting in the immediate formation of nuclei.[61] The "burst nucleation" period quickly fades away as the monomer number is drained and drops below the nucleation threshold, transitioning to the growth phase. Due to its general applicability and variety of available precursors, the hot-injection method is the most popular approach for producing many colloidal QDs. However, it has certain limitations, particularly poor scalability and strong susceptibilities of the final product to very subtle changes in the synthesis parameters.

In the heat-up approach, all the reagents are placed in one vessel from the beginning of the reaction. The control over particle parameters is achieved by conducting each synthesis step at a different temperature.[63] It requires careful selection of reagents with specific reactivity to ensure that the monomer is produced at a balanced pace and the nucleation is not triggered during the precursor dissolution phase.[58] The formation of nuclei is induced upon increasing the temperature, and the mild concentration of monomer hinders the growth of particles during nucleation. If the reagents have too low reactivity, the nucleation will be delayed until the growth temperature is reached. Too high activity of precursors also results in the coupling of nucleation and growth stages. This type of synthesis needs precise control over the heating rate, which controls the monomer conversion and thus affects other processes. The limited availability of precursors and the complexity of separating reaction

steps hamper the method's popularity. Nevertheless, if done correctly, the heat-up synthesis can match the quality of the colloidal QDs prepared by the hot-injection technique while being simpler to reproduce and scale up even to the industrial level.[58]

2.5 Materials classes of Quantum Dots

The composition of QDs is an essential factor, dictating their properties and applicability. Owning to the variety of available semiconductor materials combined with the size-dependence of the bandgap, it is possible to continuously tune the absorption and emission spectra of QDs spanning from mid-infrared (IR) through visible (Vis) and up to near ultraviolet (UV). This unique feature is demonstrated in Fig. 2.6, which shows the feasible bandgap energy for commonly utilized QD compounds. Based on atomic content, they are divided into II-VI (12-16) group metal chalcogenides, lead-based salts (PbSe, PbS), lead halide perovskites ($CsPbX_3$, X = Cl, Br, I), group IV (14) monoatomic dots (Si, C, Ge), III-V (13-15), and I-III-VI (11-13-16) group compounds.[64] Note that in the scientific literature devoted to QDs research, the traditional atomic group notations based on Roman numbers are more popular than new recommendations of the International Union of Pure and Applied Chemistry (IUPAC) given here in brackets.

The most widely studied materials are CdSe and other Cd-based QDs, like CdS and CdTe. They were historically one of the first obtained classes, becoming the model system for experimental and theoretical research related to fundamental properties as well as the development of new synthesis protocols.[65] As a result, they accompanied scientists in reaching many milestones in the QDs field, like the explanation of the quantum confinement effect[15,66] and the invention of the hot injection method[67]. The combination of different Cd-based QDs allows for covering practically the entire visible light region, which, paired with excellent stability and decades of researchers' experience, explains their continuous popularity.

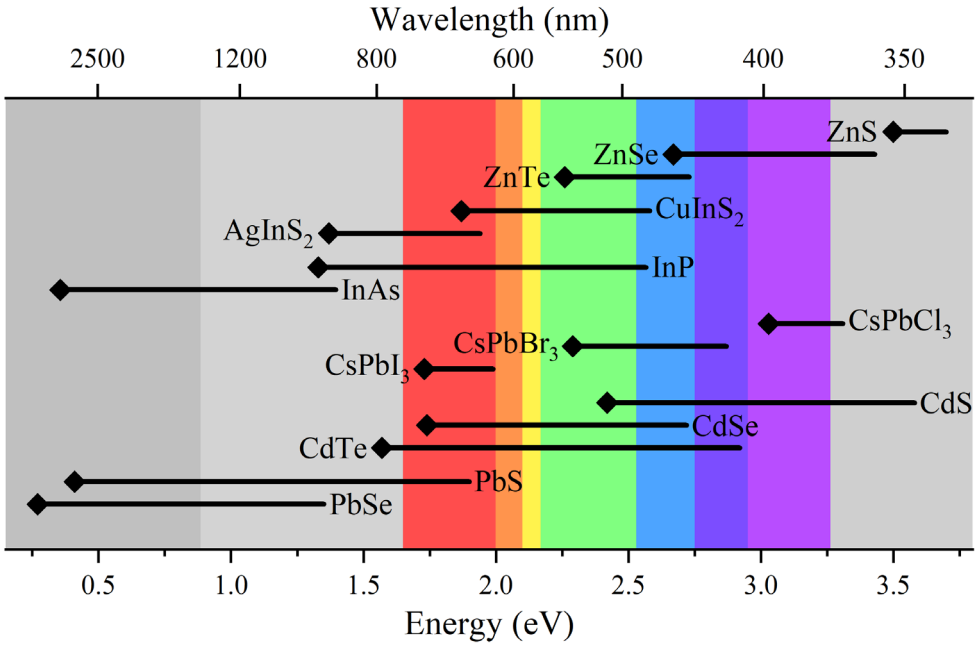

Figure 2.6 *Size-dependent bandgap energies of common QDs materials. Black diamonds denote the bulk bandgap of the semiconductor compound. The colored area marks the range of visible*

light. The shaded regions to the left denote near (light gray) and middle (dark grey) infrared regions. The shaded area to the far right marks the near ultraviolet range. The bandgap energy ranges for a specific material were estimated based on literature data.[68–77]

Similarly, Pb-based QDs, especially PbS and PbSe QDs, also have a long history of research as they complement cadmium chalcogenides, extending the bandgap energy tunability towards the IR regime. These materials are characterized by a relatively high exciton Bohr radius, meaning that the size-dependent quantum confinement effect occurs at larger NCs sizes and is much stronger than in other compounds.[78] This feature, combined with low bandgap energies, makes Pb-based QDs ideal materials for studies of QDs multicarrier dynamics, which can result in many future applications in energy conversion devices.[79,80] A distinct class of Pb-based QDs constitute recently discovered lead halide perovskite QDs. These highly ionic compounds readily form crystalline low-dimensional structures prone to further composition manipulation through ion exchange, providing a feasible way to tune their optical properties.[81] The advantages of perovskite QDs are their high tolerance to surface defects and high fluorescence quantum yields.[82] However, one of their major issues is structural stability, which requires further improvement in synthesis strategies.[81]

The past and ongoing research and engineering of the Cd- and Pb-based QDs undoubtedly push our understanding of the nanoscale quantum confined systems. Nevertheless, the potential real-life application of heavy metal-based QDs raised concerns regarding their toxic effects upon exposure to humans and the rest of the environment.[83–85] In particular, the European Restriction of Hazardous Substances Directive (RoHS) restricted the permitted amounts of heavy metals in commercial electronic devices across the European Union. The directive states that no individual homogenous component can contain more than 0.01% wt. of Cd and 0.1% of Pb (and other harmful substances like Hg or Cr^{6+}).[86] Regardless of whether these limits are justified, this severely limits the applicability of Cd-based QDs and ones containing Pb, though to a smaller extent.[87]

Fortunately, the rapidly growing field of QDs expands beyond heavy metal-based materials. Many types of QDs compliant with the RoHS directive emerged over the decades and are gaining more and more attention, both from the scientific community and the industry sector. For example, InP QDs are promising materials for many fluorescent applications as their range of possible bandgap (emission) energies and their carrier mobility exceed the respective qualities of CdSe QDs.[88,89] Likewise, the family of ternary I-III-VI QDs, for instance, $AgInS_2$ or $CuInS_2$, due to their large absorption coefficients, longer excited states lifetimes, and emission spectra extending to the IR regime, can potentially substitute other toxic materials.[90] Despite encouraging reports[91,92], these promising alternatives are still inferior to the performance of Cd- and Pb-based QDs and need more extensive studies to improve their capabilities.[88,93]

Zinc selenide (ZnSe) QDs with other Zn-based chalcogenides (ZnTe and ZnS) hold a special place among heavy metal-free compounds. Owning to their wide bandgap (2.7 eV for bulk ZnSe), they provide access to high energy part of the visible spectrum and near-UV region (blue and violet) unreachable to most commonly utilized environmentally neutral materials.[94] Having analogous II-VI structure to their Cd-based counterparts, it is possible to adapt, to some extent, previously established synthetic routes, often utilizing

similar equipment, solvents, and chalcogenide precursors.[95] Unfortunately, Zn-based QDs, in general, are more reactive and prone to undergo oxidation or hydroxylation of the surface, resulting in the appearance of many defects that often hinder their properties.[94] As such, an increasing number of researchers focus on understanding the nature of ZnSe QDs surface sates[96] and improving engineering techniques[97].

Further tunability of QDs properties can be achieved by alloying different semiconductor compounds. This operation introduces an additional pathway to extend the QDs emission and absorption simply by controlling the composition ratio of mixed materials.[98] Alloyed QDs can exhibit new features unachievable by either of the parent compounds.[99] Typically, alloying requires two compounds with matching crystal structures. For example, $ZnSe_{1-x}Te_x$ QDs are synthesized to achieve full coverage of the blue spectral region.[100] The specific emission wavelength depends on the amount and distribution of Se and Te within the fabricated QDs at a particular size.

Additionally, a popular approach to enhance certain QDs qualities is to coat one type of semiconductor with a second material, creating so-called core-shell QDs. In such heterostructures, the charge carriers' behavior is governed by the relative band alignment of both compounds. Both electron and hole will be confined within the core if CB and VB of the core compound lie in between bands of shell material. This configuration, known as type I, promotes exciton recombination, enhancing the fluorescence of QDs. In the opposite alignment, carriers will be confined in the shell part (inverse type I). In type II configuration, both bands of core and shell materials are aligned alternately. In such instances, electron and hole spatial separation can be achieved as one type of charge carrier is confined in the core and the second in the shell. Alternatively, if the energy offset between core and shell CBs or VBs is low, one carrier will be delocalized within the whole volume of QDs. The other will be restricted to only one material (quasi-type I/II). In any case, the compatibility of core and shell material lattices and the shell thickness influence the effectiveness of exciton control.[101]

2.6 Potential applications

As mentioned throughout this chapter, QDs, with their unique properties, are not only interesting scientific queries but can also serve many functions, improving our everyday lives. A popular approach involves the incorporation of QDs as a supporting element into already-existing technology to boost its performance. Alternatively, QDs can be utilized as the main active element of an electronic device. As for now, most QDs applications await their introduction to the market. However, some QDs-based devices are already commercially available to purchase.[102]

Very narrow and tunable emission peaks make QDs a promising material for high-efficiency display and lighting devices (electricity-in-light-out devices). Typically, in such instruments, a blue backlight light-emitting-diode (LED) illuminates the patterned layers of QDs, which convert part of the primary photons into red and green.[103] Compared to standard white LED backlight displays, this approach improves the color gamut and increases the light output. This technology was commercialized by Sony back in 2013 and later adopted by other companies like LG and Samsung.[104] While the decade-old scheme

keeps evolving, simultaneously, the research on the next generation of QD-based displays is already ongoing. In the new route, QDs, placed between electron and hole injecting layers, are excited electrically without any backlight source. Such design provides several advantages, for example, improved black color rendering, increased viewing angle, higher frame rates, and reduced screen thickness. However, these types of QDs LEDs (QLEDs) suffer from limited external quantum efficiency, mainly ascribed to Auger recombination.[105]

QDs' unique optical properties, combined with their low toxicity (in the case of heavy metal-free structures), find application in biomedicine, primarily bioimaging, successfully competing with organic dyes, but also in diagnostics and therapy.[106] As biomarkers, they outcompete organic dyes regarding luminescence intensity, photostability, and available emission wavelengths. With appropriate post-synthetic functionalization, it is possible to attach to QDs surface specific molecules that bind to a particular entity in the human body, for example, a specific type of cancer cell, allowing identification of a tumor with high selectivity and sensitivity.[107] Similarly, the QDs' surface can be conjugated with a cure for targeted drug delivery. In such cases, QDs perform a dual role of both imaging and treatment.[108] Currently, the main issue hindering QDs clinical usage is uncertainty regarding the potential harmful effects of their long-term accumulation in living organisms.[109]

Photodetectors that convert absorbed photons into an electronic signal (light in-electricity-out devices) are another interesting example of QDs application. Here, the carrier multiplication mechanism plays a crucial role, allowing for high external quantum efficiency of generated photocurrent. Additionally, high absorption coefficients, tunable bandgap, variety of available materials, and flexibility in their processing make QDs an attractive alternative to bulk semiconductors commonly utilized as photodetector devices. Depending on specific material type, QDs can be implemented as photodetectors covering IR range for night vision and optical communication, Vis spectrum for safety systems in modern technologies, and UV regime for fire alerts and ionizing radiation detection. Moreover, different structure arrangements of QDs-based photodetectors alter the device's performance to act as either a photoresistor, photodiode, or phototransistor. Future commercialization of this technology requires optimization of the device's performance and stability along with the substitution of heavy metal-containing structures with environmentally friendly compounds.[110,111]

Researchers worldwide also investigate the potential application of QDs' ability to convert light into electricity in the context of solar energy harvesting. Owing to the multiple exciton generation process, which is much more potent in quantum confined structures than in bulk semiconductors, it is possible to obtain QDs solar cells with power conversion efficiency exceeding the theoretical upper limit of standard single p-n junction cell (Shockley–Queisser limit).[112] Several distinct types of QD solar cell architectures are explored. One design utilizes QDs as a sensitizer, which, upon absorption of sunlight, immediately transfers electrons and holes to separate transporting media analogously to molecular dyes in the well-known dye-sensitized solar cells.[113] Alternatively, QDs can be used as both absorber and charge transporting layer, creating either Schottky or p-n junctions.[114] In another approach, QDs are dispersed within conductive polymer matrixes,

forming low-cost and efficient hybrid QD solar cells.[115] Finally, by stacking interconnected layers of QDs with progressively smaller bandgaps (controlled by the size of the particles), multijunction tandem QD solar cells are fabricated, which stands out for their efficiency among other QDs-based solar cells.[114] So far, insufficient carrier transport across multiple interfaces and the need to clarify carrier multiplication effects are the main bottlenecks of QD solar cells.[116]

QDs provide another way of transforming solar energy, namely by photocatalysis. In such a process, an optically excited catalyst produces a CB electron and VB hole, which then participate in redox reactions, converting absorbed photons to chemical energy.[117] The scientific literature provides multiple cases of critical chemical reactions driven by QDs-based photocatalysts, such as hydrogen evolution, CO_2 reduction, water purification, ammonia generation, and plastic reforming.[105] The high photocatalytic activity of QDs is related to their high surface-to-volume ratio combined with multicarrier generation pathways. Importantly, QDs, due to their diverse compositions and arrangements, can be applied as separate photocatalysts or co-catalysts typically paired with metal catalysts to boost their performance.[118] As in previous cases, more development related to engineering aspects, understanding QDs surface effects, and understanding the carrier dynamics picture is necessary for further progress.

The discussed above applications are the most important examples of QDs utilization. Many less explored and more exotic areas are currently under investigation, like QD lasers[119], single[120] and entangled[121] photon emitters for quantum technology, to name a few. With the constantly growing interest in QDs research, the commercialization of already-studied technologies and the appearance of new exciting applications will surely come in the near future. For this to happen, it is crucial to examine the current directions of QD studies to identify and fulfill present knowledge gaps.

2.7 State of art and the knowledge gap

The field of QDs has transformed drastically since the first report of tiny crystals with size-dependent optical properties in 1981.[122] Nowadays, many research directions exist, occurring in parallel. Significant progress in one area of QD science often accelerates other brunches, creating a positive feedback loop.

The studies of the CdSe QDs model system are still prevailing. However, the attention has shifted from steady-state analysis of their size-dependent properties to time-resolved measurements that allow exploration of carrier dynamics. In this context, new methodologies are being employed to push the temporal resolution of the experiment and extend the attainable information of the examined sample.[30] Novel engineering strategies emerge, adjusting the exciton behavior to fit the intended usage.[123] Although research on various core-shell and core-multishell QDs predominates in the modern literature, a trend of revisiting core-only QDs is also observed, focusing on their formation mechanism, surface effects, and role in the charge carrier relaxation processes.[124–126] At the same time, innovative hybrid architectures, like QDs-plasmonic structures[127,128] or QDs embedded in various matrixes[129,130], are being investigated to enhance material properties and broaden the possible application range even further. All the improvements are accompanied by the constant advancement of QD-based devices, for example, the recent demonstration of an

electrically pumped QDs laser[131] and the development of QLEDs with record-breaking external quantum efficiencies[132,133].

While the research on model systems is ongoing, delivering breathtaking results, scientists are simultaneously considering less-developed QD classes. As noted by Manna in his perspective on the 2023 Noble Prize in chemistry: "The chemistry and physics of the nanocrystal's surface, defects, and ligand binding are adequately known only for a handful of cases, and various classes of quantum dots still need satisfactory syntheses." .[134] Indeed, during the last few years, fundamental studies of size-dependent optical properties[74], the development of new fabrication schemes[135–137], and the demonstration of prototype devices[92,138] of other QD classes, both core and core-shell, have taken priority.

The abovementioned points apply particularly to ZnSe QDs since they do not have other RoHS-compliant alternatives that cover the same optical range. Novel engineering innovations involve superior shelling techniques[139] and blue QLEDs with unmatched efficiency compared to other heavy metal-free QDs[140]. Among recently conducted fundamental studies on the quantum confinement effect in ZnSe QDs, a work of Toufanian et al. stands out, which systematically examined a broad range of ZnSe QDs, correlating the particle size, Zn:Se ratio, and concentration to the position of lowest-energy electron transition (1S electronic state).[68] Additionally, much attention is focused on surface effects explored under different conditions.[96,141] The role of quantum confinement, surface and defects in the ZnSe QDs remains an active area of research. Discrimination of those two contributions to the total electronic structure is the next step toward the rational design of high-efficiency QDs-based devices. Such studies should be extended to time-resolved experiments to understand and control exciton interactions.

Further progress can only be realized with specialized methods that provide access to detailed information about investigated samples. The principle of operations, along with crucial instruments' descriptions of techniques of QDs' characterization, will be discussed in the following chapters.

3. Optical spectroscopy methods for QDs characterization

3.1 UV-Vis spectroscopy

Visible light was the first and, for a long time, the only part of electromagnetic radiation known to humans, serving as one of the essential senses in our perception of the surrounding world. Thus, naturally, it caught the attention of early pioneers of modern science like Isaac Newton, whose experiment conducted in 1666 of dispersing white light with a prism to obtain rainbow-ordered colors[142] is considered by some as the beginning of spectroscopy. Over the following centuries, other regions of the electromagnetic spectrum were discovered, including more energetic ultraviolet radiation. After extensive work by many prominent researchers, UV and Vis spectrometers (or spectrophotometers) emerged, first as separate instruments and later combined into one device.[143]

Today, UV-Vis absorption spectroscopy, commonly referred to as just UV-Vis spectroscopy, is a must-have tool in many laboratories devoted to research areas such as analytical chemistry, biology, biomedicine, organic chemistry, material science, and nanotechnology, with QDs as the primary example. Its popularity stems from inexpensive apparatuses, ease of implementation and use, and wide range of applicability. The technique is appropriately classified as electronic spectroscopy with photon energies corresponding to differences between electron states in atoms, molecules, and clusters. Specifically, UV-VIS spectroscopy probes electronic transitions between the outer levels induced upon absorption of photons.

In general, the principles of any absorption spectroscopy experiment are dictated by the Lambert-Beer law, relating the concentration C and thickness l of the absorbing specimens to the intensity of the incident (I_0) and transmitted light (I_1).[144] Within the UV-Vis spectroscopy community, its formula is typically written as:

$$\log\frac{I_0}{I_1} = \varepsilon C l = A \tag{3}$$

where ε is a molar absorption coefficient, and A is a dimensionless measure of sample absorption called absorbance. In UV-Vis spectroscopy, A is measured as a function of probing radiation's energy (wavelength) to obtain the absorption spectrum. The linear dependence between A and C is valid only for dilute systems evenly dispersed within the pathlength of scanning photons. As such, measurements of most species, including QDs, are conducted in the liquid solution phase placed in steady-state or flow cuvettes. Non-transparent solid samples can be studied using UV-Vis reflectance spectroscopy.

Plenty of UV-Vis spectrometers with different configurations are available on the market.[145–148] Most instruments allow spectral analysis in the 1.24-6.20 eV range, corresponding to 1000-200 nm wavelength. Although they differ in design, applicability, and performance, they all share the same main components: a light source, monochromator, sample compartment, and detector. The source of continuous UV-Vis radiation typically combines a halogen lamp, emitting in the Vis range down to the near IR, paired with a deuterium source covering the UV part of the spectrum. Alternatively, a pulsed Xenon lamp

can be utilized as a single emitter in both Vis and UV regions, but this source is usually more expensive and less stable. LED sources are also applied for applications where only a tiny part of the spectrum is needed, delivering higher-intensity light beam over a narrow range of wavelengths. For the dispersing elements, modern spectrometers exclusively utilize diffraction grates, either in double or single configuration, mounted together with slits.

Sample containers are typically made from glass, quartz, or transparent polymers like polystyrene. Polymer cuvettes are much cheaper and could be used disposably, mitigating the risk of sample contamination. On the other hand, they exhibit higher fabrication inhomogeneities, which can affect the quality and repeatability of the measurements. Additionally, most commercially available polymeric materials cannot cover the whole UV-Vis photon energies, absorbing in either the higher or lower end of the spectrum. The Quartz cuvettes are very precisely manufactured and efficiently transmit radiation from deep UV to even IR range; however, they are way more expensive. Glass containers represent a middle ground, compromising cost and performance.

While similar sources, monochromators and cuvettes are used in every type of UV-Vis spectrometer, the data collection depends on a specific setup. The main two types are array detector-based and scanning layouts[149], schematically presented in Fig. 3.1.

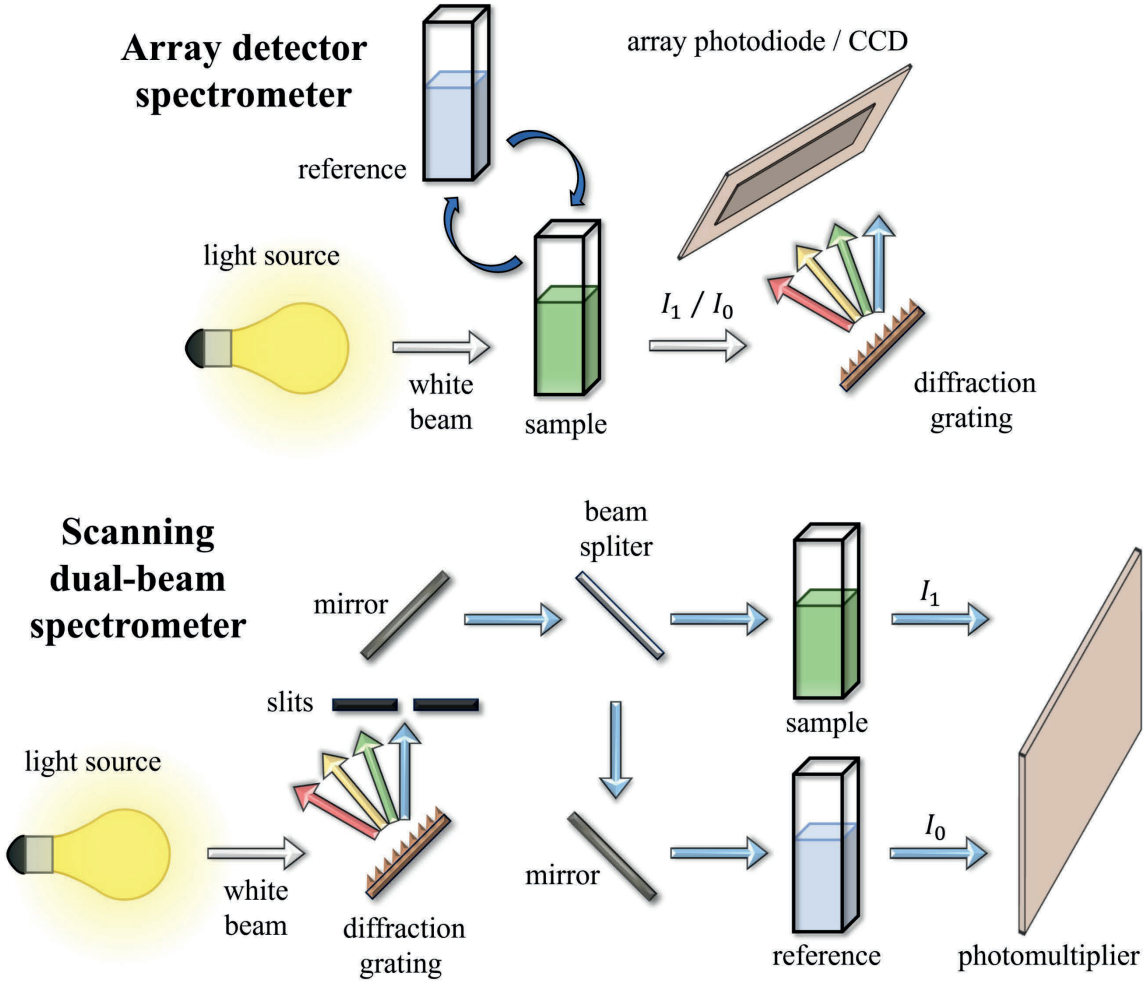

Figure 3.1 *Simplified schemes of array detector-based (top) and dual-beam scanning spectrometer (bottom).*

In the array detector-based spectrometer, the sample is illuminated with the polychromatic radiation produced by the source, and the dispersion of light occurs after the interaction with the sample. Position-sensitive multichannel instruments are utilized to detect the diffracted wavelengths, such as linear photodiode arrays or charged-couple device (CCD). All spectrum is collected at once, which is the most significant advantage of this arrangement. Moreover, these setups tend to be more compact, allowing for more flexible sample environments and easier coupling with other experimental techniques. Array detector-based spectrometers are predominantly single-beam instruments, meaning that before sample analysis, one needs to perform separate reference measurement to acquire the I_0 signal in the same apparatus conditions, which is usually realized using a cuvette filled with the solvent.

In scanning spectrometers, the diffraction grating with an appropriate number of slits is placed before the sample, and thus only a single wavelength at a time reaches the sample. The spectrum is acquired on a point-by-point basis. Hence, the single spectrum measurement takes more time than in the array detector-based setups, making this type of spectrometer ineffective for time-resolved measurements. On the other hand, scanning configurations provide several advantages. For instance, they efficiently reduce the amount of scattered light during measurement and can cover a broader range of photon energies because, during scanning, the transmitted light may be redirected to different detectors for improved quantum efficiency at distinct photon energy ranges.[149] A photomultiplier tube consisting of a cathode and anode placed between a series of dynodes is commonly applied as a detector. When a photon strikes a cathode material, it emits electrons, which quickly multiply as they bounce through the dynodes to reach the anode, translating to a higher sensitivity of the apparatus. Both single- and dual-beam models exist, but the latter become increasingly popular as it allows simultaneous measurements of the I_0 and I_1 signals. Such instruments use choppers to split the primary beam into two parts.

As QDs' size-dependent properties manifest primally in pronounced optical changes, UV-Vis spectroscopy is the suitable technique to study such systems. The method allowed the initial discovery of the quantum confinement effect and has since been commonly used to investigate QDs parameters. The example of information that can be retrieved with the UV-Vis technique in the context of measurements of QDs systems is demonstrated in Fig. 3.2. In the Figure we show UV-Vis spectra of the CdSe QDs system, recorded for two different particle sizes. As depicted, the optical absorption spectra allow for identifying distinct features corresponding to particular electron transitions (marked schematically with arrows). Note that the band structure of hole states in many QDs compounds, including CdSe and ZnSe, is more complex than in the general simplified case presented earlier in Fig. 2.1. This results from confinement-induced mixing of subbands.[150] The broadening of absorption features in QDs UV-Vis spectra arises mainly from the inhomogeneity of particle sizes.[19] This effect is the dominant contribution, even for narrow QD diameter distributions. For high-quality samples, the standard deviation of typically obtained QD size distributions is on the level of 5-15 %.[68,151–153] The commonly applied procedure of retrieving energy of specific transitions involves fitting the absorption spectrum with a sum of Gaussians and background polynomial function.[154–156] Besides, in Fig. 3.2, a prominent shift of all absorption structures with the change of QDs mean size can be observed, which

is direct evidence of the quantum confinement size effect. As such, UV-Vis spectroscopy provides a rapid and reliable estimation of QD diameters based on empirically derived fit equations. The bandgap energy is typically assumed to be equivalent to the position of the first transition maxima in the optical spectrum, here $1S_{(e)}$-$1S_{3/2(h)}$, which is referred to as the 1S peak.[68,96,151,157] It is important to emphasize that due to the quantum confinement effect, the commonly applied procedures for deriving bandgap energies of bulk semiconductors based on the UV-VIS spectra are inadequate for QDs.[158]

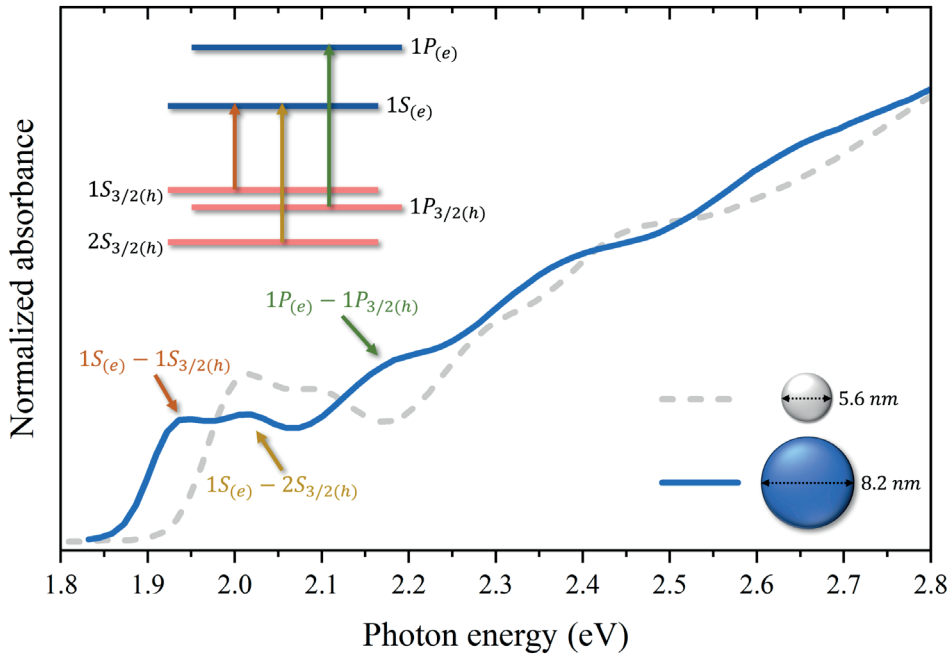

Figure 3.2 *Example of UV-Vis absorption spectra of model CdSe QDs with diameter 8.2 nm (solid blue line) and 5.6 nm (dashed grey line). Arrows on the blue spectrum indicate electron and hole states involved with specific transitions. Adapted with permission from* [19]*. Copyright 2000 American Chemical Society. The inset in the top left corner shows the energy structure of CdSe QDs.*

3.2 Photoluminescence spectroscopy

For studies of fluorophores, a method complementary to UV-Vis absorption spectroscopy involves the measurement of emission from the sample. As one of the major scopes of QDs application is associated with display and imaging applications, photoluminescence (PL) spectroscopy is another essential technique for QDs characterization.

Prior knowledge of sample absorption is required to select suitable excitation source energy to perform PL measurement. Alternatively, one may scan the probed specimen over multiple photon energies from the optical spectrum. In the case of colloidal QDs, any photon energies exceeding their bandgap can be utilized in the analysis. However, the excitation wavelength is typically well-separated from the presumed sample PL to avoid spectral overlaps between light emitted from the sample and the source.

PL measurement is conducted with a fluorescence spectrometer or fluorimeter, which shares instrumentation and design similarities with apparatus for UV-Vis absorption spectroscopy. Its schematic representation is presented in Fig. 3.3. The PL setup

predominantly uses monochromatic light to excite the sample. This is achieved by implementing diffraction grating to the traditional source like a Xenon arc lamp or applying lasers as intense monochromatic light sources. In the latter case, multiple lasers are often combined in a single apparatus, offering a selection of photon energies to analyze various specimens. The excited sample reemits light uniformly in all directions. Part of the radiation is guided through the optical fiber to the detection setup, operating either in a scanning or dispersive mode, analogous to UV-Vis configurations. An optical filter subtracts higher energy excitation photons from the measured signal. In more advanced spectrometers, the sample is placed in the center of an integrated sphere, allowing more efficient collection of its PL. Such instruments can be used to quantitatively assess sample PL quantum efficiency, which is the ratio of photons emitted to the photons absorbed by the probed specimen. Some modern spectrometer designs are suitable for measuring both sample absorption and emission. Spectrometers differ in design and complexity, ranging from simple custom-made setups based on a shoebox for routine sample characterization to cutting-edge technologies for more advanced analysis.

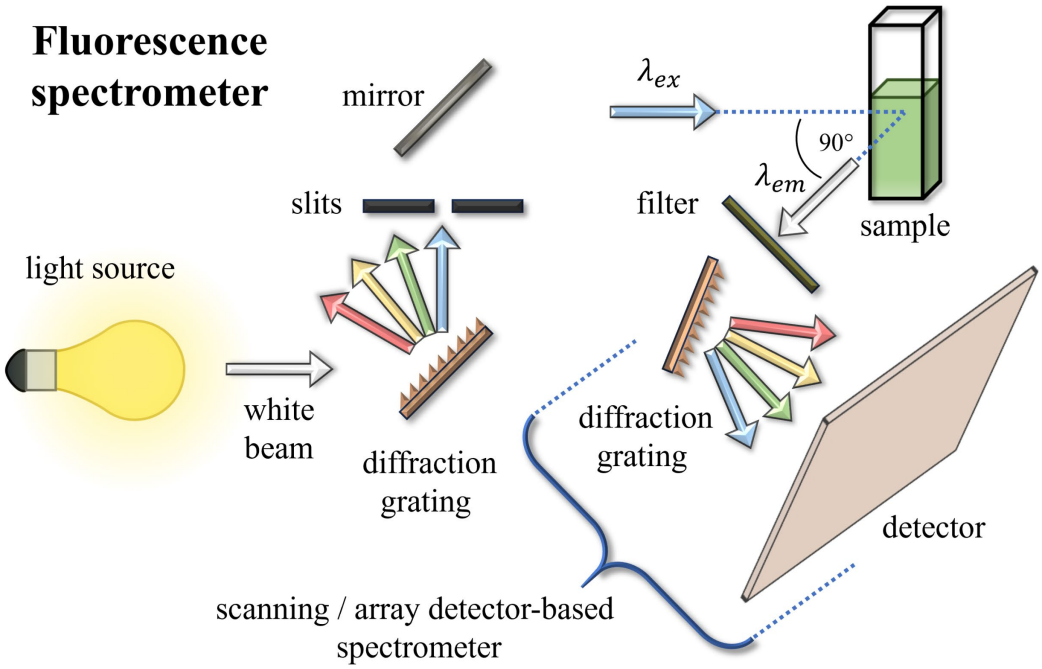

Figure 3.3 *Simplified scheme showing example of fluorescence spectrometer.*

Fig. 3.4 shows the expected emission spectrum of QDs dispersion. QDs PL occurs due to radiative recombination of the lowest-lying CB electron and VB hole states. As previously discussed, the band-edge emission is Stoke-shifted relatively to the corresponding QDs absorption spectrum. Its energy, like the energy of transitions in the absorption spectra, increases with smaller particle size for a given QDs material. Additionally, core QDs often exhibit broad emission, redshifted to the main PL feature, associated with surface states. This effect is typically more pronounced in smaller QD diameters, characterized by a higher surface-to-volume ratio.[159] As in the absorption spectra, the band-edge emission line is broadened by the inhomogeneity of particle sizes. Other contributions influencing the linewidths of the QDs PL arise from the exciton

interacting with spins, phonons, and ligands. These phenomena are collectively referred to as homogenous broadening. They are extensively investigated with single-dot spectroscopy, often conducted at cryogenic temperatures. Noteworthy is that for a single QD, the linewidth narrows with the increase of QDs' mean size. This phenomenon is attributed to the coupling between excitons and surface phonons and, as such, is more dominant for smaller particles.[160]

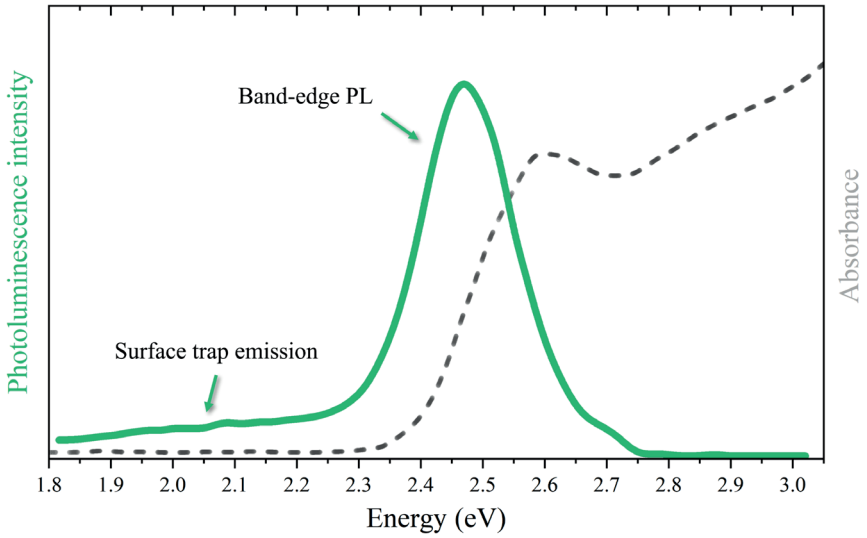

Figure 3.4 *Example of PL spectrum of CdSe QDs model system (solid green line). The arrows indicate regions of band-edge and trap-assisted PL. The corresponding UV-Vis absorption spectrum is marked with a dashed gray line. Adopted with permission from Springer Nature* [159].

The steady-state optical absorption and emission spectroscopy proved to be excellent approaches for assessing QDs' optical properties, like absorption coefficients, bandgap energy, electronic transition energies, PL wavelengths, and intensity. However, steady-state methods provide only information about the initial and final state of the studied sample without any glimpse into the charge carrier population dynamics in studied processes. Such analysis, crucial in understanding and controlling exciton interactions in QDs, requires techniques with sufficient temporal resolution matching the characteristic timescales of investigated phenomena.

3.3 Transient absorption spectroscopy

Optical transient absorption spectroscopy, or simply transient absorption (TA), is one of the most popular time-resolved methods of probing electron dynamics in QDs, and many other species. The technique measures changes in sample absorption at different times to characterize specific electron processes in matter initiated by prior photoexcitation. TA experiment is realized by the so-called pump-probe approach, schematically presented in Fig. 3.5. The sample is first excited with an intense monochromatic flash (pump) inducing temporary charge redistribution effects in the studied system. After some defined delay time, the broadband white pulse follows, imprinting the current electronic state in a collected absorption spectrum. TA spectra are typically plotted as a difference between the absorption spectra of the excited- $A(E,t)$ and ground-state $A_0(E)$ sample:

$$\Delta A(E,t) = A(E,t) - A_0(E) \quad (4)$$

where E is the photon energy and t is a pump-probe delay time. $A_0(E)$ is recorded without the pump pulse and is equivalent to the steady-state UV-Vis absorption spectrum. The pump-probe delay, defined as the distance in the time domain between the maxima of both pulses, translates directly to a specific timepoint from the start of the studied process. The TA difference spectrum typically contains both positive and negative features. Positive signal results from pump-induced excited state absorption (ESA) and negative contributions correspond to either depletion of the ground state population called ground state bleach (GSB) or stimulated emission (SE) caused by the interaction of the probe pulse with the excited states prepared by the pump. TA measurement is conducted for different pump-probe delay values until complete information regarding the dynamics of investigated phenomena is acquired.[161,162]

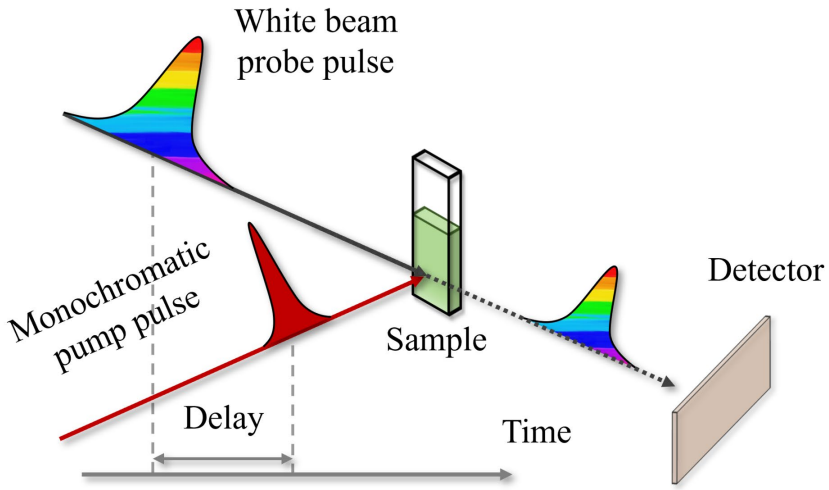

Figure 3.5 *Scheme of a pump-probe experiment in transient absorption spectroscopy.*

In general, variations of the TA apparatus exist, allowing to cover different timescales. For example, nanosecond TA is used to study the kinetics of chemical reactions. To track carrier relaxation processes (discussed in Section 2.3) in QDs, an ultrafast version of the method, with femtosecond laser pulses, is required. A typical fs-TA layout is schematically presented in Fig. 3.6. Most available setups utilize a single primary source, for example, a self-mode locked titanium dopped sapphire laser (Ti:sapphire), for generating both pump and probe pulses. Such lasers produce femtosecond IR pulses with a central photon energy of ~1.55 eV (800 nm), pulse duration in the range of several dozen fs, repetition rates around 1 kHz, and total pulse energies of a few millijoules. The emitted pulse splits into two parts, with most of the initial intensity being guided toward the pump line. Depending on the studied sample, the pump photon energies are converted to fit specific excitation requirements. This conversion can be realized using nonlinear crystals through second or third harmonic generation, producing photon energies of ~3.1 eV (400 nm) and ~4.56 eV (266 nm), respectively. Alternatively, an optical parametric amplifier is applied to tune photon energies throughout the near-UV, Vis, and IR range. Before reaching the sample,

the pump encounters a chopper, a fan-like instrument that blocks every second pump pulse, thus allowing the collection of reference unpumped spectra during the experiment. The other, less intense probe pulse is firstly delayed relatively to the pump with the help of a delay line consisting of a pair of mirrors placed on the motorized stage. Because the speed of light (c) is a known quantity, it is possible to control the pump-probe delay by adjusting the position of the mirrors, which changes the distance of the probe pulse path and the time it takes for the pulse to reach the sample. The specific pump-probe delay change (Δt) can be determined using a simple formula $\Delta t = 2 \times \Delta x/c$, where Δx is the spatial position change of the mirrors. For example, 1 ps shift of the pump-probe arrival time translates to about 150 µm of the mirrors displacement. The lower limit of the attainable delay values is determined by the precision of the moving motors, while the upper one is a matter of motor range and available space. Since TA measurements typically require a broadband probe, the IR flash is subsequently converted to white light supercontinuum by focusing it into a transparent Kerr element, like a thin plate of sapphire or CaF_2. The polychromatic probe is then directed to the sample placed in the thin quartz cuvette. The cuvette is positioned on another motorized stage, constantly moving the container with the studied solution to refresh the probed spot, avoiding sample photodegradation. After passing the sample, the probe photons are collected by a CCD camera equipped with a diffraction grating or a prism for the dispersion of white light.[161]

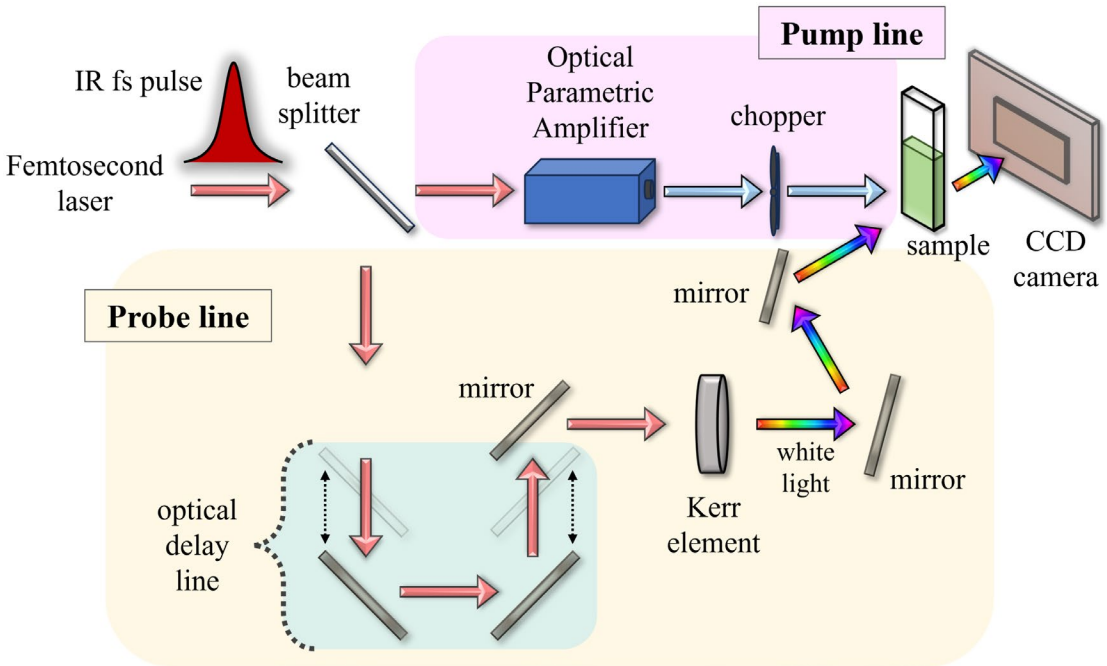

Figure 3.6 *Schematical representation of the typical pump-probe setup for fs-TA measurements.*

Data acquired in the TA experiment is usually given in the matrix form, where the first row represents the photon energy/wavelength of the probe, the first column pump-probe delay values, and the rest of the matrix consists of ΔA for a given photon energy and delay. Similarly to any spectroscopic time-resolved pump-probe experiments, the temporal resolution of the TA measurements is restricted by the cross-correlation of the pump and probe pulses, determined mainly by their time widths. Additional factors limiting the temporal resolution arise from the geometry of the TA apparatus, like sample thickness and

motor precision of the delay line. All of these effects are included in the instrument response function (IRF) that defines the uncertainty of the experiment. Before the analysis, the TA data needs to be corrected for various unwanted effects unrelated to the investigated electron dynamics in the sample. Such signal impurities include scattering light from the pump, spontaneous emission from the sample, and nonlinear effects arising from the temporal and spectral overlap between pump and probe pulses. Scattering and spontaneous emission are mitigated by subtracting from the data averaged spectra collected for negative delay (probe arrives before the pump). The latter pump-probe phenomena may significantly influence the data around time zero, and their removal is not straightforward. The simplest method involves the subtraction of the neat solvent. However, the acquired solvent signal often should be scaled with the energy-dependent factor before the background correction procedure. Another important phenomenon affecting the data is related to the group velocity dispersion (chirp) of the probe. As the white light probe pulse passes through elements of the TA setup, for example, the walls of the sample container, distinct wavelengths (photon energies) will travel at different velocities, meaning that they will reach the sample at slightly different times. Various approaches built into the commercially available programs for TA data analysis exist to correct the chirp effect.[162]

TA measurement of QDs suspensions provides time-dependent information regarding interband relaxation, intraband processes, and trap-mediated effects. Fig. 3.7 shows transitions in the ground state (a) and excited (b) sample and their corresponding signal (c) in TA analysis. As in the steady-state UV-Vis experiment, the unpumped QDs spectrum (Fig. 3.7c middle panel) unveils unoccupied CB electron levels (solid yellow lines). Prior excitation of the sample with the intense pump pulse temporarily modifies the excitonic features in the absorption spectrum (Fig. 3.7c top panel solid red lines) caused primarily by state-filling and carrier-carrier Coulombic interactions.[150] The first leads to the bleaching (loss of the intensity) of the excitonic peaks, as the CB electron already occupies the higher-energy level, reducing the number of available states. The second effect, the attractive interactions between CB electron and VB hole produced by the pump, induces an external electric field, which redshifts the following probe-generated transition. This phenomenon is known as the Stark effect and is responsible for derivative-like signals in the TA difference spectrum (Fig. 3.7c bottom panel solid blue lines).[155] TA studies of QDs primarily aim at the dynamics of those excitonic features, focusing on the identification of the relaxation channels involved with the bleach decay, determination of their characteristic lifetimes, and quantitative assessment of multiexciton states. Additionally, intraband transitions can be investigated (dotted structures in Fig. 3.7c). However, to study these processes, a separate experiment utilizing an IR probe is required, as the energy spacing between electron (or hole) levels in most QDs materials falls into the IR range. The UV-Vis TA allows investigation of the weak broadband (dashed line in Fig. 3.7c) signal generally attributed to photoinduced absorption of surface electrons and holes. Although present in the literature, this signal is less explored than widely studied excitonic transitions.[163]

In the TA experiments, the selection of pump parameters determines induced electronic processes in QDs studied by the probe pulse, affecting measurable transient spectra. As presented in Fig. 2.3, plenty of various relaxation channels exist, occurring at comparable timescales. Depending on the pump and probe qualities, different charge carrier phenomena

can be triggered and studied. If the pump photon energy significantly exceeds the bandgap energy of the sample, the exciton bleaches can provide additional information regarding intraband relaxation.[164] However, in such cases, different transitions from the same initial or to the same final state can be simultaneously triggered, complicating the analysis. State-selectivity is achieved by choosing the pump photon energy to match the maxima of specific exciton maxima obtained from the steady-state absorption spectrum. The intensity of the pump pulse also influences the acquired TA signal. For the studies regarding population dynamics of the excitonic states, pump intensity is selected so the average number of carriers per QD is well below one, meaning that the probe pulse encounters particles with either zero (predominantly) or one excited electron-hole pair. This can be evaluated based on the TA analysis assuming the Poisson distribution of charge carriers. In addition, such pump intensity levels allow investigation of the biexciton transition. More complex multicarrier dynamics are accessed with a more intense pump beam, creating multiple charge carrier pairs in a single QD.[150,163]

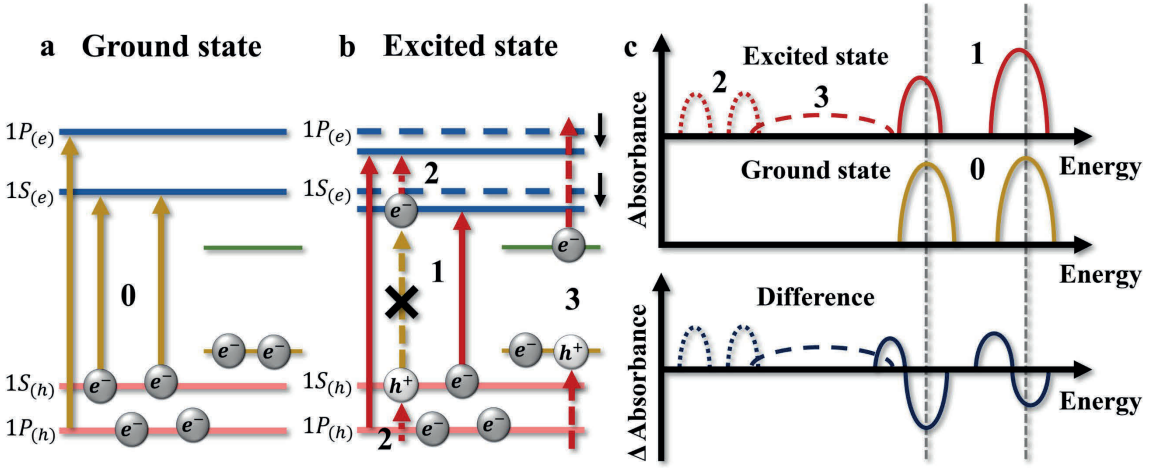

Figure 3.7 *Schematic representation of ground (a) and excited state (b) energy levels and optical transitions in QDs probed during the TA experiment. Black arrows in panel b indicate shifts in exciton transition energies in excited QDs. (c) Absorption spectra of ground and excited QDs (top panel) and their corresponding TA difference spectrum (bottom panel). Allowed charge carrier transitions in the ground and excited state QDs and their signal on the absorption spectra are marked with yellow and red, respectively. Interband transitions in the ground (0) and excited (1) states are denoted with solid lines. Intraband transitions (2) are marked with dotted lines. Photoinduced absorption of trapped electrons and holes (3) are marked with dashed lines. Used with permission of Annual Reviews, Inc., from* [163]*. Copyright 2016 Annual Reviews. Permission conveyed through Copyright Clearance Center, Inc.*

4. X-ray spectroscopy and its application in QDs research

4.1 Basics and principles

Similarly to previously discussed optical spectroscopy, X-ray spectroscopy probes electron transitions in matter. As such, it is also a subgroup of electron spectroscopies. However, because X-rays are much more energetic than UV/Vis radiation, X-ray spectroscopy techniques provide different information about studied samples, which, in the context of QDs research, complement the data obtained from optical methods.

Based on their energy, X-rays are divided into three regimes: soft (0.1-2 keV), tender (2-5 keV), and hard (above 5 keV). The energy of X-rays strictly corresponds to their ability to penetrate matter. Soft X-rays exhibit short probing depths, are highly attenuated by the air, and require vacuum conditions for their utilization in the experiment. Hard X-rays pierce through bulk materials, allowing more extreme sample environments. The tender energy range is placed in between two previous regions.

X-rays interact with atoms through various phenomena with different probabilities depending on the photon energy and atomic number (Z) of a specific atom. These are the photoelectric effect, which results in the total absorption of photon energy by a strongly bounded electron in atomic orbital, elastic (Thomson) scattering on the atomic nucleus or strongly bounded electrons without any energy transfer, inelastic (Compton) scattering on the weakly-bounded outer-shell electrons with partial energy loss of the X-ray, and positron-electron pair production. In the energy range relevant for X-ray spectroscopy experiments applied to materials studied in this thesis (~10 keV) the most dominant is the photoelectric effect. Just as in other types of absorption spectroscopy, including presented earlier UV-Vis spectroscopy, photoabsorption of X-rays by a given specimen follows the Lambert-Beer law (eq. 3). In the X-ray spectroscopy field the Lambert-Beer formula is typically written using energy-dependent mass absorption coefficient μ $[\frac{cm^2}{g}]$:

$$I_1 = I_0 e^{-\mu \rho d} \tag{5}$$

where ρ $[\frac{g}{cm^3}]$ is a density and d $[cm]$ thickness of the specimen. In general, the mass absorption coefficient of the target gradually decreases with the increasing photon energy. However, for X-ray energies corresponding to the binding energy of the inner-shell electron of the illuminated atom, a sharp increase of μ is observed, which is referred to as an absorption edge. Absorption of X-rays with above-edge energies promotes the inner-shell electron to a higher unoccupied state or the continuum level. Such X-ray-induced transition leaves the atom in the exited state with an unfilled vacancy at the initial inner-shell state. To minimize the total energy of an atom, the created core-hole will be quickly (within ~fs) filled with another electron occupying outer atomic orbitals. This process is accompanied by the emission of either an Auger electron or photon with energy equal to the difference between the two states involved with the transition.

Both processes of X-ray absorption and X-ray emission can be employed in X-ray spectroscopy experiments to probe the electronic structure of investigated materials.

Determination of the $\mu(E)$ for incident photon energies in the vicinity of the ionization energy (absorption edge) of specific inner-shell electrons is the basis of the X-ray absorption spectroscopy (XAS), which provides information regarding the unoccupied electron states of the specimen. Analogously, measuring X-ray fluorescence energy and intensity through X-ray emission spectroscopy (XES) allows studying occupied levels. Since the binding energies of core electrons vary significantly with Z (atom type), both techniques provide elemental selectivity, allowing studies that capture the average state of all atoms of a given type in the analyzed sample. Combining penetrating properties of hard X-rays with the chemical specificity of X-ray spectroscopies yields bulk-sensitive methods capable of probing gaseous, liquid, and solid samples in their native environment, determining their DOS.[165]

4.2 X-ray absorption spectroscopy

XAS provides insight into unoccupied electronic states and the local environment of the absorbing atom. Fig. 4.1 shows an example of the XAS spectrum. Two regions are distinguished, each providing different information regarding the studied object. Part of the spectrum in the vicinity of the absorption edge is referred to as X-ray absorption near edge structure (XANES), and it usually ranges from several eV below up to ~50 eV above the absorption edge energy (E_0).[166] In this regime, probed electron transitions follow dipole-allowed selection rules: $\Delta l = \pm 1$, $\Delta j = 0, \pm 1$, where l and j are the angular and azimuthal (total) momentum quantum numbers, respectively. The specific absorption edge is labeled, invoking the orbital from which the electron is promoted to higher states due to X-ray absorption. For instance, the K-edge XAS spectrum (like the one presented in Fig. 4.1) shows the sample absorption in the function of incident photon energies around the excitation energy of 1s (K shell) electron and its main features origin from 1s→np transitions. Analogously, L_1-, L_2- and L_3-edges refer to electron transitions from 2s, $2p_{1/2}$ and $2p_{3/2}$ initial state.[167] In particular, K-edge XAS is an attractive approach for examining structures with transition metals, including ZnSe QDs examined in this thesis, as it corresponds to hard X-ray energies easily achievable with most available X-ray sources, allowing bulk-sensitive studies in native sample environments. E_0 is usually determined as the maximum of the first derivative of the XAS spectrum. Its value is intrinsic to a specific element, separated by hundreds or thousands of eV from other closest absorption edges, but also sensitive to the oxidation state of the studied atom, typically shifting by a fraction to a few eV towards higher energies with the increasing charge of the ion. The low-energy part of the K-edge XAS spectrum may contain additional weak pre-edge features, which correspond to dipole-forbidden but quadrupole-allowed ($\Delta l = \pm 2$) 1s→nd transitions. For some specific symmetries of transition metal compounds, this peak is more pronounced due to the hybridization of p-d orbitals.[168] Thus, the pre-edge signal provides good insight into the local environment of target atoms, assuming they possess empty d states.[166]

The higher-energy part of the XAS spectrum, stretching even up to 1 keV above the absorption edge, is designated as the extended X-ray absorption fine structure (EXAFS). In this regime, electrons are ejected into the so-called continuum level beyond the available states of the studied atom. The excess of absorbed photon energy is converted to the kinetic

energy of the photoelectron, which undergoes backscattering at the surrounding neighbor atoms. As a result, the EXAFS structure exhibits oscillatory behavior, with pronounced maxima and minima corresponding to constructive and destructive interference between the outgoing and backscattered photoelectron waves. Since the photoelectron scattering depends on the number of ligand atoms (coordination number) and their distance from the central atom, analysis of the oscillatory features provides information about the local environment and structural disorder of the selected element in the studied sample. Unlike diffraction techniques, EXAFS measurement does not require long-range ordering of the investigated specimen.[169]

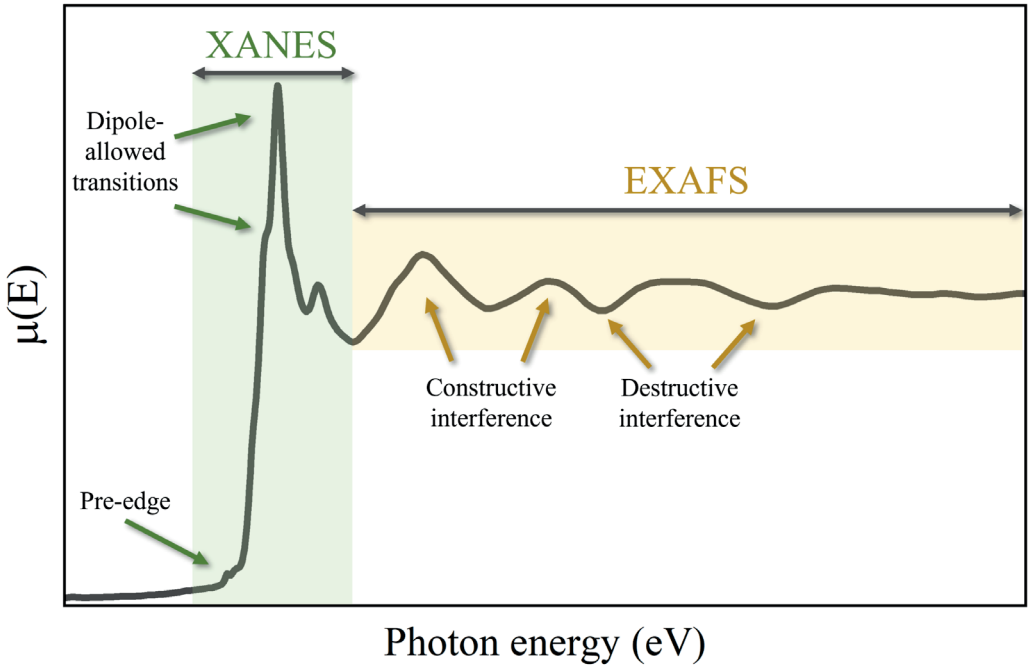

Figure 4.1 *Example of K-edge XAS spectrum with a description of main features. The spectrum was taken from the FAME open database*[170].

XAS spectra are acquired by recording various physical processes that depend on the absorption of X-rays in the sample. In the transmission mode, the mass absorption coefficient is determined directly from the Lambert-Beer law (eq. 5) based on the measurement of the incident and transmitted X-ray beam passing through the investigated target. It is the most commonly used and straightforward approach to acquiring XAS spectra, allowing bulk-sensitive analysis. Transmission mode requires uniform samples with a relatively high concentration of absorbing atoms for optimal measurement, which can be problematic in the case of expensive or difficult-to-prepare systems. On the other hand, X-ray attenuation by a probed target cannot be too high to achieve sufficient statistics of transmitted photons. Alternatively, equivalent information about specimen absorption can be obtained by detecting photons or electrons emitted from the sample excited by the monochromatic incident X-rays. The fluorescence yield (FY) mode focuses on counting secondary characteristic X-rays, collected either in a selected narrow energy window or over a broad range, depending on sample concentration, content of species in the target, intensity of scattering effects, and available instrumentation, which gives a signal proportional to the number of X-ray absorption events by the atoms of interest. Compared

to the transmission mode, this strategy is more suitable for dilute systems as it provides a clear signal over a near-zero background. However, implementing FY-XAS is more complex and may suffer from self-absorption effects, which can yield incorrect values of the mass absorption coefficient. XAS spectrum can also be obtained using electron yield (EY) mode, which detects primary photoelectrons, secondary electrons, and Auger electrons. Because of the short mean free path of electrons in matter, this approach exclusively probes near-surface atoms. In particular, EY measurements are popular among the soft X-ray community, as this regime is characterized by low penetration depth of the incident beam and high yields of Auger relaxation channels compared to radiative decays. Overall, specific sample qualities and available instrumentation dictate the choice of XAS detection mode.[171,172]

4.3 X-ray emission spectroscopy

Besides its application in FY-XAS, the process of characteristic X-ray emission from excited atoms is widely utilized in a separate technique, namely XES, providing an additional tool for materials characterization and complementing the data acquired from XAS studies. As mentioned, XES probes secondary electronic transitions filling core-hole states by measuring corresponding emission line energy. Fig. 4.2a presents the most intense emission lines arising from dipole-allowed radiative decay channels, commonly studied in XES experiments. They are labeled with a capital letter, indicating the atomic shell of the electron vacancy, and a small Greek letter that orders emission line intensity within the group with same first letter, starting from alfa as the most intense signal. This system, called Siegbahn notation, is the most widely used in the literature. However, IUPAC recommends a different nomenclature, focusing on the two electronic states involved with the transitions that lead to the characteristic fluorescence.[173] The comparison of the two systems is shown in Fig. 4.2b.

The most straightforward approach to carrying out XES measurement involves ionizing the sample with either an X-ray or accelerated particle (electrons or ions) beam. In such a case, referred to as non-resonant XES (NXES), a broad range of excitation energies can be utilized, simplifying the overall experiment. Analogously to K-edge XAS, XES analysis of K emission line series corresponding to electron transitions from higher levels to 1s core-hole state is especially appealing for Zn-based systems investigated in the thesis. Here, three distinct energy regions of X-ray emission are studied, presented in Fig. 4.2c. The most intense and concurrently least energetic is the Kα emission line originating from core-to-core 2p→1s transition, split into two separate signals $K\alpha_1$ ($2p_{3/2}\rightarrow1s$) and $K\alpha_2$ ($2p_{1/2}\rightarrow1s$) because of the spin-orbit coupling of 2p state. The intensity ratio of $K\alpha_1/K\alpha_2$ (2:1) stems from higher electron occupancy of the $2p_{3/2}$ orbital (4) compared to $2p_{1/2}$ (2). As both initial and final vacancy states involved in these electron transitions are deep inner-shell levels, in general, Kα lines carry limited information regarding the chemical state and environment of the studied system. Nevertheless, it has been demonstrated that different oxidation states of probed elements manifest in small shifts in the energies and widths of $K\alpha_1$ and $K\alpha_2$ observed in XES spectra.[174] Approximately eight times less intense is the higher-energy Kβ emission mainline resulting from core-to-

core 3p→1s transitions. The Kβ mainline XES spectrum involves predominantly the $K\beta_{1,3}$ peak, which consists of two signals from 3p spin-orbit coupling typically observed as a single feature due to the separation energy of $3p_{1/2}$ and $3p_{3/2}$ states being smaller than the respective linewidths. In some systems, the $K\beta_{1,3}$ line is accompanied by weak satellite line Kβ' arising as a consequence of 3p-3d exchange interactions. Both lines are characterized by high chemical sensitivity, providing information regarding the spin state, oxidation state, and transition metal-ligand covalency.[175–177] Towards the higher energies are X-ray lines associated with electron transitions from the occupied valence levels (valence-to-core transitions), split into two features: $K\beta_{2,5}$ and the satellite line Kβ" resulting from mixed 4d-3d metal and np-ns ligand orbitals. XES analysis of this region yields excellent insight regarding the distribution and identity of ligands bound to the investigated central atom. However, valence-to-core emission lines are very faint, about a thousand times less intense than Kα lines, which excludes valence-to-core XES experiments with conventional low-power excitation sources.[178,179]

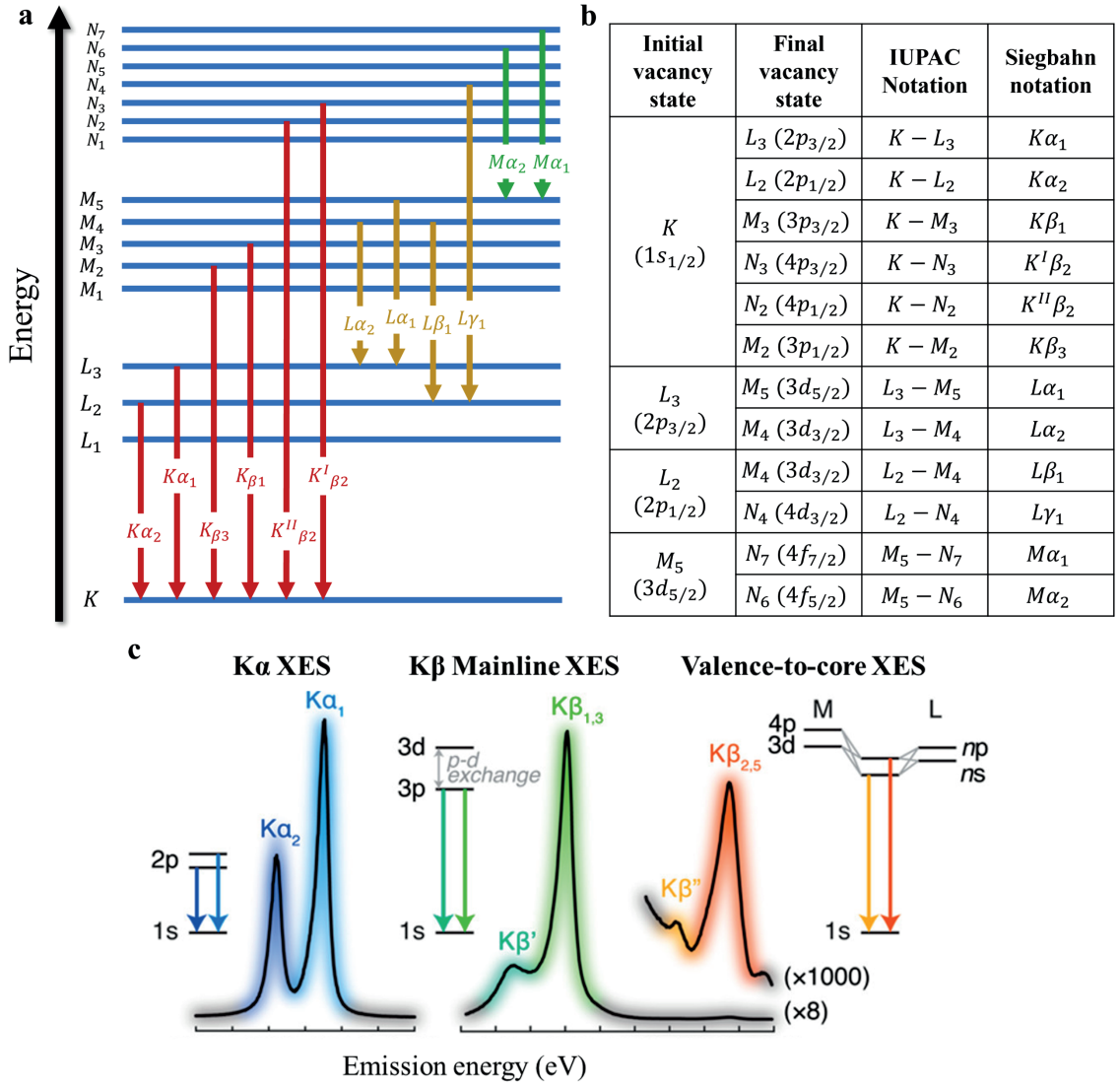

Initial vacancy state	Final vacancy state	IUPAC Notation	Siegbahn notation
K $(1s_{1/2})$	L_3 $(2p_{3/2})$	$K-L_3$	$K\alpha_1$
	L_2 $(2p_{1/2})$	$K-L_2$	$K\alpha_2$
	M_3 $(3p_{3/2})$	$K-M_3$	$K\beta_1$
	N_3 $(4p_{3/2})$	$K-N_3$	$K^I\beta_2$
	N_2 $(4p_{1/2})$	$K-N_2$	$K^{II}\beta_2$
	M_2 $(3p_{1/2})$	$K-M_2$	$K\beta_3$
L_3 $(2p_{3/2})$	M_5 $(3d_{5/2})$	L_3-M_5	$L\alpha_1$
	M_4 $(3d_{3/2})$	L_3-M_4	$L\alpha_2$
L_2 $(2p_{1/2})$	M_4 $(3d_{3/2})$	L_2-M_4	$L\beta_1$
	N_4 $(4d_{3/2})$	L_2-N_4	$L\gamma_1$
M_5 $(3d_{5/2})$	N_7 $(4f_{7/2})$	M_5-N_7	$M\alpha_1$
	N_6 $(4f_{5/2})$	M_5-N_6	$M\alpha_2$

Figure 4.2 *a) Most intense X-ray emission lines arising from dipole-allowed electron transitions. The characteristic lines are labeled according to the Siegbahn notation system. b) Comparison between Siegbahn and IUPAC nomenclature. c) example of XES spectra of various emission lines*

corresponding to electron transitions to 1s initial core-hole state. The image was reproduced from [178] *under the CC-BY 4.0 license https://creativecommons.org/licenses/by/4.0/.*

While not utilized in the presented work, it should be noted that XES measurements are also carried out in resonant conditions, where the excitation energy is tuned to induce transitions of bounded inner-shell electrons to the unoccupied atomic states instead of the continuum as in the case of NXES. This approach is referred to as resonant XES (RXES) or resonant inelastic X-ray scattering (RIXS). In RIXS experiments, a series of XES spectra are recorded for different monochromatic incident X-ray beam energies in the vicinity of selected absorption edge, coupling XAS and XES methods to obtain a two-dimensional RIXS plane providing more detailed information regarding the studied sample than either XAS or XAS applied separately.[178]

4.4 X-ray sources

One of the dominant factors dictating the capabilities of X-ray spectroscopy experiments is the source of the X-ray beam. Nowadays, XAS and XES measurements can be carried out both with low-cost instruments that can be easily installed in a typical laboratory as well as in large-scale facilities, utilizing more advanced accelerator-based sources with superior beam qualities.

Historically, X-ray tubes were the first sources utilized by scientists to record X-ray spectra, starting from the Broglie experiment in 1913.[180] While its design and materials evolved over more than a century of utilization, the physics and main components remain similar to this day. The X-ray tube consists of a cathode and anode placed in a glass vacuum chamber, as presented in Fig. 4.3a. The electrodes are connected to an external high-voltage supply, providing maximum tube voltages from tens to a few hundred kV. The cathode is a filament commonly made from tungsten that, under extensive heating, produces a free electron beam through the thermionic effect. The electrons are accelerated under the high-voltage potential towards the anode target and interact with it, gradually losing excess kinetic energy. The deacceleration of electrons leads to the production of broadband continuous X-ray radiation, known as Bremsstrahlung. Additionally, the primary electron beam with sufficient energy can excite electrons bounded in atomic orbitals of anode material, triggering secondary emission of the discrete characteristic X-rays. These two types of radiation constitute the X-ray tube spectrum depicted in Fig 4.3b. The intensity of both components depends on and increases with the tube voltage and electron current. The maximum voltage defines the maximum X-ray energy that the accelerated electrons emit, whereas the low energy part of the spectrum results from the X-ray attenuation by the beryllium exit window. The type of anode material also highly influences the tube output. In general, electrons interacting with targets made of high Z atoms produce more Bremsstrahlung radiation. Moreover, anode composition determines the energy of characteristic X-rays present in the tube spectrum, which can influence the possible application range of the instrument. Frequently used targets include anodes made of tungsten, copper, or molybdenum.[181]

The main disadvantage of X-ray tubes is their inefficient generation of X-rays, with only about 1% of initial electron energy being converted to usable radiation. The rest is

transformed into phonons, which can lead to overheating of the anode during prolonged operations, irreversibly damaging it. This issue limits the development of high-power X-ray tubes and as a result, hinders the attainable X-ray beam intensity. The problem of overheating is partially mitigated by integrating targets with cooling systems. Alternatively, X-ray tubes are equipped with rotating anodes, which allow constant refreshment of the electron-anode interaction spot. Nevertheless, relatively low spectral output and challenges with heat management are still limiting factors of this source.[182] Still, compact size, simple operation, and low price make X-ray tubes one of the only candidates suitable for laboratory-based in-house apparatuses.[183–185]

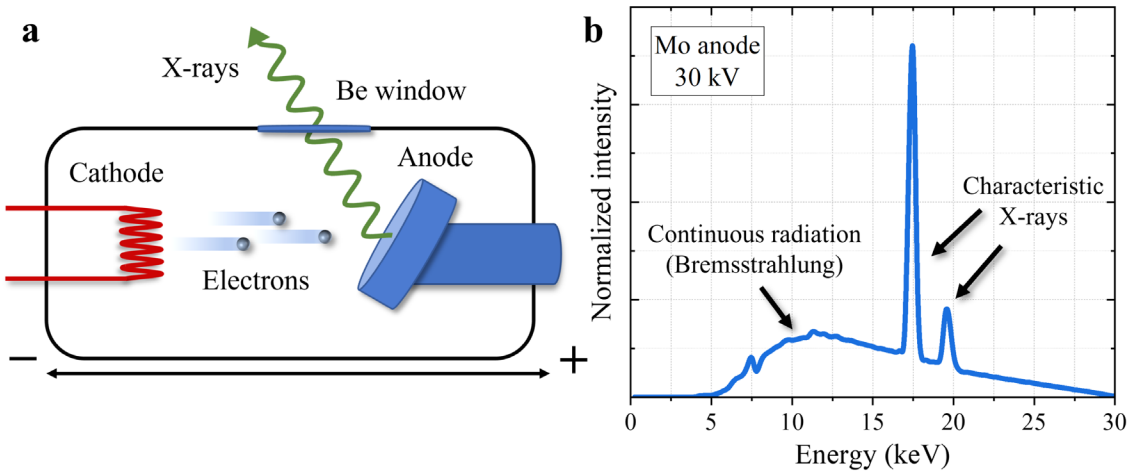

Figure 4.3 *a) Schematic construction of the X-ray tube. b) Example of X-ray tube spectrum acquired for X-ray tube with molybdenum anode, operating at 30 kV voltage. The spectrum contains continuous Bremsstrahlung radiation and the Mo $K\alpha_{1,2}$ (lower energy, higher intensity) and $K\beta_{1,3}$ (higher energy, lower intensity) emission lines. The data was taken from [186] under the CC BY 4.0 license https://creativecommons.org/licenses/by/4.0/.*

An enormous step in terms of X-ray spectroscopy applicability was the development of synchrotrons, which utilize large circular particle accelerators known as storage rings that drive electrons to relativistic speeds in curved trajectories, producing light beam of outstanding qualities known as synchrotron radiation. Fig. 4.4 presents a schematic representation of the synchrotron facility. The electron beam produced by the electron gun, analogously to the X-ray tube, is initially guided to the linear accelerator called liniac, where it reaches energies of tens to hundreds of MeV. In some synchrotrons the beam, before entering the storage ring, is further boosted to several GeV in a smaller ring appropriately named booster. Finally, the electrons are transferred to the final accelerator where, if necessary, they can be further accelerated by the radio frequency (RF) cavities installed in the straight sections to attain the desired kinetic energy. Inside the storage ring, the fully accelerated particles, moving with a speed close (~99.9999%) to the speed of light, are forced to change their trajectory by magnetic fields induced by bending magnets installed throughout the acceleration. As a result, part of their energy is released as synchrotron radiation, which is directed to beamlines where it is further adequately modified for specific experiments. The energy losses of the electrons are compensated by RF cavities, meaning that they can repeatedly cycle throughout the storage ring, producing more radiation.[187]

Bending magnets typically perform a dual function of maintaining the curved trajectory of the electrons and generating radiation. Modern facilities, also called 3rd generation synchrotrons, use so-called insertion devices for the latter, namely wigglers and undulators, consisting of periodically arranged sets of magnets installed on straight sections of the storage ring. They produce strong magnetic fields, which cause additional transverse oscillations of the accelerated electrons and increase the intensity of the generated photon beam. In the undulator, the magnets are placed closer together, which causes the amplitude of fluctuations of charged particles to decrease and their frequency to increase. In such conditions, the resulting electromagnetic waves interfere with each other, resulting in radiation with a narrower spectral range.[187] Fig. 4.5a compares spectral brightness, defined as the number of photons emitted per second per bandwidth per unit solid angle and unit area of the source[188], of synchrotron radiation generators and conventional X-ray tubes. As depicted, the utilization of insertion devices significantly improves the spectral brightness, with undulators providing the highest output. In any case, the synchrotron radiation sources deliver several orders of magnitudes more intense X-ray beams than X-ray tubes. This property, in combination with other qualities of synchrotron radiation, such as broad spectral range, narrow angular collimation, high degree of polarization, pulsed temporal structure with pulse durations as short as single ps, and high degree of collimation, makes these facilities an irreplaceable place for advanced spectroscopic, diffraction and imaging experiments. However, the construction and further maintenance of synchrotrons are very costly. There are approximately only 70 different synchrotron facilities around the world.[189]

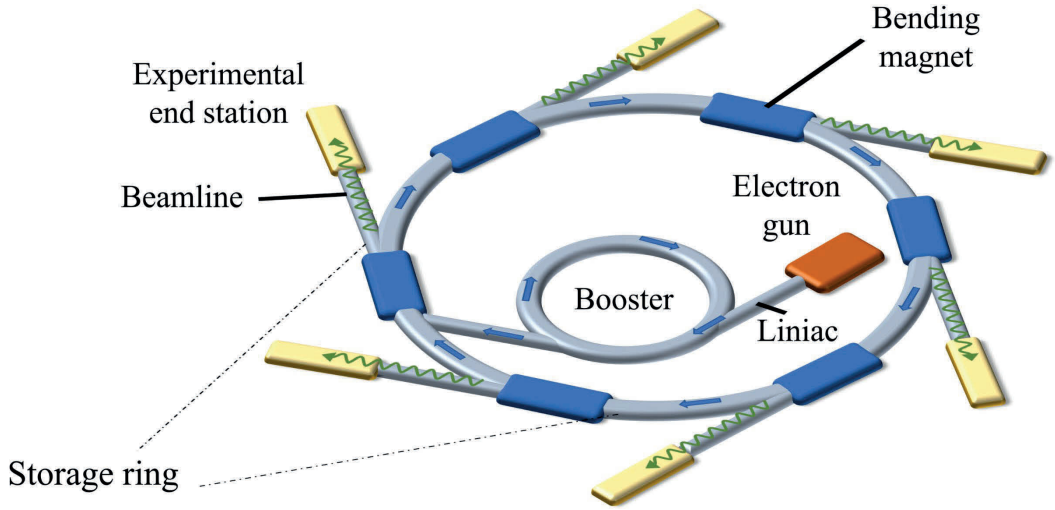

Figure 4.4 *Simplified scheme of synchrotron radiation facility.*

While the 3rd generation synchrotrons represent one of the most advanced scientific tools available to researchers, X-ray science already took another massive step with the arrival of 4th generation sources called the X-ray Free Electron Lasers (XFELs). These are large linear particle accelerators, stretching up to several kilometers, which produce ultrashort laser-like X-ray flashes with brightness unmatched by any other human-made X-ray source. Accelerated relativistic electrons are guided to the undulator, which vastly exceeds the length of those installed at synchrotrons. Inside the undulator, the electron beam moves in an oscillatory sinusoidal fashion, emitting X-rays in a process. Produced

photons interact with the electron beam, slowing down the faster particles and accelerating the slower ones. These interactions lead to the microbunching of the electrons, which is accompanied by a rapid increase in radiation intensity and high transverse coherence (within a single microbunch). Such a process is known as Self Amplified Spontaneous Emission (SASE) and is currently one of the main mechanisms of X-ray production at XFELs. SASE pulse durations correspond to the length of electron microbunch and, for now, reach the level down to single fs. The brightness of a single flash (peak brightness) vastly exceeds other pulsed X-ray sources, which is depicted in Fig. 4.5b, showing peak brightness for selected 3rd and 4th generation facilities. While the enormous XFEL pulse intensity and ultrashort duration are unmatched, the spontaneous nature of the SASE process results in a spiky temporal profile, relatively large spectral bandwidth, and significant variations of all parameters between each pulse. Nevertheless, the development of XFELs unlocked new, previously unreachable possibilities to track electron dynamics in matter, allowing it to push the frontiers of both fundamental physics and applied sciences, like biology or nanomaterial research. The cost related to the construction and operation of the XFEL facility is exceptionally high, even compared to synchrotrons. As such, at the beginning of 2024, only several XFEL facilities operate worldwide.[190,191]

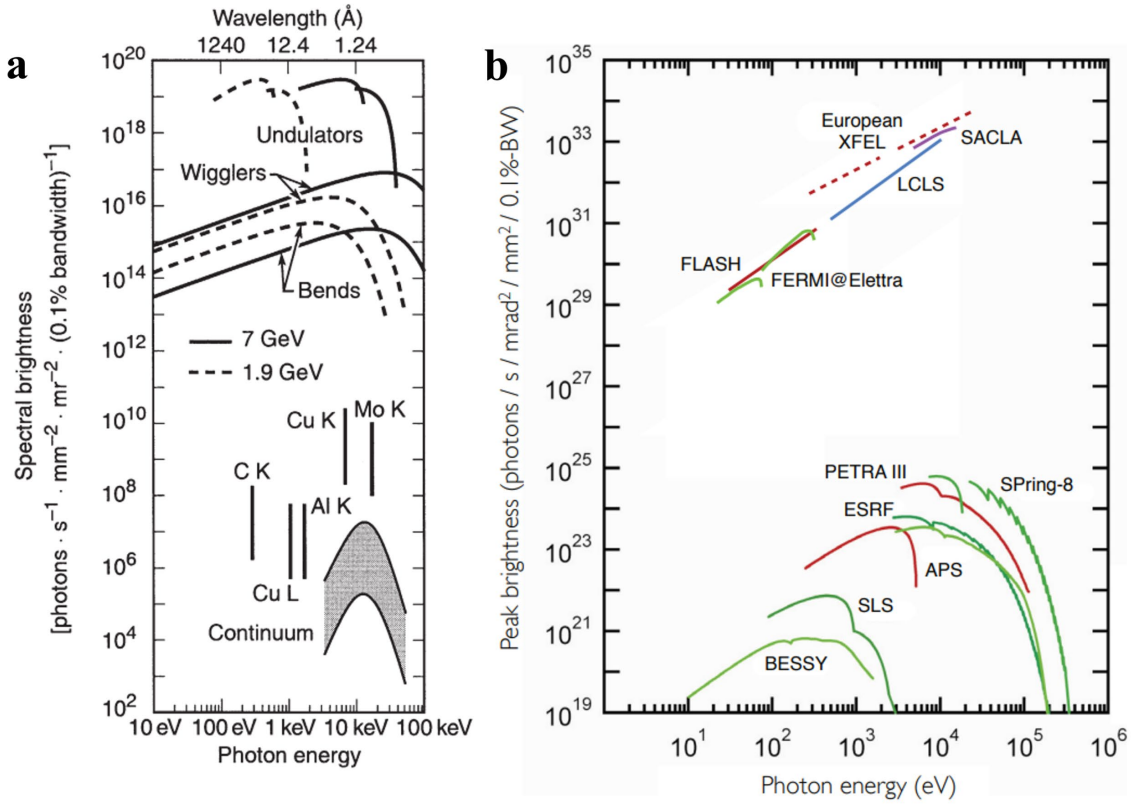

Figure 4.5 *a) Comparison of estimated spectral brightness between several synchrotron radiation sources and conventional X-ray tubes. The indicated two-order-of-magnitude ranges for the X-ray tube parameters show the approximate variation expected among stationary-anode tubes (lower end of range), rotating-anode tubes (middle), and rotating-anode tubes with microfocusing (upper end of range). Reprinted with permission from* [192]*. b) comparison of peak brightness between selected synchrotrons and XFEL facilities. Reproduced from* [193] *under CC BY 3.0 license https://creativecommons.org/licenses/by/3.0/.*

Described types of X-ray sources differ substantially in terms of performance, complexity, and accessibility. Therefore, each instrument/facility has a specific role within X-ray science. X-ray tubes provide an affordable option for in-house apparatuses that could be installed in laboratories at universities and research institutes for day-to-day routine sample examination. Moreover, they allow students to familiarize themselves with analytical techniques, instrumentation, and practical realization of experiments. Synchrotrons allow more advanced studies, however, only the highest priority cases are granted experimental time based on the prior application evaluation. Great number of proposals are rejected, primarily due to the limited availability of such facilities. This procedure is pushed to extreme levels with research at XFELs, where only a tiny fraction of applications with groundbreaking expected scientific impact are accepted. Notably, part of the large gap between X-ray tube setups and large-scale facilities is being filled with alternative instrumentation, such as laser-driven sources. These instruments are pumped by intense optical laser pulses, yielding even fs X-ray pulse durations comparable to XFEL flashes but with much smaller intensities more similar to lab-based sources. The ongoing progress at all levels of X-ray generators will undoubtedly extend the usability range of X-ray spectroscopies. Besides X-ray sources, another equipment essential for X-ray spectroscopy measurements is X-ray detection instrumentation.

4.5 X-ray spectrometry

Ideally, X-ray detection systems for spectroscopic experiments should be characterized by the highest possible counting efficiency (fraction of photons recorded by the detector to total number of X-rays) and highest energy discrimination (energy resolution) of recorded photons. In reality, one usually comes at the cost of the second (and vice versa), meaning that a compromise between efficiency and resolution needs to be made depending on the specific experiment. X-ray spectrometry approaches are commonly divided into energy-dispersive (EDS) and wavelength-dispersive (WDS) spectrometry.

In EDS, a single instrument is utilized for detecting X-rays and their energy identification. Such devices convert the energy of absorbed radiation into electrical signals. The proportional relation between photon energy and the amount of electric charge released in the detector allows the determination of X-ray energy. Scintillators, gas chambers, and semiconductor detectors are among the most applied EDS systems. The first is composed of an active element (scintillator crystal, like thallium-doped sodium iodine) that, upon X-ray absorption, reemits its energy in the form of visible photons, which subsequently are captured with coupled photodiode or photomultiplier. This approach offers high counting rates, especially for high-energy X-rays, but suffers from the poorest resolution. In gas proportional counters, noble-gas atoms are ionized by the X-ray photons, producing ions and electrons that flow towards negatively and positively charged areas inside the chamber, inducing measurable current pulses as they strike their respective targets. Such instrumentation offers wide-volume detection and flexibility in designing the experimental setup. Solid-state semiconductor detectors consist of reversely biased p-n junction that generate electron-hole pairs in depletion region resulting from interaction with captured X-rays. The voltage applied to such semiconductor materials separates and collects

respective charge carriers that produce electric signals. In particular, silicon drift detectors (SDDs) and CCDs offer energy resolution unachievable for scintillators or gas counters. In general, the main advantages of EDS are high quantum efficiency and large X-ray energy range coverage (from hundreds of eV even up to ~40 keV) in a single measurement. These qualities make EDS-based techniques ideal for elemental analysis, as multiple emission lines from various elements can be simultaneously detected. On the other hand, even the highest achievable energy resolution of such instrumentation (~120 eV for SSD detectors) is vastly insufficient to resolve all spectral features in XAS and XES spectra. For example, the Zinc $K\alpha_1$ (8639 eV) and $K\alpha_2$ (8616 eV) emissions lines are separated by ~23 eV, and their natural widths are 2.32 and 2.39 eV, respectively.[192,194] To track changes related to the chemical and structural environment of the studied atom, a much higher energy resolution of the experiment is necessary.[195]

In contrast to EDS, WDS instrumentation utilizes diffraction crystals (or gratings for soft X-ray regimes) as monochromators that spatially disperse X-ray wavelengths (energies) before X-ray interaction with the detector. The working principles of diffraction elements, also called analyzers, are described by the Braggs law:

$$n\lambda = 2dsin\theta \tag{6}$$

n denotes the order of diffraction, λ is the wavelength of the X-ray, d is the lattice spacing of the crystal layers, and θ is the angle between the incident X-ray and the diffraction plane (Bragg angle). The use of diffraction crystals allows for reaching even sub-eV energy resolution in the hard X-ray range. This enhancement of resolving power comes with a price of reduced photon flux and a smaller energy range. Nevertheless, WDS is the only approach suitable for high-resolution X-ray spectroscopy experiments.

The main parameter of a diffraction crystal is its 2d value, which determines its spectral range and energy resolution. As an implication of eq. (6), with a smaller distance between atomic planes (higher θ), the wavelength resolution increases. Simultaneously, the λ of X-rays has to be smaller than 2d. For a hard X-ray regime ($\lambda < 2.48$ Å), silicone or germanium crystals with various exposed crystallographic planes (crystal orientation) are typically employed. These materials possess well-developed fabrication and processing schemes, allowing facile implementation in X-ray spectroscopy experiments. Over the years, many different X-ray spectrometer types emerged, each with specific advantages and limitations. Analyzer crystals can be designed to either transmit (Laue-type) or reflect (Bragg-type) the incoming radiation guiding selected wavelengths to the detector. Laue-type geometry is more suitable for X-ray energies above 20 keV, as the lower-energy photons would be highly attenuated when passing through the bulk crystal. Standard Si/Ge Bragg-type monochromators cover the 7-12 keV range and will be discussed more comprehensively in the next paragraph, as this region corresponds to materials studied in the presented work.[195,196]

In general, flat and curved reflection crystals are employed in X-ray experiments. The former provides higher resolution since crystal imperfections cause geometrical aberrations in curved elements. However, flat crystals suffer from low photon collection efficiency due

to their small effective diffraction area. Bending the analyzers increases their solid angle, improving overall luminosity by 2-3 orders of magnitude. Hence, curved diffraction crystals are usually the go-to instruments for experiments with low-intensity X-ray sources or particularly photon-hungry techniques like RXES. Among the most popular geometries that utilize curved analyzers are Johann[197], Johansson[198], and von Hámos[199] spectrometers.[200]

Johann and Johansson geometry-based spectrometers operate in scanning mode, applying spherically bent crystal analyzers. In these configurations, point-to-point focusing is achieved by positioning the X-ray source, detector, and crystal on the Rowland circle. As such, in Johan and Johansson spectrometers, only a single wavelength is focused in the detector at a given time. Hence, the acquisition of a single XAS or XES spectrum is relatively time-consuming and requires synchronized movement of both crystal and detector. In both geometries, diffraction crystals are bent twice to the radius of the Rowland circle. Johannson analyzer's inner surface is additionally grounded away to a radius of the Rowland circle, improving energy resolution over the entire covered energy range.[195]

As an alternative approach, Von Hámos geometry utilizes a cylindrically bent crystal, which allows line-focusing along the curvature axis with concurrent wavelength dispersion in the perpendicular direction along a flat surface. The use of a cylindrically curved analyzer, paired with the position-sensitive detector, enables the simultaneous collection of multiple photon energies, sufficient to cover the entire XANES region or specific emission line of a given element in a single acquisition without the need to move either part of the experimental setup. This feature is also attractive from the perspective of time-resolve measurements at synchrotrons and XFELs. Simple operation and a reasonable compromise between count rates and resolution make Von Hámos geometry a suitable choice for laboratory-based spectrometers as well.[201,202]

4.6 Application of X-ray Spectroscopy in QDs research

As a result of bulk-sensitivity, elemental selectivity, and local chemical specificity of X-ray spectroscopy, these methods are frequently utilized in many research areas, including but not restricted to applied physics, chemistry, biology, medicine, cultural heritage, and material sciences. In particular, XAS/XES constitute an attractive approach to probe various nanomaterials, like QDs systems. Such structures are composed of as few as several hundred to several thousand atoms with high contributions of surface atoms and the possible presence of other in-lattice defects. These sites differ significantly from bulk atoms in their local environment, affecting the DOS of the material. Additionally, QDs are often covered with ligands, suspended in solvents, embedded in matrixes, or integrated with other hybrid species, all of which can dominate the signal acquired with many characterization techniques.[203] X-ray spectroscopy allows studies of the specific element from the QDs lattice, providing the average view of all atoms of a particular type. With the support of theoretical models and deconvolution procedures, it is, in principle, possible to separate and identify different contributions to the electronic structure of material. In the following paragraphs, two examples of XAS and XES applications are given, each addressing scientific questions regarding engineering, properties, and performance of various QDs.

Stein et al. utilized the XES to investigate structural defects at the InP QDs surface and the InP-ZnE (E = S, Se) core-shell interface created during the synthesis process. As visualized in Fig. 4.6, the group conducted P Kα XES measurements to identify P speciation in InP QDs based on the linear combination fitting procedure with recorded reference compounds. Performed analysis revealed two oxidation state contributions, 1- related to bulk InP (51% of the total signal in the presented case of InP/ZnS QDs) and 5+ arising due to oxidation of P atoms. Further, P Kα and valence-to-core P Kβ XES experiments of samples produced in various engineering approaches revealed that even with special care taken to prevent oxidation of phosphorus, all employed synthetic schemes introduced interfacial oxidative defects. Notably, compared to other experimental techniques of P chemical identification, that is, X-ray photoelectron spectroscopy and solid-state nuclear magnetic resonance spectroscopy, XES showed to be more efficient considering data acquisition time and amount of material necessary for the measurement.[204]

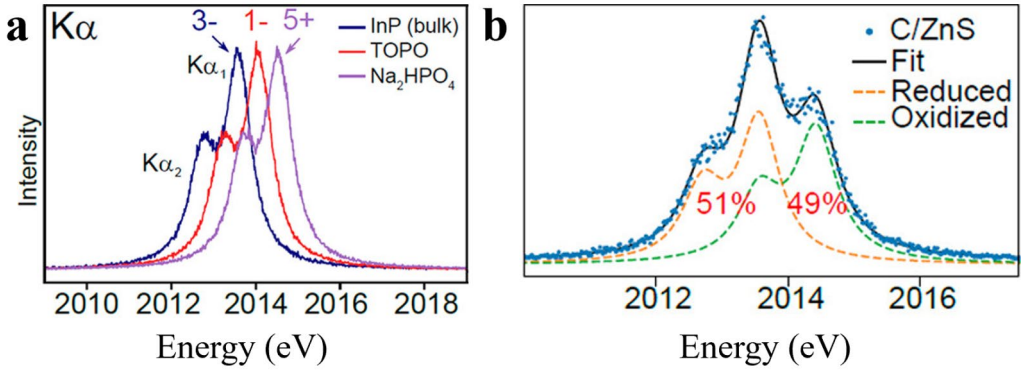

Figure 4.6 *a) P Kα XES spectra of reference compounds applied to deconvolute InP QDs signal with an indication of P atom oxidation state. The spectra shift towards higher energies with increasing oxidation state. b) P Kα XES spectrum of the InP/ZnS QDs with the contributions of each component to the total spectrum indicated as percentages. Reprinted with permission from* [204]*. Copyright 2018 American Chemical Society.*

In the second example, Khammang et al. conducted XAS to probe the cation exchange of Cu^{+} ions substituting Cd^{2+} in solution phase CdSe QDs to produce Cu_2Se crystals. Various stages of the process were mimicked by adding sub-stoichiometric amounts of metal salt $Cu(I)PF_6$ to the CdSe QDs suspension, and the recorded Cd, Se, and Cu K-edge XAS spectra, presented in Fig. 4.7, unveiled the changes related to Cu-Cd cation exchange. By applying linear combination fitting of Se K-edge spectra, two species, CdSe and Cu_2Se, were identified in the studied solution at the intermediate stages of the reaction. The fitting procedure also provided information about the concentration of Cu ions corresponding to a complete transformation of all QDs to Cu_2Se. Additional EXAFS analysis allowed the identification of diffusion as the mechanism responsible for cation exchange in the investigated system. This experiment highlighted the usefulness of X-ray spectroscopy element sensitivity and the ability to probe in-situ chemical processes occurring in a liquid environment.[205]

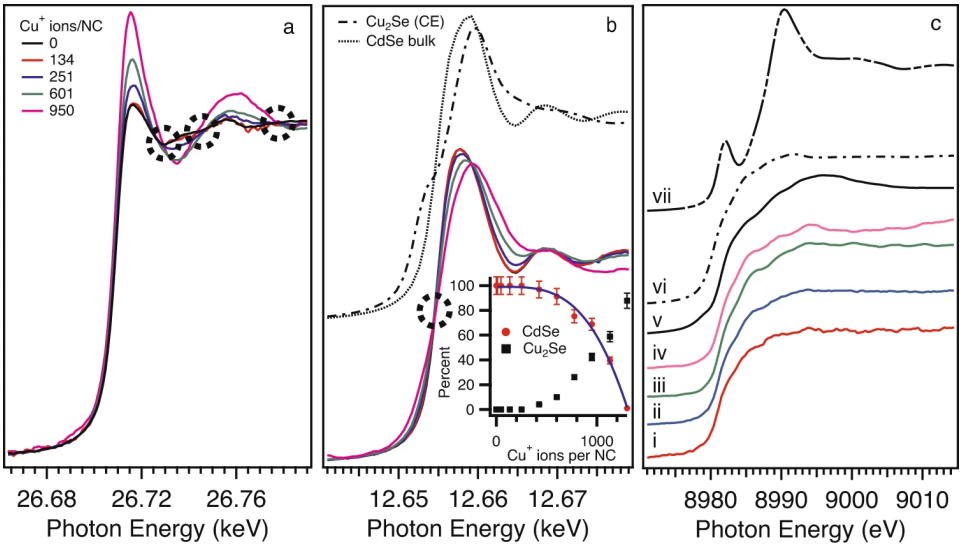

Figure 4.7 *Core level XANES during the cation exchange reaction. X-ray absorption spectra for 5.0 nm CdSe NCs at the (a) Cd K-edge, (b) Se K-edge, and (c) Cu K-edge for (i) 134, (ii) 251, (iii) 601, (iv) 950 Cu ions/NC, (v) Cu_2Se via cation exchange of CdSe, (vi) commercial Cu_2Se, and (vii) Cu(I)PF6. The inset of (b) is the LCF results for the Se K-edge using a CdSe and Cu_2Se model. Reproduced from* [205] *under CC BY 4.0 license https://creativecommons.org/licenses/by/4.0/.*

5. Aims

The thesis aims to characterize the effects influencing the electronic structure of ZnSe QDs. The main goal was realized through intermediate tasks discussed in the following chapters**.**

Chapter 6. Synthesis and characterization of ZnSe Quantum dots:

- preparation of a series of monodisperse ZnSe QDs samples with varying particle sizes;
- determination of the size-dependent quantum confinement effect on the optical absorption and emission of synthesized materials.

Chapter 7. Laboratory-based X-ray spectroscopy studies:

- optimization of the XAS and XES spectrometer;
- development of sample cell for X-ray analysis of liquid QDs suspensions;
- evaluation of the capabilities of laboratory X-ray spectroscopy;
- determination of the chemical and structural effects in the electronic structure of ZnSe QDs based on the XES and XAS spectra.

Chapter 8. Synchrotron X-ray spectroscopy experiments:

- verification of laboratory-based X-ray spectroscopy experiments;
- attribution of effects in the electronic structure of ZnSe QDs through combined experimental and theoretical approaches.

Chapter 9. Ultrafast optical transient absorption experiments:

- examination of decay kinetics of the excited charge carriers in prepared ZnSe QDs;
- quantification and attribution of all relaxation channels present in investigated materials.

Chapter 10. X-ray Chronoscopy as the potential tool for sub-fs studies of carrier dynamics:

- presentation of the X-ray Chronoscopy approach and possibilities of sub-fs time-resolved experiments at XFELs;
- evaluation of the method's capabilities to follow electron dynamics induced by ultrashort optical pulses.

6. Synthesis and characterization of ZnSe Quantum Dots

This section describes the preparation of colloidal ZnSe QDs suspensions that serve as the target material in the experiments described in the following three chapters of this thesis. Herein, besides specifying the synthetic procedures, obtained samples are characterized utilizing electron microscopy and steady-state optical spectroscopies to confirm the fabrication of the ZnSe QDs and provide information about the quality of the final products. Conducted measurements were used to assess QDs' most essential parameters, such as size distributions, mean size and bandgap energy. The acquired results regarding the size-dependent optical properties of synthesized samples are compared to literature reports.

6.1 ZnSe QDs preparation

Materials

Oleic acid (OA, 90%), 1-Octadecene (ODE, 90%), Hexane (≥95%), Zinc stearate ($Zn(St)_2$, purum 10-12% Zinc basis), Selenium (~100 mesh 99.99%), Zinc acetate dihydrate ($Zn(OAc)_2 \cdot H_2O$, >99%), Toluene (≥99.5%), Chloroform (≥99%) and Butylamine (99.5%) were purchased from Sigma-Aldrich. Acetone (analytical reagent grade), Ethanol (analytical reagent grade, 96%) and mineral oil were obtained from Pol-Aura.

Laboratory equipment

Due to the high reactivity of activated Zn and Se precursors, the synthesis of ZnSe QDs is typically conducted in an oxygen- and moisture-free environment. In the presented work, such conditions were realized utilizing the Schlenk line, schematically depicted in Fig. 6.1. The Schlenk line consists of two manifold systems: a vacuum line for evacuation of unwanted species, mainly air and water, from the reaction vessel and a second line for back-filing the sample container with a dry, purified inert gas (here nitrogen). The manifold layouts are interconnected through several ports, controlled with greased double oblique stopcocks. A sealed reaction flask containing precursors is attached to one port through a flexible, thick rubber tube. This design prevents simultaneous exposure of the synthesis solution to both systems. The vacuum line is equipped with a rotary vane pump, generating pressures $\sim 10^{-2}$-10^{-3} mbar, monitored by an implemented manometer. To prevent contamination of the vacuum pump with impurities and chemicals sucked from the sample flask, the vacuum system is integrated with a liquid nitrogen trap, constituting a durable glassware vessel placed inside a dewar filled with liquid nitrogen. The second end of the vacuum line is tightly enclosed to prevent pressure leakage. The other manifold line, on one end, is connected to the inert gas supply with a valve and a pressure gauge to regulate the flow, kept at slight over-pressure as compared to the ambient atmosphere. The exit of the line occurs through a so-called bubbler, which is a glass container filled with oil or mercury (here mineral oil) that acts as a pressure relief system and blocks the air from entering the system.

All QDs synthesis were conducted in a 50 mL three-neck round bottom flask coupled to the Schlenk line tubes via Liebling condenser as presented in Fig. 6.2. The water circulation cooling system of the condenser captures the solvent vapors back to the reaction solution at the same time preventing pressure build-up in the sealed setup caused by extensive heating during synthesis. The other flask necks are tightly sealed with a durable rubber septum or a glass stopper. A thermometer was put through the septum to monitor the temperature of the performed reactions. The entire setup was placed in a heating mantle equipped with magnetic stirring. Glass syringes were applied to inject the precursor solutions through the septum during ongoing synthesis.

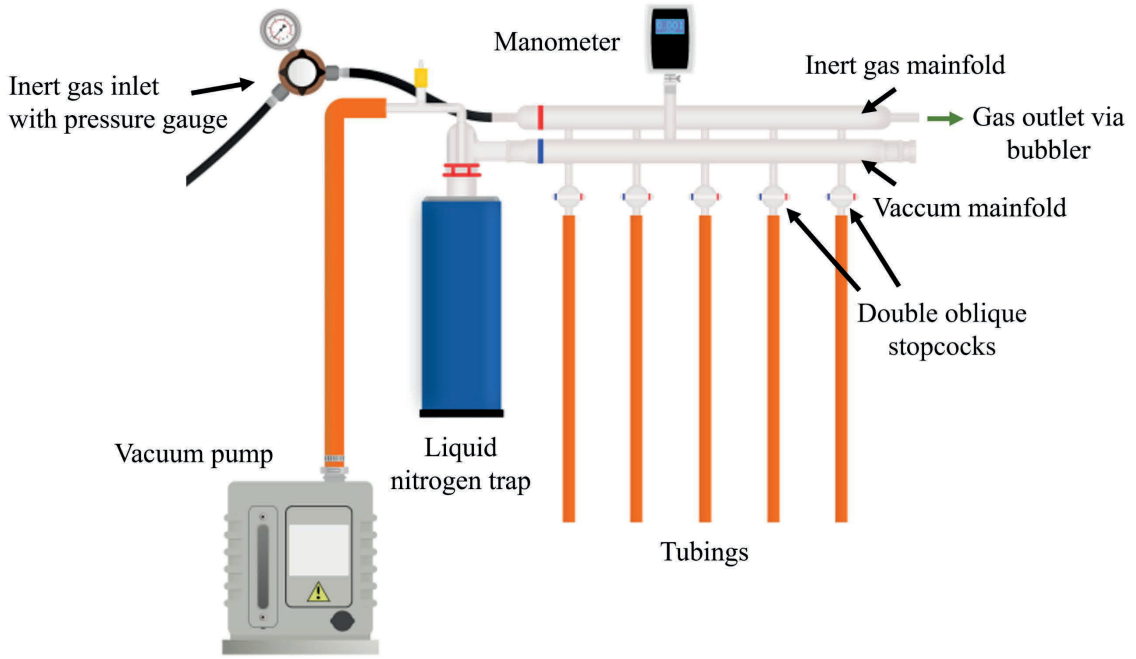

Figure 6.1 *Schematics of a Schlenk line. Adopted with graphical changes from* [206] *under CC BY-NC-ND 4.0 license https://creativecommons.org/licenses/by-nc-nd/4.0/.*

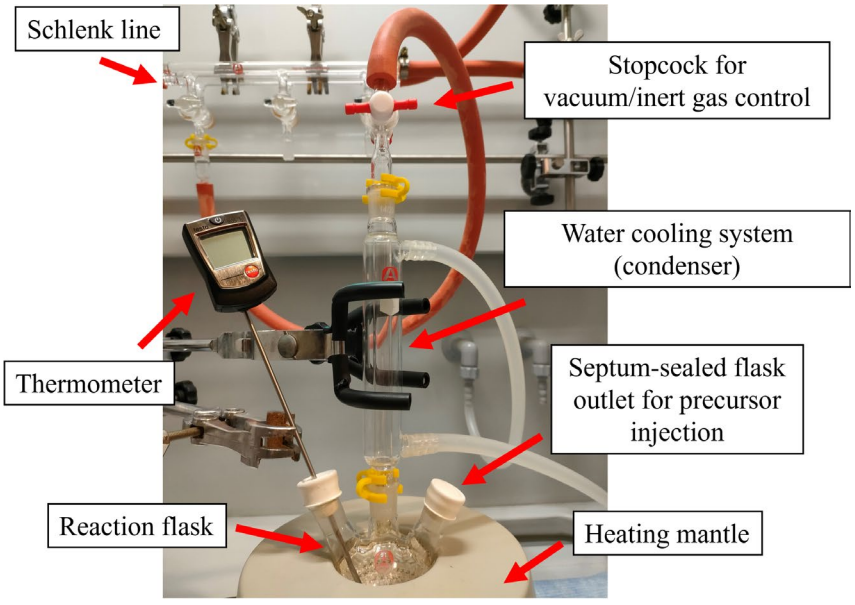

Figure 6.2 *Laboratory setup for QDs synthesis.*

All solid reagents were weighted utilizing RADWAG analytical balance. Prepared solutions/suspensions were mixed using Sunlab SU1900 vortex. Emmi-MF60 ultrasonic bath by EMAG was employed to uniformly disperse powders, particles, and nanostructures within the solvents. All centrifugation processes were carried out with a Pro-Analytical C4000 centrifuge by Centurion Scientific equipped with a BRK212 rotor.

Synthesis

ZnSe QDs were prepared utilizing the heat-up approach based on a modified procedure initially described by Jang et al.[207] In a typical synthesis, 30 mL of ODE, 2 mmol of $Zn(St)_2$ (1264.7 mg), and 1 mmol of selenium (78.9 mg) were loaded into a 50 mL three-neck round bottom flask, which was placed on a heating mantle and attached to Schlenk manifold system. For the duration of the whole procedure, the mixture was constantly stirred using a magnetic bar. In the first stage, the reaction solution was degassed by exposing it to the vacuum line. Simultaneously, the flask was gently heated to 120°C and maintained at that temperature until the completion of the degassing process, signaled by the disappearance of bubbling from the mixture. At this point, the reaction solution appeared as a clear, homogenous black color, as presented in Fig. 6.3a, indicating the dissolution of selenium powder. The synthesis atmosphere was replaced with nitrogen, followed by the temperature increase to 200°C. These conditions were preserved for 2 hours, allowing the formation of Se-ODE activated precursor, accompanied by a color change of the mixture to dark orange (Fig. 6.3b).[208] Then, the temperature was further elevated to 300°C, inducing the nucleation of ZnSe seeds (Fig. 6.3c). As-formed particles continued to grow over 2 hours. In the described procedure, zinc precursor delivers both zinc ions as well as passivating ligands covering the QDs surface. The breakdown of the as-created Se-ODE complex provides the source of Se ions for the synthesized stearate-capped ZnSe QDs.

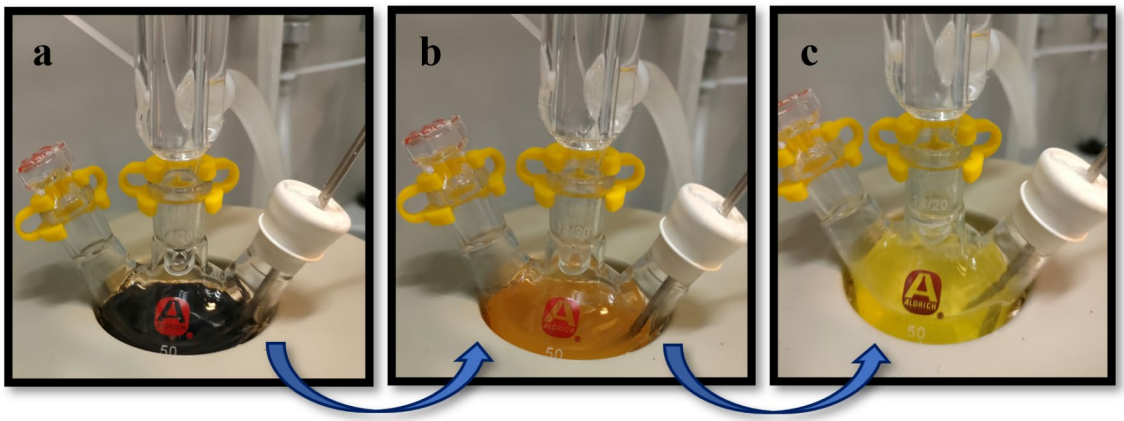

Figure 6.3 *Subsequent stages of the QDs synthesis: a) degassed reaction mixture, b) formation of Se-ODE activated precursor c) QDs formation.*

Unlike the typical synthesis schemes, the size of ZnSe QDs was controlled not by modifying the reaction temperature or time but by repeatedly replenishing fresh precursors with a glass syringe to induce further growth of initially obtained particles. The first growth was conducted by adding two Zn and Se precursor stock solutions prepared in advance. Zn solution was made by dissolving in a separate flask 0.5 mmol (109.8 mg) $Zn(OAc)_2 \cdot H_2O$ in a mixture of 0.25 mL ODE and 0.5 mL OA at 60°C. Se solution was prepared by

suspending 0.5 mmol (34.5 mg) of selenium in 1.2 mL of ODE by extensive shaking in a vortex and sonication in an ultrasound bath (5 min each). Both stock solutions were sequentially injected into the original mixture, still at 300°C, and left for 30 min to react. The second consecutive growth was carried out by injecting four times larger Zn and Se stock solutions (2 mmol $Zn(OAc)_2 \cdot H_2O$ dissolved in 1 mL ODE/2 mL OA at 60°C and 2 mmol Se suspended in 4.8 mL ODE made in identical conditions) and maintaining 300°C of the reaction mixture for 1 hour. The last growth was performed by repeating the previous step. Upon completion, the reaction was rapidly quenched by removing the heating mantle and placing the solution in an ice bath. In total, four different samples were prepared by stopping the synthesis after the initial growth of the original ZnSe QDs, and after the first, second, and third additional growth.

Purification

The as-synthesized ZnSe QDs were isolated from the unreacted species and other byproducts present in the reaction solution utilizing the modified purification procedure described by Pu et al.[209] The scheme involves multiple stages, including extraction, subsequent precipitation, and re-suspension of washed QDs. In the extraction process, the reaction solution is combined with a pair of organic solvents immiscible with each other. One of the solvents suspends the QDs within its volume while the second is a nonsolvent to the particles but instead dissolves other species in the synthesis solution. Such a mixture is extensively stirred, and then the phase with dispersed QDs is separated from the second solvent. In the applied approach, extraction was conducted in a two-step manner. First, the original reaction solution was mixed with ethanol in a centrifuge tube in a 1:2 ratio (typically 15 mL : 30 mL in a single tube) and a small amount of butylamine (0.75 mL). ODE present in the initial mixture acted as a solvent, and ethanol as nonsolvent to the ZnSe QDs. The addition of butylamine promoted the removal of fatty acids into ethanol. To further increase the efficiency of the process, the as-created mixture was maintained at 60°C with vigorous stirring followed by 10 min centrifugation at 9500 rpm to reduce the time needed for phase separation. The upper colorless ethanol phase was removed, and the bottom phase was collected and mixed with a hexane-ethanol solvent-nonsolvent pair, 7.5 mL and 30 mL, respectively, for the second extraction step, which involved a second centrifugation (performed with identical parameters) and subsequent removal of the ethanol phase as in previous step. Chloroform (0.75 mL), hexane (7.5 mL), and acetone (22.5 mL) were added to the remaining phase (containing dispersed ZnSe QDs) for the precipitation stage. Excess of nonsolvent (acetone) induced precipitation of the QDs and the presence of chloroform maintained the ODE in the acetone phase. This process was enhanced by third centrifugation (10 min, 9500 rpm), and the precipitated crystals were dried under nitrogen gas at room temperature. Obtained purified ZnSe QDs were resuspended with toluene. The series of prepared samples after the purification procedure are presented in Fig. 6.4.

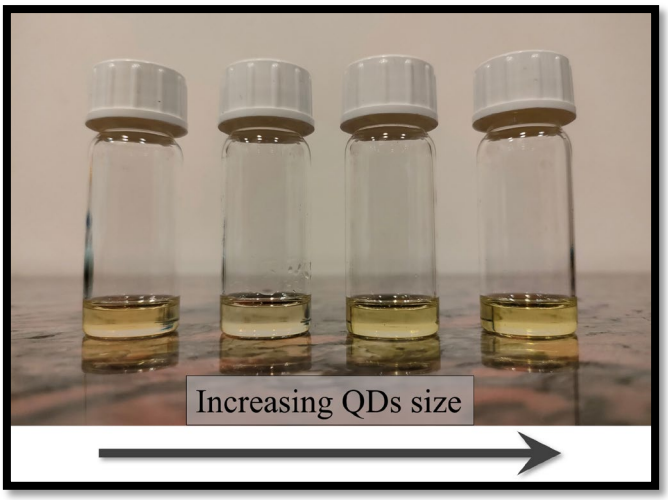

Figure 6.4 *Photograph of synthesized and purified ZnSe QDs samples.*

6.2 Experimental methods

Scanning transmission electron microscopy

Microimaging of fabricated particles was used to verify synthesis procedures and allowed assessment of QDs mean size and size distributions. Electron microscopy constitutes one of the most widely utilized methods to assess the size, shape, and other topographical information of various structures, including nanomaterials.

In electron microscopy approaches, an electron beam accelerated by a high voltage interacts with the examined specimen in high vacuum conditions, enabling its imaging at the nanometer level. Regarding their principle of operation, these techniques are divided into scanning electron microscopy (SEM) and transmission electron microscopy (TEM). In SEM, a beam of electrons, focused using a system of magnets on a small area, scans the sample, resulting in the emission of secondary and auger electrons from the analyzed material, or alternatively, the primary beam is backscattered. The signal (electrons) collected by the positively charged detector provides information about the specimen surface. TEM measures the signal from electrons transmitted through a thin pellet-shaped sample. This method allows for obtaining higher-magnification images than SEM, presenting data from the entire volume of the substance. However, its use is limited by the complicated sample preparation process and significantly higher operating costs.

Scanning transmission electron microscopy (STEM) combines the features of both described techniques and is often integrated with any method. The electron beam is focused on the small spot of the studied target, as in SEM, and passes through its bulk volume to the detector placed under the sample, as in TEM. STEM offers two main modes of imaging, namely, bright-field and dark-field. In bright-field mode, the small-area detector is located directly on the electron beam optical axis, so the electrons scattered on the studied objects are not measured, and the electrons that pass without scattering are accepted. The created microimage shows dark regions of high-scattering areas corresponding to examined objects on a white background of low-scattering. In dark-field mode, the signal is collected by the ring-shaped, off-axis detector that measures scattered electrons. Thus, the obtained

microimage shows scattering sites as bright spots on the dark background of support material that does not produce a significant number of scattering events.[210]

ZnSe QDs samples were analyzed utilizing FEI Helios G4 CX scanning electron microscope operating in a STEM mode with 18 kV accelerating voltage and 4.0 mm working distance. The measurements were conducted at the University of Groningen in the Netherlands, Zernike Institute for Advanced Materials, courtesy of Dr. Loredana Protesescu. The samples were deposited on the ultrathin grid, evaporating the solvent. QDs were imaged in the bright field mode. Obtained microphotographs were processed and analyzed in the ImageJ software. To estimate the size of examined QDs, 500 particles were measured for each sample at different spots of acquired images.

Steady-state optical spectroscopy

UV-VIS spectroscopy measurements were carried out using a table-top experimental setup presented in Fig. 6.5. The apparatus consists of a deuterium halogen light source (AvaLight-DHc), spectrometer (AvaSpec-ULS2048CL-EVO) and two optical fibers guiding the light from the lamp to the sample area and further towards the spectrometer. The source possesses an integrated electronic shutter and offers three switchable modes of operation: deuterium (3.1-5.0 eV), halogen (0.5-3.1 eV), and simultaneous use of both components. The spectrometer is designed in an array detector-based configuration with a diffraction grating covering a 1.1-6.2 eV photon energy range and a 2048-pixel complementary metal-oxide semiconductor (CMOS) linear image sensor (14×200 μm). Both elements, optical fibers and the dedicated software for data acquisition, were obtained from Avantes. The modular compact structure provides flexibility in the design of the experimental setup and allows various sample environments. Additionally, the system was equipped with a small laser module with emission energy and power of 3.06 eV (405 nm) and 1 W, respectively, bought independently for PL analysis of as-synthesized samples. Emission studies were performed separately utilizing the same AvaSpec spectrometer and collimator optics. During all measurements, the setup was enclosed with a shielding box that blocked all background light. ZnSe QDs suspensions were placed in a quartz cuvette with a 10 mm optical path length. The spectra were averaged over 100 scans, each collected for 420 ms (absorption) and 100 ms (emission).

While the presented custom-made PL spectroscopy setup offers a simple solution for quick emission properties assessment of freshly prepared QDs suspensions, the recorded QDs signal overlaps with the scattered light from the excitation source. For this reason, fluorescence measurements were later repeated with dedicated instrumentation for PL spectroscopy. This was realized using a Duetta spectrometer by Horiba Scientific located in the ELI Beamlines facility. Crucially, the spectrometer is equipped with excitation source energy (4.66 eV), far above expected QDs emission. The PL of QDs suspensions was collected for 100s (100 accumulations 1 s each).

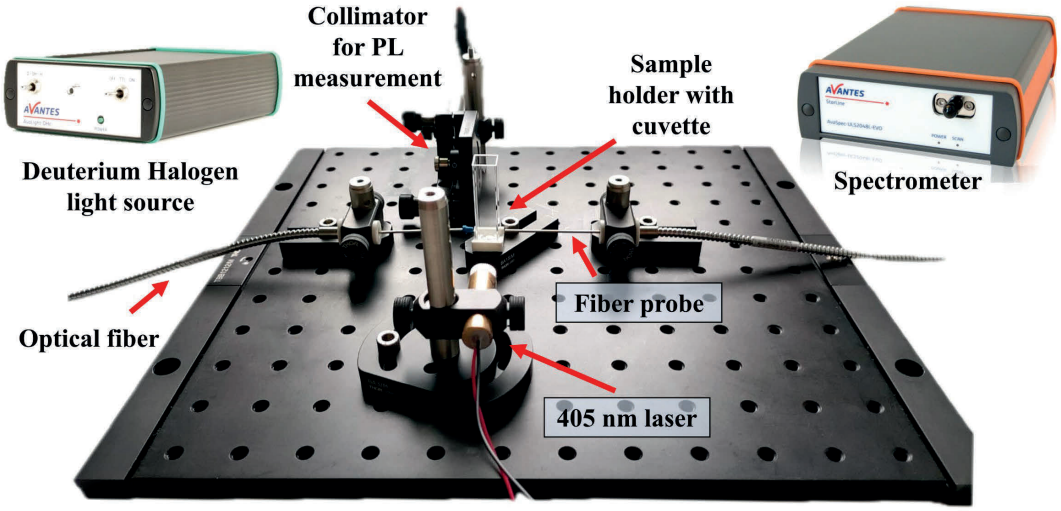

Figure 6.5 *Setup for steady-state UV-VIS and PL spectroscopy.*

6.3 Results & discussion

Fig. 6.6, left panel, presents representative STEM microphotographs of four synthesized ZnSe QDs samples. Obtained images provide direct evidence of the fabrication of nanometer-sized particles. Moreover, the additional steps introduced in the synthesis resulted in an observable increase in the particle size. The analyzed photos show homogenous particles relatively evenly distributed on the support grid, though particle clusters were observed in some parts of the examined areas, primarily Fig. 6.6a and Fig. 6.6e. As in the STEM measurements, the solvent was readily evaporated from the concentrated suspension, the self-organization of dried particles is a typical effect observed in the available reports.[68,139,211–214]

The right panel of Fig. 6.6 shows histograms that visualize the distribution of particle diameters determined for each sample. As indicated by STEM images, monodispersed QDs were obtained with a narrow ~11-12 % spread (standard deviation) of measured diameters matching the values from the scientific literature.[68,215,216] The calculated average particle sizes were 4.1 (±0.5), 5.2 (±0.6), 7.0 (±0.9), and 9.5 (±1.0) nm for initially synthesized ZnSe QDs and after first, second and third additionally induced QDs growth, respectively. Crucially, the applied synthetic strategy of subsequent particle growths by resupplying the QDs reaction mixture with fresh precursors did not affect the quality of obtained particles as the relative size distribution width is similar for all prepared specimens. The derived mean particle diameters will be used as a label, referring to specific QD samples in the following parts of the thesis.

Steady-state UV-Vis absorption (solid lines) and PL (dotted lines) spectra of four prepared QDs suspensions are depicted in Fig. 6.7. Both emission maxima and all absorption features shift towards lower energies with increasing diameter of examined QDs. The PL peaks are red-shifted with respect to the first absorption state (1S peak), which provides the estimate of material bandgap energy. The main broadening factor of observed spectral features arises from the spread of QD sizes within a single studied sample batch. Nevertheless, narrow, single-peak fluorescence confirms the monodispersity of obtained

QDs in agreement with STEM experiments. Notably, the low-energy part of the PL spectra of smaller QDs exhibits a weak signal originating from surface emission, typically observed in core QDs. The energy of PL maxima of QDs samples in an increasing average particle size order is correspondingly 2.99, 2.98, 2.87, and 2.81 eV. Evaluation of bandgap energy (1st state in absorption spectrum), that is, the energy $1S_{3/2(h)}$-$1S_{(e)}$ electron transition, is not straightforward as this feature in II-VI QDs overlaps energetically with second transition $2S_{3/2(h)}$-$1S_{(e)}$. To determine the positions of electronic transitions and the bandgap energy, the UV-Vis absorption spectra were fitted with a sum of Gaussians and a featureless background polynomial function:

$$F(E) = \left[\sum_{i=1}^{4} a_i \cdot \exp\left[-\frac{1}{2}\left(\frac{E - E_i}{\sigma_i}\right)\right]\right] + b_0 + b_1 E + b_2 E^2 \qquad (7)$$

where a_i, σ_i, and E_i, are the amplitude, linewidth, and central energy of the Gaussian function, respectively and b_0, b_1, b_2 describe the coefficients of the second-order polynomial. An example of a fitted spectrum with distinguished fitting components is presented in Fig. 6.8a. The determined 1S peak energies for all of the samples were correlated to QDs mean diameter, which is depicted in Fig. 6.8b as pink full circles. Based on the acquired data, an empirical equation was derived relating the size-dependent bandgap energy of ZnSe QDs to their diameter (D):

$$E_g(D) = 2.7\ eV + \frac{1.05\ nm}{D} + \frac{1.32\ nm^2}{D^2} \qquad (8)$$

The first component of the eq.(8) is the bandgap energy of the bulk ZnSe. The second part qualitatively describes electron-hole Coulombic interactions between charge carriers and the third term accounts for the quantum confinement effect. Fig. 6.8b also shows $E_g(D)$ dependencies proposed by other groups obtained either through analogical fitting procedures to experimental data[68,96] or ab initio calculations[217]. As presented, the results acquired in this work indicate a similar trend to literature reports. For small D values corresponding to the so-called strong confinement regime (QD diameter is much smaller than twice the exciton Bohr radius), eq (8) is in excellent agreement with other works. However, a noticeable discrepancy arises as the size of QDs increases, transitioning to the weak confinement region. This difference becomes pronounced around 6-7 nm, corresponding to one of the synthesized ZnSe QDs samples. The discrepancies between published $E_g(D)$ functions are commonly observed for all the QDs families.[77] One of the main reasons stems from different technical approaches utilized to derive particle physical dimensions and bandgap energy. For example, in the work by Toufanian et al.[68] (presented in Fig. 6.8b with cyan line), small-angle X-ray scattering (SAXS) instead of TEM/STEM was used to determine QDs diameters. While both techniques are frequently applied for evaluating nanomaterial size, it has been suggested that SAXS yields slightly higher size values for the same sample.[218,219] Simultaneously, the bandgap energy determination based on the UV-Vis spectra is also susceptible to experimental errors, especially for higher QD sizes. This is because bigger QDs are characterized by smaller energy spacings between

nearby electron transitions, making it challenging to resolve overlapped absorption features.[77] Furthermore, it has been confirmed through several studies that the chemical environment of probed QDs, especially surface ligands[220–222] and solvents[223], affects the bandgap properties of the material, even if the particles are similar in their dimensions.

The differences between the obtained relation and other experimental works are most significant for the largest examined QDs. However, it should be emphasized that this size regime was not considered in the cited studies, and the presented curves represent the extrapolation of the derived equations. Thus, these functions not necessarily should hold beyond the investigated cases. Noteworthy, the $E_g(D)$ relation empirically derived in this thesis most closely matches the theoretical work made by Li et al.[217]

6.4 Conclusions

ZnSe QDs were synthesized through a heat-up approach, combined with sequentially induced additional particle growths triggered by precursor injections. Conducted STEM microimaging and steady-state optical spectroscopy measurements confirmed the preparation of monodisperse colloidal particles and demonstrated the quality of the product. Comparison with literature indicated that fabricated samples may serve as the representative model for examining ZnSe QDs properties, which will be conducted in the following parts of this work. At the same time, the derived size equation may be useful for quick assessment of synthesized ZnSe QDs size, especially for large QDs, where the literature data is somewhat lacking. Overall, this part of the thesis was successfully realized, which is crucial for all the subsequent studies.

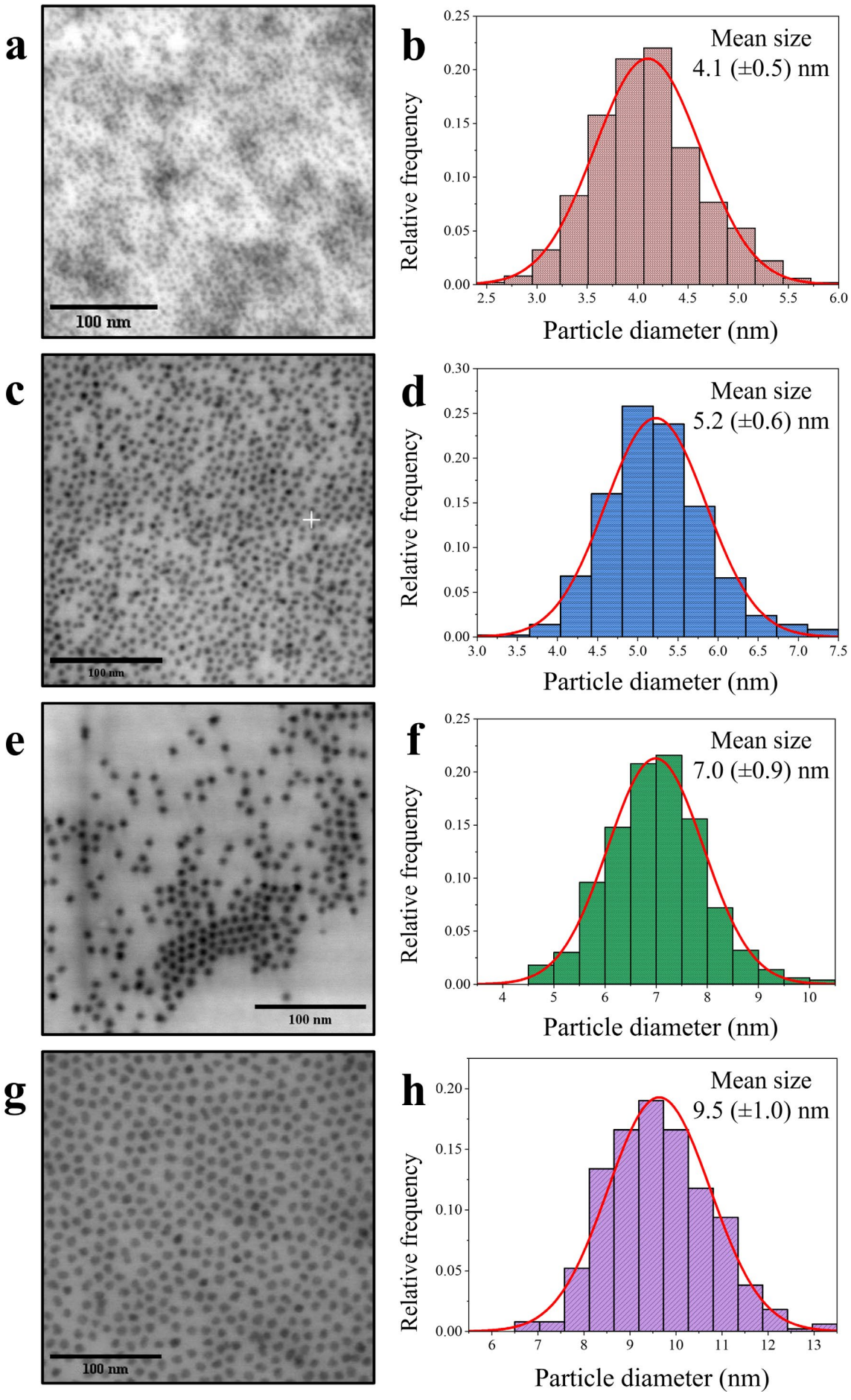
a
100 nm
b
Mean size
4.1 (±0.5) nm
Relative frequency
Particle diameter (nm)
c
100 nm
d
Mean size
5.2 (±0.6) nm
Relative frequency
Particle diameter (nm)
e
100 nm
f
Mean size
7.0 (±0.9) nm
Relative frequency
Particle diameter (nm)
g
100 nm
h
Mean size
9.5 (±1.0) nm
Relative frequency
Particle diameter (nm)

Figure 6.6 *Bright-field STEM images of prepared ZnSe QDs samples (left) and histograms showing diameter distributions of examined particles (right) for originally synthesized ZnSe QDs (a and b), ZnSe QDs after first additional growth (c and d), ZnSe QDs after second additional growth (e and f) and ZnSe QDs after third additional growth (g and h). Red lines plotted on histograms show normal distributions overlayed on the acquired data.*

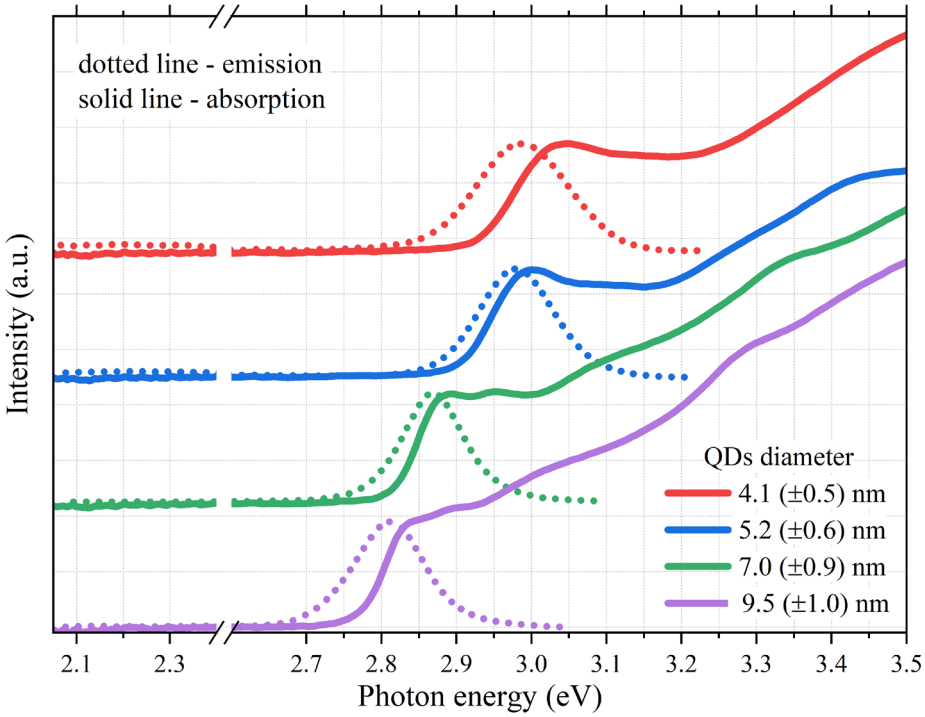

Figure 6.7. *Steady-state UV-Vis absorption (solid line) and PL (dotted line) spectra of synthesized QDs samples with mean diameters: 4.1 (±0.5) nm (red), 5.2 (±0.6) nm (blue), 7.0 (±0.9) nm (green) and 9.5 (±1.0) nm (purple).*

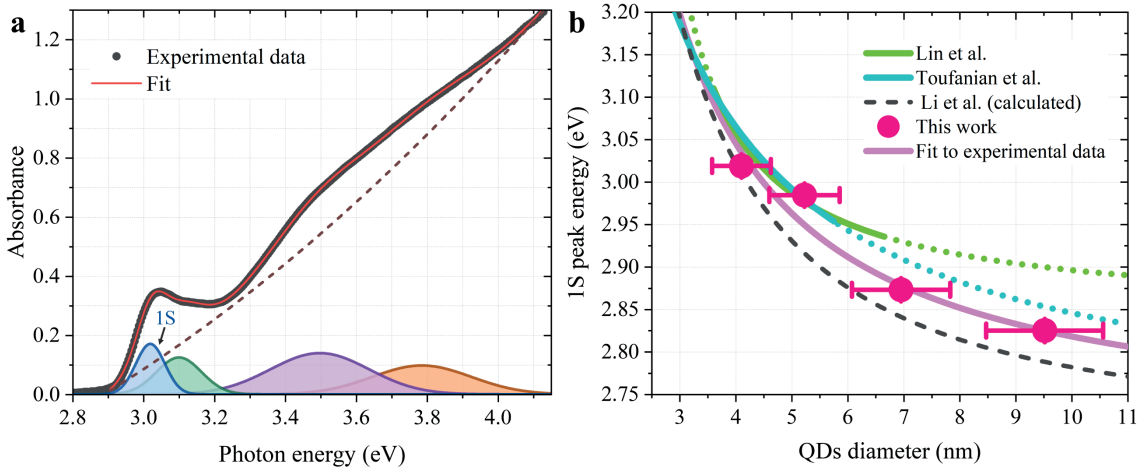

Figure 6.8 *a) Steady-state UV-Vis absorption spectrum of 4.1 (±0.5) nm QDs sample (black dots) with fitted function (red line) given by the eq. (7). The spectrum is decomposed into a series of Gaussians (full-colored features) corresponding to electron transition. The background polynomial is denoted as a dashed brown line. b) Correlation of QDs mean diameter and their band gap energy determined as the 1S peak energy (dark pink full circles) with the empirically derived fit equation (solid pink line). For comparison, $E_g(D)$ vs size relations published by other scientific groups are presented. Cyan and green lines correspond to experimentally evaluated sizing curves.*[68,96] *The solid part denotes the examined QD size range, and the dotted part extrapolates the determined fit equation. The dashed gray line corresponds to theoretical calculations.*[217]

7. Laboratory-based X-ray spectroscopy studies

This chapter is devoted to experiments conducted utilizing the laboratory-based X-ray spectrometer operating in the Department of Applied Spectroscopy of the Institute of Nuclear Physics PAN.

The laboratory-scale, in-house instrumentation plays an essential role in scientific projects related to the physics and chemistry of materials, including nano-sized QDs, because it grants unrestricted accessibility to a specific characterization technique for day-to-day on-site routine sample examination. While most scientific methods, like the UV-Vis spectroscopy applied earlier in this work, are easily implementable at the home-laboratory level, this has not been the case for X-ray spectroscopy approaches. Although the history of X-spectroscopy started with lab-based equipment and reports regarding the development of lab-based X-ray spectrometers appeared throughout the 20th century[224–227], they never caught the attention of the broader scientific community. The reasons for such a turn of events result from technological limitations and the simultaneous development of synchrotrons that turned the attention of researchers. As a result, until lately, XAS and XES measurements were conducted predominantly at synchrotron facilities. However, nowadays, they are more often implemented at the laboratory scale thanks to the development of efficient X-ray sources, X-ray optics, and X-ray detectors.[228–230]

The situation changed as the progress regarding the development of novel compact instrumentation allowed for the re-introduction of in-house X-ray apparatuses. This new generation of cost-effective XAS/XES setups referred to as modern laboratory X-ray spectrometers, appeared in the mid-2010s, enabling ground-state studies of concentrated specimens with signal quality comparable to synchrotrons achievable within hours of data acquisition. In recent years, different laboratory-based setups were showcased by scientists from Seattle[183], Berlin[231], Budapest[184], Helsinki[232], and Warsaw[201], among others.

The X-ray spectrometer utilized in this thesis was established in Kraków at IFJ PAN in late 2019[233] and is an example of custom-made modern XAS/XES laboratory-based setups. The chapter starts with its presentation and detailed description. The second subsection discusses technical aspects regarding developed spectrometer calibration schemes necessary for reliable XAS/XES examination. The next part is related to the preparation and testing of special sample cell for the optimal environment for the measurements of QD suspensions. The final section of this chapter will be devoted to the XAS/XES measurements of the synthesized ZnSe QDs samples to investigate and attribute the changes in their electronic structure.

7.1 Laboratory-based X-ray spectroscopy setup at IFJ PAN

The laboratory-based setup is presented in Fig. 7.1. It consists of an X-ray source and two von Hámos type X-ray spectrometers: one for collecting the X-rays transmitted through the investigated target for transmission mode XAS and the second, arranged in a vertical configuration, for detecting characteristic X-rays emitted from the excited sample (XES). Both spectrometers operate in parallel, allowing simultaneous acquisition of XAS and XES spectra in one measurement. As the X-ray source, a low-power air-cooled XOS X-beam

Superflux PF X-ray tube with a molybdenum anode is utilized, operating at the maximum voltage and current of 50 kV and 1 mA, respectively. The X-ray tube is equipped with polycapillary optics with a 20 mm focal length, focusing the incident X-ray beam to around 100 × 100 μm^2 spot on the sample. Each spectrometer uses a cylindrically bent silicon crystal with a 25 cm curvature radius that spatially disperses X-ray wavelengths in one direction and focuses them in the second, perpendicular axis. Several crystal cuts are available in the laboratory with different lattice spacings (2d): Si(100), Si(110), Si(111), Si(310), and Si(311) to cover different X-ray energy ranges from 5 to 12 keV. Upon interaction with the analyzer crystal, the radiation is focused in a strip onto one of the front-illuminated position- and energy-sensitive 2D CCD Andor Newton DO920P camera (detector) that consists of 1024 × 256 silicone sensors (pixels), each 26 µm in size. The detectors possess a 250 µm thick beryllium window and a vacuum-sealed thermoelectric cooling system, decreasing sensor temperature down to -70 °C to mitigate the effect of electronic noise (dark current). Based on previous studies[201], the spectrometer resolving power is estimated at around 1-2 × 10^{-4}.

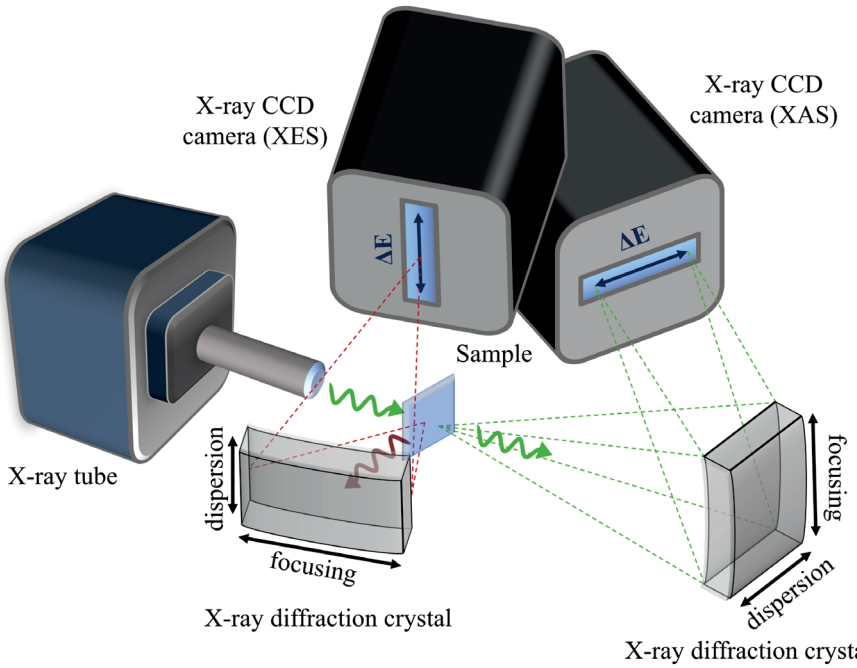

Figure 7.1 *Schematics of laboratory-based X-ray spectroscopy setup.*

It is important to highlight the compact, modular structure of the presented X-ray spectrometer. The entire setup fits on a 1.5 × 1.5 m^2 Thorlabs Breadboard table, enclosed in an X-ray hutch (10 m^2) protected with 5 mm thick lead walls. The whole area inside the hutch is maintained in ambient conditions. Each component is accessible from different sides, allowing easy manipulation of the spectrometer. Due to the dispersive nature of the utilized von Hámos geometry, the setup does not possess any moving elements during the acquisition of the XAS and XES spectra. The X-ray tube, crystals, and detectors are tightly fixed on support frames screwed to the experiment table, and the alignment of the setup for specific measurements is done manually. The absence of automatic motorized positioners for the spectrometer's elements simplifies its operation and provides additional free space to implement other equipment, such as advanced sample delivery systems. The only

motorized stage employed in the setup controls the sample position, allowing target displacement in the horizontal and vertical direction and along the incident X-ray beam. By scanning the sample, that is, performing short signal acquisition at different sample positions, homogenous areas can be identified. Paired with small beam spots enabled by the polycapillary optics, the scanning procedure mitigates the potential issue of sample uniformity, especially problematic in transmission mode XAS measurements.

In the presented work, the described laboratory-based X-ray spectroscopy setup is utilized to probe ZnSe QDs samples. For this purpose, its performance was optimized in the spectrometer configurations for Zn K-edge XAS and Zn Kα XES measurements.

7.2 Calibration and performance of XAS & XES spectrometers

XAS spectrometer

For XAS spectrometer calibration experiments, the setup was built utilizing Si(440) crystal, that is, Si(110) in the fourth order of diffraction, to allow propagation of photon energies around Zn K-shell binding energy (~9659 eV). The X-ray tube voltage and current were set to 30 kV and 0.9 mA. The detector sensors were cooled to -40 °C.

The first step of the XAS spectrometer calibration procedure involves defining the range of photon energies for further data analysis. As the X-ray tube delivers a broad polychromatic X-ray beam, the signal detected by the CCD camera consists of not only photon energies diffracted by the Si(110) analyzer in the 4th diffraction order but also contributions from other allowed diffraction orders, which is demonstrated in Fig. 7.2a presenting the low energy resolution spectrum of the X-ray tube upon interaction with diffraction crystal. The spectrum is expressed in the function of analog-to-digital units (ADUs), which describe the amount of electric charge realized in a single CCD chip due to the absorption of an X-ray. The energy sensitivity of the utilized detector allows distinguishing between photons guided by various diffraction orders (n=2, 4, 6, 8), which are marked with different colors in Fig. 7.2a. Additionally, the spectrum contains a tiny feature at about 150 ADUs, arising from characteristic X-rays emitted from iron atoms present in significant amounts near the setup, for example, in the table or detector casing. Therefore, the resolving power of the Andor camera is essential for selecting a proper ADU range and filtering the photons with energies around Zn K-shell ionization energy from unwanted background contributions.

Defining the ADUs range $[p_0 - \Delta p, p_0]$ for conversion to actual X-ray counts is not straightforward since the features related to specific diffraction order are asymmetric and contain additional tail extending towards lower pixel values. The low-ADU tail arises because the charge released in the detector's active region upon absorption of a single X-ray can be captured by two or more pixels, causing each one to return a smaller value. Narrowing the energy window (ADUs range) only to the peak related to relevant diffraction order reduces contributions of unwanted background radiation at the cost of omitting a significant number of the right photons from the low-energy tail, thus substantially decreasing the measurement count rate. Extending the pixel value range allows increasing counting statistics. However, the additional contributions from other diffraction orders might cause distortions in the features of the XAS spectrum, which might lead to

misinterpretation of acquired data. Thus, preliminary measurements of known sample are needed to establish an optimal ADU range.

For spectrometer calibration measurements, a Zn foil (10 um thickness) obtained from Goodfellow was installed as the sample. The I_0 and I_1 signals were collected for 50 min each. The data was integrated over the ADU range shown in 7.2a as the red box. Notably, further expanding the energy window to lower ADU values beyond the established range would increase the contribution of scattered radiation enlarging the point-to-point fluctuations in the spectra.

Fig. 7.2b presents the incident spectrum (I_0) and the spectrum of X-rays transmitted through the Zn foil (I_1). Both datasets were processed through the Lambert-Beer law (eq. 5) to acquire the XAS spectrum shown in Fig. 7.2c. As the raw data (Fig. 7.2b) is oversampled, the photon counts in the processed XAS signal were summed over six neighbor pixels, providing the energy step that matches the spectrometer resolution. The energy calibration was performed by fitting the experimental results to the reference Zn foil spectrum taken from the database.[234] The error bars indicate the photon counting statistics of the conducted measurement.

The characteristic features in the Zn K-edge spectra originate due to electron transitions from the 1s level to the unoccupied 4p state (structure on the rising edge) and the continuum (post-edge structure). Overall, the acquired Zn foil spectrum exhibits good agreement with the literature data with all spectral features reproduced.

The spectrometer calibration experiments were described in the article **Performance of a laboratory von Hámos type X-ray spectrometer in X-ray absorption spectroscopy study on 3d group metals** published in X-ray Spectrometry.[1]

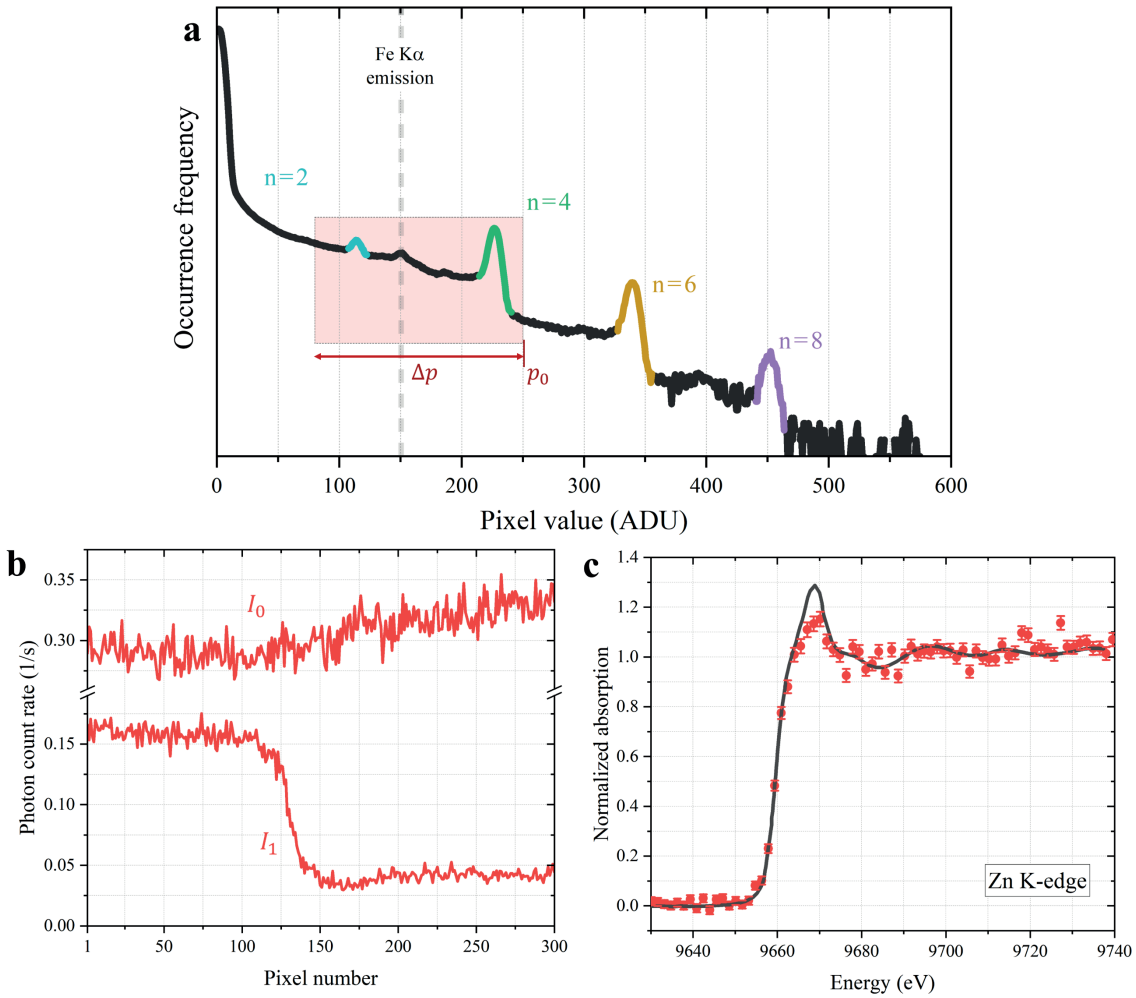

Figure 7.2 *a) Low-energy resolution spectrum of the X-ray tube output diffracted by Si(110) crystal. X-rays diffracted by a specific diffraction order (n = 2, 4, 6, 8) are marked with the same color. The red box denotes the pixel range (energy window) taken for data processing. The Grey dashed line indicates the photons emitted by the iron present in the nearby surroundings of the setup. The* Δp *and* p_0 *values are denoted with red color. b)* I_0 *and* I_1 *data integrated over pixel range shown in a). c) Zn K-edge XAS spectrum of Zn foil (red circles). The graph contains a reference synchrotron spectrum utilized for energy calibration of the spectrometer.*

XES spectrometer

Zn Kα XES measurements were carried out with identical parameters of the X-ray source and CCD camera as in previously described XAS experiments. The crystal used for the analysis was Si(400). When acquiring the XES spectra, besides $K\alpha_1$ and $K\alpha_2$ photons diffracted by Si(400), no other allowed diffraction orders contribute to the detected signal as the studied sample emits a series of discrete emission lines rather than a broad beam like an X-ray tube. Nevertheless, for a polychromatic primary source in XES experiments, dedicated procedures for the energy calibration of the spectrometer are necessary.

At synchrotrons (monochromatic X-ray sources), the measurements of elastically scattered photons provide reliable energy calibration of XES spectra.[235] In the case of laboratory-based non-resonant XES, similarly, as in XAS, the conversion of CCD pixels to photon energies has to be done based on the reference measurements of the well-known sample (typically metallic foil). However, the position of the recorded XES features on the

detector dispersive axis (energy scale) depends not only on the average chemical state of the studied element but also on the sample position along the primary X-ray beam. This effect is demonstrated in Fig. 7.3a, presenting the series of Zn $K\alpha_1$ and $K\alpha_2$ XES spectra of the Zn foil in the function of its distance from the X-ray tube. The two observed features on all plots originate from $2p_{3/2}$ ($K\alpha_1$) and $2p_{1/2}$ ($K\alpha_2$) to 1s transitions. The green circles represent the data acquired for the sample placed in the X-ray beam focal point 20 mm from the exit of the polycapillary optics. This spectrum was selected for x-axis calibration based on the reference table.[192] The dashed grey lines mark the maxima of the $K\alpha_1$ and $K\alpha_2$ lines. The peak energies were determined by fitting the obtained data in the PeakFit v4.12 software with two peak Voigt profiles (green curve), which is a convolution of Lorentzian function, describing the natural atomic shape, with Gaussian, corresponding to the spectrometer resolution:

$$y(E) = \sum_{i=1}^{2} \frac{a_{0i}(\Gamma_i/2)}{2\pi\sqrt{\pi}\sigma_i^2} \int_{-\infty}^{\infty} \frac{\exp(-t^2)}{\frac{(\Gamma_i/2)^2}{2\sigma_i^2} + (\frac{E - E_i}{\sqrt{2}\sigma_i} - t)^2} dt \qquad (9)$$

where a_{0i}, E_i, Γ_i, and σ_i denote the area, the maximum, and the Lorentzian and Gaussian width of the $K\alpha_1$ ($i = 1$) or $K\alpha_2$ ($i = 2$) line, respectively. The other spectra in Fig. 7.3a were measured by moving the sample either away (purple and yellow) or towards (blue and red) the X-ray source with the step of 1 mm. Fig. 7.3b shows the difference spectra derived by subtracting data of displaced targets from the spectrum of Zn foil located in the focal spot. The results clearly indicate a gradual shift of the Kα features when modifying the sample position with the average spectral change of about 0.17 eV per 1 mm of sample displacement, calculated by comparing the peak maxima of all measured spectra.

It should be noted that the effect of sample misposition is partially mitigated by the vertical configuration of the XES spectrometer (in relation to the primary X-ray beam). For comparison, Zymaková et al.[236] reported ~3.17 eV shift of Fe $K\alpha_1$ and $K\alpha_2$ features (~6.4 keV) per 1 mm sample displacement in a horizontally aligned von Hámos spectrometer composed of similar X-ray tube, diffraction crystals, and detector. While vertical alignment of the XES setup decreases the experiment sensitivity to target position alterations by an order of magnitude, the determined deviations are still comparable to energy shifts, expected to occur with the chemical changes of Zn atoms (~0.1-0.3 eV). Therefore, precise control of sample position between different measurements is required for valid XES spectra interpretation.

Discussed challenges in the absolute energy calibration of X-ray emission spectrometers are of general interest for any laboratory-type X-ray spectrometers. So far, different approaches have been discussed in the literature to mitigate this problem. In the present case, two microscope cameras were implemented into the experimental setup, providing reliable determination of the studied target position. This approach was adopted from earlier work by another group.[236] Fig. 7.4a presents the sample positioning system installed in the laboratory for X-ray spectroscopy measurements. Both microscopes are fixed closely to the investigated specimen. The first camera enables a front view of the sample, and the second allows precise control of the target distance from the X-ray source

by providing the side view of the sample, as shown in Fig. 7.4b. As determined experimentally by utilizing the microscope aligning procedure, the sample position could be restored with a precision of about 20 μm. Fig. 7.4c shows two spectra of Zn foil acquired with the implemented sample positioning system. After the first measurement (grey), the sample was removed from the motorized state and realigned again (blue) to the same position based on the microscope images. Additionally, Fig. 7.4c contains a spectrum of ZnO NPs (purchased from Sigma-Aldrich) deposited on the tin glass and measured with the same sample aligning procedure. Although the analysis of the difference signal, presented in Fig. 7.4d with the orange line, shows subtle discrepancies between the two spectra of Zn foil, the magnitude of changes is negligible compared to the observable shift associated with oxidation state change from 0 to +2.

Based on the Voigt fit of the Zn foil XES spectra, the experimental resolution of 1.54 (±0.06) eV was obtained. The determined Lorentzian widths were 2.74 (±0.10) and 2.88 (±0.12) eV for $K\alpha_1$ and $K\alpha_2$, respectively. These values slightly differ from the tabulated natural line widths of 2.32 and 2.39 eV [194] and most likely result from the employed single-peak fitting procedure to each measured emission line. Actually, X-ray irradiation with a broadband X-ray source will lead to the creation of so-called satellite structures as a result of shake-off and knock-out processes. However, addressing these features in the fitting procedure would require support from theoretical modeling and would be beyond the scope of the thesis. Overall, the conducted measurements demonstrate the reproductivity of the sample positioning system and the ability of the XES spectrometer to resolve small shifts related to the different average chemical environment of Zn atoms in the sample based on the difference spectra analysis.

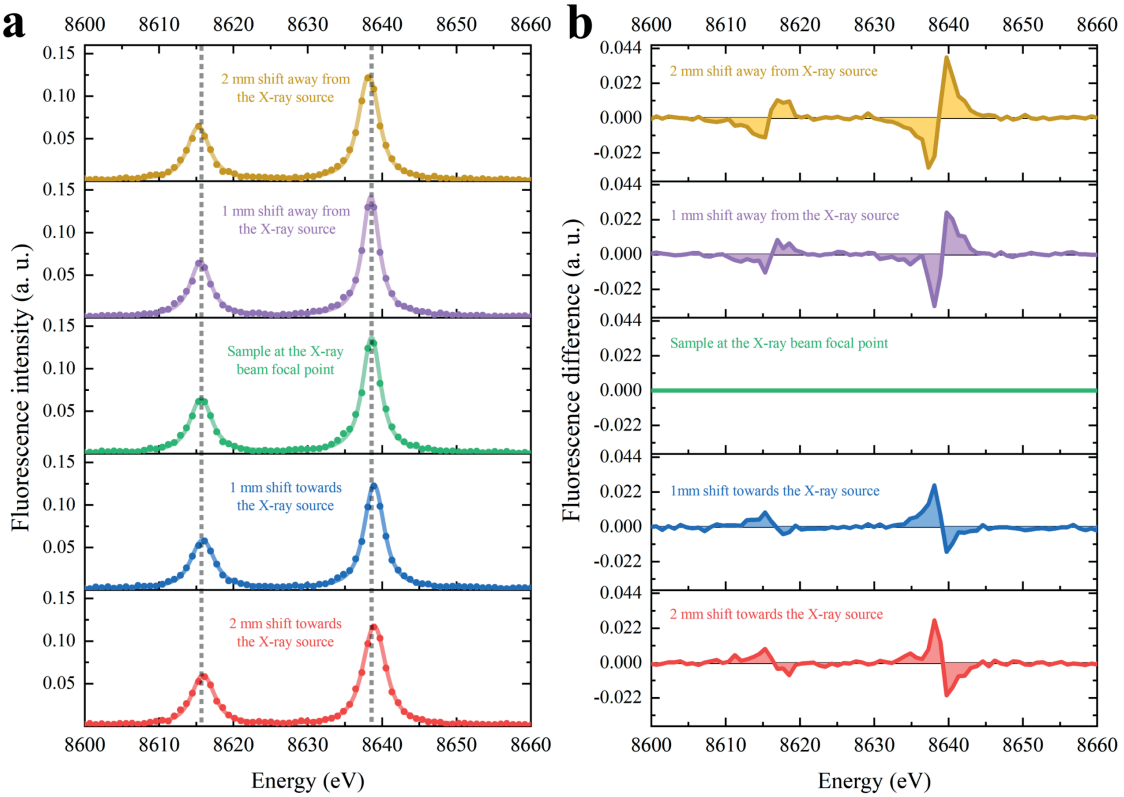

Figure 7.3 *a) Series of Zn Kα XES spectra obtained for Zn foil at different positions along the primary X-ray beam. The circles denote experimentally measured data, and the solid lines mark*

fitted Voigt functions. The spectrum in the middle (green) corresponds to the sample placed in the focal point of the X-ray tube and was used for energy calibration of the x-axis. The grey dashed line represents the position of $K\alpha_1$ and $K\alpha_2$ maxima obtained for the middle spectrum from the Voigt fits. b) difference spectra calculated by subtracting spectra presented in (a) from the data acquired for the sample in the beam focal spot.

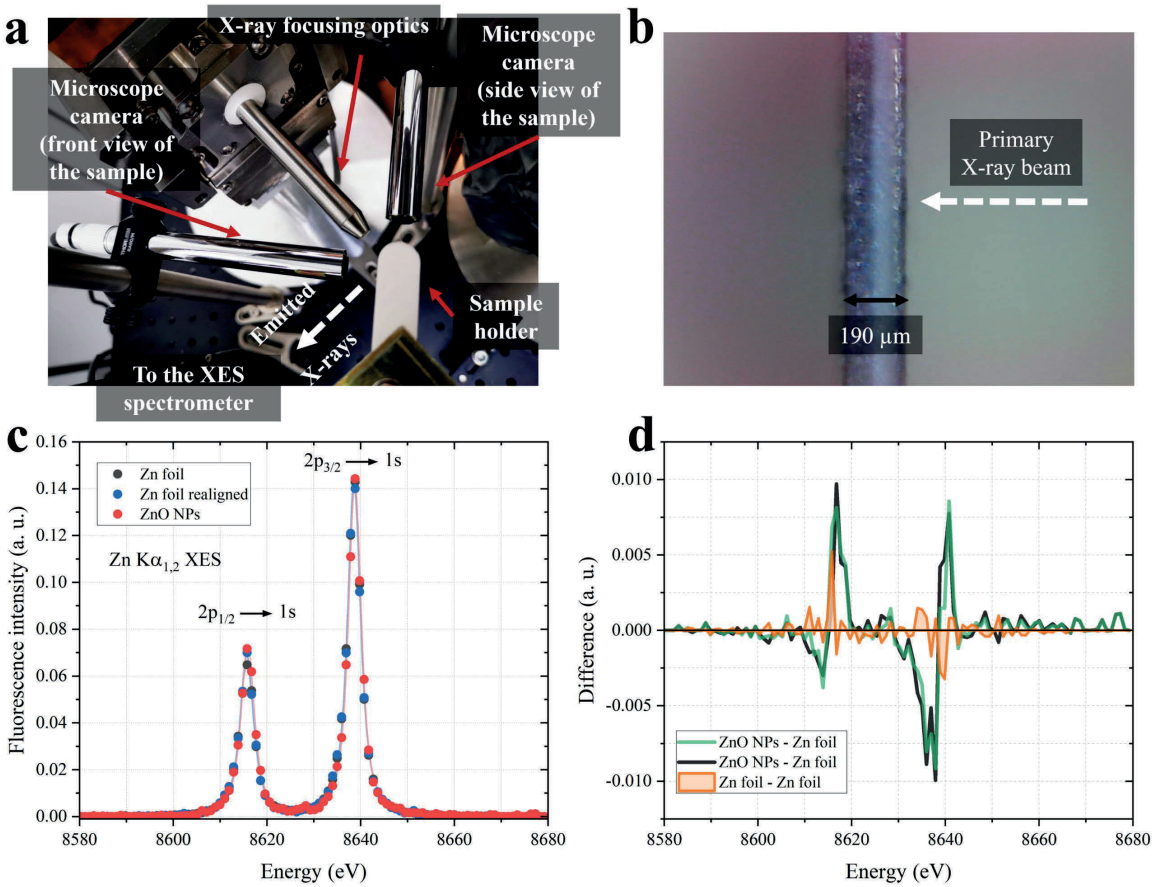

Figure 7.4 *a) Sample aligning system based on two microscope cameras providing front and side view on the examined sample. b) image of the side view camera of Zn foil placed in a polymer support. White dashed arrow marks the sample side illuminated by the X-ray beam. c) Zn Kα XES spectra of Zn foil measured twice (grey and blue) and ZnO NPs (red). Each sample was aligned using the microscope system. Solid lines represent fitted Voigt functions. d) Difference spectra of the data presented in (c). The orange line indicates the spectral changes between two measurements of Zn foil. Green and black curves show differences between ZnO and Zn (for two measured Zn foil spectra).*

7.3 Microliter-stirred sample cell for QDs suspension analysis

Challenges in analysis of nanomaterials in suspensions

As the prepared ZnSe QDs samples were synthesized and stored in a liquid environment, the preferred measurement condition is the native suspension form. This is especially relevant because drying the samples might cause their excessive oxidation, changing the chemical properties of the material. While solvents significantly attenuate the incident X-ray beam, the penetrative properties of hard X-rays enable the study of liquid solutions shaped in thin layers by jet nozzles or other sample containers.[237] However, analysis of QD suspensions involves issues specifically associated with nanomaterial suspensions.

Firstly, when synthesizing various nanostructures, as in the case of ZnSe QDs, one often encounters difficulties in preparing sufficient sample quantities necessary for optimal measurements. This is because the relatively high cost of ingredients paired with the fact that wet-chemical synthesis procedures are problematic to scale up to higher volumes as the temperature and precursor concentration gradients, introduced, for example, when injecting additional precursor portions, would lead to inhomogeneous particle growth within the reaction solution.[238]

The second limiting factor arises from nanomaterials' tendency to agglomerate[239,240], forming larger loosely bounded structures. This process results mainly from attractive weak van der Waals interactions between particles and their excess surface energy, favoring minimalization of their surface area.[241–243] Besides altering nanomaterial properties[244–246], agglomeration eventually triggers the subsequent sedimentation process when the size of the agglomerated clusters becomes so big that the gravitational force overcomes other interactions in the solution, causing the particles to settle down on the bottom of the sample container.[247] Sedimentation occurs on timescales from several weeks to even a few minutes[248–256] depending on multiple aspects related to particles (like size, shape concentration, and surface chemistry), solvent properties (density, viscosity, and pH), or the presence of additional species such as surfactants.

Agglomeration and secondary sedimentation severely hinder the measurements of all nanomaterial suspensions, including investigated QDs samples. Commonly applied procedures to mitigate these instability issues involve sonication, shaking, and intensive mixing of the liquid sample before its analysis. While such approaches generally succeed in temporarily dispersing the nanoobjects in the solvent, afterward, the sample will still be prone to re-agglomeration as the interaction balance of the system has not changed.[257] For experiments requiring a long time of data acquisition, like X-ray tube-based XAS/XES measurements, nanomaterial suspensions should be continuously refreshed to avoid changes related to their self-clustering effects.

To overcome the abovementioned issues, a dedicated sample cell was designed and constructed, allowing examination of microliter sample volumes and, at the same time, maintaining the physical stability of the studied suspension.

Developed sample cell

Fig. 7.5 presents a schematical drawing of the constructed sample cell (a) along with its photograph from the X-ray laboratory as installed for the XAS/XES measurements (b). The system for nanomaterial suspension analysis consists of three major elements: a sample vessel for microliter volumes, a sample mixing device, and a 3D-printed holder made from polylactide (PLA) that stabilizes both elements and allows the mounting of the entire cell to the motorized stage. A polyimide tube (Kapton, obtained from Goodfellow) was utilized as a liquid sample container. The high transparency for X-ray radiation, wide temperature tolerance range, and good chemical resistance to many solvents make this polymer an ideal choice for X-ray spectroscopy experiments. The tube has 30 μm-thick walls and a 2.94 mm inner diameter. Its dimensions were selected to compromise sufficient path length for the incident photons to interact with target atoms while minimizing the X-ray attenuation by the solvent and reducing the sample amounts needed for the analysis. The height of the tube

can be easily adjusted to hold volumes down to 50 µL. The bottom of the Kapton tube is plugged with a 3D-printed PLA stopper sealed additionally with parafilm. To provide constant sample mixing during measurements, the sample cell was equipped with a miniature electric engine MT51 manufactured by OEM with a thin shaft coated with polyvinyl chloride (PVC) cover. When connecting the engine to the external voltage supply, the shaft immersed in the sample suspension rotates rapidly dispersing the particles, preventing the agglomeration and sedimentation processes. The mixing rate of the stirrer is controlled by regulating the applied voltage up to 3V.

The main advantages of the developed microliter-stirred sample cell are its compact size, simple operation, and relatively low price of its components. With the total construction being around 2 cm in height, it leaves plentiful space and accessibility in the immediate sample environment, allowing the implementation of X-ray spectroscopy techniques to study the nanomaterial suspension. The system can be shipped to other facilities (in a tiny package or even in the traveler's pocket) and quickly assembled on-site. Additionally, the cell is prone to various modifications, as every component is easily interchangeable (for example, a Kapton tube can be replaced with a quartz one), extending the range of its possible applications.

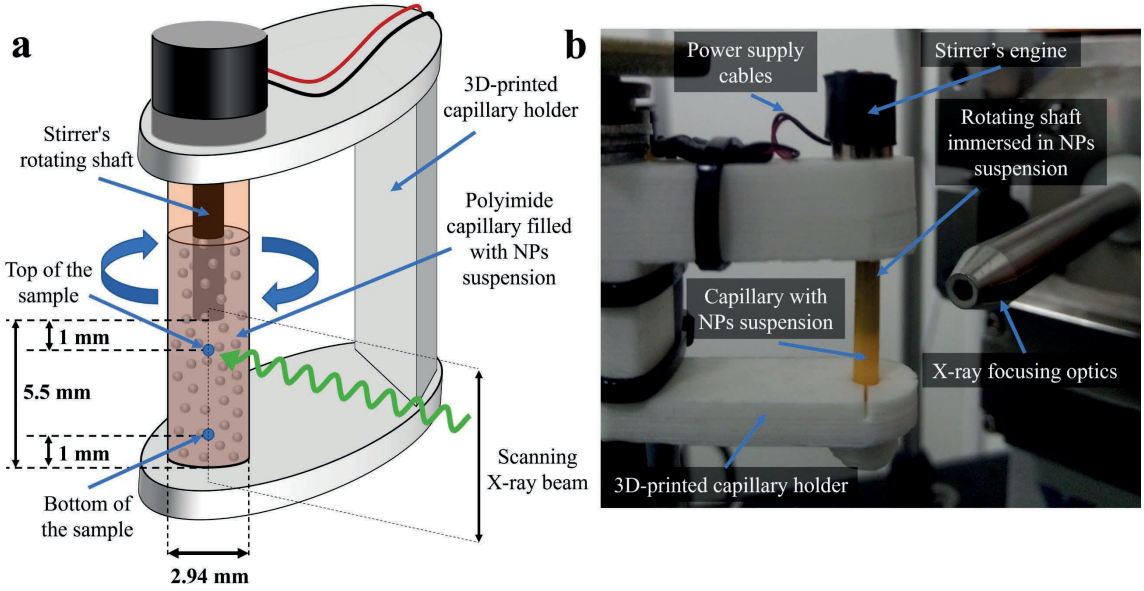

Figure 7.5 *Microliter-stirred sample setup: a) schematics with the description of its main components and the area probed by the incident X-ray beam b) photograph of the sample cell taken in the laboratory.*

Description of performed cell testing experiments

Before ZnSe QDs measurements, the microliter-stirred cell was tested with XAS/XES experiments utilizing ZnO NPs suspended in distilled water with a 40 nm average particle diameter purchased from Sigma-Aldrich. The sample concentration was set to 200 mM of Zn atoms, which provides the best compromise for simultaneous XAS and XES experiments. The Kapton tube volume was adjusted to 150 µL, providing sufficient area (5.5 mm in the vertical axis) to investigate possible agglomeration and sedimentation of the ZnO NPs by acquiring X-ray spectroscopy signals at different tube heights. The Zn K-edge XAS and Zn Kα XES measurements were conducted with 30 kV and 0.9 mA of X-ray tube

voltage and current and 0.6 V of stirrer voltage. The X-ray beam was focused at the center of the tube in the horizontal plane. In the vertical axis, two spots denoted in Fig. 7.5a have been selected for data acquisition: the first one, 1 mm below the stirrer's shaft, and the second, 1 mm above the PLA holder. These two points are labeled as the top and bottom of the sample, respectively. At each position (top and bottom), the XAS and XES were conducted twice, with the working stirrer and with the stirrer switched off, adding to the four sets of collected data. For each dataset, a series of twenty XAS and twenty XES spectra were obtained simultaneously, each collected for 4.4 min, allowing time-dependent analysis of spectral changes that could be assigned to agglomeration and sedimentation processes.

Sample cell performance

Fig. 7.6 presents Zn Kα XES (a) and Zn K-edge XAS (b) spectra of the in-situ stirred ZnO NPs suspension. The spectra constitute the sum of the top and bottom datasets, adding up to 3h of total signal acquisition time. The emission spectrum was fitted with the Voigt profile analogously as calibration experiments in section 7.3. The derived Gaussian width of the sample of 1.6 (±0.13) eV is a few percent higher than the determined value for thin Zn foil. This discrepancy results from the extended sample (X-ray emission source) size in the direction of the primary X-ray beam. As such, the irradiated sample area at the entrance (tube walls) and at the central point differs by about 10%, causing a broadening of the observed emission lines. The increase of the Gaussian width does not scale linearly with the sample thickness, as other contributions, for example, detector parameters and diffraction crystal geometrical effects, also influence the overall experimental energy resolution. The XAS spectrum (brown points) shows good agreement with reference synchrotron data (yellow line) of ZnO NPs recorded at similar sample concentrations. Noteworthily, the acquired data exhibit a similar decrease in white line intensity compared to the literature result, just as in the case of Zn foil (Fig. 7.2d). Still, both XES and XAS measurements present high-quality of detected signals obtained with relatively thick sample cell.

To track the changes associated with agglomeration and sedimentation effects manifested in local concentration changes, two parameters, determined from XES and XAS measurements, were defined that linearly depend on the amount of Zn atoms in the X-ray beam. The first parameter was simply the count rate within the measured Zn $K\alpha_1$ and $K\alpha_2$ emission lines, as this signal is directly proportional to the sample concentration within the examined range. The integration area of summed photons, shown in Fig. 7.7a, was about 50 eV (~150 pixels on the CCD camera). The second parameter was established based on the transmittance spectra of ZnO NPs depicted in Fig. 7.7b. Specifically, the natural logarithm of the ratio of pre-edge and post-edge signal was selected as the quantity of interest, averaged over ranges presented in Fig. 7.7b as continuous blue and red lines. To link evaluated parameters to ZnO NPs concentration, a series of reference XES and XAS measurements were conducted using sample concentrations from 50 to 400 mM. The experimentally derived calibration curves (insets to Fig. 7.7a and 7.7b were utilized to scale obtained XES and XAS signals into ZnO NPs concentrations.

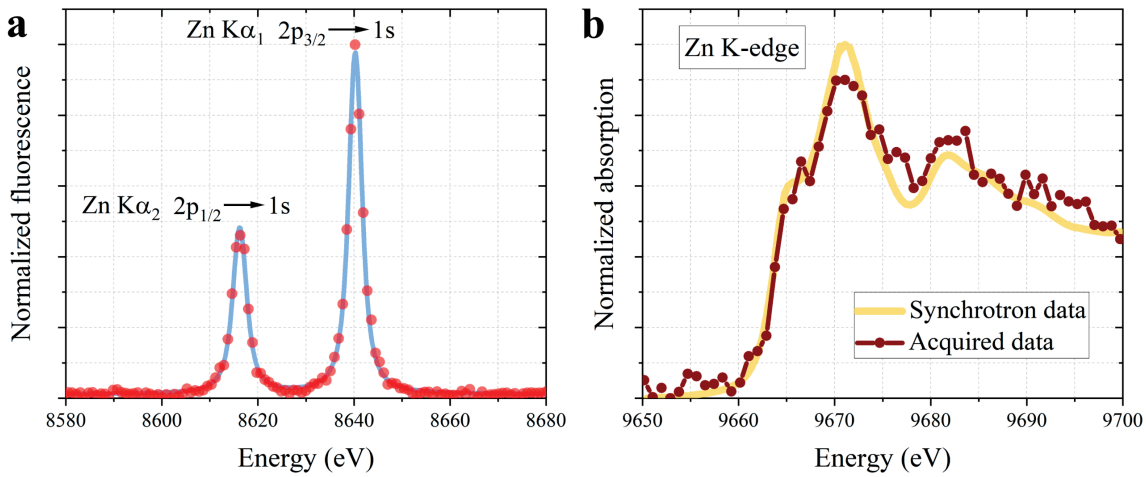

Figure 7.6 *Zn Kα XES (a) and Zn K-edge XAS (b) spectra of ZnO NPs spectra obtained with a properly working microliter string cell. The experimentally measured XAS data (red circles) is fitted with a two-peak Voigt profile (solid blue line). The lab-based XAS spectrum acquired with the presented sample system (brown circles) is compared to the reference synchrotron data taken from* [258] *(continuous yellow line).*

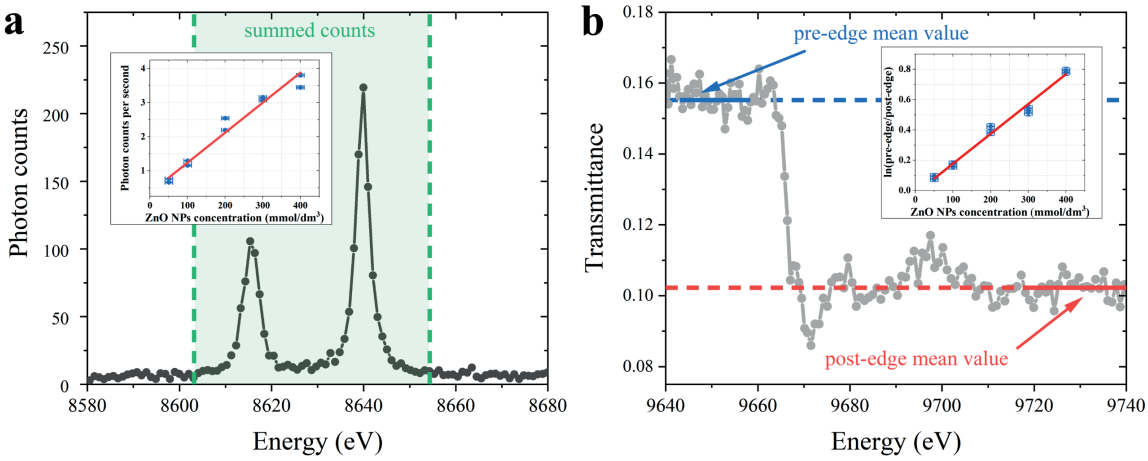

Figure 7.7 *XES (a) and transmittance spectra of the 200 mM ZnO NPs suspension. The green area between dashed lines on the XES spectrum presents the photon counting range for Zn concentration analysis. Analogously, the continuous blue and red lines on the transmittance spectrum show pre-edge and post-edge regions averaged to quantify concentration changes with XAS measurements. Dashed lines are the extensions of the derived values. Insets to both figures depict determined calibration curves for XES and XAS that correlate evaluated parameters to sample concentration.*

The temporal ZnO NPs concentration changes of all four collected datasets are depicted in Fig. 7.8a and 7.8b for the XES and XAS measurements, respectively. The signal obtained with the properly working cell stirring is indicated with green and blue full circles for the top and bottom sample positions. The temporal resolution of experiments (4.4 min) was chosen to achieve sufficient statistics of detected X-rays. The error bars arise mainly from statistical uncertainty and uncertainties related to calibration procedures. Results acquired at both positions indicated a stable signal over the entire experiment, confirming the reliable performance of the sample cell.

On the other hand, the physical stability of ZnO NPs suspension was not preserved in the instances when the mechanical sample mixing was not applied. The signal at the bottom

of the sample (open blue curricles) increased significantly with time. An analogous decrease in NPs concentration was observed when the signal was recorded at the top of the sample tube (open green circles). Both datasets strongly point to agglomeration and sedimentation processes, further confirmed by visual inspection of the Kapton tube. Performed X-ray spectroscopy experiments provided detailed insight into the dynamics of these phenomena. The sedimentation of ZnO NPs exhibited a sigmoid pattern, split into three stages, marked in Fig. 7.8. Initially, up to around 22 mins, the sample concentration at both tube positions showed only subtle changes. Then, as the experiment proceeded, the rapid change of both XAS and XES observables occurred with the maximum concentration drop/rise rate of about 2.5% per minute at 40 min of the experiment. Because sedimentation occurs only when particles reach a size where gravity overcomes other forces, and its velocity tends to increase with larger clusters, the initial phase is likely attributed to the agglomeration process. This phenomenon initiates a sedimentation stage and the appearance of sediment as the growing clusters attain their critical size.

Obtained particle sedimentation behavior correlates with other literature reports that studied the instability phenomena of nanoparticle suspensions. For example, Azman et al.[259] evaluated the sedimentation time for water suspension of Cu NPs to 45 min. Additionally, the particle settlement showed similar dynamics as in the case presented here. Similar timescales and mechanisms of sedimentation were presented by Ming et al.[260] while investigating the kinetics of iron oxide magnetic nanoparticle clustering effects.

The comparison of results acquired with and without sample stirring demonstrates the importance of maintaining suspension stability during prolonged measurements. As such, all of the XAS/XES measurements of the ZnSe QDs samples, outlined in the following subsection, were conducted utilizing the microliter stirred sample cell.

The presented sample setup with its performance was described in the article **Microliter-stirred sample setup for X-ray spectroscopy analysis of nanomaterials in suspension** published in Spectrochimica Acta Part B: Atomic Spectroscopy.[2]

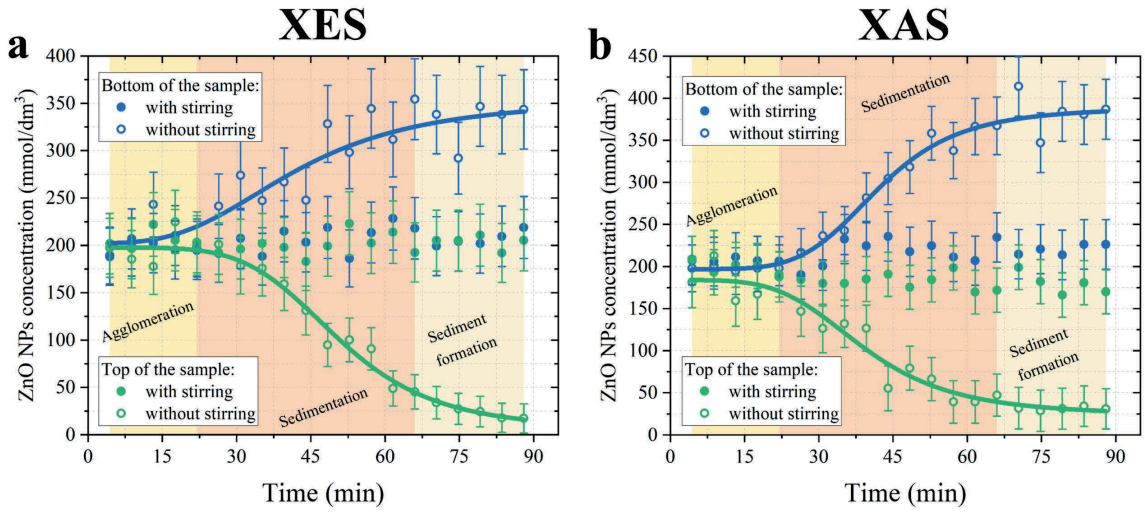

Figure 7.8 *Time-dependent concentration changes of Zn atoms (ZnO NPs) in the probed areas were acquired based on the (a) XES and (b) XAS analysis. The full-colored circles correspond to data obtained with the applied mechanical mixing probed at the top (green) and bottom (blue) of the sample. Open circles depict measurements conducted for unstirred suspensions. Sigmoidal*

functions fitted to the datasets determined without a working stirrer are represented with solid green and blue lines, respectively.

7.4 Laboratory-based XAS & XES studies of ZnSe QDs

With the developed experimental schemes for laboratory XAS and XES analysis of nanomaterial suspensions, it is possible to address the main goal of the present chapter, which is to examine the electronic structure of ZnSe QDs samples and evaluate the impact of structural and confinement effects. Furthermore, performed measurements provide a direct assessment of in-house X-ray spectroscopy capabilities in the context of addressing cases related to material science.

Samples

Laboratory X-ray spectroscopy experiments were conducted on four synthesized ZnSe QDs suspensions with varying particle size distributions, as described in Chapter 6. For the measurements, 80 μL of QDs toluene suspension at a Zn concentration of about 200 mM was injected into the microliter-stirred cell. Simultaneous Zn K-edge XAS and Zn Kα XES measurements of the samples were carried out for 6 hours with X-ray tube parameters of 50 kV and 0.9 mA. The reference samples involved water suspension of ZnO NPs (200 mM) as well as four solids: Zn foil, bulk-like ZnSe powder (99.99%, 10 μm particle size, obtained from Sigma-Aldrich), $Zn(St)_2$ (Zinc Stearate) and $Zn(OAc)_2{\cdot}H_2O$ (Zinc acetate dihydrate). The powder samples were mixed with cellulose to adjust the concentration of Zn atoms to 3% wt. and shaped into a pellet form using a hydraulic press.

Results & discussion

Fig. 7.9a presents the Zn K-edge X-ray absorption spectra of all samples. The spectra obtained for QD suspensions in the increasing particle size order are marked by red, blue, green, and purple lines, respectively. The data corresponding to bulk ZnSe is denoted with a yellow curve, and the rest of the Zn^{+2} references are depicted with shades of brown. The dark line indicates results acquired for metallic Zn. As discussed in earlier sections, the XANES region in Zn K-edge absorption spectra of all species is dominated by the 1s→4p electron transition, observed as the shoulder in the rising edge for Zn foil (~9663 eV) and ZnO NPs (~9666 eV). For other samples, this transition overlaps with the feature of the highest intensity at ~9666 eV. The pre-edge peak, characteristic of the K-edge spectra of 3d transition metals, is absent in the present case, as Zn possesses a fully occupied 3d orbital. The higher energy fine structure features are related to the scattering processes of photoelectrons at neighbor atoms, providing local structural information. The absorption edge energy (E_0), commonly taken as a direct measure of the oxidation state of a studied element, was determined based on the maximum of the spectra first derivative, presented in Fig. 7.9b. The maxima positions obtained for the reference samples with known chemical states of Zn atoms were indicated with dashed grey for metallic Zn, yellow for ZnSe and ZnO NPs, and pink line for $Zn(St)_2$ and $Zn(OAc)_2{\cdot}H_2O$. The derived E_0 values of four reference Zn^{+2} compounds, presented in Fig. 7.10a, differ despite the same oxidation state. Such edge energy shifts have been previously reported in other Zn K-edge XAS studies and are typically attributed to changes in local ligand site occupancy and

coordination of central Zn atom.[261,262] These observations are consistent with the obtained results for the examined reference Zn^{+2} species, whose structures are shown in Fig. 7.10b. For example, Zn atoms in $Zn(OAc)_2 \cdot H_2O$ possess octahedral geometries[263], coordinated with six oxygen atoms, and its E_0 is expected to shift towards higher energies relative to ZnO and ZnSe with tetrahedral Zn coordination.[264,265] Additionally, the prominent changes in the shape of the ZnSe and ZnO spectra can be explained by the variations in the Zn-anion bond distances (2.45 Å for Zn-Se and 1.97 Å for Zn-O) and the electronegativity differences of Se (2.55) and O (3.44) atoms, that is, different intrinsic tendencies of these elements to attract electrons shared in the chemical bonds. The analysis of the reference samples demonstrates that Zn K-edge XAS is sensitive to not only the Zn oxidation state but also carries information regarding the nature of Zn coordination and bonding ligands. This quality is crucial in the context of ZnSe QDs electronic structure investigation, as it allows the identification of possible defect states or surface atoms characterized by coordination alterations in relation to bulk lattice Zn atoms.

The spectra collected for ZnSe QDs (Fig. 7.9a) resemble the data acquired for the ZnSe powder with two pronounced features, the lower-energy one, probing the unoccupied 4p state, and the higher-energy scattering maxima. Similarly, the determined first derivative maxima overlap with the bulk-like ZnSe, yielding the same E_0 values for all ZnSe QDs suspensions. The direct comparison between the QDs absorption spectrum and reference bulk material is presented in Fig. 7.11a. For clarity, only a single spectrum from the series of QDs samples was depicted (green curve) as the other spectra exhibit similar spectral shapes within the resolution limits of the experimental setup. The difference spectra, determined by subtracting bulk ZnSe from the QDs spectrum, for all four suspensions are plotted in Fig. 7.11b. The colors of the QDs spectra curves are consistent with the spectra in Fig. 7.9. The point-to-point fluctuations in the measured XAS spectra cause a significant noise level that dominates the difference signal, preventing detailed quantitative data analysis. However, some changes stand out from the background and are possible to evaluate. In particular, the intensity increase of two main features (~9665-9675 eV) in spectra of QDs as compared to bulk powder are visible for all four samples. The rise of 1s→4p transition strength in XAS spectra was observed in earlier studies related to ZnO NPs and associated with the presence of the Zn vacancies within the crystal lattice of the nanostructures.[266] A high concentration of cation defects could also explain the changes in the second feature, which is broader for QDs. Missing Zn sites would likely prompt position readjustment of nearby Se atoms or even further lattice distortions in subsequent coordination shells, modifying photoelectron scattering paths and, consequently, post-edge XAS signal. On the other hand, the high amount of unoccupied Se sites in the QDs lattice would be manifested as the appearance of the pre-edge features in the absorption spectrum, as anion vacancies would alter the Zn oxidation state, unlocking its fully occupied 3d orbital.[267,268] Hence, the absence of a pre-edge signal suggests the low concentration of Se vacancies in the studied materials. Nevertheless, confirmation and possible refinement of the initial data interpretation, supported by theoretical calculations, require a better signal quality by applying a higher-intensity X-ray source, such as a synchrotron facility, for the XAS examination of ZnSe QDs.

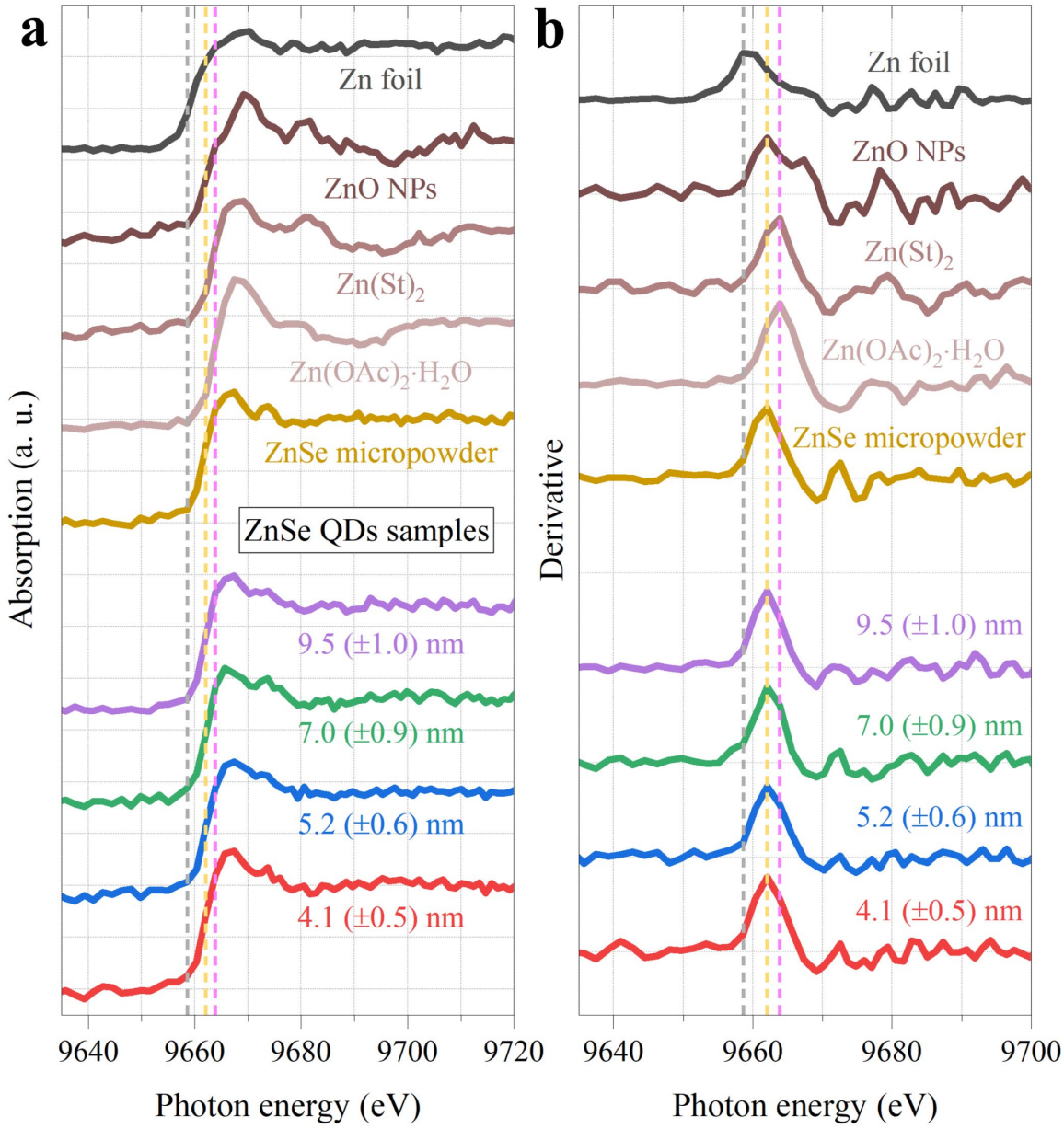

Figure 7.9 *a) Laboratory Zn K-edge XAS spectra of studied ZnSe QDs (red, blue, green and purple line for the samples with increasing mean diameters) and reference Zn compounds. b) The first derivative of X-ray absorption spectra presented in (a). Dashed lines show derivative maxima (E_0) determined for metallic Zn (grey), bulk ZnSe and ZnO NPs (yellow) and $Zn(St)_2$ and $Zn(OAc)_2 \cdot H_2O$ (pink).*

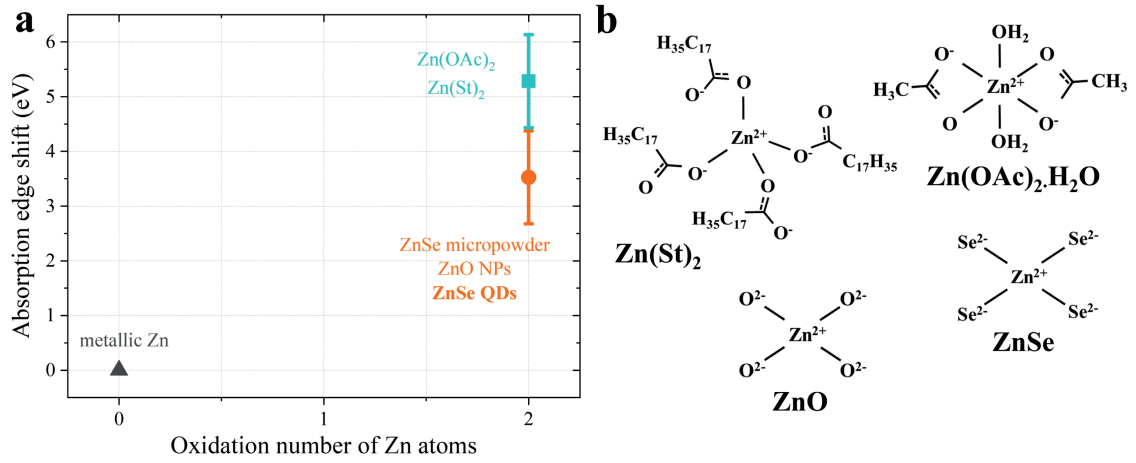

Figure 7.10 *a) The oxidation state of Zn atoms in studied samples correlated to the absorption shift compared to the metallic Zn. b) Schematical drawing of reference compound structures.*

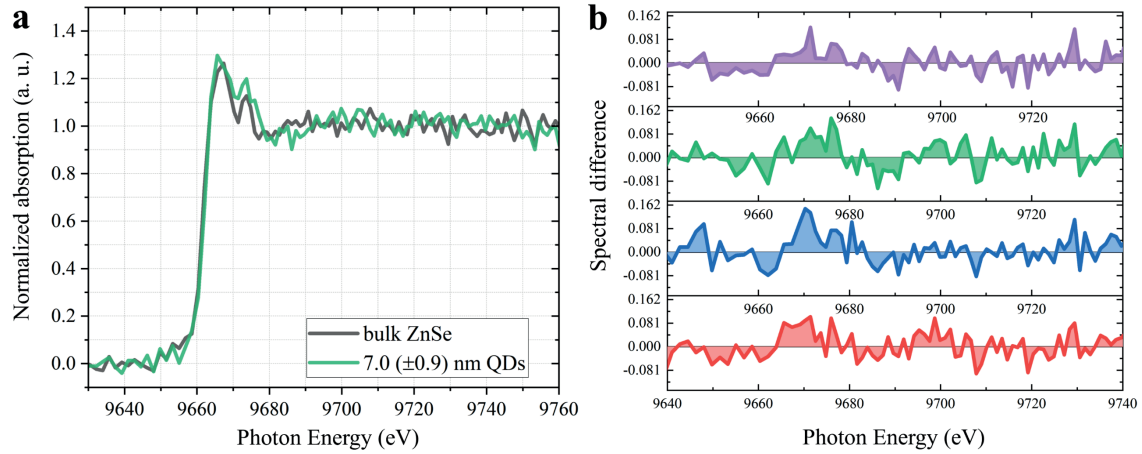

Figure 7.11 *a) Comparison between bulk-like ZnSe (grey line) and ZnSe QDs (green line) X-ray absorption spectra. b) Difference spectra acquired by subtracting bulk ZnSe absorption spectrum from the QDs data. The difference signals corresponding to QDs in the increasing order of their particle size are marked with red, blue, green, and purple lines, respectively.*

While the laboratory Zn K-edge XAS suffers from limited photon counting rates and the contribution of background photons from different allowed diffraction orders, both issues are avoided in the laboratory Zn Kα XES. In general, XES experiments more efficiently utilize the X-ray tube's Bremsstrahlung radiation since all photons with energies above the ionization energy of 1s Zn electron can excite the target, leading to secondary X-ray fluorescence. Although the improved signal quality comes with a price of restricted information about studied specimens, earlier work demonstrated that Kα lines are sensitive to defect states in other Zn-based nanostructures.[258] Fig. 7.12a presents the Kα X-ray emission spectra of four ZnSe QDs samples. Analogously to the Zn K-edge XAS measurements, difference spectra were obtained by subtracting the bulk ZnSe signal from QDs results, as shown in Fig. 7.12b. The high signal-to-noise ratio of acquired Kα lines allows for attributing small observable spectral differences to the chemical changes in Zn atoms. All QDs spectra shift towards lower energies, indicating the reduction of average effective electronic charge on Zn atoms compared to bulk ZnSe. As suggested by Penfold et al.[258] in studies dedicated to much more explored ZnO NPs, the redshift of Zn Kα is a

good indication of the lattice vacancies. Furthermore, the intensity of acquired difference signals is comparable between the three QDs samples with the largest particle sizes and decreases noticeably for the sample with the smallest QDs diameters. This result suggests that the main contributions to the observed changes are charge effects associated with in-lattice atoms rather than atoms at the surface. However, such a signal could be caused by several overlapped effects. Combined with the discussed Zn K-edge XAS results, performed lab-based X-ray spectroscopy measurements indeed suggest Zn in-lattice vacancies as the main factor influencing the electronic structure of ZnSe QDs.

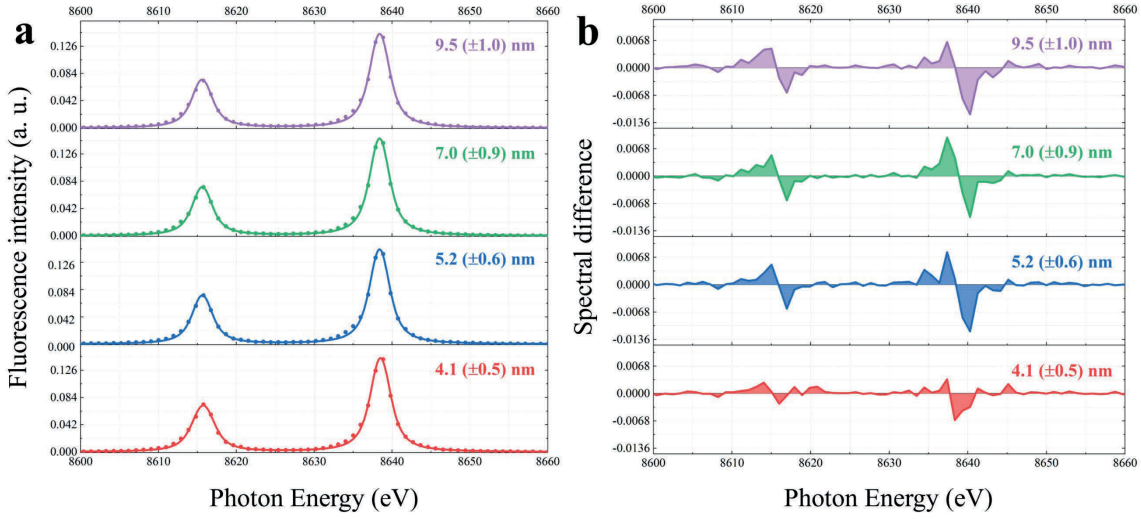

Figure 7.12 *a) Zn Kα XES spectra of ZnSe QDs. b) Difference spectra acquired by subtracting bulk ZnSe spectrum from the QDs data. The color labeling of QD samples is consistent with other figures presented in this section.*

7.5 Conclusions

Performed experiments involving the laboratory-based von Hámos double X-ray spectrometer provided insight into the electronic structure of synthesized ZnSe QDs samples, linking the detected XAS and XES intensities to the possible existence of the defects states in the material crystal lattice.

The calibration measurements allowed the optimization of spectrometer parameters, prioritizing high counting statistics of the measurement while preserving the satisfactory quality of the collected X-ray absorption spectra. In the case of the XES spectrometer, the adopted sample positioning system based on the two microscope cameras paired with the motorized stage allowed reliable restoration of the studied target position, mitigating the effect of sample displacement on the obtained X-ray emission spectra.

A significant aspect of the presented chapter was the development of specialized sample cell, which enabled long-lasting X-ray spectroscopy experiments on low volumes of nanomaterial suspensions, maintaining its physical stability. The prepared microliter-stirred system is expected to serve in future studies expanding beyond described laboratory X-ray spectroscopy studies of ZnSe QDs, including in-situ measurements of chemical reactions and investigation of other nanostructures such as plasmonic NPs.

The laboratory XAS and XES measurements of ZnSe QDs samples unveiled the changes in the chemical state and local structural environment of Zn atoms relative to the macroscopic ZnSe semiconductor particles. Based on the conducted experiments, supported with literature data, the most likely explanation of observed spectral signals is the existence of excess Zn vacancies in QDs samples. Such defect type already prevails in the bulk ZnSe material[264], and nanostructures, in general, are characterized by a higher relative fraction of native lattice defects compared to macroscale objects.[269] Moreover, the proposed defect type and its in-lattice nature are consistent with the newest report, which pointed to Zn vacancies as the most dominant source of defects limiting quantum yields of ZnSe shells in core-shell QDs structures rather than interface or surface sites.[270]

The presented results demonstrate the application range of in-house X-ray spectroscopy. Obtained spectra show that XAS and XES applied at the laboratory level can serve as tools in solving scientific cases that advance beyond sample screening and determining the oxidation state of the investigated specimen. Simultaneously, performed experiments established limitations of utilized von Hámos lab-based setup. In particular, the low-intensity and polychromatic output of the X-ray tube translated into noisy spectral features in Zn K-edge XAS, hindering the quantitative assessment of the detected subtle changes. It should also be emphasized that besides a single study[258] cited in the present work, the literature data regarding the application of Zn Kα XES to probe the electronic structure of Zn-based nanosystems is lacking. The next step towards expanding the presented hypothesis involves turning to large-scale facilities with intense X-ray sources.

8. Synchrotron X-ray spectroscopy experiments

This chapter describes the experiments performed at the SOLARIS National Synchrotron Radiation Centre at the ASTRA (Absorption Spectroscopy beamline for Tender energy Range and Above) beamline. As demonstrated in the previous section, the Zn K-edge XAS unveiled the structural and chemical effects in ZnSe QDs. However, the data obtained with the laboratory-based setup was insufficient to fully resolve details in the absorption spectra features of studied materials. This limitation can be overcome with high-intensity, monochromatic synchrotron radiation, extending the sensitivity of the Zn K-edge spectra. The chapter starts with a presentation of the ASTRA beamline and its experimental end station, providing information regarding the instrumentation and parameters applied in the conducted measurements. The following subsection describes the software utilized in the thesis to simulate X-ray absorption spectra to explain experimental results. Afterward, the Zn K-edge XAS measurements of ZnSe QDs samples are shown and discussed. Obtained results are first compared to the data acquired with the laboratory setup to assess the reliability of in-house X-ray spectroscopy. Finally, the acquired spectral changes in the ZnSe QDs XAS spectra are investigated with the support of theoretical calculations to identify all dominant factors affecting the electronic structure of examined samples.

8.1 ASTRA beamline and XAS end station description

Fig. 8.1 presents a schematical representation of the ASTRA beamline layout. The synchrotron radiation is produced by the double bend 1.31 T bending magnet with 2 keV critical energy. The polychromatic beam passes the shielding wall of the storage ring, encountering a diagnostic module and fixed aperture as it falls into the monochromator chamber. The monochromator consists of two Bragg-type diffraction crystals mounted parallel to each other on a motorized positioner controlled by a stepper motor, providing angular resolution on the level ~0.0001° and the Bragg angle range of 10-65°. Rotation of the first crystal causes translation of the second analyzer perpendicularly to its surface owning to a fixed cam. Such a design called double crystal monochromator (DCM) allows maintaining the stable exit direction of the outgoing monochromatized X-ray beam during energy scanning, which cannot be achieved using a single crystal. The available photon energy spans from 1 to 15 keV, with the Zn K-edge range covered by a pair of Ge(220) diffraction crystals. Before accessing the end station, the radiation is shaped with exit slits to about 10 x 1 mm spot at the sample with the flux in order of $5 \cdot 10^{10}$ photons per second (at 400 mA electron current) for energies corresponding to Zn K shell ionization energy. The front end of the beamline is maintained at ultra-high vacuum conditions (~10^{-10} mbar) by a compact ion pump, and the monochromator chamber is kept at ~10^{-6} mbar. The monochromatic X-ray beam enters the beamline end station through the window made of thin polypropylene foil.

Fig 8.2 shows the photograph of the ASTRA end station for transmission mode XAS. The incident (I_0) and transmitted (I_1) beam intensity is measured in the two ionization chambers positioned between the sample area. The simple design of the sample chamber shortens the sample exchange process. Additionally, the end station possesses a second

sample chamber for a reference compound (metallic foil) paired with the third ionization chamber, allowing simultaneous acquisition of the sample and reference spectra, which preserves the energy calibration between measurements. The XAS end station section is maintained at ambient conditions or low vacuum, depending on the utilized photon energies and sample requirements. The lack of optical lenses or focusing mirrors allows quick alignment of specific experiments and simplifies user operation.

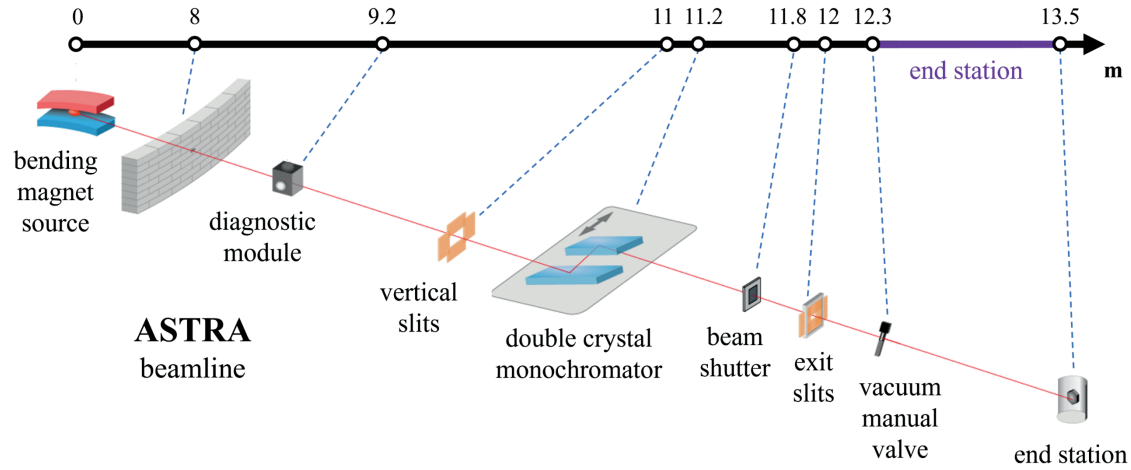

Figure 8.1 *Schematics of the ASTRA beamline construction. Adopted from SOLARIS webpage, © 2010-2024 Jagiellonian University in Kraków, JU Website.*

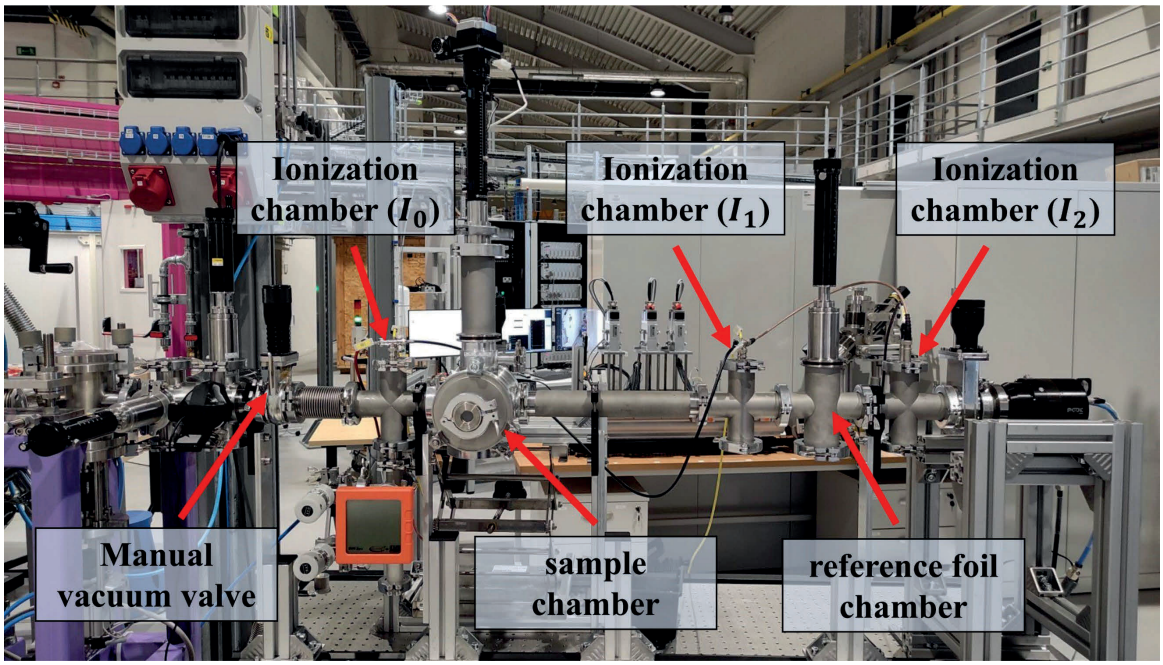

Figure 8.2 *Photograph of the ASTRA beamline XAS end station with the description of the main elements.*

8.2 FEFF 9.6 software for XAS spectra calculation

In this chapter, the analysis of collected synchrotron spectra is supported with theoretical calculations to attribute the effects influencing the electronic structure of ZnSe QDs. The X-ray absorption spectra were simulated utilizing the FEFF 9.6 package. It is an automated ab initio code that applies the multiple scattering approach, providing

reliable prediction of the spectral shape and density of states (DOS) based on the structure of examined compounds.

FEFF 9.6 program adopts the well-developed independent quasi-particle XAS theory implemented in the real-space Green's function formalism. A detailed description of the software and its methodology can be found in the provided literature.[271,272] Briefly, the calculated absorption coefficient, described by effective one-particle Green's function, is expressed as two separated contributions from the absorbing central atom and multiple scattering on the neighbor atoms. The first intra-atomic part is the dominant term defined by the solid-state potential at the absorption site, and the second determines the fine structure of the simulated spectra.

The scattering potentials are determined based on the muffin tin approximation, which treats atomic sites as potentials with spherical symmetry and assumes constant potential in the interstitial region between absorbing centers. In reality, the potential of a given specimen is more complex. The spherical approximation is very accurate near the atomic nucleus due to the large charge density. However, in the outer part of atoms and the space between the atoms, the potential is typically anisotropic, dictated by the bonding type and specific elements present in the material. The interatomic potential is particularly important in the simulation of the XANES region. The FEFF code allows adjusting the overlap of interatomic potential for a more accurate determination of the absorption coefficient.

Fig. 8.3 presents an image of the FEEF 9.6 program interface with a loaded exemplary input file for the Zn K-edge XANES spectrum calculation. To simulate the absorption coefficient, the input file must contain structural information about atom types and their relative positions presented in cartesian coordinates. The output spectrum will vary depending on the parameters picked in the software main window. In the spectrum settings panel, the user selects the type of spectral signal (here XANES) with the range and step of the spectrum given in k value (photoelectron wave vector). The FMS parameter defines the sphere radius (in Å) centered at an absorbing atom for full multiple scattering computation. In the module options section, The SCF card, if activated, unlocks self-consistent potential calculations according to the selected SCF radius and other optional parameters. The Exchange panel determines the exchange-correlation potential for the fine structure and atomic background. Two further windows allow modification of the Fermi level and the addition of instrumental and final state broadening (in eV). The Corehole card specifies the interaction model between the core hole and the photoelectron treatment. The three options are Final State Rule, Random Phase Approximation, or no interaction included. The S_0^2 at the bottom of the module option panel fixes the so-called amplitude reduction factor. An extensive review of all available parameters is given in the official tutorial.[273]

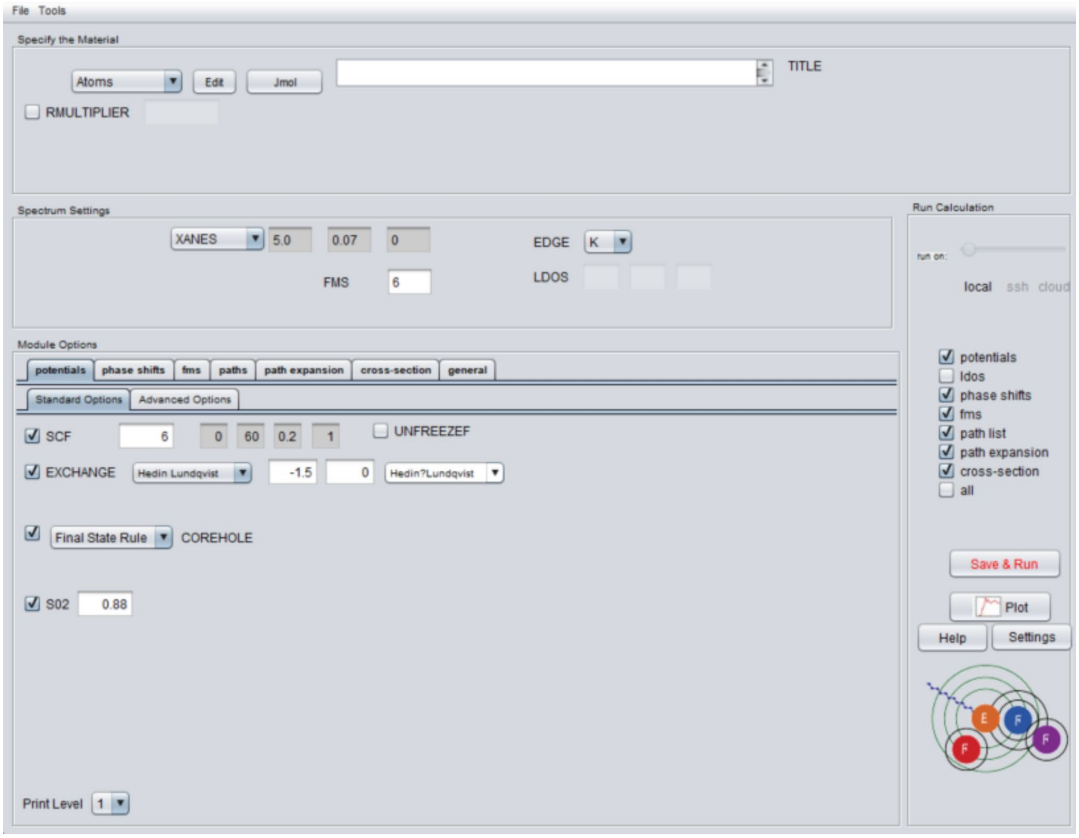

Figure 8.3 *Screenshot of the FEEF 9.6 program interface with the loaded exemplary input file for Zn K-edge XANES spectrum calculation.*

8.3 Zn K-edge XAS synchrotron measurements

Experimental details

The Zn K-edge XAS experiments at the ASTRA beamline were conducted in transmission mode utilizing a pair of Ge(220) diffraction crystals. The studied samples involved all specimens investigated using laboratory XAS/XES setup, including synthesized ZnSe QDs suspensions in toluene and four pellet-shaped powder references mixed with cellulose (3% wt. of Zn): ZnSe powder, ZnO NPs, $ZnSt_2$ and $Zn(OAc)_2{\cdot}H_2O$. To fully utilize the wide X-ray beam (10 x 1 mm), the QDs suspensions were placed into a custom-made steady-state cell with Kapton walls, creating a 5 mm thick liquid sheet. As a single synchrotron measurement lasted significantly shorter than a laboratory-based X-ray spectroscopy experiment, the stirred sample setup was unnecessary to preserve suspension stability. The concentration of ZnSe QDs (Zn atoms) was around 150 mM. Each sample was scanned in the photon energy range 9560-9750 eV with an energy step of 0.3 eV (~0.0006°) around the Zn absorption edge. Four scans per sample were obtained, each collected over ~8 min of signal acquisition. The

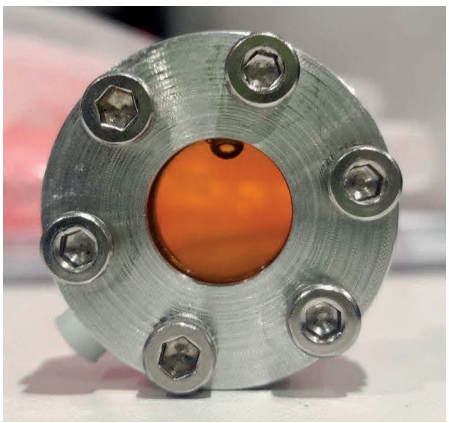

Figure 8.4 *Prepared sample cell for XAS experiments of QDs liquid suspensions.*

measurements were controlled using the AstraLibra program. Data processing and further analysis were conducted using Athena software.[274]

Results & discussion

Fig. 8.5a presents synchrotron absorption spectra of Zn species marked with thick color lines. The interpretation of the main spectral features is identical to the considerations made in the previous chapter regarding laboratory X-ray spectroscopy (section 7.4). For comparison, Fig. 8.5a also includes results obtained with the lab-based von Hámos setup depicted with thin grey lines. Both datasets were calibrated by adjusting the position of the measured Zn foil spectrum in each experimental run to the equivalent literature data[234] and shifting all of the other spectra by the same energy value. As shown, while synchrotron measurements yielded improved spectra quality, the data collected in laboratory experiments accurately mapped the spectral shape and peak positions of all studied samples. However, some discrepancies do occur. Primarily, the intensity of the main feature is noticeably weaker for lab XAS spectra regardless of the measured target. This behavior was observed in earlier experiments (Fig. 7.2 and 7.6) when laboratory results of reference compounds were compared to literature synchrotron spectra. Other reports attribute such changes to either sample thickness effect or background photons that alter the measured absorption coefficient, like contributions of other allowed diffraction orders and spectrometer low energy tail distortions.[275,276] In the present case, the decrease in white line intensity transpires for relatively thick samples (ZnSe QDs suspensions) as well as thin pellets or foil, which rules out the sample thickness or inhomogeneity effects as the only factor causing depicted spectral distortions. Thus, the high contribution of unwanted background X-rays is clearly the main reason for observable discrepancies.

The first derivatives of synchrotron spectra (thick color lines) and equivalent laboratory data (thin black lines) are shown in Fig. 8.5b. Analogously to the obtained XAS spectra, the overall shape of derivative functions for both datasets is similar, with some minor differences in the intensity of local extrema. The determined E_0 values based on the derivatives maxima for all of the samples are presented in Fig. 8.5c. Blue spheres correspond to synchrotron data, and the laboratory spectrometer results are marked with red triangles. The error bars reflect the energy step of derivative data. For most specimens, especially ZnSe samples, the E_0 values match well between both measurements. However, the values derived for Zn foil, ZnO NPs, and $Zn(OAc)_2 \cdot H_2O$ diverge for the two applied approaches. As presented in Fig 8.5b, these three species are characterized by the complex multi-peak shapes of the main feature in their derivative spectra. In such cases, the determination of absolute E_0 is inaccurate for lab-based XAS spectroscopy due to the large energy step of data introduced as a consequence of limited counting statistics. Additionally, the synchrotron data provide increased sensitivity of E_0 to bonding environment and coordination number of Zn species.

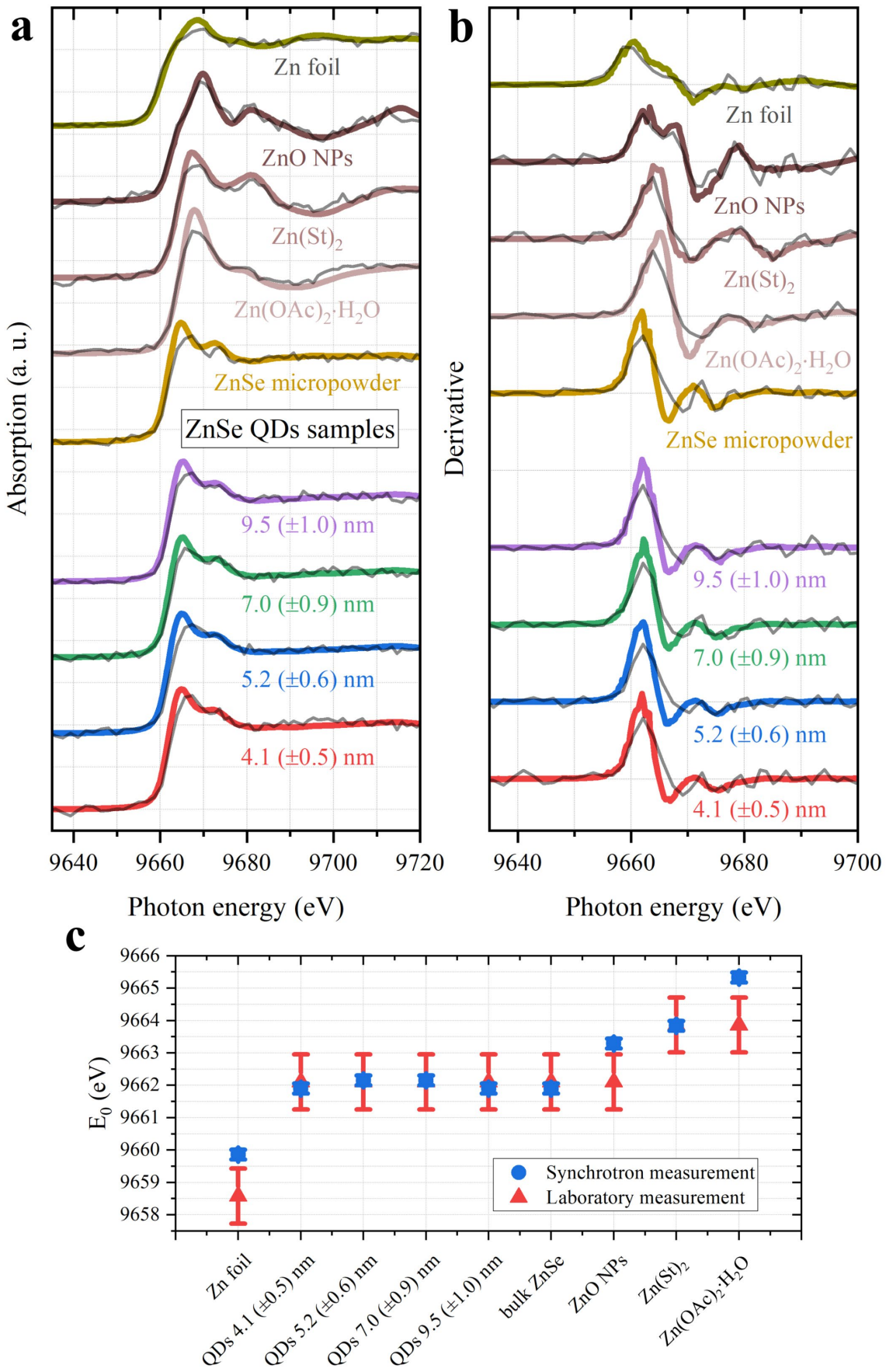

Figure 8.5 *a) Comparison between synchrotron (thick color lines) and laboratory (thin grey lines) Zn K-edge XAS spectra of investigated samples. b) First derivative of absorption spectra presented*

in (a). c) E0 values obtained for all Zn samples from the maximum of the first derivative of synchrotron (blue spheres) and laboratory (red triangles) X-ray absorption spectra. The error bars indicate the energy step of the respective datasets selected based on the photon counting statistics of each measurement.

It should be noted that the superior signal quality of synchrotron spectra arises due to significantly larger photon flux (~10^{10} vs ~10^{3} photons per sec at Zn K-edge energies)[1,277] and discussed above lack of background photons provide better energy resolution. In fact, the lab-based setup utilizes higher diffraction orders of analyzer crystal, that is, Si(440), with larger 2d lattice spacing compared to the Ge(220), translating to the improved resolving power of the von Hámos spectrometer. However, the composition of several factors discussed and noise-free synchrotron data allow more detailed insight into subtle effects in the electronic structure of examined materials.

ZnSe QDs synchrotron spectra with bulk-like ZnSe reference are replotted in Fig. 8.6a. The high intensity of the synchrotron X-ray source revealed tiny spectral changes in the fine structure, previously hindered by point-to-point fluctuations of X-ray tube-based laboratory setup. The difference spectra, presented in Fig. 8.6b, show a series of features related to chemical and structural effects in QDs samples. Three regions of high signal difference are present in the vicinity of the rising edge, outlined in Fig. 8.6a as grey dotted boxes with their magnification shown in Fig. 8.6c.

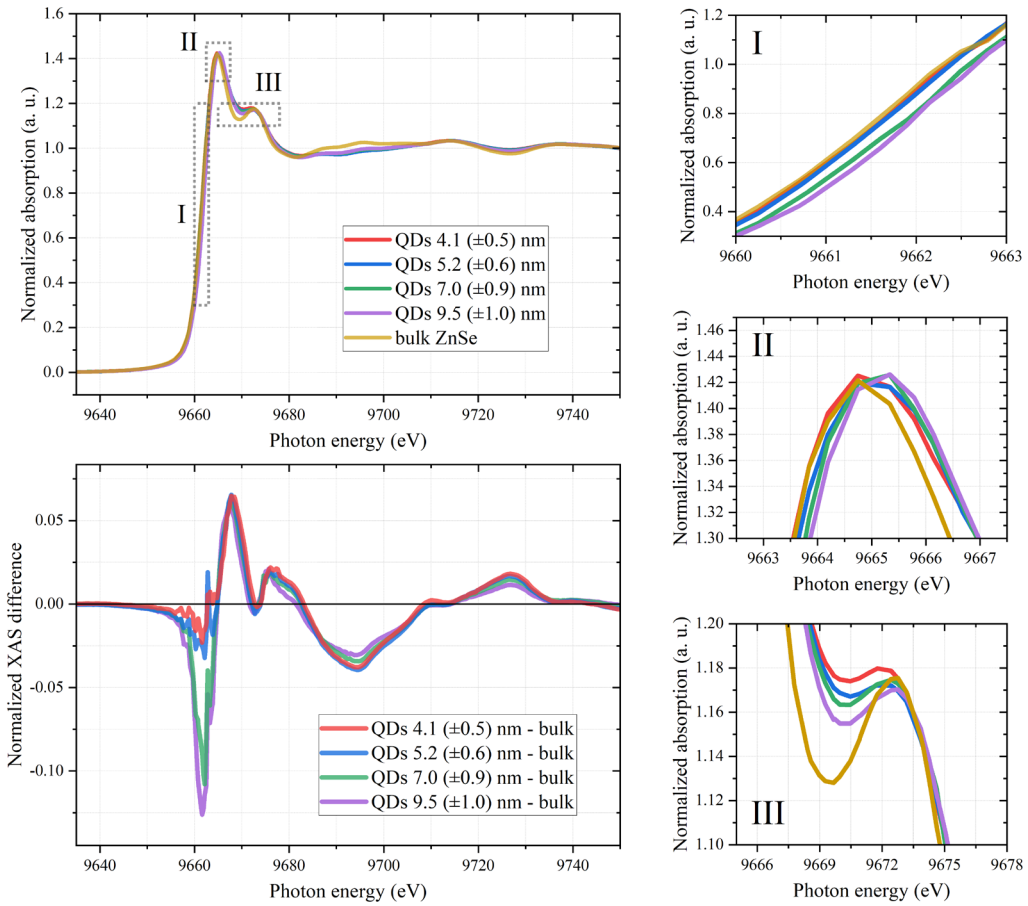

Figure 8.6 *a) ZnSe QDs synchrotron spectra compared to bulk ZnSe powder. The b) difference spectra obtained by subtracting bulk XAS signal from QDs samples. c) magnification of spectral regions marked in (a) with grey dotted rectangles.*

QDs spectra exhibit a shift towards higher energies of the absorption edge (region I) and the main peak (region II) compared to the bulk ZnSe spectrum. Such behavior is manifested by the Fano-like profile in the difference spectra (~9650-9673 eV), which symptomizes chemical changes in the Zn atoms related to average oxidation state shifts or alterations in their coordination environment. The spectra blueshift increases with the increase of mean QD size in the studied sample, signalized by the intensity variations of the first feature in the difference signal (~9662 eV). The second positive part of the Fano-like shape (~9668 eV) does not show the same pattern. This is caused by the broadening of the main peak observed for QDs samples, which additionally display a slight increase of intensity, as seen in Fig 8.6c in region II. All of the above-discussed factors contribute to the observed near-edge difference signal.

Spectral changes in the higher-energy part of the XAS data indicate the structural modifications that alter photoelectron scattering paths. Specifically, the scattering maximum at around 9673 eV (region III) is more pronounced in the case of bulk ZnSe, which suggests a more defective nature of QDs relative to their macroscopic counterpart. The differences in the post-edge part of the spectra continue to occur, especially at ~9690 and ~9727 eV. Overall, the spectral signal related to structural effects varies little with QD size, with the slightly smaller magnitude of changes determined for large QD diameters.

It should be emphasized that although such detailed analysis of X-ray spectra as provided in this chapter was not possible with the laboratory-based X-ray spectroscopy setup, measurements conducted utilizing in-house instrumentation were able to detect both chemical and structural effects in the QDs electronic structure with the former spotted through shift in Kα emission lines and the latter observed in the post-edge scattering feature distortions of XAS spectra.

FEFF calculations

In an attempt to explain the observable effects in QDs spectra, FEEF 9.6 calculations were applied. The simulations were conducted based on the ZnSe zincblende crystal structure acquired from The Atoms archive[278] and transferred into the FEFF input file using the WebAtoms[279] webpage. The determined optimal calculation parameters are equivalent to those shown in Fig. 8.3.

Fig. 8.7a compares the experimentally derived bulk ZnSe XAS spectrum (dark yellow line) to simulated data acquired with different sizes of the ZnSe cluster included in computations. The cluster structures are presented in Fig. 8.7b. As visualized, after adding the third coordination layer of the central Zn atom (cluster with 5 Å radius), the calculated spectrum does not change, simultaneously reconstructing the main features of the experimental result, though some discrepancies in the strength and energy position of the two major peaks occur. The third scattering feature, pronounced in the simulated data, is significantly broader and less intense in the synchrotron spectrum. In the higher-energy part, the agreement between theoretical and measured spectra is rather poor. Nevertheless, the FEFF 9.6 code allows reasonable reproduction of the XANES region. Thus, the analysis of the performed calculation will be restricted to the energy range of 9650-9700 eV.

Performed shell-by-shell computations (Fig. 8.7a) provide insights regarding the origin and sensitivity of the features in the ZnSe absorption spectrum. The white line is already

noticeable when only the first coordination shell of four Se atoms is accounted for in simulations. The second maximum around 9670 eV appears only after including the second coordination layer (12 closest Zn atoms). Both features exhibit significant intensity alterations depending on the coordination environment, which may hint at the main explanation of spectral changes in ZnSe QDs.

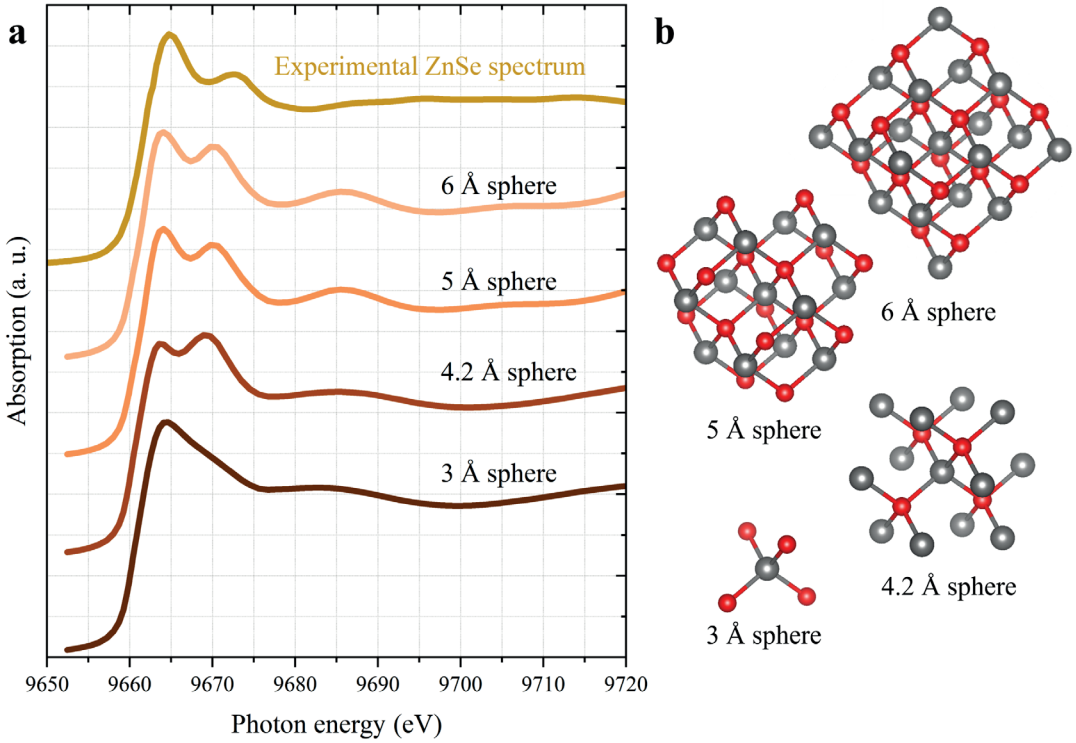

Figure 8.7 *a) Experimental Zn K-edge XAS spectrum of bulk ZnSe (dark yellow line) compared to spectra simulated using FEEF 9.6 code with increasing number coordinating shells of central Zn atom, b) Structures used in the spectra simulations visualized in VESTA software. Zinc and selenium atoms are marked with grey and red spheres, respectively.*

The average local environment of Zn atoms in QDs is expected to be altered by the high number of surface atoms. The synthesized ZnSe QDs samples were passivated with stearate ligands that adsorb on the particle surface through oxygen coordination bonds. Additionally, the electronic structure of Zn-based nanomaterials is known to be influenced by the abundance of native lattice defects, predominantly anion and cation vacancies. Additional FEEF simulations were conducted to evaluate defect and surface effects based on four structure models presented in Fig. 8.8a: uncoordinated Zn surface atom, Zn surface atom passivated with stearate ligand with 2Å distance between the central atom and nearby oxygen, bulk ZnSe structure with missing Se site and missing Zn atom in the second coordination shell. From calculated data, spectral differences were derived by subtracting the simulated unperturbed ZnSe spectrum.

Fig. 8.8b presents computed signals for each model structure compared to the experimental results obtained for QDs. Qualitatively, the signal simulated for Zn vacancy resembles the shape of the measured XAS data, especially for the large QD particle sizes. The slight misfit of the main positive difference features (at ~9667 and ~9675 eV) is likely due to the shift of two main peaks in the calculated ZnSe absorption spectra relative to the

experimental spectrum. Adjusting the intensity of the simulated signal to match structural changes (positive features) observed in experimental spectra, as visualized in Fig. 8.9, yields about 3 % Zn vacancies concentration in QDs samples, assuming negligible defect concentration in bulk ZnSe. This result is consistent with other reports concerning Zn vacancies in Zn-based QDs.[280,281]

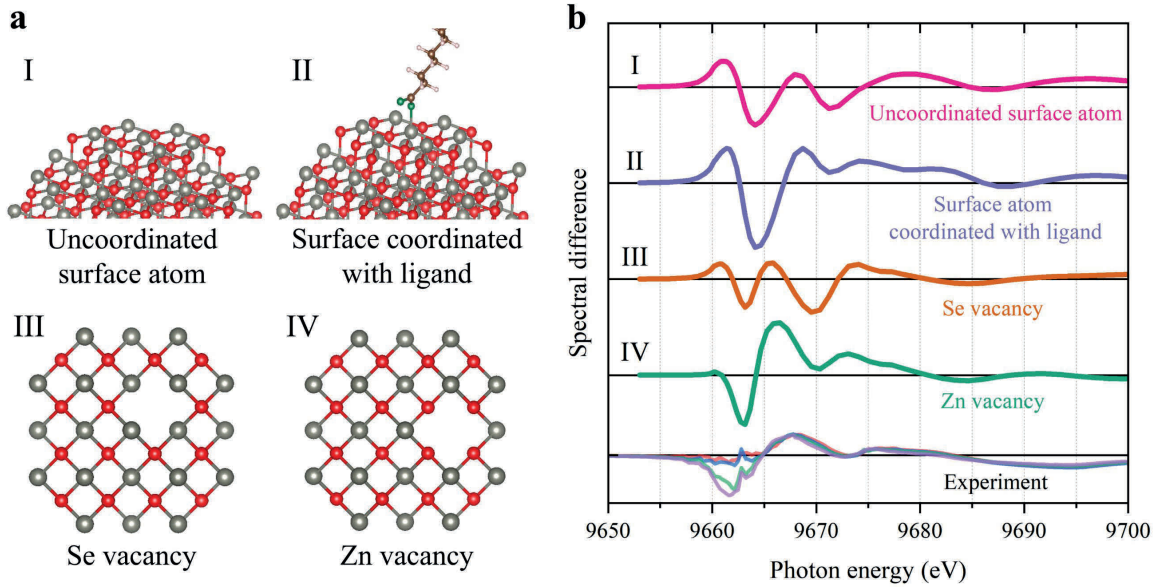

Figure 8.8 *a) Model structures utilized in FEFF calculations of XAS spectra. Zn and Se atoms are marked with grey and red colors. The surface atom in II is additionally coordinated with the O atom to form a stearate chain. b) difference spectra obtained by subtracting the calculated spectrum of "perfect" ZnSe structure from spectra of four models presented in (a) compared to the experimentally determined QDs signal differences.*

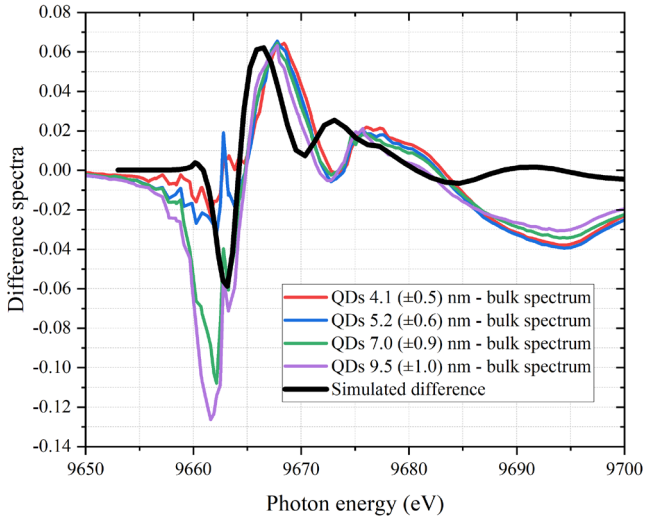

Figure 8.9 *Simulated adjusted spectral difference signal for 3% concentration of Zn vacancies in the model structure (black) compared to the experimental results (color lines).*

The presence of native point defects at cationic sites does not account for the size-dependent chemical effect (~9662 eV) that increases with the size of examined QDs. Such a signal cannot be explained with any of the four examined model structures or their combination. One could suspect that the quantum confinement effect, pronounced in optical

PL and absorption spectra, would also shift the XAS spectra. However, the observable QDs X-ray absorption shifts exhibit opposite size-dependent behavior as in the UV-Vis spectroscopy measurements. Similarly, the lack of prominent surface effects, which are expected to be the most intense for the smallest QDs, is also intriguing. The signal simulated for surface atoms is unable to explain experimental data. This could be due to a simplified model structure applied in FEEF computations that, for example, does not account for possible surface defects. Moreover, the surface signal could be overlapped with other contributions. More sophisticated models require refinement of the spectra calculation approach, accurately reproducing conducted XAS measurements. An additional factor to consider is the surface composition of produced QDs. Although, based on the synthesis reaction conditions, the expected surface termination is with Zn atoms, there are reports regarding Se-terminated ZnSe[96] and CdSe[282] QDs obtained with similar precursors and procedures as in this work. Depending on the surface termination, the Zn K-edge XAS spectra will be more or less sensitive to surface effects. In this context, performed synchrotron measurements should be supplemented with future surface-sensitive measurements, assessing the chemistry behind the surface atoms.

8.4 Conclusions

Zn K-edge XAS experiments at ASTRA beamline were conducted to study the effects in the electronic structure of ZnSe QDs suspensions.

First, performed synchrotron experiments provided a reference to evaluate the unexplored capabilities of laboratory X-ray spectroscopy. Good agreement between the two experiments and confirmation of the initial interpretation of the spectral signals confirms the reliability of in-house instrumentation. This result is significant in the context of lab-based setups' popularization as a complementary tool in X-ray science, which can partially relieve the oversubscribed synchrotron facilities from less demanding experiments.

The high quality of acquired synchrotron data revealed subtle effects in the QDs absorption spectra, allowing expanding the observations made based on the laboratory X-ray spectroscopy measurements. The analysis of XAS spectral changes was supported with FEEF calculations based on the prepared model structures. Although inaccuracies between theory and experimental data hindered the identification of all difference signals, results pointed to the existence of Zn vacancies in all QDs samples that cause structural changes in the acquired spectra.

The presence of Zn defect states has a few implications regarding material electronic properties. Specifically, it is expected to significantly alter the electron and hole dynamics, trapping one of the charge carriers and acting as additional relaxation pathways in excited QDs. Thus, the application of time-resolved optical transient absorption (TA), which allows tracking the excited charge carriers, should provide further insight into the role of Zn vacancies. Additionally, TA can capture the contribution of surface effects not pronounced in the measured Zn K-edge XAS spectra.

9. Ultrafast optical transient absorption experiments

The following part describes ultrafast TA measurements performed at the Extreme Light Infrastructure (ELI) Beamlines laser research center in Dolní Břežany (Czech Republic), a part of the European Research Infrastructure Consortium (ERIC). This experimental campaign aimed to characterize and attribute the dominant sources influencing charge carrier dynamics in ZnSe QDs. Specifically, the TA spectroscopy setup available at the ELI facility provided sub-ps temporal resolution sufficient to probe the impact of defect effects, including surface states and lattice vacancies.

The chapter starts with an overview of the utilized TA instrumentation followed by a brief description of conducted measurements and applied data processing procedures. The obtained results are presented, discussed, and juxtaposed with literature reports and other experiments outlined in this work, in particular, acquired the synchrotron data.

9.1 TA experiment description

Experimental setup at ELI Beamlines

The schematic of the experimental setup employed in preformed TA measurements is presented in Fig. 9.1. The primary photon source is a table-top Spectra Physics Femtopower Ti:Sapphire amplifier with integrated seed oscillator and used in conjunction with an argon-filled hollow core fiber delivering uncompressed white beam probe pulses in the energy range 1.13-4.59 eV (270-1050 nm), at 1 kHz repetition rate and ~20 fs pulse duration. The pump pulse with photon energies ~3.15 eV (394 nm), pulse energy 20 nJ and duration ~30 fs is obtained through second harmonic generation (SHG) of compressed and filtered probe pulse subsection. The setup operates in a transmission geometry, with pump and probe pulses focused into ~100 µm spot at the sample at a 2-5° angle. A prism-based spectrometer with a 1 kHz CCD camera is employed for the detection system.

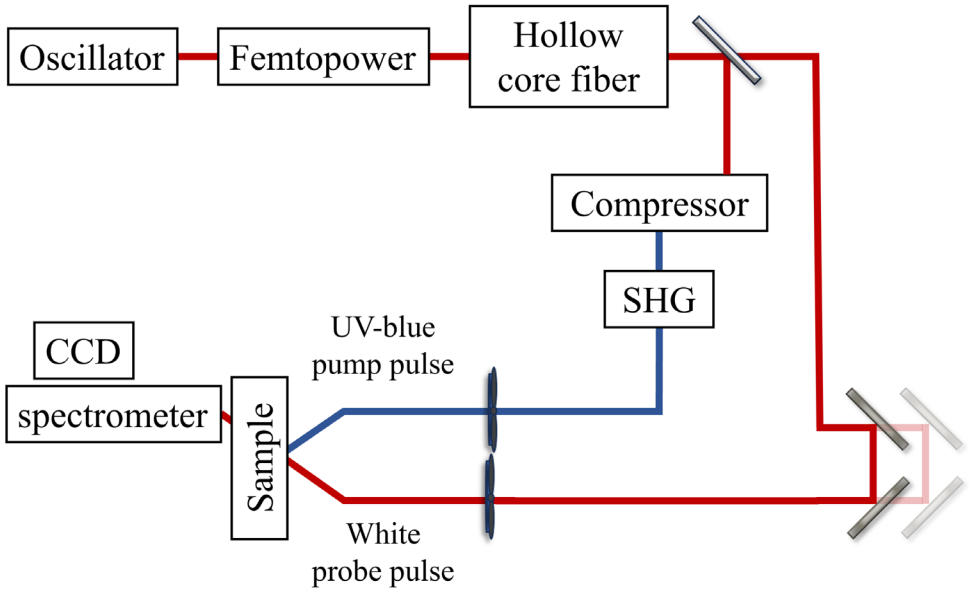

***Figure 9.1**. Schematics of the TA setup utilized in performed experiments. Adopted from ELI User Portal.*[283]

Samples and measurements

For TA experiments, the ZnSe QDs suspensions were placed in a thin quartz cuvette with a 1 mm optical path length. Before the measurement, the samples' optical density (absorbance) was adjusted to ~0.2-0.3 at the maximum of the first resonance (1S peak) in the steady-state UV-Vis spectra. During signal acquisition, the cuvette with liquid QDs suspension was automatically moved in a transversal direction to the pump and probe pulses to avoid sample degradation with prolonged illumination of the same spot. The pump pulse intensity was tuned to avoid excitation of multiple electron-hole pairs in a single particle, based on the transient signal intensity relative to the maximum ground state absorbance (ΔA/A).[150,284] Each sample was measured with pump-probe delays from -20 ps to 5 ns in 262 steps. Negative delay values denote arrival of the probe pulse prior to the pump. Every second measurement was conducted without a pump pulse to collect the ground-state signal. The temporal resolution of the experiment, evaluated based on the pump-pulse cross-correlation, was about 100 fs.

Data processing

Data processing was performed in Surface Xplorer software dedicated to TA analysis. Fig. 9.2a presents a raw signal obtained in a single conducted measurement of the ZnSe QD sample. Acquired datasets, such as the presented one, consist of a series of TA spectra, each obtained at a specific pump-probe delay value, stacked together to form a 2D matrix. The color scale indicates the intensity of the ΔA signal.

The main factor causing distortions in the TA analysis is the group velocity dispersion (chirp) of the broadband probe, resulting in different arrival times (t_0) for each wavelength, as seen in the raw matrix plot. The Surface Xplorer allows correcting for the chirp effect, as demonstrated in Fig. 9.2b. Other data processing procedures involved the subtraction of the light scattered from the pump pulse and the background removal by subtracting the average of the first few transient spectra collected at negative delays. TA spectra at specific pump-probe delay values are obtained by performing cuts along the x-axis of the corrected matrix plot. Cuts along the y-axis show the kinetics of the measured ΔA signal at a selected photon energy.

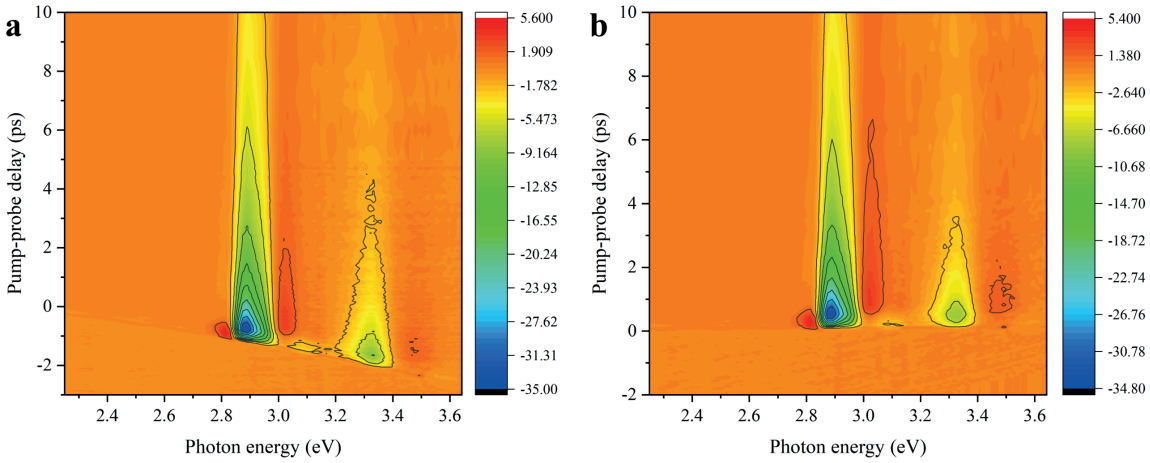

Figure 9.2 *TA matrix collected for the ZnSe QDs sample: (a) raw data and (b) corrected for the chirp effect. The color scale reflects the intensity of the ΔA signal (mOD).*

9.2 Results and discussion

Fig. 9.3 presents steady-state (a) and selected transient (b) spectra for the four ZnSe QDs samples in a decreasing QDs mean diameter order from top to bottom. In ground-state QDs, all of the electrons are bonded in the valance levels, and the steady-state UV-Vis spectra provide a view of the available unoccupied states. By exciting the sample with the intense pump pulse, whose spectrum is marked in Fig. 9.3a, the discrete absorption states with transition energies below or equal to the pump photon energies become partially populated. Due to partial occupation of conduction levels, the absorbance of the excited spectrum decreases, which is manifested by the negative ground-state bleach (GSB) signals in the TA spectra that correspond to the position of resonances in the steady-state spectrum. For example, the ZnSe QDs sample with 9.5 (±1.0) nm particle size has four absorption maxima in the examined photon energy range (denoted with arrows) and four bleaches in the TA signal (first two lowest-energy GSBs are overlapped). Note that the highest-energy feature (~3.28 eV) in the steady-state spectrum lies outside the pump pulse excitation energy but still is bleached in the TA spectrum. This is because the electronic transition associated with the 4^{th} peak shares the final state with the 1^{st} and 2^{nd} transitions, as schematically presented in the inset to Fig 9.3a (top plot). Therefore, by inducing the lower-energy excitations, the occupancy of the final state changes, decreasing the probability of the higher-energy transition. As such, the 4^{th} feature should exhibit similar kinetics as the 1^{st} most intense bleach.

The GSB intensities change with subsequent pump-probe delays, showing different behaviors between examined QD samples. At early times from the target excitation (black and red lines in TA spectra), the main TA feature grows, indicating the filling of either CB electron or/and VB hole states involved with the 1^{st} electron transition. The increase in bleach intensity observable between spectra collected at 250 fs and 500 fs delay is due to intraband relaxation of charge carriers from higher levels. The growth of the main GSB is more prominent for samples with larger QDs, where the gap between pump photon energy and energy of 1st absorption state is the highest. The growth occurs almost instantly in the case of the smallest QDs (bottom spectrum).

After the initial short expansion period, the GSBs in all samples undergo decay, corresponding to the depopulation of excited states (carrier relaxation). The decline of the bleach features is rapid, with most of the changes occurring within the first 10 ps from the pump pulse excitation. Significant picosecond and sub-picosecond changes of bleach intensity in QDs TA spectra signalize the non-radiative carrier relaxation through surface or defects trapping.[34] The acquired result indicates the dominant role of these effects, dictating the charge carrier dynamics in investigated materials.

Besides the main excitonic bleaches, QDs TA spectra show positive signals related to the photogeneration of new states. The features in the vicinity of the GSBs that are pronounced at the earliest pump-probe delay times arise from the Stark effect described earlier in this work in section 3.3. Additionally, the low-energy region exhibits a weak broadband photoinduced absorption (PA) signal, depicted in more detail in the inset to the QDs 4.1 (±0.5) nm TA spectrum. As this featureless PA occurs at energies below QDs bandgap energies (the 1st maximum in steady-state spectra) and well above energy spacing

of CB/VB intraband levels (~100s meV), it has to carry information about the contribution of in-gap trap states. Time-resolved experiments on the CdSe QDs model system attribute the origin of the broadband PA signal to hole trapping occurring at the surface[285], though the conclusions do not necessarily have to be valid for ZnSe QDs.

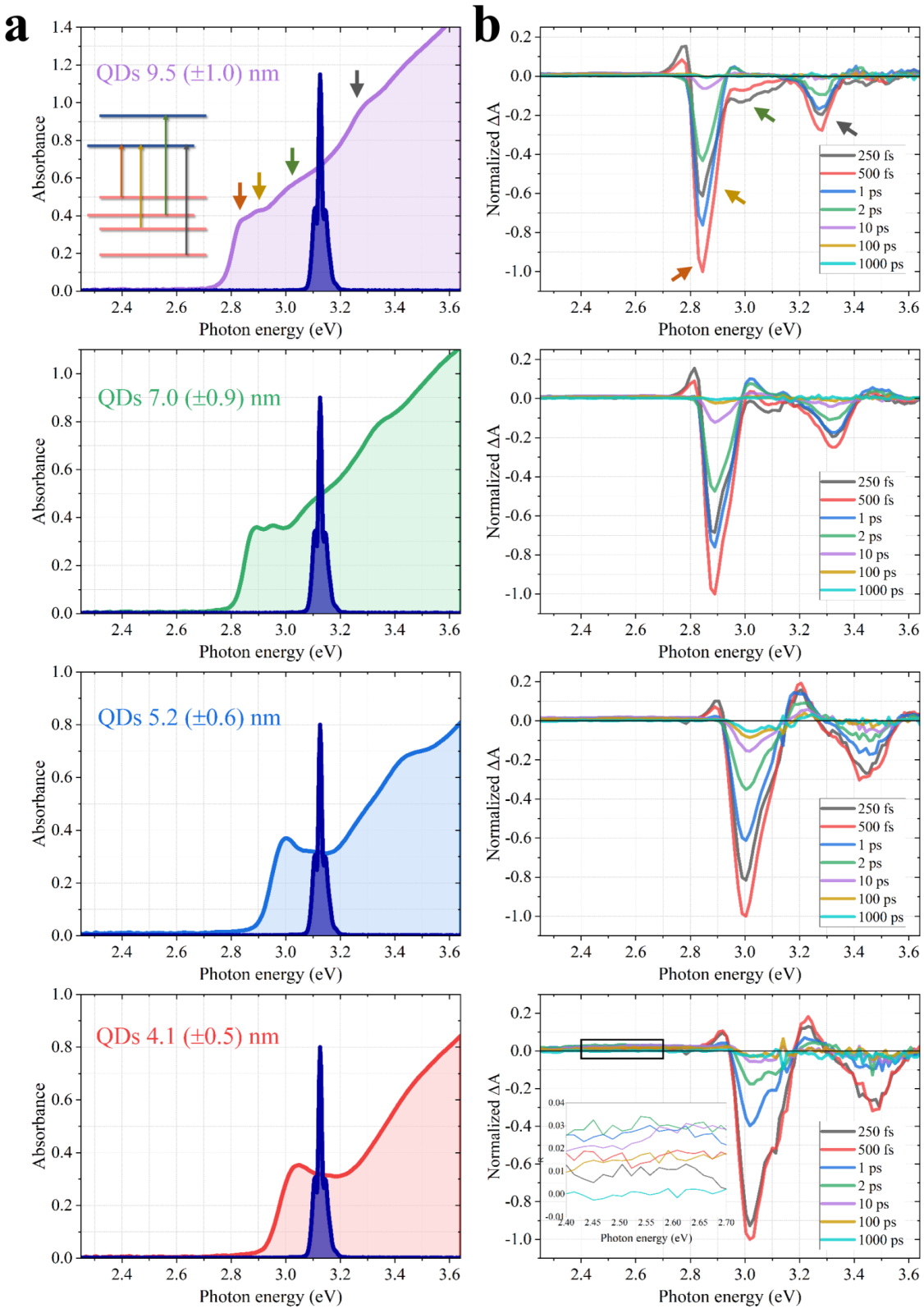

Figure 9.3 *a) Steady-state and b) transient absorption spectra at selected pump-probe delays of ZnSe QDs samples presented in the decreasing QDs average size from top to bottom. The spectrum*

of the pump pulse (navy blue color) is included in the ground-state spectra plot. Inset to the first spectrum (from the top-left) indicates the electronic transitions associated with the maxima in the ground-state absorption and its corresponding transient absorption spectra (marked with color-coded arrows). Inset to the bottom TA spectrum shows the magnification of the broadband PA signal.

More detailed insight into carrier relaxation pathways is obtained through the kinetic traces analysis of the main GSB and sub-bandgap PA signal, presented in Fig 9.4a and 9.4b, respectively. Data obtained for each sample was normalized to the maximum measured ΔA intensity. The PA signal was averaged over the predefined range of photon energies (ΔE = 0.3 eV) away from the main GSB features, as shown in the bottom TA spectrum of Fig. 9.3b with a black rectangle, to avoid overlapping with the kinetics of other processes. The depicted pump-probe delay range (-2 to 10 ps) corresponds to the region of most extreme signal changes due to trapping effects as determined by the inspection of discussed TA spectra.

The obtained decay traces of the 1st absorption state bleach show complex behavior. In the first 1.5-2 ps from the sample excitations, the amplitude of ΔA decreases most significantly for the smallest QDs particle sizes while dropping more slowly for the two large QDs mean diameters. Such size-dependent tendencies indicate the surface-mediated depopulation of the excitonic state as smaller particles are characterized by a higher surface-to-volume ratio. In the later stages of the signal decay, the relation between the samples shifts, suggesting the existence of other additional relaxation channels.

The broadband PA signal exhibits initial growth, presumably caused by surface hole states filling from the higher-energy discrete valence levels. The point-to-point fluctuations of the weak PA signal in the examined energy range are the major source of the experimental uncertainty. Data for each sample shows similar kinetics, but amplitude is the highest for the smallest average QDs size. The correlation between the PA growth period (0-2 ps) and the initial GSB decay is striking. Following the initial rise saturates for all samples, which most likely marks the complete occupation of surface states. Noteworthy, at the same pump-probe delays, excitonic bleach continues to decay, but its kinetic alters as the surface recombination channel deactivates, and the signal recovery in larger QDs becomes faster than in the smaller ones. This effect is demonstrated in Fig. 9.4c, which shows the incremental GSB amplitude change for all QD samples between the early time of PA growth phase completion (2 ps delay) and prolonged PA saturation (10 ps delay). GSB analysis in the surface saturation period allows isolating the second (or more) alternative charge carrier relaxation pathway. As depicted, the second contribution to GSB decay displays the opposite tendency to the first surface-assisted channel, that is, the depopulation magnitude of QDs absorption states increases with the increase of particle size. Such a trend may hint that the second channel could be related to traps/defects in the bulk QDs lattice. Based on the synchrotron experiments, a reasonable guess would imply Zn vacancies as the source of the defect-assisted channel.

To acquire further information regarding different contributions to the relaxation of excited CB electrons, the obtained decay curves were fitted with multiple exponential decay functions. The fitting range was set from 600 fs delay to avoid the initial growth of the GSB associated with intraband relaxation. The best agreement with the experimental data (R-square > 0.99) has been achieved by fitting the sum of four exponentials:

$$y(t) = \sum_{i=1}^{4} A_i e^{-t/\tau_i} \tag{10}$$

where A_i and τ_i denote amplitude and decay constant of i^{th} exponential, respectively.

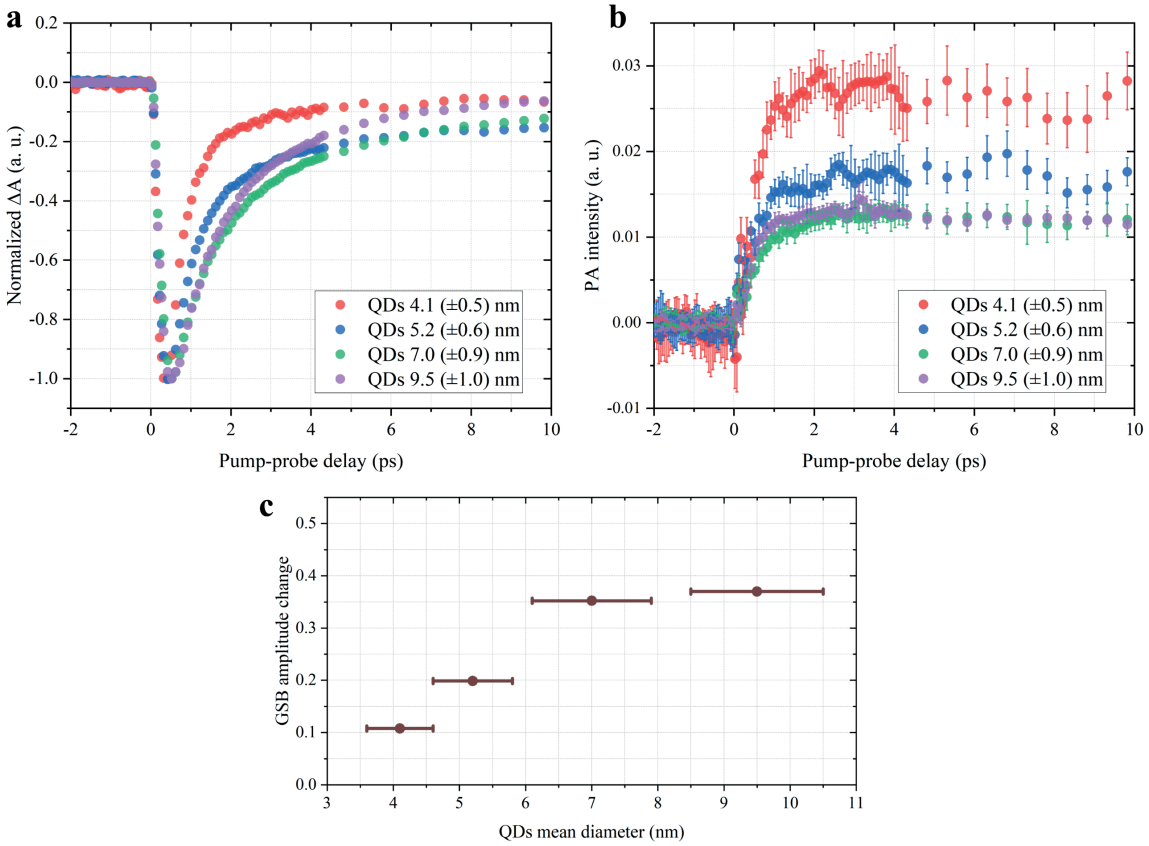

Figure 9.4 *Kinetic traces of the first (low-energy) GSB decay (a) and broadband PA growth for all examined ZnSe QDs samples. c) The change of GSB during deactivation of the surface state decay pathway calculated as: |ΔA(2ps)| - |ΔA(10ps)|.*

Based on the acquired fits, the two most dominant processes, occurring during the first ps of the relaxation, were determined, which together account for over 90% of the main GSB decrease. Their characteristic time and fractional amplitude, calculated for each ZnSe QDs sample, are presented in Fig. 9.5a and Fig.9.5b. The fastest component is characterized by sub-ps time constant (τ_1) for all samples, which increases with higher QD size. Moreover, this process affects significantly smaller particles, as seen by the amplitude (A_1) comparison, matching well with the discussed surface effects. The second GSB decay contribution shows a complex relation between QD samples, demonstrated by the calculated decay constraints. Quantitatively, this component impact on carrier dynamics is more prominent for QDs with larger average diameters. In all examined cases, the effect of second contribution is smaller compared to the first one. The acquired results indicate the existence of the alternative fast relaxation pathway to the surface-mediated channel.

Besides two main ~ps phenomena, the performed fitting procedure indicates the presence of two additional constituents, whose parameters are presented in Table 9.1, which summarizes all the results acquired for ZnSe QDs samples. The contribution of the two longer processes to the GSB decay is considerably lower than the fast trapping

channels. The third component is characterized by decay times in the range of tens of ps. Such timescales have been previously assigned to electronic transitions from discrete CB electron absorption states to trap levels deeply buried in the forbidden gap (so-called deep traps).[286,287] The fourth ns component attributes for radiative recombination of excited charge carriers. As its contribution is small and the complete recovery of the GSB was not observed within the examined pump-probe delay value, the characteristic times of the radiative recombination could not be accurately derived from TA experiments. The small amplitude obtained for all samples suggests low fluorescence efficiency, which is common for the core-type QDs.[139]

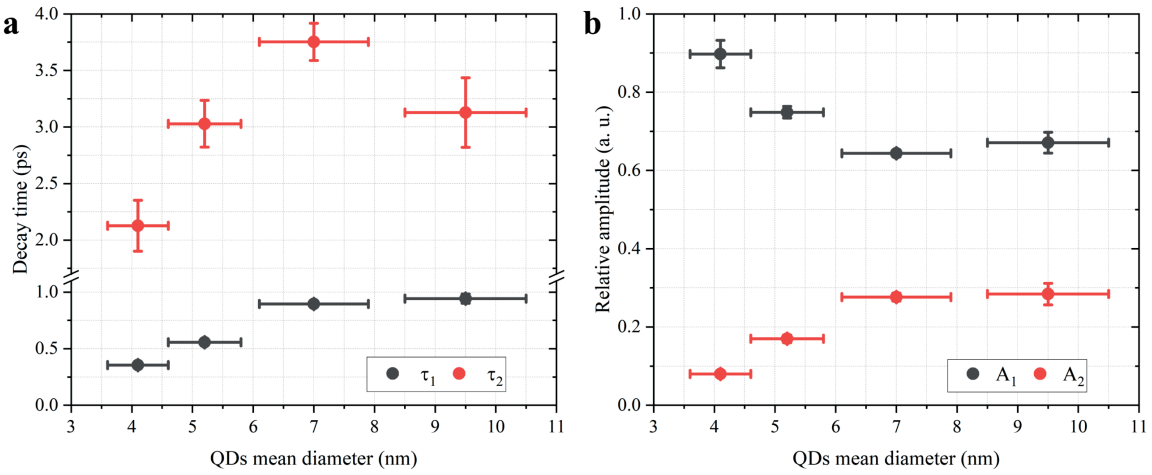

Figure 9.5 *Time constants (a) and fractional amplitudes (b) of the two most intense contributions of the multiexponential fitting of experimental data plotted in the function of QDs mean diameter. The data corresponding to parameters for the fastest and second decay components are marked with grey and red points, respectively.*

Table 9.1 *List of fit parameters derived for ZnSe QDs samples. The amplitude values has been normalized to show the relative contribution of each component (from 0 to 1) for a given sample.*

QDs size [nm]	τ_1 [ps]	A_1	τ_2 [ps]	A_2	τ_3 [ps]	A_3	τ_4	A_4
4.1 (±0.5)	0.36 (±0.02)	0.90 (±0.04)	2.13 (±0.23)	0.08 (±0.01)	27.9 (±6.2)	0.01 (±0.01)	~ ns	0.01 (±0.01)
5.2 (±0.6)	0.56 (±0.02)	0.75 (±0.02)	3.03 (±0.21)	0.17 (±0.01)	41.9 (±3.7)	0.04 (±0.01)	~ ns	0.04 (±0.01)
7.0 (±0.9)	0.90 (±0.02)	0.64 (±0.01)	3.75 (±0.17)	0.28 (±0.01)	30.26 (±1.7)	0.07 (±0.01)	~ ns	< 0.01
9.5 (±1.0)	0.95 (±0.04)	0.67 (±0.03)	3.13 (±0.31)	0.28 (±0.01)	17.56 (±2.8)	0.04 (±0.01)	~ ns	< 0.01

Obtained time constants correlate with literature TA studies of Zn-based and Cd-based QDs. For example, Gogoi et al. determined the surface trapping time of 1 ps for CdS QDs synthesized by a sol-gel method.[288] Li et al. reported a defect-assisted trapping time of 2.9 ps for cysteamine-coated ZnSe QDs.[286] In general, the impact of trap effects in the studied samples was more significant compared to the CdSe QDs regarded as a model

system in the QDs research. This is likely due to the more reactive nature of Zn atoms, which leads to more lattice/surface defects in the material structure. The high contribution of surface effects promotes applications where charge separation is required, like photocatalysis.[289] For more effective radiative recombination, surface passivation with a second semiconductor to create core-shell particles is necessary. However, as presented, the surface states may not be the only source of charge carrier trapping. Thus, core-shell structures with ZnSe applied as either core or shell may still suffer from insufficient fluorescence yields. This observation is consistent with a recent study, which attributed the trapping at bulk Zn vacancies as the main source that decreases photoluminescence intensity in CdSe-ZnSe core-shell QDs.[270] Concurrently, the existence of bulk defects might also be partially responsible for the general trend of lower fluorescence quantum yields for ZnSe-based QDs as compared to CdSe-based systems.

9.3 Conclusions

Conducted TA experiments revealed complex charge carrier dynamics phenomena in the prepared ZnSe QDs suspensions. The kinetic traces analysis of the first absorption state bleach decay indicated two dominant processes that govern the relaxation of excited electrons and holes. The first, more intense, occurring with a characteristic time of 0.36-0.95 ps and accounting for 64-90% of total GSB decay depending on the QDs size, was attributed to surface trapping, based on the observed size-dependent relation of trapping time/amplitude and correlation with the kinetics of broadband PA signal. The second, indicating a 2-3 ps time constant and 8-28% of fractional amplitude does not show a clear size-dependent relation. Previously described Zn K-edge XAS synchrotron experiments point to Zn vacancy as the possible explanation for this additional trapping mechanism. Two additional decay channels (τ_3 ~ 20-40 ps and τ_4 ~ ns) corresponding to deep trapping and radiative recombination showed negligible contribution to charge carrier relaxation.

The obtained results correlate with the literature data regarding the determined decay constants and the presence of Zn vacancies that influence the electronic structure of ZnSe QDs. Simultaneously, acquired results raise questions for future experiments. For instance, the assignment of either holes or electrons as the source of each determined decay process needs to be confirmed. In most studies related to CdSe QDs, the main bleach decay contributions were attributed exclusively to the relaxation of electrons, and the presence of hole contributions has become a hot debate among many researchers.[30,290–293] Determining the role of hole decay in ZnSe QDs may help resolve the controversy in other systems. This could be achieved with supplementary experiments by coupling synthesized QDs to electron/hole scavenger molecules that strip QDs from one carrier type. Additionally, the role of Zn vaccines calls for more studies aimed at determining their position in the bandgap structure of the material and evaluation of their spatial distribution. Photoluminescence measurements conducted at cryogenic temperatures were able to isolate the contribution of Zn vacancies in the PL signal, allowing its detailed time-dependent analysis.[270] Understanding the formation of these defect states may eventually

lead to total control of its synthetic implementation or prevention, providing an additional degree of freedom to tune the optoelectronic properties of ZnSe QDs.

The presented results demonstrated the application of time-resolved techniques to probe effects in the electronic structure of ZnSe QDs. In the future, time-resolved analysis of presented materials can be expanded to X-ray-based approaches, providing element specificity and structural sensitivity, which are lacking in optical spectroscopy techniques. The final chapter will explore the possibility of time-resolved experiments at X-ray free electron lasers with fs or even sub-fs resolution using the novel concept of X-ray Chronoscopy.

10. X-ray Chronoscopy as the potential tool for sub-fs studies of carrier dynamics

In the performed experiments, I used steady-state X-ray spectroscopy methods to understand electronic and structural size-dependent correlations in ZnSe QDs and then time-resolved UV-vis experiments to study the photoinduced charge carrier dynamics. The scientific questions arising from these studies can be complemented with time-resolved X-ray spectroscopy methods as the charge carrier dynamics can be observed with the element- and site-selective sensitivity. This part presents theoretical considerations of time-dependent X-ray experiments at X-ray free electron lasers (XFELs) with single fs or even sub-fs temporal resolution. Here, the goal was to evaluate the capabilities of the recently introduced X-ray Chronoscopy approach to follow electron dynamics in materials at XFELs induced by ultrashort optical pulses, which was conducted through numerical computations, simulating interactions between ultrashort X-ray pulses and matter. The X-ray Chronoscopy might be applied in future ZnSe QDs studies for sub-fs, element-specific investigation of the earliest decay processes. The chapter starts with a brief introduction regarding the current state and limitations of time-resolved X-ray spectroscopy experiments, transitioning to the concept of X-ray Chronoscopy as a complementary approach that potentially addresses some present restrictions. Following, a description of the applied theoretical model and selected parameters for performed simulations is given. The results are presented and discussed in the context of potential applications.

10.1 Time-resolved XFEL experiments

While time-resolved X-ray spectroscopy experiments are successfully conducted at synchrotron and laser-driven sources, currently, XFELs provide the shortest temporal resolution and highest peak brightness. Development of these facilities in the last decade is considered by many as a true revolution in X-ray science,[294,295] already spawning breakthrough results.[296–299]

Among other schemes,[300–302] time-dependent measurements at XFEL are conducted utilizing the pump-probe approach, typical for other techniques such as previously described optical TA. In an exemplary case of transient XAS experiment initially, the ultrashort intense optical pulse excites the sample, inducing temporal electronic or structural modifications in the material. Then, at some defined delay time, the X-ray pulse produced by XFEL probes the current state of the specimen and records it in the transient XAS spectrum. Such a procedure proved to be very successful and currently allows tracking processes in matter with hard X-rays occurring at timescales down to tens of femtoseconds.[303] However, the relevant timescales of fundamental phenomena in matter related to electron motion in molecules and other systems are in order of single femtoseconds or even a few hundred attoseconds, which are right now inaccessible with XFELs.

Two major limiting factors hinder the temporal resolution of a pump-probe experiment at XFEL facilities. The first is determined by the shortest pulse durations of generated X-ray flashes that simultaneously possess sufficient intensity. For hard X-ray energies, the

shortest attainable pulses correspond to ~5 fs full width at half maximum (FWHM). The second restriction arises because of the fluctuation in the arrival time of XFEL pulses, which impedes their accurate synchronization with the optical pump pulse, resulting in so-called timing jitters. The reported timing jitter at the European XFEL facility is in order of 10-25 fs.[303,304]

The above-discussed restrictions of time-resolved experiments can be bypassed to some extent by utilizing an alternative approach referred to as X-ray Chronoscopy, broadening the scope of research at the XFELs.[305] This technique measures time profiles of the X-ray pulses and changes in their temporal structures caused upon interaction with the studied target, shifting from energy-domain spectroscopic measurement to time-domain experiments. Practical implementation of X-ray Chronoscopy at XFELs would require non-invasive temporal characterization of X-ray pulses with fs or sub-fs resolution. While such diagnostic procedures are still under development, this chapter attempts to evaluate the concept capabilities of X-ray Chronoscopy to investigate electron dynamics in an optical pump-X-ray probe experiment. Numerical computations were performed, simulating the interaction of X-ray pulses with an idealized ZnSe QDs sample excited by the ultrashort pump pulse. Based on the calculated time profiles, information on the sample relaxation time was extracted, estimating the expected precision of the X-ray Chronoscopy pump-probe experiment at the XFEL facility.

10.2 Simulation model

Interaction between pump and probe pulses with the target was simulated employing a four-state atom representation, schematically depicted in Fig. 10.1. Each level corresponds to a specific electron configuration of the sample's atoms. In the employed model, pump pulse photons carry energy sufficient to interact exclusively with the outer-shell valance electron of the examined target via the photoabsorption process. Similarly, X-ray (probe photons) energy is defined to match the core 1s state binding energy, maximalizing the probability of their interaction with K-shell electrons. Photoabsorption of a single optical (pump) photon induces a transition in one atom from the initial ground state (state 1) to the higher level (state 2). In such case, the propagation can be described by the time-dependent Lambert-Beer law:

$$dI_{Opt}(x,t) = -I_{Opt}(x,t) \cdot n \cdot N_1(x,t) \cdot \sigma_{1\to2} \cdot dx \qquad (11)$$

where $I_{Opt}(x,t)$ denotes a pump photon flux [$cm^{-2} \cdot s^{-1}$] at the depth x and time t, n is the concentration of absorption centers [cm^{-3}], $N_1(x,t)$ constitutes the average population of ground state atoms at specific x and t, expressed by the dimensionless value from 0 to 1, and $\sigma_{1\to2}$ [cm^2] is the energy-dependent cross section for the 1→2 transition. Target atoms promoted to state 2 will eventually undergo relaxation back to state 1, which occurs after the average time $\tau_{2\to1}$. Excitations of the valence state result in a temporal change of the atom interaction with the X-ray probe pulse. Therefore, the sample X-ray absorption will depend on the current population of ground-state and optically-excited centers:

$$dI_{Xray}(x,t) = -I_{Xray}(x,t) \cdot n \cdot [N_1(x,t) \cdot \sigma_{1\to3} + N_2(x,t) \cdot \sigma_{2\to4}] \cdot dx \qquad (12)$$

$\sigma_{1\to3}$ and $\sigma_{2\to4}$ denote the cross sections for X-ray-induced transitions from unpumped and optically excited atoms. X-ray absorption causes depopulation of state 1 and state 2 (decrease of $N_1(x,t)$ and $N_2(x,t)$) while simultaneously increasing the number of atoms in core-excited state 3 and state 4, represented by $N_3(x,t)$ and $N_4(x,t)$, respectively. The evolution of state occupancies in the considered system can be followed by the set of differential equations:

$$\begin{cases} dN_1(x,t) = [-I_{Opt}(x,t) \cdot N_1(x,t) \cdot \sigma_{1\to2} - I_{Xray}(x,t) \cdot N_1(x,t) \cdot \sigma_{1\to3} + \frac{N_2(x,t)}{\tau_{2\to1}} + \frac{N_3(x,t)}{\tau_{3\to1}} + \frac{N_4(x,t)}{\tau_{4\to1}}] \cdot dt \\ dN_2(x,t) = [I_{Opt}(x,t) \cdot N_1(x,t) \cdot \sigma_{1\to2} - I_{Xray}(x,t) \cdot N_2(x,t) \cdot \sigma_{2\to4} - \frac{N_2(x,t)}{\tau_{2\to1}} + \frac{N_3(x,t)}{\tau_{3\to2}} + \frac{N_4(x,t)}{\tau_{4\to2}}] \cdot dt \\ dN_3(x,t) = \left[I_{Xray}(x,t) \cdot N_1(x,t) \cdot \sigma_{1\to3} - \frac{N_3(x,t)}{\tau_{3\to1}} - \frac{N_3(x,t)}{\tau_{3\to2}} + \frac{N_4(x,t)}{\tau_{4\to3}}\right] \cdot dt \\ N_4(x,t) = 1 - N_1(x,t) - N_2(x,t) - N_3(x,t) \end{cases} \qquad (13)$$

where $\tau_{i\to j}$ is the characteristic relaxation time from state i to lower-energy level j. The last equation guarantees the constant number of states, which preserves the self-consistency of simulations.[306–308]

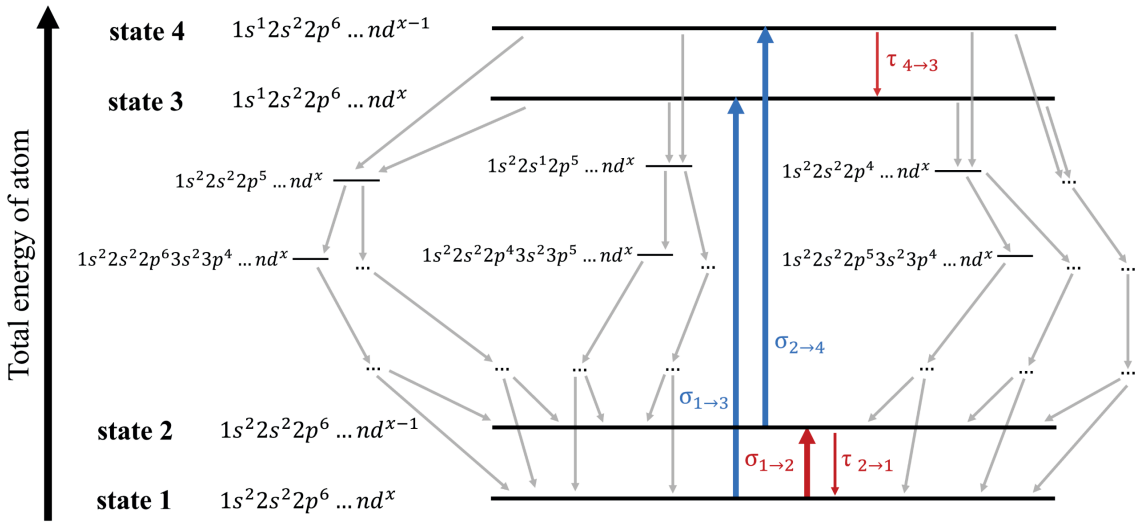

Figure 10.1 *Diagram of the electronic transitions considered in the conducted simulations. Presented states correspond to specific atomic levels with different total energy of the atom. The optically induced excitations and the following relaxation are marked with red arrows. Analogously, the X-ray-induced transitions are denoted as blue arrows. The decay of core-excited states constitutes multiple branched pathways, visualized with grey arrows.*

As shown in Fig. 10.1, the 1s hole state formed upon X-ray absorption undergoes branched and stepwise relaxation, accompanied by the emission of secondary photons of or Auger electrons, creating more additional hole states in the atom's outer shells.[309–311] In the applied model, the lifetimes of X-ray-excited core levels $\tau_{3\to1}$, $\tau_{3\to2}$, $\tau_{4\to1}$, and $\tau_{4\to2}$ account for the complete recovery of the target atom back to its original state, which corresponds to nanosecond timescales.[312] During this decay, the ionization energy of the rapidly filled (~fs) 1s state shifts to higher energies compared to ground-state atoms as

multiple valance holes (by-products of 1s hole relaxation) increase the total energy of the system. Thus, X-rays with energies tuned to the K-edge energy of the ground-state atom cannot excite the same atom until its original state recovers. As such, in the case of XFEL experiments, where ~fs pump and probe pulse durations are utilized, the X-ray excited atom will remain excited long after both pulses pass the sample. The set of equations (13) paired with formulas for pump and probe pulse propagation given by eq. (11) and (12) were utilized to simulate X-ray Chronoscopy pump-probe experiments.

Table 10.1 lists all major parameters selected for the conducted simulations. The ZnSe QDs explored thorough the presented thesis were taken as the target sample. However, it should be emphasized that X-ray Chronoscopy can be applied to any system. The pump parameters were set to 3.1 eV of photon energy, 3.72 μJ pulse energy, and 5 fs FWHM. Such pulses can be produced by the second harmonic generation of Ti:Sapphire laser flash.[313] Low energy X-ray pulses were utilized (0.1 μJ) with photon energies matching the Zn K-edge of Zn^{2+} (9661.5 eV). The simulations were conducted for probe pulse durations (FWHM) from 5 to 100 fs. In the initial tests, Gaussian functions described the optical and X-ray pulse photon temporal distribution. Then, the calculations were expanded by substituting a Gaussian X-ray pulse with a SASE-like spiky profile typical for XFEL experiments. The SASE-like pulses were generated by modifying the Gaussian profiles with a fixed FWHM and intensity, using a simple algorithm that pseudo-randomly alters the point-to-point normal distribution. As a result, a series of spikes were obtained with varying intensity and an average width of 0.2 fs, matching the attainable coherence length of hard XFEL pulses.[314,315] The comparison of exemplary SASE-like pulse with Gaussian profile is presented in Fig. 10.2. In all performed simulations, monochromatic X-ray pulses were assumed, as in other reported works.[316–318] The $\sigma_{1\to2}$ and $\sigma_{1\to3}$ were taken from the literature.[68,319] The $\sigma_{1\to4}$ was determined assuming that the Zn K-edge XAS spectrum of optically-excited atoms blue-shifts by 1.5 eV. The $\tau_{2\to1}$ was fixed to 10 fs. The relaxation times $\tau_{3\to1}$, $\tau_{3\to2}$, $\tau_{4\to1}$, and $\tau_{4\to2}$ were set to 1 ns. The $\tau_{4\to3}$ was also 10 fs, but this parameter contributes negligibly as in the discussed model states 3 and 4 do not interact with either pump or probe pulses. Unless explicitly stated, the pump-probe delay, understood as the distance in the time domain between pump and probe maxima, was 0 fs. Simulations were performed with 0.05 fs timestep (dt), corresponding to $dx = c \times dt$ of 15 nm, where c is the speed of light in vacuum.

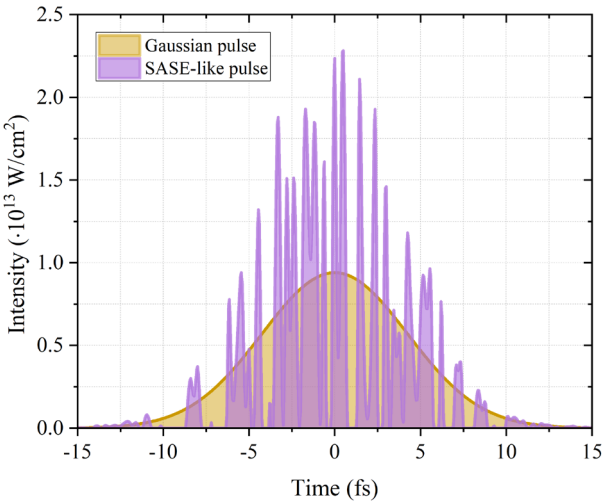

Fig. 10.2 *Comparison of single generated SASE-like pulse with a Gaussian profile. The pulse durations of both pulses were fixed to 10 fs.*

The applied model assumes a single decay pathway of optically-excited state 2 with the 10 fs decay time ($\tau_{2\to1}$). In reality, multiple optically-trigged processes can simultaneously occur, covering timescales from single fs to even ms.[30–35,320,321] This statement is also true for the ZnSe QDs, as shown in previous chapters. The selected lifetime reflects the interest of XFELs' research since other regimes can be successfully investigated by utilizing synchrotrons. The simplified case of a single relaxation channel is sufficient to achieve the goal of this chapter, which is to demonstrate that information regarding electron dynamics in the studied sample can be extracted from temporal structures of X-ray pulses measured in the X-ray Chronoscopy experiment.

Table 10.1. List of parameters utilized for conducted simulations.

Parameter	**Value**
Sample	ZnSe quantum dots
Target atom concentration	$2.20 \cdot 10^{22}$ cm^{-3}
Target thickness	3 µm
$\sigma_{1\to2}$	$1.26 \cdot 10^{-18}$ cm^2
$\sigma_{1\to3}$	$3.34 \cdot 10^{-20}$ cm^2
$\sigma_{2\to4}$	$1.10 \cdot 10^{-20}$ cm^2
$\tau_{2\to1}$ ($\tau_{4\to3}$)	10 fs
$\tau_{3\to1}, \tau_{3\to2}, \tau_{4\to1}, \tau_{4\to2}$	1 ns
Optical pulse energy	3.72 µJ
Optical photon energy	3.10 eV
Optical pulse duration (FWHM)	5 fs
X-ray pulse energy	0.1 µJ
X-ray photon energy	9661.5 eV
X-ray pulse duration (FWHM)	5 – 100 fs
Pump-probe delay	0 fs
Timestep of the simulations	0.05 fs

10.3 Results

Fig 10.3a shows calculated time profiles of the incident Gaussian X-ray probe pulse $I_0(t)$ (blue) and the same pulse after passing through the optically-pumped target $I_{1\ pump\ on}(t)$ (green). The red line denotes the time structure of the optical pump pulse, perfectly synchronized with the X-ray probe (0 fs pump-probe delay). The time envelope of the X-ray probe transmitted through the ground-state specimen $I_{1\ pump\ off}(t)$ (dashed blue) is also included for the comparison. In the case without an applied pump pulse, the Gaussian photon distribution does not change after interaction with the sample since subsequently arriving X-rays are absorbed with the same probability. The absorption of the X-ray pulse becomes more complicated when the optical pump pulse is considered in calculations. Initially, the front of the X-ray pulse, the left side of Fig. 10.3a, interacts with the target similarly, as in the unpumped case. This behavior is because the probe pulse has a broader temporal photon distribution, and the front section of the X-ray pulse reaches the sample before the arrival of the pump. When the optical photons arrive at the target, part of its atoms shifts to state 2, altering their response to X-rays, which increases the probe transmission, as seen in the middle part of Fig. 10.3a. Concurrently, excited atoms begin decaying back to state 1, restoring original X-ray transmission properties. Hence, when the pump pulse exits the target, the last part of the X-ray pulse again matches the ground-state case.

More detailed insight into the temporal evolution of the X-ray absorption coefficient (cross section) is obtained by relating the incident and transmitted pulses analogously to any spectroscopic experiment. Fig. 10.3b presents sample absorption of subsequent parts of the X-ray pulse. Throughout the chapter this plot will be referred to as an X-ray Chronoscopy signal. When the studied target was not excited by the pump pulse (dashed blue line), the X-ray Chronoscopy signal lacked any characteristic features and simply measured the absorption coefficient of the examined target. When the optical excitation preludes the X-ray pulse, the obtained X-ray Chronoscopy signal (green) additionally probes electron population dynamics in the sample equivalently to kinetic traces acquired in TA experiments, discussed in the previous chapter (Fig. 9.4a). However, contrary to TA analysis, in the proposed methodology, the entire dynamics of the studied process can be recovered, in principle, with only a single pump-probe cycle. Crucially, the X-ray Chronoscopy signal and conveyed information regarding carrier dynamics are not affected by the noisy shape of XFEL SASE pulses. This effect is demonstrated in Fig. 10.3c and 10.3d, depicting calculated SASE time structures and their corresponding X-ray Chronoscopy signal. The acquired result is identical to the case with Gaussian profiles. The experimental technique impervious to pulse shape effects is desired for XFEL experiments as the SASE pulses vary from shot to shot in their time structure.

When considering time-resolved experiments at XFELs, one has to account for the timing jitter of the pump-probe arrival time, as it is currently one of the main factors hindering the temporal resolution of the measurement. This effect was investigated with another iteration of simulations originally presented in Fig. 10.3a, this time modifying the pump-probe delay from 0 fs (perfect overlap) to -10 fs (probe before the pump) and +10 fs

(pump before the probe). Fig. 10.4 presents the results for these two delay values. Although the shape of $I_{1\ pump\ on}(t)$ probe pulses changes for various pump-probe delays, the X-ray Chronoscopy signal preserves its shape, with the only noticeable difference being the signal shift along the x-axis, which is an arbitrary time-domain scale, relating the X-ray Chronoscopy signal to the incident X-ray pulse center. This observation has few experimental implications. Predominantly, the timing jitter forces the shot-by-shot data acquisition and further processing of X-ray Chronoscopy measurement. Fortunately, as visualized in Fig. 10.4b and 10.4d, perfect synchronization of pump and probe pulses is not required to extract the information regarding sample relaxation kinetics. If, during a single pump-probe cycle, the overlap between two pulses is attained, the X-ray Chronoscopy signal will capture the atomic decay, including the time zero (t_0) of the studied process, which would allow calibration of the data from subsequent pump-probe cycles. The case when, in a given pump-probe cycle, the pump-probe temporal overlap is not achieved (or the overlap is insufficient) can be identified and rejected from the analysis based on the measured X-ray Chronoscopy signal. However, such cases can be avoided by applying X-ray pulse durations substantially longer than the expected arrival timing jitters, which, according to the available reports, are in order of tens of fs.

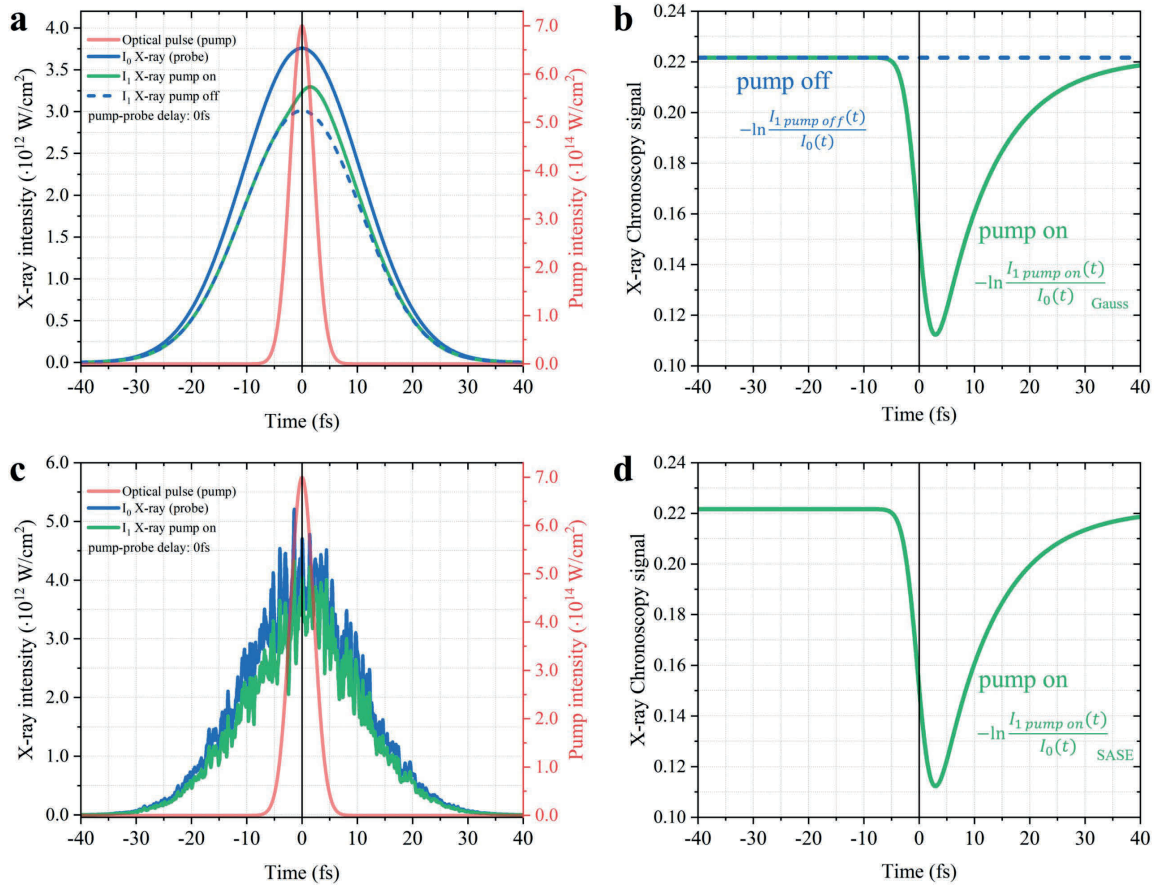

Figure 10.3 *a) Temporal Gaussian profile of the incident X-ray probe pulse ($I_0(t)$) and the envelopes of X-ray pulses transmitted through unpumped ($I_{1\ pump\ off}(t)$) and excited sample ($I_{1\ pump\ on}(t)$). The figure also includes the optical pump pulse (not to scale with X-ray pulses) overlapped with the $I_0(t)$ pulse. The FWHM of the incident X-ray pulse was 25 fs. b) X-ray Chronoscopy signal acquired for Gaussian-like X-ray probe derived as absorption of subsequent parts of the X-ray pulse by the unpumped (blue line) and excited (green line) sample. c) Temporal*

profile of generated SASE-like incident probe pulse and its structure after passing through the pumped target sample. d) X-ray Chronoscopy signal determined for SASE-like pulse (green line).

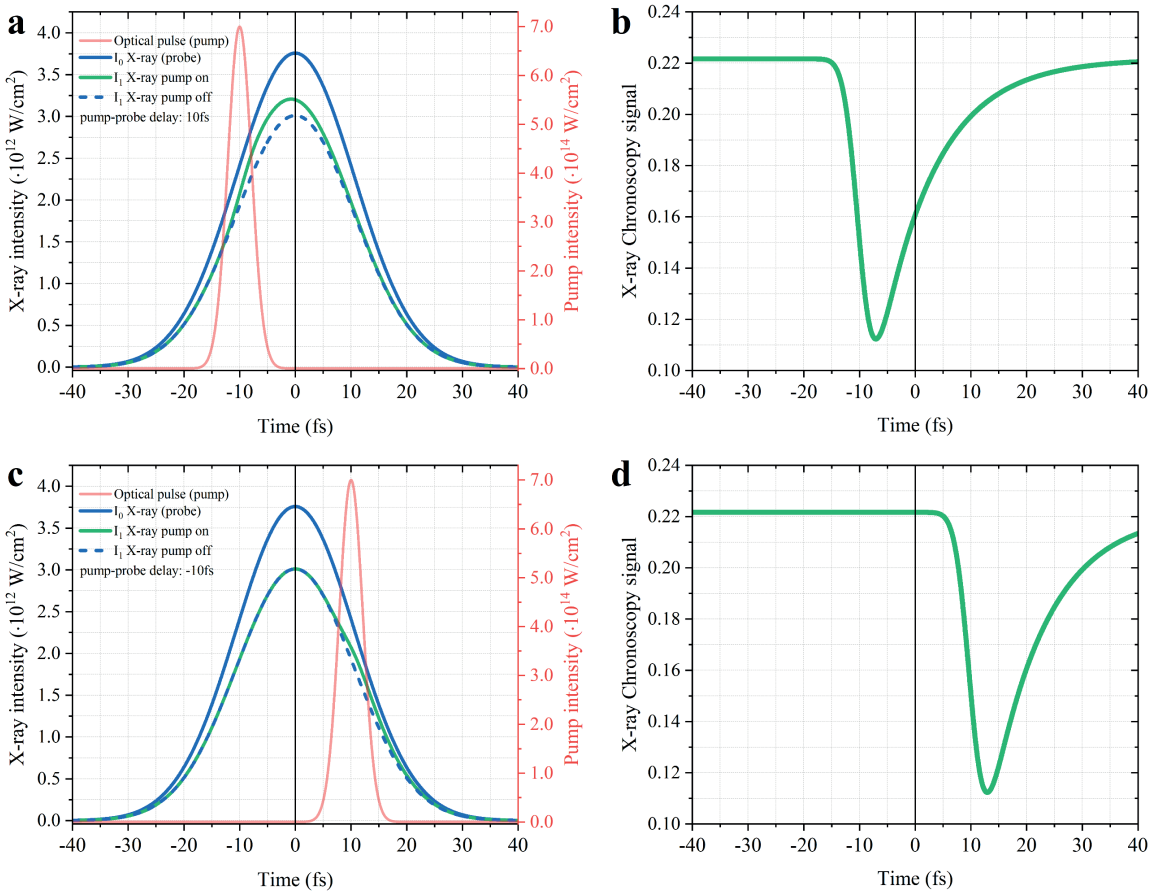

Figure 10.4 *a) Time profiles of X-ray and optical pulses simulated by adjusting the delay between the centers of pump and probe pulses to 10 fs. b) X-ray Chronoscopy signal determined from X-ray pulses shown in (a). c) Temporal profiles of X-ray and optical pulses simulated for -10fs delay between the centers of pump and probe pulses; d) X-ray Chronoscopy signal determined from X-ray pulses presented in (c);*

The above-discussed cases provided a qualitative introduction to the advantages of the X-ray Chronoscopy approach. Further calculations were performed to quantify the method's ability to retrieve the characteristic lifetime of the explored process (here, the relaxation time of the valence state $\tau_{2\to1}$ fixed at 10 fs). Fig. 10.5a presents the X-ray Chronoscopy signal (with subtracted background $I_{1\ pump\ off}(t)$ contribution) obtained for different X-ray pulse durations with SASE-like profiles taking into account statistical counting uncertainty, simulated with 50 pump-probe cycles, 10 % quantum efficiency, and 1 fs time resolution of the detectors. While varying time widths of the probe pulse do not change the shape of the obtained signal (black dots), it drastically influences the point-to-point uncertainty of computed data (color-coded areas). The experimental uncertainty quickly rises for the short X-ray pulses, blurring the information of sample kinetics. On the other hand, longer X-ray pulses expand the usable data range.

To recover the excited decay time $\tau_{2\to1}$, the simulated datasets were fitted with the Gaussian function (pump contribution) convoluted with the exponential decay function, describing the relaxation of target atoms (similarly as in optical TA experiments):

$$S(t) = \frac{2}{FWHM}\sqrt{\frac{\ln 2}{\pi}}\exp\left(-\frac{4\ln 2\,(t-t_0)^2}{FWHM^2}\right) * A \cdot \exp\left(\frac{t}{\tau_{2\to1}}\right) \qquad (14)$$

where t_0 is the pump pulse center, A denotes amplitude of the exponential, and * is a convolution sign. The fitting function, given in eq. (14) shows the impact of the pump pulse on the acquired X-ray Chronoscopy signal. The variations in pump intensity and widths would change the A and FWHM parameters of the fit function. Notably, optical pulses could be transformed into a different profile by well-developed pulse shaping techniques.[322–324] Depending on the pump profile, other fitting functions may be more appropriate to correctly derive the excited state lifetime.

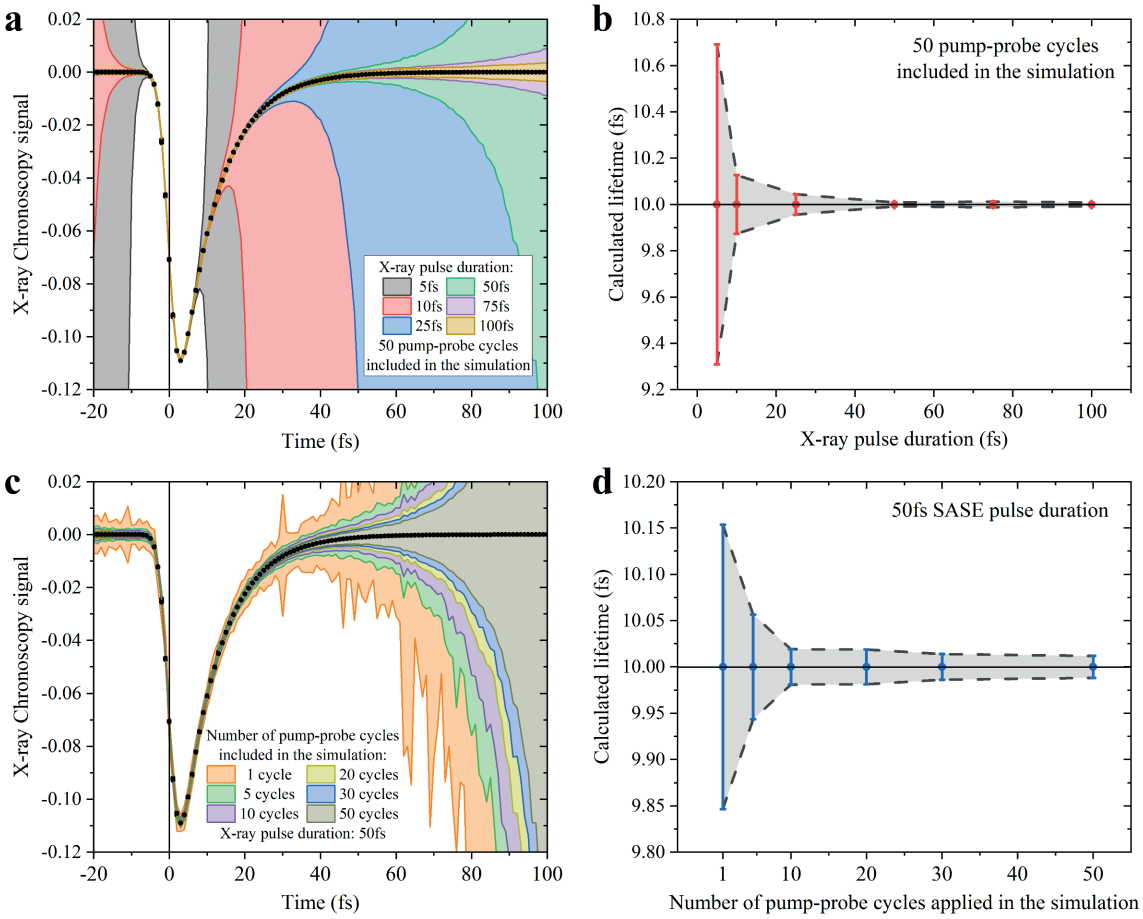

Figure 10.5 a) X-ray Chronoscopy signal acquired by applying 50 pump-probe cycles for different X-ray probe pulse durations. b) Estimation of X-ray Chronoscopy measurement precision evaluated for X-ray probe durations from (a). c) X-ray Chronoscopy signal simulated for 50 fs probe pulse and various numbers of utilized pump-probe cycles. d) X-ray Chronoscopy experiment precision estimated for pump-probe pulse cycle number from (d).

The fits were acquired, fixing the pump pulse FWHM to 5 fs and setting the other parameters as variables. Based on the derived uncertainty of obtained decay constants, the precision of the X-ray Chronoscopy experiment for each of the investigated X-ray pulse durations was calculated, presented in Fig. 10.5b. Results show that the reasonable precision of the determined $\tau_{2\to1}$ is achieved already with X-ray pulse durations comparable to the characteristic lifetime of the studied process. For the wider probe flashes

(50, 75, 100 fs), the simulated uncertainty of the measurement is below 1% when 50 pump-probe cycles are included in the calculations. The computations were also performed with fewer pump-probe cycles for the longer probe pulse (50 fs FWHM). The irregular propagation of the statistical error observed when a single pump-probe sequence is applied results from the SASE spiky profile. The precision of calculated lifetimes, shown in Fig. 10.5d, increases as more pump-probe cycles are integrated and satisfactory results are acquired already with a few applied sequences.

10.4 Conclusions

Conducted simulations revised the potential application of X-ray Chronoscopy to track electron processes in matter induced by ultrashort optical pump pulses. The simple four-state atomic representation adopted in the calculations showed that the information regarding characteristic lifetimes of carrier relaxation could be derived from the temporal structure measurement of the incident and transmitted XFEL pulses. The presented results showcased several advantages of the X-ray Chronoscopy method compared to typical time-resolved pump-probe X-ray spectroscopy experiments. Specifically, the proposed approach enables exploring processes faster than the duration of the probe pulse, bypassing one of the restrictions for time-dependent spectroscopic measurements at XFEL. The specificity of the X-ray Chronoscopy shifts the strict requirement of the ultrashort probe pulse duration to precise measurement of probe temporal structure with, for example, THz streaking methods. Additionally, contrary to pump-probe spectroscopy experiment, where hundreds of pump-probe cycles with strict control of delay are necessary to recover complete kinetics of a studied phenomenon, in X-ray Chronoscopy, the same is possible in principle with only a single pump-probe cycle, provided that X-ray probe pulse is substantially longer (in the time domain) than the explored reaction and the temporal overlap between pump and probe pulses is obtained. On the other hand, it should be remembered that the presented investigation was performed for only one incidence X-ray beam energy. To recover full time-dependent XAS spectrum, an X-ray Chronoscopy and X-ray Spectroscopy methods would have to be combined.

Although X-ray Chronoscopy potentially unlocks new opportunities to access previously unreachable timescales of electron dynamics, its experimental confirmation is still needed. The ongoing development of various sophisticated procedures to measure time profiles of XFEL pulses[318,325,326] every year brings the X-ray Chronoscopy a little closer to realization. For the ZnSe QDs explored in this work, X-ray Chronoscopy would allow accessing the first stages of electron-hole pairs population dynamics essential for expanding fundamental knowledge of nanoscale physics and optimizing the design of advanced optoelectronic devices.

11. Summary

In the thesis, the size-dependent effects on the electronic structure of ZnSe QDs were investigated through a combination of optical and X-ray spectroscopy techniques. Based on the applied wet chemical heat-up approach, a series of QDs samples with mean particle size ranging from 4.1 (±0.5) nm to 9.5 (±1.0) nm were prepared, corresponding to deliver controlled optical bandgap energies of the material in the range 3.02-2.83 eV. The derived size-dependent relation between QDs diameter and its bandgap energy was consistent with experimental and theoretical studies reported by other groups on other QDs systems.

The Zn K-edge XAS and Zn Kα XES conducted utilizing the laboratory-based von Hámos X-ray spectrometer showed structural and chemical differences in the obtained QDs X-ray spectra compared to bulk ZnSe that were initially ascribed to defects states, influencing coordination environment of zinc atoms. Notably, up to now, the attention of laboratory-based X-ray spectroscopy studies has been focused predominantly only on the analysis of reference materials or concentrated powder samples. The work presented in this thesis extended the application scope of in-house equipment to more demanding systems such as liquid suspensions of synthesized in low-amounts nanostructures. This was achieved owing to the developed specialized microliter-stirred sample cell that enabled long-lasting experiments of nanomaterial suspensions, maintaining its physical stability during measurements. Such instrumentation could be applied to other liquid systems to investigate in-situ various chemical processes. Comparison with the synchrotron measurements confirmed the reliability of the in-house instrumentation and approved its full applicability to conduct projects where sample screening or immediate control of synthesis procedures is necessary.

The Zn K-edge XAS experiments at the SOLARIS synchrotron facility revealed more subtle, as compared to lab-based experiments, features in the absorption spectra of studied ZnSe QDs. Conducted FEFF 9.6 calculations indicated the presence of Zn vacancies as the dominant source of structural changes in the nanometer ZnSe relative to bulk-like powder. Notably, the FEFF 9.6 simulations were not able to identify the origin of the chemical size-dependent effect observed in certain energy ranges of the XAS difference signal, partially due to inaccuracies in the calculated model spectrum compared to the experimentally measured data. The chemical shift in QDs XAS spectra could result from a few overlapping factors, such as the quantum confinement effect, surface contribution, or other defects that alter the oxidation state of central Zn atoms. This matter may be clarified in the future with time-dependent XAS and X-ray diffraction experiments designed to follow in-situ the process of QDs synthesis. In principle, such studies could be realized by modification of the developed microliter-stirred cell.

Ultrafast optical TA measurements at the ELI Beamlines facility allowed the determination of the decay channels of excited band-edge carriers in examined QDs materials. Based on the performed femtosecond pump-probe experiments, two dominant carrier relaxation pathways were discovered. The first was attributed to surface trapping, while the second arose because of trapping at defects sites. The obtained results align with the synchrotron Zn K-edge XAS experiments suggesting the Zn vaccines as a major size-dependent contribution. This observation is in pair with recent literature regarding the role

of Zn vacancies in Zn-based QDs systems. Two additional minor components of the GSB decay were assigned to deep trapping and radiative recombination. However, their combined impacts were significantly less pronounced than the two major processes. Future work should be focused on discriminating the electron and hole contributions in the four determined decay channels. Moreover, the separation of surface effects from other relaxation phenomena may be achieved by passivation of ZnSe QDs with a wider bandgap material. This approach would confine both charge carriers in the ZnSe core, allowing selective studies of in-lattice processes. The controlled implementation of Zn vacancies into the QDs lattice would be beneficial for photocatalytic applications. Few studies[327,328] demonstrated that abundant Zn vacancies in other Zn-based systems enhance photocatalytic H_2 evolution, which is believed to serve as a clean energy supply in the future.

In the final part of the presented work, the concept of X-ray Chronoscopy was introduced as a potential future methodology to investigate sub-fs electron dynamics in ZnSe QDs samples, bypassing some technical restrictions of conventional time-resolved XFEL experiments. Conducted numerical calculations, simulating the interaction of X-ray pulses with the target excited by the ultrashort optical pump flash, showcased the advantages over typical pump-probe spectroscopy experiments when studying dynamical processes in matter. Based on the performed simulations, the expected precision of X-ray Chronoscopy measurements at XFEL was evaluated. If successfully realized, the X-ray Chronoscopy may be utilized for element-specific and structural-sensitive time-resolved studies of ZnSe QDs, capturing their first stages of carrier relaxation phenomena.

Overall, the results acquired in the presented thesis contribute to the current initiatives aimed at introducing ZnSe QDs into real-life applications. These would require integrating prepared materials into more advanced structures. For example, by coupling the ZnSe QDs to the plasmonic NPs, a multifunctional hybrid system may be obtained. A size-dependent behavior of both nanomaterials would significantly extend the tunability degree of optical properties of such hybrid material, selectively enhancing absorption or emission or promoting new charge transfer pathways. Based on the alignment of absorption and emission band of ZnSe QDs, plasmonic Ag NPs would constitute the most optimal choice for ZnSe QDs – plasmonic NPs system design. Potential applications of these structures involve bioimaging, energy conversion, and sensing.

References

(1) Fanselow, R.; Sobstel, M.; Błachucki, W.; Szlachetko, J. Performance of a Laboratory von Hámos Type X-Ray Spectrometer in x-Ray Absorption Spectroscopy Study on 3d Group Metals. *X-Ray Spectrom.* **2023**, *52* (5), 247–253. https://doi.org/10.1002/xrs.3317.

(2) Fanselow, R.; Wach, A.; Błachucki, W.; Szlachetko, J. Microliter-Stirred Sample Setup for X-Ray Spectroscopy Analysis of Nanomaterials in Suspension. *Spectrochim. Acta - Part B At. Spectrosc.* **2022**, *189* (December 2021). https://doi.org/10.1016/j.sab.2022.106367.

(3) Klingshirn, C. F. *Semiconductor Optics*, 4th ed.; Springer Berlin, Heidelberg, 2012. https://doi.org/10.1007/978-3-642-28362-8.

(4) Koch, S. W.; Kira, M.; Khitrova, G.; Gibbs, H. M. Semiconductor Excitons in New Light. *Nat. Mater.* **2006**, *5*, 523–531. https://doi.org/https://doi.org/10.1038/nmat1658.

(5) Smyder, J. A.; Krauss, T. D. Coming Attractions for Semiconductor Quantum Dots. *Mater. Today* **2011**, *14* (9), 382–387. https://doi.org/10.1016/S1369-7021(11)70182-1.

(6) Mohamed, W. A. A.; Abd El-Gawad, H.; Mekkey, S.; Galal, H.; Handal, H.; Mousa, H.; Labib, A. Quantum Dots Synthetization and Future Prospect Applications. *Nanotechnol. Rev.* **2021**, *10* (1), 1926–1940. https://doi.org/10.1515/ntrev-2021-0118.

(7) Kambhampati, P. Nanoparticles, Nanocrystals, and Quantum Dots: What Are the Implications of Size in Colloidal Nanoscale Materials? *J. Phys. Chem. Lett.* **2021**, *12* (20), 4769–4779. https://doi.org/10.1021/acs.jpclett.1c00754.

(8) Baig, N.; Kammakakam, I.; Falath, W.; Kammakakam, I. Nanomaterials: A Review of Synthesis Methods, Properties, Recent Progress, and Challenges. *Mater. Adv.* **2021**, *2* (6), 1821–1871. https://doi.org/10.1039/d0ma00807a.

(9) Boholm, M.; Arvidsson, R. A Definition Framework for the Terms Nanomaterial and Nanoparticle. *Nanoethics* **2016**, *10* (1), 25–40. https://doi.org/10.1007/s11569-015-0249-7.

(10) Klaessig, F. Current Perspectives in Nanotechnology Terminology and Nomenclature. In *Nanotechnology Standards. Nanostructure Science and Technology*; Murashov, V., Howard, J., Eds.; Springer, New York, NY, 2011. https://doi.org/10.1007/978-1-4419-7853-0_2.

(11) Montanarella, F.; Kovalenko, M. V. Three Millennia of Nanocrystals. *ACS Nano* **2022**, *16* (4), 5085–5102. https://doi.org/10.1021/acsnano.1c11159.

(12) Joudeh, N.; Linke, D. Nanoparticle Classification, Physicochemical Properties, Characterization, and Applications: A Comprehensive Review for Biologists. *J. Nanobiotechnology* **2022**, *20* (1), 1–29. https://doi.org/10.1186/s12951-022-01477-8.

(13) Geoffrion, L. D.; Guisbiers, G. Quantum Confinement: Size on the Grill! *J. Phys. Chem. Solids* **2020**, *140* (November 2019). https://doi.org/10.1016/j.jpcs.2019.109320.

(14) Efros, A. L.; Efros, A. L. Interband Light Absorption in Semiconductor Spheres. *Sov. Phys. Semicond.* **1982**, *16* (7), 772–775.

(15) Brus, L. E. Electron-Electron and Electron-Hole Interactions in Small Semiconductor Crystallites: The Size Dependence of the Lowest Excited Electronic State. *J. Chem. Phys.* **1984**, *80* (9), 4403–4409. https://doi.org/10.1063/1.447218.

(16) Brus, L. Electronic Wave Functions in Semiconductor Clusters: Experiment and Theory. *J. Phys. Chem.* **1986**, *90* (12), 2555–2560. https://doi.org/10.1021/j100403a003.

(17) Pietryga, J. M.; Park, Y. S.; Lim, J.; Fidler, A. F.; Bae, W. K.; Brovelli, S.; Klimov, V. I. Spectroscopic and Device Aspects of Nanocrystal Quantum Dots. *Chem. Rev.* **2016**, *116* (18), 10513–10622. https://doi.org/10.1021/acs.chemrev.6b00169.

(18) Klimov, V. I. Nanocrystal Quantum Dots From Fundamental Photophysics to Multicolor Lasing. Los Alamos National Laboratory 2003.

(19) Klimov, V. I. Optical Nonlinearities and Ultrafast Carrier Dynamics in Semiconductor Nanocrystals. *J. Phys. Chem. B* **2000**, *104* (26), 6112–6123. https://doi.org/10.1021/jp9944132.

(20) Qenawy, M. Ultrafast Photoinduced Processes in Core and Core–Shell Quantum Dots for Solar Cell Applications "Tiny Crystals for Big Applications," Lund University, 2015.

(21) Bagga, A.; Chattopadhyay, P. K.; Ghosh, S. Stokes Shift in Quantum Dots: Origin of Dark Exciton. *Proc. 14th Int. Work. Phys. Semicond. Devices, IWPSD* **2007**, No. iii, 876–879. https://doi.org/10.1109/IWPSD.2007.4472661.

(22) Nirmal, M.; Norris, D. J.; Kuno, M.; Bawendi, M. G.; Efros, A. L.; Rosen, M. Observation of the "Dark Exciton" in CdSe Quantum Dots. *Phys. Rev. Lett.* **1995**, *75* (20), 3728–3731. https://doi.org/10.1103/PhysRevLett.75.3728.

(23) Resch-Genger, U.; Grabolle, M.; Cavaliere-Jaricot, S.; Nitschke, R.; Nann, T. Quantum Dots versus Organic Dyes as Fluorescent Labels. *Nat. Methods* **2008**, *5* (9), 763–775. https://doi.org/10.1038/nmeth.1248.

(24) Goldman, E. R.; Clapp, A. R.; Anderson, G. P.; Uyeda, H. T.; Mauro, J. M.; Medintz, I. L.; Mattoussi, H. Multiplexed Toxin Analysis Using Four Colors of Quantum Dot Fluororeagents. *Anal. Chem.* **2004**, *76* (3), 684–688. https://doi.org/10.1021/ac035083r.
(25) Shekhawat, D.; Vauth, M.; Pezoldt, J. Size Dependent Properties of Reactive Materials. *Inorganics* **2022**, *10* (4). https://doi.org/10.3390/inorganics10040056.
(26) Roduner, E. Size Matters: Why Nanomaterials Are Different. *Chem. Soc. Rev.* **2006**, *35* (7), 583–592. https://doi.org/10.1039/b502142c.
(27) Pu, C.; Qin, H.; Gao, Y.; Zhou, J.; Wang, P.; Peng, X. Synthetic Control of Exciton Behavior in Colloidal Quantum Dots. *J. Am. Chem. Soc.* **2017**, *139* (9), 3302–3311. https://doi.org/10.1021/jacs.6b11431.
(28) Harvie, A. J.; Smith, C. T.; Ahumada-Lazo, R.; Jeuken, L. J. C.; Califano, M.; Bon, R. S.; Hardman, S. J. O.; Binks, D. J.; Critchley, K. Ultrafast Trap State-Mediated Electron Transfer for Quantum Dot Redox Sensing. *J. Phys. Chem. C* **2018**, *122* (18), 10173–10180. https://doi.org/10.1021/acs.jpcc.8b02551.
(29) Nanda, S.; Nanda, K. K. Identifying the Accuracy of Various Approaches for Determining the Fraction of Surface Atoms in a Nanoparticle to Deepen Students' Understanding of Size-Dependent Properties. *J. Chem. Educ.* **2021**, *98* (6), 1982–1987. https://doi.org/10.1021/acs.jchemed.0c01247.
(30) Brosseau, P. J.; Geuchies, J. J.; Jasrasaria, D.; Houtepen, A. J.; Rabani, E.; Kambhampati, P. Ultrafast Hole Relaxation Dynamics in Quantum Dots Revealed by Two-Dimensional Electronic Spectroscopy. *Commun. Phys.* **2023**, *6* (1), 1–9. https://doi.org/10.1038/s42005-023-01169-1.
(31) Lou, Y.; Chen, X.; Samia, A. C.; Burda, C. Femtosecond Spectroscopic Investigation of the Carrier Lifetimes in Digenite Quantum Dots and Discrimination of the Electron and Hole Dynamics via Ultrafast Interfacial Electron Transfer. *J. Phys. Chem. B* **2003**, *107* (45), 12431–12437. https://doi.org/10.1021/jp035618k.
(32) Ginger, D. S.; Dhoot, A. S.; Finlayson, C. E.; Greenham, N. C. Long-Lived Quantum-Confined Infrared Transitions in CdSe Nanocrystals. *Appl. Phys. Lett.* **2000**, *77* (18), 2816–2818. https://doi.org/10.1063/1.1322369.
(33) Shim, M.; Shilov, S. V.; Braiman, M. S.; Guyot-Sionnest, P. Long-Lived Delocalized Electron States in Quantum Dots: A Step-Scan Fourier Transform Infrared Study. *J. Phys. Chem. B* **2000**, *104* (7), 1494–1496. https://doi.org/10.1021/jp994107o.
(34) Wheeler, D. A.; Zhang, J. Z. Exciton Dynamics in Semiconductor Nanocrystals. *Adv. Mater.* **2013**, *25* (21), 2878–2896. https://doi.org/10.1002/adma.201300362.
(35) Keene, J. D.; Freymeyer, N. J.; McBride, J. R.; Rosenthal, S. J. Ultrafast Spectroscopy Studies of Carrier Dynamics in Semiconductor Nanocrystals. *iScience* **2022**, *25* (2), 103831. https://doi.org/10.1016/j.isci.2022.103831.
(36) Kambhampati, P. Unraveling the Structure and Dynamics of Excitons in Semiconductor Quantum Dots. *Acc. Chem. Res.* **2011**, *44* (1), 1–13. https://doi.org/10.1021/ar1000428.
(37) Melnychuk, C.; Guyot-Sionnest, P. Multicarrier Dynamics in Quantum Dots. *Chem. Rev.* **2021**, *121* (4), 2325–2372. https://doi.org/10.1021/acs.chemrev.0c00931.
(38) Yang, Z.; Gao, M.; Wu, W.; Yang, X.; Sun, X. W.; Zhang, J.; Wang, H. C.; Liu, R. S.; Han, C. Y.; Yang, H.; Li, W. Recent Advances in Quantum Dot-Based Light-Emitting Devices: Challenges and Possible Solutions. *Mater. Today* **2019**, *24* (April), 69–93. https://doi.org/10.1016/j.mattod.2018.09.002.
(39) Pietryga, J. M.; Zhuravlev, K. K.; Whitehead, M.; Klimov, V. I.; Schaller, R. D. Evidence for Barrierless Auger Recombination in PbSe Nanocrystals: A Pressure-Dependent Study of Transient Optical Absorption. *Phys. Rev. Lett.* **2008**, *101* (21), 1–4. https://doi.org/10.1103/PhysRevLett.101.217401.
(40) Robel, I.; Gresback, R.; Kortshagen, U.; Schaller, R. D.; Klimov, V. I. Universal Size-Dependent Trend in Auger Recombination in Direct-Gap and Indirect-Gap Semiconductor Nanocrystals. *Phys. Rev. Lett.* **2009**, *102* (17), 1–4. https://doi.org/10.1103/PhysRevLett.102.177404.
(41) Dyakonov, M. I.; Kachorovskii, V. Y. Nonthreshold Auger Recombination in Quantum Wells. *Phys. Rev. B* **1994**, *49* (24), 17130–17138. https://doi.org/10.1103/PhysRevB.49.17130.
(42) Philbin, J. P.; Rabani, E. Electron-Hole Correlations Govern Auger Recombination in Nanostructures. *Nano Lett.* **2018**, *18* (12), 7889–7895. https://doi.org/10.1021/acs.nanolett.8b03715.
(43) Klimov, V. I. Multicarrier Interactions in Semiconductor Nanocrystals in Relation to the Phenomena of Auger Recombination and Carrier Multiplication. *Annu. Rev. Condens. Matter Phys.* **2014**, *5* (1), 285–316. https://doi.org/10.1146/annurev-conmatphys-031113-133900.
(44) Schaller, R. D.; Klimov, V. I. High Efficiency Carrier Multiplication in PbSe Nanocrystals: Implications for Solar Energy Conversion. *Phys. Rev. Lett.* **2004**, *92* (18), 1–4. https://doi.org/10.1103/PhysRevLett.92.186601.

(45) Ellingson, R. J.; Beard, M. C.; Johnson, J. C.; Yu, P.; Micic, O. I.; Nozik, A. J.; Shabaev, A.; Efros, A. L. Highly Efficient Multiple Exciton Generation in Colloidal PbSe and PbS Quantum Dots. *Nano Lett.* **2005**, *5* (5), 865–871. https://doi.org/10.1021/nl0502672.
(46) Cooney, R. R.; Sewall, S. L.; Dias, E. A.; Sagar, D. M.; Anderson, K. E. H.; Kambhampati, P. Unified Picture of Electron and Hole Relaxation Pathways in Semiconductor Quantum Dots. *Phys. Rev. B* **2007**, *75*, 1–14. https://doi.org/10.1103/PhysRevB.75.245311.
(47) Alizadeh-Ghodsi, M.; Pourhassan-Moghaddam, M.; Zavari-Nematabad, A.; Walker, B.; Annabi, N.; Akbarzadeh, A. State-of-the-Art and Trends in Synthesis, Properties, and Application of Quantum Dots-Based Nanomaterials. *Part. Part. Syst. Charact.* **2019**, *36* (2), 1–20. https://doi.org/10.1002/ppsc.201800302.
(48) Abid, N.; Khan, A. M.; Shujait, S.; Chaudhary, K.; Ikram, M.; Imran, M.; Haider, J.; Khan, M.; Khan, Q.; Maqbool, M. Synthesis of Nanomaterials Using Various Top-down and Bottom-up Approaches, Influencing Factors, Advantages, and Disadvantages: A Review. *Adv. Colloid Interface Sci.* **2022**, *300* (December 2021). https://doi.org/10.1016/j.cis.2021.102597.
(49) Polte, J. Fundamental Growth Principles of Colloidal Metal Nanoparticles - a New Perspective. *CrystEngComm* **2015**, *17* (36), 6809–6830. https://doi.org/10.1039/c5ce01014d.
(50) Wu, K. J.; Tse, E. C. M.; Shang, C.; Guo, Z. Nucleation and Growth in Solution Synthesis of Nanostructures – From Fundamentals to Advanced Applications. *Prog. Mater. Sci.* **2022**, *123*, 100821. https://doi.org/10.1016/j.pmatsci.2021.100821.
(51) Thanh, N. T. K.; Maclean, N.; Mahiddine, S. Mechanisms of Nucleation and Growth of Nanoparticles in Solution. *Chem. Rev.* **2014**, *114* (15), 7610–7630. https://doi.org/10.1021/cr400544s.
(52) Van Embden, J.; Sader, J. E.; Davidson, M.; Mulvaney, P. Evolution of Colloidal Nanocrystals: Theory and Modeling of Their Nucleation and Growth. *J. Phys. Chem. C* **2009**, *113* (37), 16342–16355. https://doi.org/10.1021/jp9027673.
(53) Reiss, H. The Growth of Uniform Colloidal Dispersions. *J. Chem. Phys.* **1951**, *19* (4), 482–487. https://doi.org/10.1063/1.1748251.
(54) Peng, X.; Wickham, J.; Alivisatos, A. P. Kinetics of II-VI and III-V Colloidal Semiconductor Nanocrystal Growth : " Focusing " of Size Distributions. *J. Am. Chem. Soc.* **1998**, *7863* (98), 5343–5344. https://doi.org/10.1021/ja9805425.
(55) Yin, Y.; Alivisatos, A. P. Colloidal Nanocrystal Synthesis and the Organic-Inorganic Interface. *Nature* **2005**, *437* (7059), 664–670. https://doi.org/10.1038/nature04165.
(56) Abe, S.; Čapek, R. K.; De Geyter, B.; Hens, Z. Tuning the Postfocused Size of Colloidal Nanocrystals by the Reaction Rate: From Theory to Application. *ACS Nano* **2012**, *6* (1), 42–53. https://doi.org/10.1021/nn204008q.
(57) De Roo, J. The Surface Chemistry of Colloidal Nanocrystals Capped by Organic Ligands. *Chem. Mater.* **2023**, *35* (10), 3781–3792. https://doi.org/10.1021/acs.chemmater.3c00638.
(58) Van Embden, J.; Chesman, A. S. R.; Jasieniak, J. J. The Heat-up Synthesis of Colloidal Nanocrystals. *Chem. Mater.* **2015**, *27* (7), 2246–2285. https://doi.org/10.1021/cm5028964.
(59) Jain, V.; Roy, S.; Roy, P.; Pillai, P. P. When Design Meets Function: The Prodigious Role of Surface Ligands in Regulating Nanoparticle Chemistry †. *Chem. Mater.* **2022**, *34* (17), 7579–7597. https://doi.org/10.1021/acs.chemmater.2c01941.
(60) De Mello Donegá, C.; Liljeroth, P.; Vanmaekelbergh, D. Physicochemical Evaluation of the Hot-Injection Method, a Synthesis Route for Monodisperse Nanocrystals. *Small* **2005**, *1* (12), 1152–1162. https://doi.org/10.1002/smll.200500239.
(61) Kwon, S. G.; Hyeon, T. Formation Mechanisms of Uniform Nanocrystals via Hot-Injection and Heat-up Methods. *Small* **2011**, *7* (19), 2685–2702. https://doi.org/10.1002/smll.201002022.
(62) Farkhani, S. M.; Valizadeh, A. Review: Three Synthesis Methods of CdX (X = Se, S or Te) Quantum Dots. *IET Nanobiotechnology* **2014**, *8* (2), 59–76. https://doi.org/10.1049/iet-nbt.2012.0028.
(63) Kwon, S. G. U.; Hyeon, T. Colloidal Chemical Synthesis and Formation Kinetics of Uniformly Sized Nanocrystals of Metals, Oxides, and Chalcogenides. *Acc. Chem. Res.* **2008**, *41* (12). https://doi.org/10.1021/ar8000537.
(64) Giroux, M. S.; Zahra, Z.; Salawu, O. A.; Burgess, R. M.; Ho, K. T.; Adeleye, A. S. Assessing the Environmental Effects Related to Quantum Dot Structure, Function, Synthesis and Exposure†‡. *Environ. Sci. Nano* **2021**, *9* (3), 867–910. https://doi.org/10.1039/d1en00712b.
(65) Kuno, M. Colloidal Quantum Dots: A Model Nanoscience System. *J. Phys. Chem. Lett.* **2013**, *4* (4), 680. https://doi.org/10.1021/jz400036r.
(66) Rossetti, R.; Nakahara, S.; Brus, L. E. Quantum Size Effects in the Redox Potentials, Resonance Raman Spectra, and Electronic Spectra of CdS Crystallites in Aqueous Solution. *J. Chem. Phys.* **1983**, *79* (2), 1086–1088. https://doi.org/10.1063/1.445834.
(67) Murray, C. B.; Norris, D. J.; Bawendi, M. G. Synthesis and Characterization of Nearly Monodisperse

CdE (E = S, Se, Te) Semiconductor Nanocrystallites. *J. Am. Chem. Soc.* **1993**, *115* (19), 8706–8715. https://doi.org/10.1021/ja00072a025.

(68) Toufanian, R.; Zhong, X.; Kays, J. C.; Saeboe, A. M.; Dennis, A. M. Correlating ZnSe Quantum Dot Absorption with Particle Size and Concentration. *Chem. Mater.* **2021**, *33* (18), 7527–7536. https://doi.org/10.1021/acs.chemmater.1c02501.

(69) Harrison, M. T.; Kershaw, S. V.; Burt, M. G.; Rogach, A. L.; Kornowski, A.; Eychmüller, A.; Weller, H.; Rogach, A. L. Colloidal Nanocrystals for Telecommunications. Complete Coverage of the Low-Loss Fiber Windows by Mercury Telluride Quantum Dot. *Pure Appl. Chem.* **2000**, *72* (1–2), 295–307. https://doi.org/10.1351/pac200072010295.

(70) Hamanaka, Y.; Ogawa, T.; Tsuzuki, M.; Kuzuya, T. Photoluminescence Properties and Its Origin of AgInS2 Quantum Dots with Chalcopyrite Structure. *J. Phys. Chem. C* **2011**, *115* (5), 1786–1792. https://doi.org/10.1021/jp110409q.

(71) Donegá, C. D. M.; Koole, R. Size Dependence of the Spontaneous Emission Rate and Absorption Cross Section of CdSe and CdTe Quantum Dots. *J. Phys. Chem. C* **2009**, *113* (16), 6511–6520. https://doi.org/10.1021/jp811329r.

(72) Straus, D. B.; Cava, R. J. Tuning the Band Gap in the Halide Perovskite CsPbBr3through Sr Substitution. *ACS Appl. Mater. Interfaces* **2022**, *14* (30), 34884–34890. https://doi.org/10.1021/acsami.2c09275.

(73) Xia, C.; Wu, W.; Yu, T.; Xie, X.; Van Oversteeg, C.; Gerritsen, H. C.; De Mello Donega, C. Size-Dependent Band-Gap and Molar Absorption Coefficients of Colloidal CuInS2 Quantum Dots. *ACS Nano* **2018**, *12* (8), 8350–8361. https://doi.org/10.1021/acsnano.8b03641.

(74) Almeida, G.; van der Poll, L.; Evers, W. H.; Szoboszlai, E.; Vonk, S. J. W.; Rabouw, F. T.; Houtepen, A. J. Size-Dependent Optical Properties of InP Colloidal Quantum Dots. *Nano Lett.* **2023**. https://doi.org/10.1021/acs.nanolett.3c02630.

(75) Moreels, I.; Lambert, K.; Smeets, D.; De Muynck, D.; Nollet, T.; Martins, J. C.; Vanhaecke, F.; Vantomme, A.; Delerue, C.; Allan, G.; Hens, Z. Size-Dependent Optical Properties of Colloidal PbS Quantum Dots. *ACS Nano* **2009**, *3* (10), 3023–3030. https://doi.org/10.1021/nn900863a.

(76) Moreels, I.; Lambert, K.; De Muynck, D.; Vanhaecke, F.; Poelman, D.; Martins, J. C.; Allan, G.; Hens, Z. Composition and Size-Dependent Extinction Coefficient of Colloidal PbSe Quantum Dots. *Chem. Mater.* **2007**, *19* (25), 6101–6106. https://doi.org/10.1021/cm071410q.

(77) Kuno, M.; Gushchina, I.; Toso, S.; Trepalin, V. No One Size Fits All: Semiconductor Nanocrystal Sizing Curves. *J. Phys. Chem. C* **2022**, *126* (29), 11867–11874. https://doi.org/10.1021/acs.jpcc.2c04734.

(78) Kang, I.; Wise, F. W. Electronic Structure and Optical Properties of PbS and PbSe Quantum Dots. *J. Opt. Soc. Am. B* **1997**, *14* (7), 1632. https://doi.org/10.1364/josab.14.001632.

(79) Liu, Y.; Li, F.; Shi, G.; Liu, Z.; Lin, X.; Shi, Y.; Chen, Y.; Meng, X.; Lv, Y.; Deng, W.; Pan, X.; Ma, W. PbSe Quantum Dot Solar Cells Based on Directly Synthesized Semiconductive Inks. *ACS Energy Lett.* **2020**, *5* (12), 3797–3803. https://doi.org/10.1021/acsenergylett.0c02011.

(80) Yue, L.; Li, J.; Qi, Y.; Chen, J.; Wang, X.; Cao, J. Auger Recombination and Carrier-Lattice Thermalization in Semiconductor Quantum Dots under Intense Excitation. *Nano Lett.* **2023**, *23* (7), 2578–2585. https://doi.org/10.1021/acs.nanolett.2c04804.

(81) Huang, H.; Bodnarchuk, M. I.; Kershaw, S. V.; Kovalenko, M. V.; Rogach, A. L. Lead Halide Perovskite Nanocrystals in the Research Spotlight: Stability and Defect Tolerance. *ACS Energy Lett.* **2017**, *2* (9), 2071–2083. https://doi.org/10.1021/acsenergylett.7b00547.

(82) Protesescu, L.; Yakunin, S.; Bodnarchuk, M. I.; Krieg, F.; Caputo, R.; Hendon, C. H.; Yang, R. X.; Walsh, A.; Kovalenko, M. V. Nanocrystals of Cesium Lead Halide Perovskites (CsPbX3, X = Cl, Br, and I): Novel Optoelectronic Materials Showing Bright Emission with Wide Color Gamut. *Nano Lett.* **2015**, *15* (6), 3692–3696. https://doi.org/10.1021/nl5048779.

(83) Sobhanan, J.; Jones, P.; Kohara, R.; Sugino, S.; Vacha, M.; Subrahmanyam, C.; Takano, Y.; Lacy, F.; Biju, V. Toxicity of Nanomaterials Due to Photochemical Degradation and the Release of Heavy Metal Ions. *Nanoscale* **2020**, *12* (43), 22049–22058. https://doi.org/10.1039/d0nr03957h.

(84) Patsiou, D.; del Rio-Cubilledo, C.; Catarino, A. I.; Summers, S.; Mohd Fahmi, A.; Boyle, D.; Fernandes, T. F.; Henry, T. B. Exposure to Pb-Halide Perovskite Nanoparticles Can Deliver Bioavailable Pb but Does Not Alter Endogenous Gut Microbiota in Zebrafish. *Sci. Total Environ.* **2020**, *715* (January). https://doi.org/10.1016/j.scitotenv.2020.136941.

(85) Modlitbová, P.; Novotný, K.; Pořízka, P.; Klus, J.; Lubal, P.; Zlámalová-Gargošová, H.; Kaiser, J. Comparative Investigation of Toxicity and Bioaccumulation of Cd-Based Quantum Dots and Cd Salt in Freshwater Plant Lemna Minor L. *Ecotoxicol. Environ. Saf.* **2018**, *147* (March 2017), 334–341. https://doi.org/10.1016/j.ecoenv.2017.08.053.

(86) Directive 2011/65/EU of the European Parliament and of the Council of 8 June 2011 on the restriction

of the use of certain hazardous substances in electrical and electronic equipment (recast) https://eur-lex.europa.eu/legal-content/EN/TXT/?uri=CELEX:32011L0065.

(87) Akkerman, Q. A.; Rainò, G.; Kovalenko, M. V.; Manna, L. Genesis, Challenges and Opportunities for Colloidal Lead Halide Perovskite Nanocrystals. *Nat. Mater.* **2018**, *17* (5), 394–405. https://doi.org/10.1038/s41563-018-0018-4.

(88) Click, S. M.; Rosenthal, S. J. Synthesis, Surface Chemistry, and Fluorescent Properties of InP Quantum Dots. *Chem. Mater.* **2023**, *35* (3), 822–836. https://doi.org/10.1021/acs.chemmater.2c03074.

(89) Jiang, X.; Fan, Z.; Luo, L.; Wang, L. Advances and Challenges in Heavy-Metal-Free InP Quantum Dot Light-Emitting Diodes. *Micromachines* **2022**, *13* (5). https://doi.org/10.3390/mi13050709.

(90) Lu, H.; Hu, Z.; Zhou, W.; Wei, J.; Zhang, W.; Xie, F.; Guo, R. Synthesis and Structure Design of I-III-VI Quantum Dots for White Light-Emitting Diodes. *Mater. Chem. Front.* **2022**, *6* (4), 418–429. https://doi.org/10.1039/d1qm01452h.

(91) Chao, W. C.; Chiang, T. H.; Liu, Y. C.; Huang, Z. X.; Liao, C. C.; Chu, C. H.; Wang, C. H.; Tseng, H. W.; Hung, W. Y.; Chou, P. T. High Efficiency Green InP Quantum Dot Light-Emitting Diodes by Balancing Electron and Hole Mobility. *Commun. Mater.* **2021**, *2* (1), 1–10. https://doi.org/10.1038/s43246-021-00203-5.

(92) Won, Y. H.; Cho, O.; Kim, T.; Chung, D. Y.; Kim, T.; Chung, H.; Jang, H.; Lee, J.; Kim, D.; Jang, E. Highly Efficient and Stable InP/ZnSe/ZnS Quantum Dot Light-Emitting Diodes. *Nature* **2019**, *575* (7784), 634–638. https://doi.org/10.1038/s41586-019-1771-5.

(93) Yang, L.; Zhang, S.; Xu, B.; Jiang, J.; Cai, B.; Lv, X.; Zou, Y.; Fan, Z.; Yang, H.; Zeng, H. I-III-VI Quantum Dots and Derivatives: Design, Synthesis, and Properties for Light-Emitting Diodes. *Nano Lett.* **2023**, *23* (7), 2443–2453. https://doi.org/10.1021/acs.nanolett.2c03138.

(94) Deng, X.; Zhang, F.; Zhang, Y.; Shen, H. Heavy-Metal-Free Blue-Emitting ZnSe(Te) Quantum Dots: Synthesis and Light-Emitting Applications. *J. Mater. Chem. C* **2023**, 14495–14514. https://doi.org/10.1039/d3tc02699j.

(95) Munro, A. M. Synthetic Approaches for Growing Zinc Sulfide and Zinc Selenide Colloidal Nanocrystals. *J. Vac. Sci. Technol. A Vacuum, Surfaces, Film.* **2020**, *38* (2). https://doi.org/10.1116/1.5141992.

(96) Lin, S.; Li, J.; Pu, C.; Lei, H.; Zhu, M.; Qin, H.; Peng, X. Surface and Intrinsic Contributions to Extinction Properties of ZnSe Quantum Dots. *Nano Res.* **2020**, *13* (3), 824–831. https://doi.org/10.1007/s12274-020-2703-2.

(97) Yang, Z.; Wu, Q.; Zhou, X.; Cao, F.; Yang, X.; Zhang, J.; Li, W. A Seed-Mediated and Double Shell Strategy to Realize Large-Size ZnSe/ZnS/ZnS Quantum Dots for High Color Purity Blue Light-Emitting Diodes. *Nanoscale* **2021**, *13* (8), 4562–4568. https://doi.org/10.1039/d0nr05025c.

(98) Ebrahim, F.; Al-hartomy, O.; Wageh, S. Cadmium-Based Quantum Dots Alloyed Structures: Synthesis, Properties , and Applications. *Materials (Basel).* **2023**. https://doi.org/10.3390/ma16175877.

(99) Bailey, R. E.; Nie, S. Alloyed Semiconductor Quantum Dots: Tuning the Optical Properties without Changing the Particle Size. *J. Am. Chem. Soc.* **2003**, *125* (23), 7100–7106. https://doi.org/10.1021/ja035000o.

(100) Lee, S. H.; Han, C. Y.; Song, S. W.; Jo, D. Y.; Jo, J. H.; Yoon, S. Y.; Kim, H. M.; Hong, S.; Hwang, J. Y.; Yang, H. ZnSeTe Quantum Dots as an Alternative to InP and Their High-Efficiency Electroluminescence. *Chem. Mater.* **2020**, *32* (13), 5768–5775. https://doi.org/10.1021/acs.chemmater.0c01596.

(101) Wang, Z. M. *Core / Shell Quantum Dots*; Xin Tong, Z. M. W., Ed.; Springer Cham. https://doi.org/10.1007/978-3-030-46596-4.

(102) Cotta, M. A. Quantum Dots and Their Applications: What Lies Ahead? *ACS Appl. Nano Mater.* **2020**, *3* (6), 4920–4924. https://doi.org/10.1021/acsanm.0c01386.

(103) Agarwal, K.; Rai, H.; Mondal, S. Quantum Dots: An Overview of Synthesis, Properties, and Applications. *Mater. Res. Express* **2023**, *10* (6). https://doi.org/10.1088/2053-1591/acda17.

(104) Quantum dot display https://en.wikipedia.org/wiki/Quantum_dot_display.

(105) García de Arquer, F. P.; Talapin, D. V.; Klimov, V. I.; Arakawa, Y.; Bayer, M.; Sargent, E. H. Semiconductor Quantum Dots: Technological Progress and Future Challenges. *Science (80-.).* **2021**, *373* (6555). https://doi.org/10.1126/science.aaz8541.

(106) Wagner, A. M.; Knipe, J. M.; Orive, G.; Peppas, N. A. Quantum Dots in Biomedical Applications. *Acta Biomater.* **2019**, *94*, 44–63. https://doi.org/10.1016/j.actbio.2019.05.022.

(107) Kairdolf, B. A.; Smith, A. M.; Stokes, T. H.; Wang, M. D.; Young, A. N.; Nie, S. Semiconductor Quantum Dots for Bioimaging and Biodiagnostic Applications. *Annu. Rev. Anal. Chem.* **2013**, *6*, 143–162. https://doi.org/10.1146/annurev-anchem-060908-155136.

(108) Kargozar, S.; Hoseini, S. J.; Milan, P. B.; Hooshmand, S.; Kim, H. W.; Mozafari, M. Quantum Dots: A Review from Concept to Clinic. *Biotechnol. J.* **2020**, *15* (12), 1–18. https://doi.org/10.1002/biot.202000117.
(109) Yukawa, H.; Sato, K.; Baba, Y. Theranostics Applications of Quantum Dots in Regenerative Medicine, Cancer Medicine, and Infectious Diseases. *Adv. Drug Deliv. Rev.* **2023**, *200*, 114863. https://doi.org/10.1016/j.addr.2023.114863.
(110) Guo, R.; Zhang, M.; Ding, J.; Liu, A.; Huang, F.; Sheng, M. Advances in Colloidal Quantum Dot-Based Photodetectors. *J. Mater. Chem. C* **2022**, *10* (19), 7404–7422. https://doi.org/10.1039/d2tc00219a.
(111) Yadav, P. V. K.; Ajitha, B.; Kumar Reddy, Y. A.; Sreedhar, A. Recent Advances in Development of Nanostructured Photodetectors from Ultraviolet to Infrared Region: A Review. *Chemosphere* **2021**, *279*, 130473. https://doi.org/10.1016/j.chemosphere.2021.130473.
(112) Carey, G. H.; Abdelhady, A. L.; Ning, Z.; Thon, S. M.; Bakr, O. M.; Sargent, E. H. Colloidal Quantum Dot Solar Cells. *Chem. Rev.* **2015**, *115* (23), 12732–12763. https://doi.org/10.1021/acs.chemrev.5b00063.
(113) Mora-Seró, I. Current Challenges in the Development of Quantum Dot Sensitized Solar Cells. *Adv. Energy Mater.* **2020**, *10* (33), 1–6. https://doi.org/10.1002/aenm.202001774.
(114) Lu, H.; Huang, Z.; Martinez, M. S.; Johnson, J. C.; Luther, J. M.; Beard, M. C. Transforming Energy Using Quantum Dots. *Energy Environ. Sci.* **2020**, *13* (5), 1347–1376. https://doi.org/10.1039/c9ee03930a.
(115) Nguyen, D. T.; Sharma, S.; Chen, S. A.; Komarov, P. V.; Ivanov, V. A.; Khokhlov, A. R. Polymer-Quantum Dot Composite Hybrid Solar Cells with a Bi-Continuous Network Morphology Using the Block Copolymer Poly(3-Hexylthiophene)-: B -Polystyrene or Its Blend with Poly(3-Hexylthiophene) as a Donor. *Mater. Adv.* **2021**, *2* (3), 1016–1023. https://doi.org/10.1039/d0ma00770f.
(116) Sogabe, T.; Shen, Q.; Yamaguchi, K. Recent Progress on Quantum Dot Solar Cells: A Review. *J. Photonics Energy* **2016**, *6* (4), 040901. https://doi.org/10.1117/1.jpe.6.040901.
(117) Jouyandeh, M.; Mousavi Khadem, S. S.; Habibzadeh, S.; Esmaeili, A.; Abida, O.; Vatanpour, V.; Rabiee, N.; Bagherzadeh, M.; Iravani, S.; Reza Saeb, M.; Varma, R. S. Quantum Dots for Photocatalysis: Synthesis and Environmental Applications. *Green Chem.* **2021**, *23* (14), 4931–4954. https://doi.org/10.1039/d1gc00639h.
(118) Rao, V. N.; Reddy, N. L.; Kumari, M. M.; Cheralathan, K. K.; Ravi, P.; Sathish, M.; Neppolian, B.; Reddy, K. R.; Shetti, N. P.; Prathap, P.; Aminabhavi, T. M.; Shankar, M. V. Sustainable Hydrogen Production for the Greener Environment by Quantum Dots-Based Efficient Photocatalysts: A Review. *J. Environ. Manage.* **2019**, *248* (July), 109246. https://doi.org/10.1016/j.jenvman.2019.07.017.
(119) Jung, H.; Ahn, N.; Klimov, V. I. Prospects and Challenges of Colloidal Quantum Dot Laser Diodes. *Nat. Photonics* **2021**, *15* (9), 643–655. https://doi.org/10.1038/s41566-021-00827-6.
(120) Senellart, P.; Solomon, G.; White, A. High-Performance Semiconductor Quantum-Dot Single-Photon Sources. *Nat. Nanotechnol.* **2017**, *12* (11), 1026–1039. https://doi.org/10.1038/nnano.2017.218.
(121) Basset, F. B.; Valeri, M.; Roccia, E.; Muredda, V.; Poderini, D.; Neuwirth, J.; Spagnolo, N.; Rota, M. B.; Carvacho, G.; Sciarrino, F.; Trotta, R. Quantum Key Distribution with Entangled Photons Generated on Demand by a Quantum Dot. *Sci. Adv.* **2021**, *7* (12), 1–8. https://doi.org/10.1126/sciadv.abe6379.
(122) Ekimov, A. I.; Onushchenko, A. A. Quantum Size Effect in Three-Dimensional Microscopic Semiconductor Crystals. *Soviet Journal of Experimental and Theoretical Physics Letters*. 1981, pp 345–348.
(123) Zhang, J.; Li, C.; Li, J.; Peng, X. Synthesis of CdSe/ZnSe Core/Shell and CdSe/ZnSe/ZnS Core/Shell/Shell Nanocrystals: Surface-Ligand Strain and CdSe-ZnSe Lattice Strain. *Chem. Mater.* **2023**, *35* (17), 7049–7059. https://doi.org/10.1021/acs.chemmater.3c01333.
(124) Liu, M.; Chen, Z. Y.; He, X. H.; Liu, X. Y.; Hu, H. L.; Tian, H.; Liu, Y.; Jiang, F. L. Thermodynamics of Ligand Exchange with Aromatic Ligands on the Surface of CdSe Quantum Dots. *Chem. Mater.* **2023**, *35* (5), 1868–1876. https://doi.org/10.1021/acs.chemmater.2c02651.
(125) Yu, Q.; Song, J.; LI, K.; Xiao, L. Revisiting the Single-Step Synthesis of Quantum Dots: The Hidden Ligand-Promoted Surface Reaction Channels. *Nano Res.* **2023**, *16* (4), 5817–5825. https://doi.org/10.1007/s12274-022-5165-x.
(126) Dana, J.; Haggag, O. S.; Dehnel, J.; Mor, M.; Lifshitz, E.; Ruhman, S. Testing the Fate of Nascent Holes in CdSe Nanocrystals with Sub-10 Fs Pump-Probe Spectroscopy. *Nanoscale* **2021**, *13* (3), 1982–1987. https://doi.org/10.1039/d0nr07651a.
(127) Gupta, S. N.; Bitton, O.; Neuman, T.; Esteban, R.; Chuntonov, L.; Aizpurua, J.; Haran, G. Complex

Plasmon-Exciton Dynamics Revealed through Quantum Dot Light Emission in a Nanocavity. *Nat. Commun.* **2021**, *12* (1), 1–9. https://doi.org/10.1038/s41467-021-21539-z.
(128) Babaze, A.; Esteban, R.; Borisov, A. G.; Aizpurua, J. Electronic Exciton-Plasmon Coupling in a Nanocavity beyond the Electromagnetic Interaction Picture. *Nano Lett.* **2021**, *21* (19), 8466–8473. https://doi.org/10.1021/acs.nanolett.1c03202.
(129) Jiang, R.; Wu, H.; Manzani, D.; Zhang, W.; Liu, C. Effect of Surface Defects on Photoluminescence Properties of CdSe Quantum Dots in Glasses. *Appl. Surf. Sci.* **2023**, *622* (January), 156931. https://doi.org/10.1016/j.apsusc.2023.156931.
(130) Li, W.; Li, K.; Zhao, X.; Liu, C.; Coudert, F. X. Defective Nature of CdSe Quantum Dots Embedded in Inorganic Matrices. *J. Am. Chem. Soc.* **2022**, *144* (25), 11296–11305. https://doi.org/10.1021/jacs.2c03039.
(131) Ahn, N.; Livache, C.; Pinchetti, V.; Jung, H.; Jin, H.; Hahm, D.; Park, Y. S.; Klimov, V. I. Electrically Driven Amplified Spontaneous Emission from Colloidal Quantum Dots. *Nature* **2023**, *617* (7959), 79–85. https://doi.org/10.1038/s41586-023-05855-6.
(132) Deng, Y.; Peng, F.; Lu, Y.; Zhu, X.; Jin, W.; Qiu, J.; Dong, J.; Hao, Y.; Di, D.; Gao, Y.; Sun, T.; Zhang, M.; Liu, F.; Wang, L.; Ying, L.; Huang, F.; Jin, Y. Solution-Processed Green and Blue Quantum-Dot Light-Emitting Diodes with Eliminated Charge Leakage. *Nat. Photonics* **2022**, *16* (7), 505–511. https://doi.org/10.1038/s41566-022-00999-9.
(133) Wang, L.; Lin, J.; Lv, Y.; Zou, B.; Zhao, J.; Liu, X. Red, Green, and Blue Microcavity Quantum Dot Light-Emitting Devices with Narrow Line Widths. *ACS Appl. Nano Mater.* **2020**, *3* (6), 5301–5310. https://doi.org/10.1021/acsanm.0c00695.
(134) Manna, L. The Bright and Enlightening Science of Quantum Dots. *Nano Lett.* **2023**, *23* (21), 9673–9676. https://doi.org/10.1021/acs.nanolett.3c03904.
(135) Kowalik, P.; Bujak, P.; Penkala, M.; Maroń, A. M.; Ostrowski, A.; Kmita, A.; Gajewska, M.; Lisowski, W.; Sobczak, J. W.; Pron, A. Indium(II) Chloride as a Precursor in the Synthesis of Ternary (Ag-In-S) and Quaternary (Ag-In-Zn-S) Nanocrystals. *Chem. Mater.* **2022**, *34* (2), 809–825. https://doi.org/10.1021/acs.chemmater.1c03800.
(136) Akkerman, Q. A.; Nguyen, T. P. T.; Boehme, S. C.; Montanarella, F.; Dirin, D. N.; Wechsler, P.; Beiglböck, F.; Rainò, G.; Erni, R.; Katan, C.; Even, J.; Kovalenko, M. V. Controlling the Nucleation and Growth Kinetics of Lead Halide Perovskite Quantum Dots. *Science (80-.).* **2022**, *377* (6613), 1406–1412. https://doi.org/10.1126/science.abq3616.
(137) Van Avermaet, H.; Schiettecatte, P.; Hinz, S.; Giordano, L.; Ferrari, F.; Nayral, C.; Delpech, F.; Maultzsch, J.; Lange, H.; Hens, Z. Full-Spectrum InP-Based Quantum Dots with Near-Unity Photoluminescence Quantum Efficiency. *ACS Nano* **2022**, *16* (6), 9701–9712. https://doi.org/10.1021/acsnano.2c03138.
(138) Jeong, S. J.; Cho, S.; Moon, B.; Teku, J. A.; Jeong, M. H.; Lee, S.; Kim, Y.; Lee, J. S. Zero Dimensional-Two Dimensional Hybrid Photodetectors Using Multilayer MoS2 and Lead Halide Perovskite Quantum Dots with a Tunable Bandgap. *ACS Appl. Mater. Interfaces* **2023**, *15* (4), 5432–5438. https://doi.org/10.1021/acsami.2c17200.
(139) Ji, B.; Koley, S.; Slobodkin, I.; Remennik, S.; Banin, U. ZnSe/ZnS Core/Shell Quantum Dots with Superior Optical Properties through Thermodynamic Shell Growth. *Nano Lett.* **2020**, *20*, 2387–2395. https://doi.org/10.1021/acs.nanolett.9b05020.
(140) Kim, T.; Kim, K. H.; Kim, S.; Choi, S. M.; Jang, H.; Seo, H. K.; Lee, H.; Chung, D. Y.; Jang, E. Efficient and Stable Blue Quantum Dot Light-Emitting Diode. *Nature* **2020**, *586* (7829), 385–389. https://doi.org/10.1038/s41586-020-2791-x.
(141) Min, J.; Zhang, Y.; Zhou, Y.; Xu, D.; Garoufalis, C. S.; Zeng, Z.; Shen, H.; Baskoutas, S.; Jia, Y.; Du, Z. Size Engineering of Trap Effects in Oxidized and Hydroxylated ZnSe Quantum Dots. *Nano Lett.* **2022**. https://doi.org/10.1021/acs.nanolett.2c00118.
(142) Newton, I. A Letter of Mr. Isaac Newton, Professor of the Mathematicks in the University of Cambridge; Containing His New Theory about Light and Colors: Sent by the Author to the Publisher from Cambridge, Febr. 6. 1671/72; in Order to Be Communicated to the R. Socie. *Philos. Trans. R. Soc. London* **1672**, *6* (80), 3075–3087. https://doi.org/10.1098/rstl.1671.0072.
(143) Thomas, N. C. The Early History of Spectroscopy. *J. Chem. Educ.* **1991**, *68* (8), 631–634. https://doi.org/10.1021/ed068p631.
(144) Föster, H. UV/VIS Spectroscopy. In *Molecular Sieves - Science and Technology*; Karage, H. G., Weitkamp, J., Eds.; Springer, Berlin, Heidelberg, 2004. https://doi.org/10.1007/b94239.
(145) Avantes https://www.avantes.com/products/spectrometers (accessed May 13, 2024).
(146) Agilent https://www.agilent.com/en/product/molecular-spectroscopy/uv-vis-uv-vis-nir-spectroscopy/uv-vis-uv-vis-nir-systems (accessed May 13, 2024).
(147) Thermo Fisher Scientific https://www.thermofisher.com/search/browse/category/us/en/90207149

(accessed May 13, 2024).
(148) SHIMADZU (Shimadzu Corporation) https://www.ssi.shimadzu.com/products/molecular-spectroscopy/uv-vis/index.html (accessed May 13, 2024).
(149) Tissue, B. M. Ultraviolet and Visible Absorption Spectroscopy. In *Characterization ofMaterials*; Kaufmann, E. N., Ed.; John Wiley & Sons, Inc., 2012. https://doi.org/10.1002/0471266965.com059.pub2.
(150) Klimov, V. I. Spectral and Dynamical Properties of Multiexcitons in Semiconductor Nanocrystals. *Annu. Rev. Phys. Chem.* **2007**, *58*, 635–673. https://doi.org/10.1146/annurev.physchem.58.032806.104537.
(151) Jasieniak, J.; Smith, L.; Van Embden, J.; Mulvaney, P.; Califano, M. Re-Examination of the Size-Dependent Absorption Properties of CdSe Quantum Dots. *J. Phys. Chem. C* **2009**, *113* (45), 19468–19474. https://doi.org/10.1021/jp906827m.
(152) Veamatahau, A.; Jiang, B.; Seifert, T.; Makuta, S.; Latham, K.; Kanehara, M.; Teranishi, T.; Tachibana, Y. Origin of Surface Trap States in CdS Quantum Dots: Relationship between Size Dependent Photoluminescence and Sulfur Vacancy Trap States. *Phys. Chem. Chem. Phys.* **2015**, *17* (4), 2850–2858. https://doi.org/10.1039/c4cp04761c.
(153) Yu, Y.; Fan, G.; Fermi, A.; Mazzaro, R.; Morandi, V.; Ceroni, P.; Smilgies, D. M.; Korgel, B. A. Size-Dependent Photoluminescence Efficiency of Silicon Nanocrystal Quantum Dots. *J. Phys. Chem. C* **2017**, *121* (41), 23240–23248. https://doi.org/10.1021/acs.jpcc.7b08054.
(154) Palato, S.; Seiler, H.; Baker, H.; Sonnichsen, C.; Brosseau, P.; Kambhampati, P. Investigating the Electronic Structure of Confined Multiexcitons with Nonlinear Spectroscopies. *J. Chem. Phys.* **2020**, *152* (10). https://doi.org/10.1063/1.5142180.
(155) Zhang, C.; Do, T. N.; Ong, X.; Chan, Y.; Tan, H. S. Understanding the Features in the Ultrafast Transient Absorption Spectra of CdSe Quantum Dots. *Chem. Phys.* **2016**, *481*, 157–164. https://doi.org/10.1016/j.chemphys.2016.08.027.
(156) Norris, D.; Bawendi, M. Measurement and Assignment of the Size-Dependent Optical Spectrum in CdSe Quantum Dots. *Phys. Rev. B - Condens. Matter Mater. Phys.* **1996**, *53* (24), 16338–16346. https://doi.org/10.1103/PhysRevB.53.16338.
(157) Suresh, S. Studies on the Dielectric Properties of CdS Nanoparticles. *Appl. Nanosci.* **2014**, *4* (3), 325–329. https://doi.org/10.1007/s13204-013-0209-x.
(158) Feng, Y.; Lin, S.; Huang, S.; Shrestha, S.; Conibeer, G. Can Tauc Plot Extrapolation Be Used for Direct-Band-Gap Semiconductor Nanocrystals? *J. Appl. Phys.* **2015**, *117* (12). https://doi.org/10.1063/1.4916090.
(159) Kim, S. H.; Shin, T.; Man, M. T.; Lee, H. S. Size-Dependent Energy Spacing and Surface Defects of CdSe Quantum Dots in Strong Confinement Regime. *Appl. Nanosci.* **2022**, *12* (11), 3297–3302. https://doi.org/10.1007/s13204-021-02310-8.
(160) Nguyen, H. A.; Dixon, G.; Dou, F. Y.; Gallagher, S.; Gibbs, S.; Ladd, D. M.; Marino, E.; Ondry, J. C.; Shanahan, J. P.; Vasileiadou, E. S.; Barlow, S.; Gamelin, D. R.; Ginger, D. S.; Jonas, D. M.; Kanatzidis, M. G.; Marder, S. R.; Morton, D.; Murray, C. B.; Owen, J. S.; Talapin, D. V.; Toney, M. F.; Cossairt, B. M. Design Rules for Obtaining Narrow Luminescence from Semiconductors Made in Solution. *Chem. Rev.* **2023**, *123* (12), 7890–7952. https://doi.org/10.1021/acs.chemrev.3c00097.
(161) Changenet, P.; Gustavsson, T.; Lampre, I. Introduction to Femtochemistry: Excited-State Proton Transfer from Pyranine to Water Studied by Femtosecond Transient Absorption. *J. Chem. Educ.* **2020**, *97* (12), 4482–4489. https://doi.org/10.1021/acs.jchemed.0c01056.
(162) Beckwith, J. S.; Rumble, C. A.; Vauthey, E. Data Analysis in Transient Electronic Spectroscopy–an Experimentalist's View. *Int. Rev. Phys. Chem.* **2020**, *39* (2), 135–216. https://doi.org/10.1080/0144235X.2020.1757942.
(163) Zhu, H.; Yang, Y.; Wu, K.; Lian, T. Charge Transfer Dynamics from Photoexcited Semiconductor Quantum Dots. *Annu. Rev. Phys. Chem.* **2016**, *67*, 259–281. https://doi.org/10.1146/annurev-physchem-040215-112128.
(164) Makkar, M.; Moretti, L.; Maiuri, M.; Cerullo, G.; Viswanatha, R. Ultrafast Electron Hole Relaxation Dynamics in CdS Nanocrystals. *JPhys Mater.* **2021**, *4* (3). https://doi.org/10.1088/2515-7639/abf546.
(165) Newville, M. *Fundamentals of XAFS*; University of Chicago, Chicago, IL, 2004.
(166) Ketenoglu, D. A General Overview and Comparative Interpretation on Element-Specific X-Ray Spectroscopy Techniques: XPS, XAS, and XRS. *X-Ray Spectrom.* **2022**, *51* (5–6), 422–443. https://doi.org/10.1002/xrs.3299.
(167) Chantler, C. T. X-Ray Absorption Spectroscopy Definitions. *Int. Tables Crystallogr.* **2021**, *I*, 1–9. https://doi.org/10.1107/s1574870720003785.
(168) Yamamoto, T. Assignment of Pre-Edge Peaks in K-Edge x-Ray Absorption Spectra of 3d Transition Metal Compounds: Electric Dipole or Quadrupole? *X-Ray Spectrom.* **2008**, *37*, 572–584.

https://doi.org/10.1002/xrs.1103 Review Assignment.
(169) Iglesias-Juez, A.; Chiarello, G. L.; Patience, G. S.; Guerrero-Pérez, M. O. Experimental Methods in Chemical Engineering: X-Ray Absorption Spectroscopy—XAS, XANES, EXAFS. *Can. J. Chem. Eng.* **2022**, *100* (1), 3–22. https://doi.org/10.1002/cjce.24291.
(170) Carriere, M.; Pignol, D.; Arnoux, P. Co K edge XAS transmission and XAS fluorescence of organic and inorganic Co(II) and Co(III) reference compounds for the study of Co in bacteria https://doi.org/10.26302/SSHADE/EXPERIMENT_MC_20141201_001 (accessed Jan 31, 2024).
(171) Gianolio, D. How to Start an XAS Experiment. In *X-Ray Absorption and X-Ray Emission Spectroscopy: Theory and Applications*; van Bokhoven, J. A., Lamberti, C., Eds.; John Wiley & Sons, Ltd: Chichester, 2016; pp 99–124. https://doi.org/10.1002/9781118844243.ch5.
(172) Schnohr, C. S.; Ridgway, M. C. *X-Ray Absorption Spectroscopy of Semiconductors*; Springer Berlin, Heidelberg, 2015. https://doi.org/10.1007/978-3-662-44362-0.
(173) Jenkins, R.; Manne, R.; Robin, R.; Senemaud, C. International Union of Pure and Applied Chemistry: Analytical Chemistry Division Commission on Spectrochemical and Other Optical Procedures for Analysis Nomenclature, Symbols, Units and Their Usage in Spectrochemical Analysis - VIII. *Pure Appl. Chem.* **1991**, *63* (5), 735–746. https://doi.org/10.1351/pac199163050735.
(174) Kawai, J.; Suzuki, C.; Adachi, H.; Konishi, T.; Gohshi, Y. Charge-Transfer Effect on the Linewidth of Fe Kα x-Ray Fluorescence Spectra. *Phys. Rev. B* **1994**, *50* (16). https://doi.org/10.1103/PhysRevB.50.11347.
(175) Pollock, C. J.; Delgado-Jaime, M. U.; Atanasov, M.; Neese, F.; Debeer, S. Kβ Mainline X-Ray Emission Spectroscopy as an Experimental Probe of Metal-Ligand Covalency. *J. Am. Chem. Soc.* **2014**, *136* (26), 9453–9463. https://doi.org/10.1021/ja504182n.
(176) Castillo, R. G.; Henthorn, J. T.; McGale, J.; Maganas, D.; DeBeer, S. Kβ X-Ray Emission Spectroscopic Study of a Second-Row Transition Metal (Mo) and Its Application to Nitrogenase-Related Model Complexes. *Angew. Chemie - Int. Ed.* **2020**, *59* (31), 12965–12975. https://doi.org/10.1002/anie.202003621.
(177) Vankó, G.; Neisius, T.; Molnár, G.; Renz, F.; Kárpáti, S.; Shukla, A.; De Groot, F. M. F. Probing the 3D Spin Momentum with X-Ray Emission Spectroscopy: The Case of Molecular-Spin Transitions. *J. Phys. Chem. B* **2006**, *110* (24), 11647–11653. https://doi.org/10.1021/jp0615961.
(178) Cutsail, G. E.; Debeer, S. Challenges and Opportunities for Applications of Advanced X-Ray Spectroscopy in Catalysis Research. *ACS Catal.* **2022**, 5864–5886. https://doi.org/10.1021/acscatal.2c01016.
(179) Glatzel, P.; Bergmann, U. High Resolution 1s Core Hole X-Ray Spectroscopy in 3d Transition Metal Complexes - Electronic and Structural Information. *Coord. Chem. Rev.* **2005**, *249* (1–2), 65–95. https://doi.org/10.1016/j.ccr.2004.04.011.
(180) Broglie, D. Sur Une Nouveau Procede Permettant d'obtenir La Photographie Des Spectres de Raies Des Rayons Rontgen. *C. R. Acad. Sci.* **1913**, *157*, 924–926.
(181) Jenkins, R. *X-Ray Fluorescence Spectrometry*; John Wiley & Sons, Inc., 1999. https://doi.org/10.1002/9781118521014.
(182) Chen, S.; Wang, P.; Zhang, X.; Huang, S.; Wang, Y.; Hu, M.; Zhang, C.; Gong, Y. Thermionic Enhanced Heat Transfer in X-Ray Tubes. *Appl. Phys. Lett.* **2024**, *124* (1). https://doi.org/10.1063/5.0185921.
(183) Seidler, G. T.; Mortensen, D. R.; Remesnik, A. J.; Pacold, J. I.; Ball, N. A.; Barry, N.; Styczinski, M.; Hoidn, O. R. A Laboratory-Based Hard x-Ray Monochromator for High-Resolution x-Ray Emission Spectroscopy and x-Ray Absorption near Edge Structure Measurements. *Rev. Sci. Instrum.* **2014**, *85* (11). https://doi.org/10.1063/1.4901599.
(184) Németh, Z.; Szlachetko, J.; Bajnóczi, É. G.; Vankó, G. Laboratory von Hámos X-Ray Spectroscopy for Routine Sample Characterization. *Rev. Sci. Instrum.* **2016**, *87* (10). https://doi.org/10.1063/1.4964098.
(185) Hoszowska, J.; Dousse, J. C.; Kern, J.; Rhême, C. High-Resolution von Hamos Crystal X-Ray Spectrometer. *Nucl. Instruments Methods Phys. Res. Sect. A Accel. Spectrometers, Detect. Assoc. Equip.* **1996**, *376* (1), 129–138. https://doi.org/10.1016/0168-9002(96)00262-8.
(186) Ketelhut, S. Catalogue of unfiltered x-ray spectra from tungsten-, molybdenum-, and rhodium-anode-based x-ray tubes with generating voltages from 10kV to 50kV in steps of 1kV https://oar.ptb.de/resources/show/10.7795/720.20201118 (accessed Jan 11, 2024). https://doi.org/10.7795/720.20201118.
(187) Bonino, F.; Groppo, E.; Prestipino, C.; Agostini, G.; Piovano, A.; Gianolio, D.; Mino, L.; Gallo, E.; Lamberti, C. *Synchrotron Radiation*, 1st ed.; Mobilio, S., Boscherini, F., Meneghini, C., Eds.; Springer Berlin, Heidelberg, 2015. https://doi.org/10.1007/978-3-642-55315-8.
(188) Mills, D. M.; Helliwell, J. R.; Kvick, Å.; Ohta, T.; Robinson, I. A.; Authier, A. Report of the Working

Group on Synchrotron Radiation Nomenclature - Brightness, Spectral Brightness or Brilliance? *J. Synchrotron Radiat.* **2005**, *12* (3), 385. https://doi.org/10.1107/S090904950500796X.
(189) Diamond https://www.diamond.ac.uk/Home/About/FAQs/About-Synchrotrons.html (accessed Mar 22, 2024).
(190) Lightsources.org https://lightsources.org/lightsources-of-the-world/ (accessed Mar 22, 2024).
(191) Huang, N.; Deng, H.; Liu, B.; Wang, D.; Zhao, Z. Features and Futures of X-Ray Free-Electron Lasers. *Innovation* **2021**, *2* (2), 100097. https://doi.org/10.1016/j.xinn.2021.100097.
(192) Thompson; Thompson, A.; Attwood, D.; Gullikson, E.; Howells, M.; Kim, K.-J.; Kirz, J.; Kortright, J.; Lindau, I.; Liu, Y.; Pianetta, P.; Robinson, A.; Scofield, J.; Underwood, J.; Williams, G.; Winick, H. X-Ray Data Booklet. *Lawrence Berkeley National Laboratory*. 2009, p 176.
(193) Huang, Z. Brightness and Coherence of Synchrotron Radiation and Fels. *IPAC 2013 Proc. 4th Int. Part. Accel. Conf.* **2013**, 16–20.
(194) Krause, M. O.; Oliver, J. H. Natural Widths of Atomic K an L Levels, Kα X-Ray Lines and Several KLL Auger Lines. *J. Phys. Chem. Ref. Data* **1979**, *8* (2), 329–338. https://doi.org/10.1063/1.555595.
(195) Scholze, F.; Longoni, A.; Fiorini, C.; Strüder, L.; Meidinger, N.; Hartmann, R.; Kawahara, N.; Shoji, T. X-Ray Detectors and XRF Detection Channels. In *Handbook of Practical X-Ray Fluorescence Analysis*; Burkhard, B., Kanngießer, B., Langhoff, N., Wedell, R., Wolff, H., Eds.; Springer Berlin, Heidelberg: Berlin, 2006; pp 199–308. https://doi.org/10.1007/978-3-540-36722-2_4.
(196) Szlachetko, M.; Berset, M.; Dousse, J. C.; Hoszowska, J.; Szlachetko, J. High-Resolution Laue-Type DuMond Curved Crystal Spectrometer. *Rev. Sci. Instrum.* **2013**, *84* (9). https://doi.org/10.1063/1.4821621.
(197) Johann, H. H. Die Erzeugung Lichtstarker Röntgenspektren Mit Hilfe Yon Konkavkristallen. *Zeitschrift für Phys.* **1931**, *69*, 185–206. https://doi.org/10.1007/BF01798121.
(198) Johansson, T. Über Ein Neuartiges, Genau Fokussierendes Röntgenspektrometer. *Zeitschrift für Phys.* **1933**, *82* (7–8), 507–528. https://doi.org/10.1007/BF01342254.
(199) v. Hámos, L. Röntgenspektroskopie Und Abbildung Mittels Gekrümmter Kristallreflektoren. *Naturwissenschaften* **1932**, *20* (38), 705–706. https://doi.org/10.1007/BF01494468.
(200) Zimmermann, P.; Peredkov, S.; Abdala, P. M.; DeBeer, S.; Tromp, M.; Müller, C.; van Bokhoven, J. A. Modern X-Ray Spectroscopy: XAS and XES in the Laboratory. *Coord. Chem. Rev.* **2020**, *423*, 213466. https://doi.org/10.1016/j.ccr.2020.213466.
(201) Błachucki, W.; Czapla-Masztafiak, J.; Sá, J.; Szlachetko, J. A Laboratory-Based Double X-Ray Spectrometer for Simultaneous X-Ray Emission and X-Ray Absorption Studies. *J. Anal. At. Spectrom.* **2019**, *34* (7), 1409–1415. https://doi.org/10.1039/c9ja00159j.
(202) Szlachetko, J.; Nachtegaal, M.; De Boni, E.; Willimann, M.; Safonova, O.; Sa, J.; Smolentsev, G.; Szlachetko, M.; Van Bokhoven, J. A.; Dousse, J. C.; Hoszowska, J.; Kayser, Y.; Jagodzinski, P.; Bergamaschi, A.; Schmitt, B.; David, C.; Lücke, A. A von Hamos X-Ray Spectrometer Based on a Segmented-Type Diffraction Crystal for Single-Shot x-Ray Emission Spectroscopy and Time-Resolved Resonant Inelastic x-Ray Scattering Studies. *Rev. Sci. Instrum.* **2012**, *83* (10). https://doi.org/10.1063/1.4756691.
(203) Mino, L.; Agostini, G.; Borfecchia, E.; Gianolio, D.; Piovano, A.; Gallo, E.; Lamberti, C. Low-Dimensional Systems Investigated by x-Ray Absorption Spectroscopy: A Selection of 2D, 1D and 0D Cases. *J. Phys. D. Appl. Phys.* **2013**, *46* (42). https://doi.org/10.1088/0022-3727/46/42/423001.
(204) Stein, J. L.; Holden, W. M.; Venkatesh, A.; Mundy, M. E.; Rossini, A. J.; Seidler, G. T.; Cossairt, B. M. Probing Surface Defects of InP Quantum Dots Using Phosphorus Kα and Kβ X-Ray Emission Spectroscopy. *Chem. Mater.* **2018**, *30* (18), 6377–6388. https://doi.org/10.1021/acs.chemmater.8b02590.
(205) Khammang, A.; Wright, J. T.; Meulenberg, R. W. Mechanistic Insight into Copper Cation Exchange in Cadmium Selenide Semiconductor Nanocrystals Using X-Ray Absorption Spectroscopy. *Nat. Commun.* **2021**, *12* (1), 1–8. https://doi.org/10.1038/s41467-020-20712-0.
(206) Borys, A. The Schlenk Line Survival Guide https://schlenklinesurvivalguide.com (accessed Feb 12, 2024).
(207) Jang, E. P.; Han, C. Y.; Lim, S. W.; Jo, J. H.; Jo, D. Y.; Lee, S. H.; Yoon, S. Y.; Yang, H. Synthesis of Alloyed ZnSeTe Quantum Dots as Bright, Color-Pure Blue Emitters. *ACS Appl. Mater. Interfaces* **2019**, *11* (49), 46062–46069. https://doi.org/10.1021/acsami.9b14763.
(208) Banski, M.; Afzaal, M.; Malik, M. A.; Podhorodecki, A.; Misiewicz, J.; O'Brien, P. Special Role for Zinc Stearate and Octadecene in the Synthesis of Luminescent ZnSe Nanocrystals. *Chem. Mater.* **2015**, *27* (11), 3797–3800. https://doi.org/10.1021/acs.chemmater.5b00347.
(209) Pu, C.; Zhou, J.; Lai, R.; Niu, Y.; Nan, W.; Peng, X. Highly Reactive, Flexible yet Green Se Precursor for Metal Selenide Nanocrystals: Se-Octadecene Suspension (Se-SUS). *Nano Res.* **2013**, *6* (9), 652–670. https://doi.org/10.1007/s12274-013-0341-7.

(210) Goldstein, J. I.; Newbury, D. E.; Michael, J. R.; Ritchie, N. W. M.; Scott, J. H. J.; Joy, D. C. *Scanning Electron Microscopy and X-Ray Microanalysis*, 4th ed.; Springer New York, NY, 2018. https://doi.org/10.1007/978-1-4939-6676-9.
(211) Mansur, A.; Mansur, H.; González, J. Enzyme-Polymers Conjugated to Quantum-Dots for Sensing Applications. *Sensors* **2011**, *11* (10), 9951–9972. https://doi.org/10.3390/s111009951.
(212) Du, T.; Cai, K.; Han, H.; Fang, L.; Liang, J.; Xiao, S. Probing the Interactions of CdTe Quantum Dots with Pseudorabies Virus. *Sci. Rep.* **2015**, *5*, 1–10. https://doi.org/10.1038/srep16403.
(213) Qu, J.; Jiang, D.; Wang, L.; Liu, K.; Xu, X.; Yao, C.; Sun, W. Optical Nonlinear Enhancement through Interaction between Ag Nanoparticles and CdSe Quantum Dots. *J. Mater. Sci.* **2019**, *54* (11), 8450–8460. https://doi.org/10.1007/s10853-019-03487-8.
(214) Liu, J.; Xue, W.; Jin, G.; Zhai, Z.; Lv, J.; Hong, W.; Chen, Y. Preparation of Tin Oxide Quantum Dots in Aqueous Solution and Applications in Semiconductor Gas Sensors. *Nanomaterials* **2019**, *9* (2), 2–11. https://doi.org/10.3390/nano9020240.
(215) Darwan, D.; Lim, L. J.; Wang, T.; Wijaya, H.; Tan, Z. K. Ultra-Confined Visible-Light-Emitting Colloidal Indium Arsenide Quantum Dots. *Nano Lett.* **2021**, *21* (12), 5167–5172. https://doi.org/10.1021/acs.nanolett.1c01223.
(216) Wang, H.; Gao, J.; Zhang, M.; Liu, P.; Guo, Y.; Li, H.; Zhao, G.; Hu, S.; Cheng, Z.; Zang, J.; Wen, R.; Liu, T.; Tong, Y.; Sun, Z.; Wang, H. ZnSe/ZnS Core-Shell Quantum Dots Doped with Mn2+Ions for Magnetic State-Manipulated Light Sources. *ACS Appl. Nano Mater.* **2022**, *5* (6), 8448–8456. https://doi.org/10.1021/acsanm.2c01570.
(217) Li, J.; Wang, L. W. Band-Structure-Corrected Local Density Approximation Study of Semiconductor Quantum Dots and Wires. *Phys. Rev. B - Condens. Matter Mater. Phys.* **2005**, *72* (12). https://doi.org/10.1103/PhysRevB.72.125325.
(218) Weidman, M. C.; Beck, M. E.; Hoffman, R. S.; Prins, F.; Tisdale, W. A. Monodisperse, Air-Stable PbS Nanocrystals via Precursor Stoichiometry Control. *ACS Nano* **2014**, *8* (6), 6363–6371. https://doi.org/10.1021/nn5018654.
(219) Maes, J.; Castro, N.; De Nolf, K.; Walravens, W.; Abécassis, B.; Hens, Z. Size and Concentration Determination of Colloidal Nanocrystals by Small-Angle x-Ray Scattering. *Chem. Mater.* **2018**, *30* (12), 3952–3962. https://doi.org/10.1021/acs.chemmater.8b00903.
(220) Frederick, M. T.; Weiss, E. A. Relaxation of Exciton Confinement in CdSe Quantum Dots by Modification with a Conjugated Dithiocarbamate Ligand. *ACS Nano* **2010**, *4* (6), 3195–3200. https://doi.org/10.1021/nn1007435.
(221) Koole, R.; Luigjes, B.; Tachiya, M.; Pool, R.; Vlugt, T. J. H.; De Mello Donegá, C.; Meijerink, A.; Vanmaekelbergh, D. Differences in Cross-Link Chemistry between Rigid and Flexible Dithiol Molecules Revealed by Optical Studies of CdTe Quantum Dots. *J. Phys. Chem. C* **2007**, *111* (30), 11208–11215. https://doi.org/10.1021/jp072407x.
(222) Frederick, M. T.; Amin, V. A.; Cass, L. C.; Weiss, E. A. A Molecule to Detect and Perturb the Confinement of Charge Carriers in Quantum Dots. *Nano Lett.* **2011**, *11* (12), 5455–5460. https://doi.org/10.1021/nl203222m.
(223) Leatherdale, C. A.; Bawendi, M. G. Observation of Solvatochromism in CdSe Colloidal Quantum Dots. *Phys. Rev. B - Condens. Matter Mater. Phys.* **2001**, *63* (16), 1–6. https://doi.org/10.1103/PhysRevB.63.165315.
(224) Bahgat, A. A.; Gupta, K. Das. A New Type of X-Ray Absorption Spectrometer. *Rev. Sci. Instrum.* **1979**, *50* (8), 1020–1021. https://doi.org/10.1063/1.1135970.
(225) Tohji, K.; Udagawa, Y. Development of a Laboratory Exafs Facility. *Japanese J. Appl. Physics, Part 1 Regul. Pap. Short Notes* **1983**, *22* (5), 882–885. https://doi.org/10.1143/jjap.22.882.
(226) Lecante, P.; Jaud, J.; Mosset, A.; Galy, J.; Burian, A. A Laboratory EXAFS Spectrometer in Transmission Dispersive Mode. *Rev. Sci. Instrum.* **1994**, *65* (4), 845–849. https://doi.org/10.1063/1.1144909.
(227) Williams, A. Laboratory X-Ray Spectrometer for EXAFS and XANES Measurements. *Rev. Sci. Instrum.* **1983**, *54* (2), 193–197. https://doi.org/10.1063/1.1137344.
(228) XOS https://www.xos.com/ (accessed Jun 17, 2024).
(229) Bruker https://www.bruker.com/en.html (accessed Jun 17, 2024).
(230) Oxford Instruments Andor https://andor.oxinst.com/ (accessed Jun 17, 2024).
(231) Schlesiger, C.; Anklamm, L.; Stiel, H.; Malzer, W.; Kanngießer, B. XAFS Spectroscopy by an X-Ray Tube Based Spectrometer Using a Novel Type of HOPG Mosaic Crystal and Optimized Image Processing. *J. Anal. At. Spectrom.* **2015**, *30* (5), 1080–1085. https://doi.org/10.1039/c4ja00303a.
(232) Honkanen, A. P.; Ollikkala, S.; Ahopelto, T.; Kallio, A. J.; Blomberg, M.; Huotari, S. Johann-Type Laboratory-Scale x-Ray Absorption Spectrometer with Versatile Detection Modes. *Rev. Sci. Instrum.* **2019**, *90* (3). https://doi.org/10.1063/1.5084049.

(233) Błachucki, W.; Wach, A.; Czapla-Masztafiak, J.; Kwiatek, W. M.; Szlachetko, J. Laboratory for High Energy Resolution X-Ray Spectroscopy at the Institute of Nuclear Physics of the Polish Academy of Sciences. *Synchrotron Radiat. Nat. Sci.* **2020**, *19*, 5–7. https://doi.org/10.36184/SRNS.2020.19.005.
(234) Reference X-ray Spectra of Metal Foils https://www.exafsmaterials.com/reference-spectra (accessed Apr 29, 2024).
(235) Wansleben, M.; Kayser, Y.; Hönicke, P.; Holfelder, I.; Wählisch, A.; Unterumsberger, R.; Beckhoff, B. Experimental Determination of Line Energies, Line Widths and Relative Transition Probabilities of the Gadolinium l x-Ray Emission Spectrum. *Metrologia* **2019**, *56* (6). https://doi.org/10.1088/1681-7575/ab40d2.
(236) Zymaková, A.; Precek, M.; Picchiotti, A.; Błachucki, W.; Zymak, I.; Szlachetko, J.; Vankó, G.; Németh, Z.; Sá, J.; Wiste, T.; Andreasson, J. X-Ray Spectroscopy Station for Sample Characterization at ELI Beamlines. *Sci. Rep.* **2023**, *13* (1), 1–9. https://doi.org/10.1038/s41598-023-43924-y.
(237) Fanselow, R. Synthesis of Plasmonic Copper Nanoparticles Dedicated for Analysis Using Novel X-Ray Spectroscopy Techniques, Jagiellonian University, 2020.
(238) Su, S. S.; Chang, I. Review of Production Routes of Nanomaterials. In *Commercialization of Nanotechnologies-A Case Study Approach*; Brabazon, D., Pellicer, E., Zivic, F., Sort, J., Baró, M. D., Grujovic, N., Choy, K. L., Eds.; 2017; pp 1–315. https://doi.org/10.1007/978-3-319-56979-6.
(239) Agglomeration (Except in Polymer Science). *The IUPAC Compendium of Chemical Terminology*; 2008; Vol. 1801, p 2014. https://doi.org/10.1351/goldbook.a00182.
(240) Sommer, M.; Stenger, F.; Peukert, W.; Wagner, N. J. Agglomeration and Breakage of Nanoparticles in Stirred Media Mills - A Comparison of Different Methods and Models. *Chem. Eng. Sci.* **2006**, *61* (1), 135–148. https://doi.org/10.1016/j.ces.2004.12.057.
(241) Ganguly, S.; Chakraborty, S. Sedimentation of Nanoparticles in Nanoscale Colloidal Suspensions. *Phys. Lett. Sect. A Gen. At. Solid State Phys.* **2011**, *375* (24), 2394–2399. https://doi.org/10.1016/j.physleta.2011.04.018.
(242) Endres, S. C.; Ciacchi, L. C.; Mädler, L. A Review of Contact Force Models between Nanoparticles in Agglomerates, Aggregates, and Films. *J. Aerosol Sci.* **2021**, *153* (November 2020). https://doi.org/10.1016/j.jaerosci.2020.105719.
(243) Henry, F.; Marchal, P.; Bouillard, J.; Vignes, A.; Dufaud, O.; Perrin, L. The Effect of Agglomeration on the Emission of Particles from Nanopowders Flow. *Chem. Eng. Trans.* **2013**, *31*, 811–816. https://doi.org/10.3303/CET1331136.
(244) Lorite, I.; Romero, J. J.; Fernandez, J. F. Influence of the Nanoparticles Agglomeration State in the Quantum-Confinement Effects: Experimental Evidences. *AIP Adv.* **2015**, *5* (3). https://doi.org/10.1063/1.4914107.
(245) Zare, Y.; Rhee, K. Y.; Hui, D. Influences of Nanoparticles Aggregation/Agglomeration on the Interfacial/Interphase and Tensile Properties of Nanocomposites. *Compos. Part B Eng.* **2017**, *122*, 41–46. https://doi.org/10.1016/j.compositesb.2017.04.008.
(246) Ma, X.; Zare, Y.; Rhee, K. Y. A Two-Step Methodology to Study the Influence of Aggregation/Agglomeration of Nanoparticles on Young's Modulus of Polymer Nanocomposites. *Nanoscale Res. Lett.* **2017**, *12*, 0–6. https://doi.org/10.1186/s11671-017-2386-0.
(247) Midelet, J.; El-Sagheer, A. H.; Brown, T.; Kanaras, A. G.; Werts, M. H. V. The Sedimentation of Colloidal Nanoparticles in Solution and Its Study Using Quantitative Digital Photography. *Part. Part. Syst. Charact.* **2017**, *34* (10). https://doi.org/10.1002/ppsc.201700095.
(248) Yang, Y. J.; Corti, D. S.; Franses, E. I. Use of Close-Packed Vesicular Dispersions to Stabilize Colloidal Particle Dispersions against Sedimentation. *Langmuir* **2015**, *31* (32), 8802–8808. https://doi.org/10.1021/acs.langmuir.5b02133.
(249) Jang, Y. R.; Ryu, C. H.; Chu, J. H.; Nam, J. B.; Kim, H. S. Multiple Intense Pulsed Light Sintering of Silane Surface Modified Cu Oxide Nanoparticle Paste on Si Wafer Substrate for Solar Cell Electrode. *Thin Solid Films* **2021**, *722* (February), 138577. https://doi.org/10.1016/j.tsf.2021.138577.
(250) Abdullah, M.; Malik, S. R.; Iqbal, M. H.; Sajid, M. M.; Shad, N. A.; Hussain, S. Z.; Razzaq, W.; Javed, Y. Sedimentation and Stabilization of Nano-Fluids with Dispersant. *Colloids Surfaces A Physicochem. Eng. Asp.* **2018**, *554* (April), 86–92. https://doi.org/10.1016/j.colsurfa.2018.06.030.
(251) Ordóñez, F.; Chejne, F.; Pabón, E.; Cacua, K. Synthesis of ZrO2 Nanoparticles and Effect of Surfactant on Dispersion and Stability. *Ceram. Int.* **2020**, *46* (8), 11970–11977. https://doi.org/10.1016/j.ceramint.2020.01.236.
(252) Yi, S.; Babadagli, T.; Li, H. Stabilization of Nickel Nanoparticle Suspensions with the Aid of Polymer and Surfactant: Static Bottle Tests and Dynamic Micromodel Flow Tests. *Pet. Sci.* **2020**, *17* (4), 1014–1024. https://doi.org/10.1007/s12182-020-00433-1.
(253) Witharana, S.; Hodges, C.; Xu, D.; Lai, X.; Ding, Y. Aggregation and Settling in Aqueous

Polydisperse Alumina Nanoparticle Suspensions. *J. Nanoparticle Res.* **2012**, *14* (5), 1–19. https://doi.org/10.1007/s11051-012-0851-3.
(254) Singh, R. P.; Sharma, K.; Mausam, K. Dispersion and Stability of Metal Oxide Nanoparticles in Aqueous Suspension: A Review. *Mater. Today Proc.* **2019**, *26* (2020), 2021–2025. https://doi.org/10.1016/j.matpr.2020.02.439.
(255) Kumar, A.; Dixit, C. K. Methods for Characterization of Nanoparticles. *Adv. Nanomedicine Deliv. Ther. Nucleic Acids* **2017**, 44–58. https://doi.org/10.1016/B978-0-08-100557-6.00003-1.
(256) Kamiya, H.; Otani, Y.; Fuji, M.; Miyahara, M. *Characteristics and Behavior of Nanoparticles and Its Dispersion Systems*; 2018. https://doi.org/10.1016/B978-0-444-64110-6.00003-2.
(257) Murdock, R. C.; Braydich-Stolle, L.; Schrand, A. M.; Schlager, J. J.; Hussain, S. M. Characterization of Nanomaterial Dispersion in Solution Prior to in Vitro Exposure Using Dynamic Light Scattering Technique. *Toxicol. Sci.* **2008**, *101* (2), 239–253. https://doi.org/10.1093/toxsci/kfm240.
(258) Penfold, T. J.; Szlachetko, J.; Santomauro, F. G.; Britz, A.; Gawelda, W.; Doumy, G.; March, A. M.; Southworth, S. H.; Rittmann, J.; Abela, R.; Chergui, M.; Milne, C. J. Revealing Hole Trapping in Zinc Oxide Nanoparticles by Time-Resolved X-Ray Spectroscopy. *Nat. Commun.* **2018**, *9* (1), 1–9. https://doi.org/10.1038/s41467-018-02870-4.
(259) Azman, A.; Yusoff, M. Z.; Hassan, M. Z.; Yazid, H.; Gunnasegaran, P.; Ng, K. C. Preliminary Study to Determine the Maximum Settling Velocity and Model Parameter of Cu Nanoparticle by Settling Method. *IOP Conf. Ser. Mater. Sci. Eng.* **2020**, *785* (1). https://doi.org/10.1088/1757-899X/785/1/012026.
(260) Ng, W. M.; Katiyar, A.; Mathivanan, V.; Teng, X. J.; Leong, S. S.; Low, S. C.; Lim, J. K. Sedimentation Kinetics of Magnetic Nanoparticle Clusters: Iron Oxide Nanospheres vs Nanorods. *Langmuir* **2020**, *36* (19), 5085–5095. https://doi.org/10.1021/acs.langmuir.0c00135.
(261) McCubbin Stepanic, O.; Ward, J.; Penner-Hahn, J. E.; Deb, A.; Bergmann, U.; Debeer, S. Probing a Silent Metal: A Combined X-Ray Absorption and Emission Spectroscopic Study of Biologically Relevant Zinc Complexes. *Inorg. Chem.* **2020**, *59* (18), 13551–13560. https://doi.org/10.1021/acs.inorgchem.0c01931.
(262) Castorina, E.; Ingall, E. D.; Morton, P. L.; Tavakoli, D. A.; Lai, B. Zinc K-Edge XANES Spectroscopy of Mineral and Organic Standards. *J. Synchrotron Radiat.* **2019**, *26*, 1302–1309. https://doi.org/10.1107/S160057751900540X.
(263) van Niekerk, J. N.; Schoening, F. R. L.; Talbot, J. H. The Crystal Structure of Zinc Acetate Dihydrate, Zn(CH3COO)2.2H2O. *Acta Crystallogr.* **1953**, *6* (8), 720–723. https://doi.org/10.1107/s0365110x53002015.
(264) Wu, Y.; Mirrielees, K. J.; Irving, D. L. On Native Point Defects in ZnSe. *Appl. Phys. Lett.* **2022**, *120* (23). https://doi.org/10.1063/5.0092736.
(265) Nadupalli, S.; Repp, S.; Weber, S.; Erdem, E. About Defect Phenomena in ZnO Nanocrystals. *Nanoscale* **2021**, *13* (20), 9160–9171. https://doi.org/10.1039/d1nr00943e.
(266) Rossi, T.; Penfold, T. J.; Rittmann-Frank, M. H.; Reinhard, M.; Rittmann, J.; Borca, C. N.; Grolimund, D.; Milne, C. J.; Chergui, M. Characterizing the Structure and Defect Concentration of ZnO Nanoparticles in a Colloidal Solution. *J. Phys. Chem. C* **2014**, *118* (33), 19422–19430. https://doi.org/10.1021/jp505559u.
(267) Hsu, H. S.; Huang, J. C. A.; Huang, Y. H.; Liao, Y. F.; Lin, M. Z.; Lee, C. H.; Lee, J. F.; Chen, S. F.; Lai, L. Y.; Liu, C. P. Evidence of Oxygen Vacancy Enhanced Room-Temperature Ferromagnetism in Co-Doped ZnO. *Appl. Phys. Lett.* **2006**, *88* (24). https://doi.org/10.1063/1.2212277.
(268) Kahraman, A.; Socie, E.; Nazari, M.; Kazazis, D.; Buldu-Akturk, M.; Kabanova, V.; Biasin, E.; Smolentsev, G.; Grolimund, D.; Erdem, E.; Moser, J. E.; Cannizzo, A.; Bacellar, C.; Milne, C. Tailoring P-Type Behavior in ZnO Quantum Dots through Enhanced Sol-Gel Synthesis: Mechanistic Insights into Zinc Vacancies. *J. Phys. Chem. Lett.* **2024**, *15* (6), 1755–1764. https://doi.org/10.1021/acs.jpclett.3c03519.
(269) Gubicza, J. *Defect Structure and Properties of Nanomaterials*; Woodhead Publishing, Elsevier, 2017. https://doi.org/10.1016/B978-0-08-101917-7.01001-X.
(270) Kim, B. J.; Kim, H.; Jung, W. H.; Choi, Y.; Kim, D. H.; Lee, H.; Park, K.; Jeong, M. S.; Park, J. S.; Lim, J. Unlocking Invisible Defects of ZnSe Alloy Shells in Giant Quantum Dots with Near Unity Quantum Yield. *Adv. Energy Mater.* **2024**, *2400148*, 1–12. https://doi.org/10.1002/aenm.202400148.
(271) Rehr, J. J.; Kas, J. J.; Vila, F. D.; Prange, M. P.; Jorissen, K. Parameter-Free Calculations of X-Ray Spectra with FEFF9. *Phys. Chem. Chem. Phys.* **2010**, *12* (21), 5503–5513. https://doi.org/10.1039/b926434e.
(272) Rehr, J. J.; Albers, R. C. Theoretical Approaches to X-Ray Absorption Fine Structure. *Rev. Mod. Phys.* **2000**, *72* (3), 621–654. https://doi.org/10.1103/RevModPhys.72.621.
(273) Rehr, J. J.; Jorissen, K.; Ankudinov, A.; Ravel, B. Feff9.6 User's Guide

https://feff.phys.washington.edu/feff/Docs/feff9/feff90/feff90_users_guide.pdf (accessed Apr 24, 2024).
(274) Ravel, B.; Newville, M. ATHENA, ARTEMIS, HEPHAESTUS: Data Analysis for X-Ray Absorption Spectroscopy Using IFEFFIT. *J. Synchrotron Radiat.* **2005**, *12* (4), 537–541. https://doi.org/10.1107/S0909049505012719.
(275) Stern, E. A.; Kim, K. Thickness Effect on the Extended-x-Ray-Absorption-Fine-Structure Amplitude. *Phys. Rev. B* **1981**, *23* (8), 3781–3787. https://doi.org/10.1103/PhysRevB.23.3781.
(276) Mottram, L. M.; Dixon Wilkins, M. C.; Blackburn, L. R.; Oulton, T.; Stennett, M. C.; Sun, S. K.; Corkhill, C. L.; Hyatt, N. C. A Feasibility Investigation of Laboratory Based X-Ray Absorption Spectroscopy in Support of Nuclear Waste Management. *MRS Adv.* **2020**, *5*, 27–35. https://doi.org/10.1557/adv.2020.44.
(277) Astra beamline layout https://synchrotron.uj.edu.pl/en_GB/linie-badawcze/astra/schemat-linii (accessed Apr 29, 2024).
(278) The Atoms.inp Archive https://millenia.cars.aps.anl.gov/atomsdb/index.html (accessed May 1, 2024).
(279) WebAtoms https://millenia.cars.aps.anl.gov/webatoms?url=https://millenia.cars.aps.anl.gov/atomsdb/Adamite.inp (accessed May 1, 2024).
(280) Chattopadhyay, S.; Kulkarni, N. V.; Choudhury, K.; Prasad, R.; Shahee, A.; Raja Sekhar, B. N.; Sen, P. Lattice Expansion in ZnSe Quantum Dots. *Mater. Lett.* **2011**, *65* (11), 1625–1627. https://doi.org/10.1016/j.matlet.2011.03.002.
(281) Pimachev, A.; Proshchenko, V.; Horoz, S.; Sahin, O.; Dahnovsky, Y. The Effect of Spatial Distribution of Zn Vacancies in ZnS Quantum Dots on Optical Absorption Spectra. *Solid State Commun.* **2017**, *257* (March), 47–49. https://doi.org/10.1016/j.ssc.2017.04.004.
(282) Jasieniak, J.; Mulvaney, P. From Cd-Rich to Se-Rich - The Manipulation of CdSe Nanocrystal Surface Stoichiometry. *J. Am. Chem. Soc.* **2007**, *129* (10), 2841–2848. https://doi.org/10.1021/ja066205a.
(283) ELI USER PORTAL https://up.eli-laser.eu/equipment/fsrs-ta-819626062 (accessed May 4, 2024).
(284) Rakshit, S.; Datta, A.; Das, S. Interplay of Multiexciton Relaxation and Carrier Trapping in Photoluminescent CdS Quantum Dots Prepared in Aqueous Medium. *J. Phys. Chem. C* **2020**, *124* (51), 28313–28322. https://doi.org/10.1021/acs.jpcc.0c09366.
(285) Jasrasaria, D.; Philbin, J. P.; Yan, C.; Weinberg, D.; Alivisatos, A. P.; Rabani, E. Sub-Bandgap Photoinduced Transient Absorption Features in CdSe Nanostructures: The Role of Trapped Holes. *J. Phys. Chem. C* **2020**, *124* (31), 17372–17378. https://doi.org/10.1021/acs.jpcc.0c04746.
(286) Li, D.; He, X.; Zhao, L.; Li, H.; Zhao, Y.; Zhang, S.; Zhang, X.; Chen, J.; Jin, Q.; Xu, J. The Interaction between Semiconductor ZnSe Quantum Dots and Graphene Oxide: Ultrafast Charge Transfer Dynamics. *J. Lumin.* **2022**, *252* (October), 119422. https://doi.org/10.1016/j.jlumin.2022.119422.
(287) Klimov, V.; Bolivar, P. H.; Kurz, H. Ultrafast Carrier Dynamics in Semiconductor Quantum Dots. *Phys. Rev. B - Condens. Matter Mater. Phys.* **1996**, *53* (3), 1463–1467. https://doi.org/10.1103/PhysRevB.53.1463.
(288) Gogoi, H.; Pathak, S. S.; Dasgupta, S.; Panchakarla, L. S.; Nath, S.; Datta, A. Exciton Dynamics in Colloidal CdS Quantum Dots with Intense and Stokes Shifted Photoluminescence in a Single Decay Channel. *J. Phys. Chem. Lett.* **2022**, *13* (29), 6770–6776. https://doi.org/10.1021/acs.jpclett.2c01623.
(289) Wu, K.; Du, Y.; Tang, H.; Chen, Z.; Lian, T. Efficient Extraction of Trapped Holes from Colloidal CdS Nanorods. *J. Am. Chem. Soc.* **2015**, *137* (32), 10224–10230. https://doi.org/10.1021/jacs.5b04564.
(290) He, S.; Li, Q.; Jin, T.; Lian, T. Contributions of Exciton Fine Structure and Hole Trapping on the Hole State Filling Effect in the Transient Absorption Spectra of CdSe Quantum Dots. *J. Chem. Phys.* **2022**, *156* (5). https://doi.org/10.1063/5.0081192.
(291) Dana, J.; Haggag, O. S.; Dehnel, J.; Mor, M.; Lifshitz, E.; Ruhman, S. Testing the Fate of Nascent Holes in CdSe Nanocrystals with Sub-10 Fs Pump-Probe Spectroscopy. *Nanoscale* **2021**, *13* (3), 1982–1987. https://doi.org/10.1039/d0nr07651a.
(292) Grimaldi, G.; Geuchies, J. J.; Van Der Stam, W.; Du Fossé, I.; Brynjarsson, B.; Kirkwood, N.; Kinge, S.; Siebbeles, L. D. A.; Houtepen, A. J. Spectroscopic Evidence for the Contribution of Holes to the Bleach of Cd-Chalcogenide Quantum Dots. *Nano Lett.* **2019**, *19* (5), 3002–3010. https://doi.org/10.1021/acs.nanolett.9b00164.
(293) Morgan, D. P.; Kelley, D. F. What Does the Transient Absorption Spectrum of CdSe Quantum Dots Measure? *J. Phys. Chem. C* **2020**, *124* (15), 8448–8455. https://doi.org/10.1021/acs.jpcc.0c02566.
(294) Mcneil, B. W. J.; Thompson, N. R. X-Ray Free-Electron Lasers. *Nat. Photonics* **2010**, *4* (12), 814–

821. https://doi.org/10.1038/nphoton.2010.239.
(295) Kraus, P. M.; Zürch, M.; Cushing, S. K.; Neumark, D. M.; Leone, S. R. The Ultrafast X-Ray Spectroscopic Revolution in Chemical Dynamics. *Nat. Rev. Chem.* **2018**, *2* (6), 82–94. https://doi.org/10.1038/s41570-018-0008-8.
(296) Nguyen, R. C.; Davis, I.; Dasgupta, M.; Wang, Y.; Simon, P. S.; Butryn, A.; Makita, H.; Bogacz, I.; Dornevil, K.; Aller, P.; Bhowmick, A.; Chatterjee, R.; Kim, I. S.; Zhou, T.; Mendez, D.; Paley, D. W.; Fuller, F.; Alonso Mori, R.; Batyuk, A.; Sauter, N. K.; Brewster, A. S.; Orville, A. M.; Yachandra, V. K.; Yano, J.; Kern, J. F.; Liu, A. In Situ Structural Observation of a Substrate- and Peroxide-Bound High-Spin Ferric-Hydroperoxo Intermediate in the P450 Enzyme CYP121. *J. Am. Chem. Soc.* **2023**, *145* (46), 25120–25133. https://doi.org/10.1021/jacs.3c04991.
(297) Ekeberg, T.; Assalauova, D.; Bielecki, J.; Boll, R.; Daurer, B. J.; Eichacker, L. A.; Franken, L. E.; Galli, D. E.; Gelisio, L.; Gumprecht, L.; Gunn, L. H.; Hajdu, J.; Hartmann, R.; Hasse, D.; Ignatenko, A.; Koliyadu, J.; Kulyk, O.; Kurta, R.; Kuster, M.; Lugmayr, W.; Lübke, J.; Mancuso, A. P.; Mazza, T.; Nettelblad, C.; Ovcharenko, Y.; Rivas, D. E.; Rose, M.; Samanta, A. K.; Schmidt, P.; Sobolev, E.; Timneanu, N.; Usenko, S.; Westphal, D.; Wollweber, T.; Worbs, L.; Xavier, P. L.; Yousef, H.; Ayyer, K.; Chapman, H. N.; Sellberg, J. A.; Seuring, C.; Vartanyants, I. A.; Küpper, J.; Meyer, M.; Maia, F. R. N. C. Observation of a Single Protein by Ultrafast X-Ray Diffraction. *Light Sci. Appl.* **2024**, *13* (1). https://doi.org/10.1038/s41377-023-01352-7.
(298) Bortel, G.; Tegze, M.; Sikorski, M.; Bean, R.; Bielecki, J.; Kim, C.; Koliyadu, J. C. P.; Koua, F. H. M.; Ramilli, M.; Round, A.; Sato, T.; Zabelskii, D.; Faigel, G. 3D Atomic Structure from a Single X-Ray Free Electron Laser Pulse. *Nat. Commun.* **2024**, *15* (1), 2–8. https://doi.org/10.1038/s41467-024-45229-8.
(299) Thielemann-Kühn, N.; Amrhein, T.; Bronsch, W.; Jana, S.; Pontius, N.; Engel, R. Y.; Miedema, P. S.; Legut, D.; Carva, K.; Atxitia, U.; van Kuiken, B. E.; Teichmann, M.; Carley, R. E.; Mercadier, L.; Yaroslavtsev, A.; Mercurio, G.; Guyader, L. Le; Agarwal, N.; Gort, R.; Scherz, A.; Beye, M.; Oppeneer, P. M.; Weinelt, M.; Schüßler-Langeheine, C. Optical Control of 4f Orbital State in Rare-Earth Metals. *Sci. Adv.* **2021**, *9522* (April), 1–10. https://doi.org/10.1126/sciadv.adk9522.
(300) Callegari, C.; Grum-Grzhimailo, A. N.; Ishikawa, K. L.; Prince, K. C.; Sansone, G.; Ueda, K. Atomic, Molecular and Optical Physics Applications of Longitudinally Coherent and Narrow Bandwidth Free-Electron Lasers. *Phys. Rep.* **2021**, *904*, 1–59. https://doi.org/10.1016/j.physrep.2020.12.002.
(301) Prince, K. C.; Allaria, E.; Callegari, C.; Cucini, R.; De Ninno, G.; Di Mitri, S.; Diviacco, B.; Ferrari, E.; Finetti, P.; Gauthier, D.; Giannessi, L.; Mahne, N.; Penco, G.; Plekan, O.; Raimondi, L.; Rebernik, P.; Roussel, E.; Svetina, C.; Trovò, M.; Zangrando, M.; Negro, M.; Carpeggiani, P.; Reduzzi, M.; Sansone, G.; Grum-Grzhimailo, A. N.; Gryzlova, E. V.; Strakhova, S. I.; Bartschat, K.; Douguet, N.; Venzke, J.; Iablonskyi, D.; Kumagai, Y.; Takanashi, T.; Ueda, K.; Fischer, A.; Coreno, M.; Stienkemeier, F.; Ovcharenko, Y.; Mazza, T.; Meyer, M. Coherent Control with a Short-Wavelength Free-Electron Laser. *Nat. Photonics* **2016**, *10* (3), 176–179. https://doi.org/10.1038/nphoton.2016.13.
(302) Maroju, P. K.; Grazioli, C.; Di Fraia, M.; Moioli, M.; Ertel, D.; Ahmadi, H.; Plekan, O.; Finetti, P.; Allaria, E.; Giannessi, L.; De Ninno, G.; Spezzani, C.; Penco, G.; Spampinati, S.; Demidovich, A.; Danailov, M. B.; Borghes, R.; Kourousias, G.; Sanches Dos Reis, C. E.; Billé, F.; Lutman, A. A.; Squibb, R. J.; Feifel, R.; Carpeggiani, P.; Reduzzi, M.; Mazza, T.; Meyer, M.; Bengtsson, S.; Ibrakovic, N.; Simpson, E. R.; Mauritsson, J.; Csizmadia, T.; Dumergue, M.; Kühn, S.; Nandiga Gopalakrishna, H.; You, D.; Ueda, K.; Labeye, M.; Bækhøj, J. E.; Schafer, K. J.; Gryzlova, E. V.; Grum-Grzhimailo, A. N.; Prince, K. C.; Callegari, C.; Sansone, G. Attosecond Pulse Shaping Using a Seeded Free-Electron Laser. *Nature* **2020**, *578* (7795), 386–391. https://doi.org/10.1038/s41586-020-2005-6.
(303) Rivas, D. E.; Serkez, S.; Baumann, T. M.; Boll, R.; Czwalinna, M. K.; Dold, S.; de Fanis, A.; Gerasimova, N.; Grychtol, P.; Lautenschlager, B.; Lederer, M.; Jezynksi, T.; Kane, D.; Mazza, T.; Meier, J.; Müller, J.; Pallas, F.; Rompotis, D.; Schmidt, P.; Schulz, S.; Usenko, S.; Venkatesan, S.; Wang, J.; Meyer, M. High-Temporal-Resolution X-Ray Spectroscopy with Free-Electron and Optical Lasers. *Optica* **2022**, *9* (4), 429. https://doi.org/10.1364/optica.454920.
(304) Sato, T.; Letrun, R.; Kirkwood, H. J.; Liu, J.; Vagovič, P.; Mills, G.; Kim, Y.; Takem, C. M. S.; Planas, M.; Emons, M.; Jezynski, T.; Palmer, G.; Lederer, M.; Schulz, S.; Mueller, J.; Schlarb, H.; Silenzi, A.; Giovanetti, G.; Parenti, A.; Bergemann, M.; Michelat, T.; Szuba, J.; Grünert, J.; Chapman, H. N.; Mancuso, A. P. Femtosecond Timing Synchronization at Megahertz Repetition Rates for an X-Ray Free-Electron Laser. *Optica* **2020**, *7* (6), 716. https://doi.org/10.1364/optica.396728.
(305) Błachucki, W.; Wach, A.; Czapla-Masztafiak, J.; Delcey, M.; Arrell, C.; Fanselow, R.; Juranić, P.; Lundberg, M.; Milne, C.; Sá, J.; Szlachetko, J. Approaching the Attosecond Frontier of Dynamics in Matter with the Concept of X-Ray Chronoscopy. *Appl. Sci.* **2022**, *12* (3).

https://doi.org/10.3390/app12031721.
(306) Hatada, K.; Di Cicco, A. Modeling Saturable Absorption for Ultra Short X-Ray Pulses. *J. Electron Spectros. Relat. Phenomena* **2014**, *196*, 177–180. https://doi.org/10.1016/j.elspec.2014.02.012.
(307) Lipp, V.; Tkachenko, V.; Stransky, M.; Aradi, B.; Frauenheim, T.; Ziaja, B. Density Functional Tight Binding Approach Utilized to Study X-Ray-Induced Transitions in Solid Materials. *Sci. Rep.* **2022**, *12* (1), 1–10. https://doi.org/10.1038/s41598-022-04775-1.
(308) Engel, R. Y.; Alexander, O.; Atak, K.; Bovensiepen, U.; Buck, J.; Carley, R.; Cascella, M.; Chardonnet, V.; Chiuzbaian, G. S.; David, C.; Döring, F.; Eschenlohr, A.; Gerasimova, N.; Groot, F. De; Guyader, L. Le; Humphries, O. S.; Izquierdo, M.; Jal, E.; Kubec, A.; Laarmann, T.; Lambert, C.; Lüning, J.; Marangos, J. P.; Mercadier, L.; Mercurio, G.; Miedema, P. S.; Ollefs, K.; Pfau, B.; Rösner, B.; Rossnagel, K.; Rothenbach, N.; Scherz, A.; Schlappa, J.; Scholz, M.; Schunck, J. O.; Setoodehnia, K.; Stamm, C.; Techert, S.; Vinko, S. M.; Wende, H.; Yaroslavtsev, A. A.; Yin, Z.; Beye, M.; Engel, R. Y.; Alexander, O.; Atak, K.; Bovensiepen, U.; Carley, R.; Cascella, M.; Guyader, L. Le; Izquierdo, M.; Jal, E.; Lambert, C. Electron Population Dynamics in Resonant Non-Linear x-Ray Absorption in Nickel at a Free-Electron Laser. *Struct. Dyn.* **2023**, *10* (June 2019), 054501, 1–21. https://doi.org/10.1063/4.0000206.
(309) Carlson, T. A.; Krause, M. O. Atomic Readjustment to Vacancies in the K and L Shells of Argon. *Phys. Rev.* **1965**, *137* (6A). https://doi.org/10.1103/PhysRev.137.A1655.
(310) Chen, M. H. Relativistic Calculation of Atomic Transition Probabilities. *At. Inn. Phys.* **1985**, 31–95. https://doi.org/10.1007/978-1-4613-2417-1_2.
(311) Chaynikov, A. P.; Kochur, A. G.; Dudenko, A. I.; Yavna, V. A. Cascade Energy Reemission after Inner-Shell Ionization of Atomic Gold. Role of Photo- and Cascade-Produced Electrons in Radiosensitization Using Gold-Containing Agents. *J. Quant. Spectrosc. Radiat. Transf.* **2023**, *302*. https://doi.org/10.1016/j.jqsrt.2023.108561.
(312) Durbin, S. M.; Clevenger, T.; Graber, T.; Henning, R. X-Ray Pump Optical Probe Cross-Correlation Study of GaAs. *Nat. Photonics* **2012**, *6* (2), 111–114. https://doi.org/10.1038/nphoton.2011.327.
(313) Chang, H.-T.; Zürch, M.; Kraus, P. M.; Borja, L. J.; Neumark, D. M.; Leone, S. R. Simultaneous Generation of Sub-5-Femtosecond 400 Nm and 800 Nm Pulses for Attosecond Extreme Ultraviolet Pump–Probe Spectroscopy. *Opt. Lett.* **2016**, *41* (22), 5365. https://doi.org/10.1364/ol.41.005365.
(314) Zhou, G.; Jiao, Y.; Raubenheimer, T. O.; Wang, J.; Holman, A. J.; Tsai, C.-Y.; Wu, J. Y.; Wu, W.; Yang, C.; Yoon, M.; Wu, J. Coherence Time Characterization Method for Hard X-Ray Free-Electron Lasers. *Opt. Express* **2020**, *28* (8), 10928. https://doi.org/10.1364/oe.28.010928.
(315) Zhou, G.; Decker, F. J.; Ding, Y.; Jiao, Y.; Lutman, A. A.; Maxwell, T. J.; Raubenheimer, T. O.; Wang, J.; Holman, A. J.; Tsai, C. Y.; Wu, J. Y.; Wu, W.; Yang, C.; Yoon, M.; Wu, J. Attosecond Coherence Time Characterization in Hard X-Ray Free-Electron Laser. *Sci. Rep.* **2020**, *10* (1), 4–11. https://doi.org/10.1038/s41598-020-60328-4.
(316) Sun, Y. P.; Liu, J. C.; Wang, C. K.; Gel'Mukhanov, F. Propagation of a Strong X-Ray Pulse: Pulse Compression, Stimulated Raman Scattering, Amplified Spontaneous Emission, Lasing without Inversion, and Four-Wave Mixing. *Phys. Rev. A - At. Mol. Opt. Phys.* **2010**, *81* (1), 1–11. https://doi.org/10.1103/PhysRevA.81.013812.
(317) Savchenko, V.; Gel'mukhanov, F.; Laarmann, T.; Polyutov, S. P.; Kimberg, V. Dynamical Phase Shift in X-Ray Absorption and Ionization Spectra by Two Delayed x-Ray Laser Fields. *Phys. Rev. A* **2021**, *104* (1), 1–9. https://doi.org/10.1103/PhysRevA.104.013114.
(318) Wieland, M.; Kabachnik, N. M.; Drescher, M.; Deng, Y.; Arbelo, Y.; Stojanovic, N.; Steffen, B.; Roensch-Schulenburg, J.; Ischebeck, R.; Malyzhenkov, A.; Prat, E.; Juranić, P. Deriving X-Ray Pulse Duration from Center-of-Energy Shifts in THz-Streaked Ionized Electron Spectra. *Opt. Express* **2021**, *29* (21), 32739. https://doi.org/10.1364/oe.432761.
(319) Schoonjans, T.; Brunetti, A.; Golosio, B.; Sanchez Del Rio, M.; Solé, V. A.; Ferrero, C.; Vincze, L. The Xraylib Library for X-Ray-Matter Interactions. Recent Developments. *Spectrochim. Acta - Part B At. Spectrosc.* **2011**, *66* (11–12), 776–784. https://doi.org/10.1016/j.sab.2011.09.011.
(320) Abdellah, M.; Karki, K. J.; Lenngren, N.; Zheng, K.; Pascher, T.; Yartsev, A.; Pullerits, T. Ultra Long-Lived Radiative Trap States in CdSe Quantum Dots. *J. Phys. Chem. C* **2014**, *118* (37), 21682–21686. https://doi.org/10.1021/jp506536h.
(321) Neukirch, A. J.; Neumark, D. M.; Kling, M. F.; Prezhdo, O. V. Resolving Multi-Exciton Generation by Attosecond Spectroscopy. *Opt. Express* **2014**, *22* (21), 26285. https://doi.org/10.1364/oe.22.026285.
(322) Weiner, A. M. Ultrafast Optical Pulse Shaping: A Tutorial Review. *Opt. Commun.* **2011**, *284* (15), 3669–3692. https://doi.org/10.1016/j.optcom.2011.03.084.
(323) Goswami, D. Intense Femtosecond Optical Pulse Shaping Approaches to Spatiotemporal Control. *Front. Chem.* **2023**, *10* (January), 1–12. https://doi.org/10.3389/fchem.2022.1006637.

(324) Guo, B.; Sun, J.; Hua, Y.; Zhan, N.; Jia, J.; Chu, K. *Femtosecond Laser Micro/Nano-Manufacturing: Theories, Measurements, Methods, and Applications*; Springer Singapore, 2020; Vol. 3. https://doi.org/10.1007/s41871-020-00056-5.

(325) Hartmann, N.; Hartmann, G.; Heider, R.; Wagner, M. S.; Ilchen, M.; Buck, J.; Lindahl, A. O.; Benko, C.; Grünert, J.; Krzywinski, J.; Liu, J.; Lutman, A. A.; Marinelli, A.; Maxwell, T.; Miahnahri, A. A.; Moeller, S. P.; Planas, M.; Robinson, J.; Kazansky, A. K.; Kabachnik, N. M.; Viefhaus, J.; Feurer, T.; Kienberger, R.; Coffee, R. N.; Helml, W. Attosecond Time-Energy Structure of X-Ray Free-Electron Laser Pulses. *Nat. Photonics* **2018**, *12* (4), 215–220. https://doi.org/10.1038/s41566-018-0107-6.

(326) Duris, J.; Li, S.; Driver, T.; Champenois, E. G.; MacArthur, J. P.; Lutman, A. A.; Zhang, Z.; Rosenberger, P.; Aldrich, J. W.; Coffee, R.; Coslovich, G.; Decker, F. J.; Glownia, J. M.; Hartmann, G.; Helml, W.; Kamalov, A.; Knurr, J.; Krzywinski, J.; Lin, M. F.; Marangos, J. P.; Nantel, M.; Natan, A.; O'Neal, J. T.; Shivaram, N.; Walter, P.; Wang, A. L.; Welch, J. J.; Wolf, T. J. A.; Xu, J. Z.; Kling, M. F.; Bucksbaum, P. H.; Zholents, A.; Huang, Z.; Cryan, J. P.; Marinelli, A. Tunable Isolated Attosecond X-Ray Pulses with Gigawatt Peak Power from a Free-Electron Laser. *Nat. Photonics* **2020**, *14* (1), 30–36. https://doi.org/10.1038/s41566-019-0549-5.

(327) Yu, K.; Huang, H. B.; Wang, J. T.; Liu, G. F.; Zhong, Z.; Li, Y. F.; Cao, H. L.; Lü, J.; Cao, R. Engineering Cation Defect-Mediated Z-Scheme Photocatalysts for a Highly Efficient and Stable Photocatalytic Hydrogen Production. *J. Mater. Chem. A* **2021**, *9* (12), 7759–7766. https://doi.org/10.1039/d0ta12269f.

(328) Mo, Z.; Zhu, X.; Jiang, Z.; Song, Y.; Liu, D.; Li, H. Applied Catalysis B : Environmental Porous Nitrogen-Rich g-C 3 N 4 Nanotubes for e Ffi Cient Photocatalytic CO 2 Reduction. *Appl. Catal. B Environ.* **2019**, *256* (June), 117854.

List of publications

1. Wojciech Błachucki, Yves Kayser, Anna Wach, Rafał Fanselow, Christopher Milne, Jacinto Sá and Jakub Szlachetko, ***Resonant X-ray Emission Spectroscopy with a SASE Beam***, MDPI, Applied Sciences, 11, 8775 (2021).

2. Rafał Fanselow, Anna Wach, Wojciech Błachucki and Jakub Szlachetko, ***Microliter-stirred sample setup for X-ray spectroscopy analysis of nanomaterials in suspension***, Elsevier, Spectrochimica Acta Part B: Atomic Spectroscopy, 189, 106367 (2022).

3. Wojciech Błachucki, , Anna Wach, Joanna Czapla-Masztafiak, Mickaël Delcey, Christopher Arrell, Rafał Fanselow, Pavle Juranic, Marcus Lundberg, Christopher Milne, Jacinto Sá and Jakub Szlachetko, ***Approaching the Attosecond Frontier of Dynamics in Matter with the Concept of X-ray Chronoscopy***, MDPI, Applied Sciences, 12, 1721 (2022).

4. Michał Nowakowski, Aleksandr Kalinko, Jakub Szlachetko, Rafał Fanselow and Matthias Bauer, ***High resolution off resonant spectroscopy as a probe of the oxidation state***, the Royal Society of Chemistry, Journal of Analytical Atomic Spectrometry, 37, 2383 (2022).

5. Rafał Fanselow, Michał Sobstel, Wojciech Błachucki and Jakub Szlachetko, ***Performance of a laboratory von Hamos type x-ray spectrometer in x-ray absorption spectroscopy study on 3d group metals***, Wiley, X-ray Spectrometry, 52, 247 (2022).

6. Anna Wach, Gabriela Imbir, Rafał Fanselow, Wojciech Błachucki and Jakub Szlachetko, ***Consideration of the Potential of High Energy Resolution X-ray Absorption and X-ray Emission Experiments to Track Changes in Oxidation States on Nanoparticle Materials***, Institute of Physics Polish Academy of Sciences, Acta Physica Polonica A, 145, 97 (2024).

Conferences

1. European XFEL Users' Meeting 2021, online, 25-29.01.2021, poster presentation: ***Lab-based X-ray spectroscopy setup for measurements of liquid samples***;

2. XFELs for Beginners 2021, online, 27-28.04.2021, oral presentation: ***Is my liquid jet system ready for XFEL experiment? – laboratory XES verification***;

3. XFELs for Beginners 2021, online, 27-28.04.2021, oral presentation: ***Preparing the sample for an XFEL campaign***;

4. XAFS2021 Virtual, online, 11-13.07.2021, oral presentation: ***Microliter-stirred sample setup for X-ray spectroscopy analysis of nanomaterials in suspension***;

5. European XFEL Users' Meeting 2022, online, 21-27.01.2022, poster presentation: ***Development of the sample setup for X-ray spectroscopy analysis of nanomaterials in suspension***;

6. Visegrad closure meeting, Kraków, Poland, 29-31.05.2022, oral presentation: ***Laboratory X-ray spectroscopy at IFJ PAN – current status and recent developments***;

7. European Conference on X-ray Spectrometry 2022 (EXRS 2022), Brugge, Belgium, 26.06-01.07.2022, poster presentation: ***Special microliter-stirred sample system dedicated for X-ray spectroscopy studies of nanomaterial suspensions***;

8. ISSRNS 2022 The 15th International School and Symposium on Synchrotron Radiation in Natural Science, Kraków, Poland, 22-25.08.2022, oral presentation: ***Development of the sample setup for X-ray spectroscopy analysis of nanomaterials in suspension***;

9. Joint Meeting of PSRS Members and SOLARIS Centre Users, Kraków, Poland, 20-23.09.2022, poster presentation: ***Application of X-ray spectroscopy in studies of ZnSe quantum dots***;

10. Joint Meeting of PSRS Members and SOLARIS Centre Users, Kraków, Poland, 20-23.09.2022, poster presentation: ***Sensitivity of the Astra beamline at hard X-ray energies***;

11. International Workshop on Laboratory-based Spectroscopies 2022, Helsinki, Finland, 24-25.11.2022, oral presentation: ***Laboratory-based x-ray spectroscopy as a tool for probing nanomaterials***;

12. Zakopane School of Physics 2023, Zakopane, Poland, 23-27.05.2023, oral presentation: ***Clocking ultrashort processes with X-ray Chronoscopy***;

13. European X-ray Spectrometry Conference - EXRS 2024, Athens, Greece, 24-28.06.2024, oral presentation: ***Exploring the electronic structure of Zinc Selenide Quantum Dots with X-ray Spectroscopy***;

14. European X-ray Spectrometry Conference - EXRS 2024, Athens, Greece, 24-28.06.2024, poster presentation: ***Spectroscopic study of quantum dot-plasmonic nanoparticle hybrid systems***;